DISSERTATION | DOCTORAL THESIS

Titel | Title

A complex of MAST1 and 14-3-3 eta regulates Tau phosphorylation in the developing cortex

verfasst von | submitted by

Sumire Antonioli

angestrebter akademischer Grad | in partial fulfilment of the requirements for the degree of

Doctor of Philosophy (PhD)

Wien | Vienna, 2026

Studienkennzahl lt. Studienblatt | Degree programme code as it appears on the student record sheet:	UA 794 620 490
Dissertationsgebiet lt. Studienblatt | Field of study as it appears on the student record sheet:	Molekulare Biologie
Betreut von | Supervisor:	Thomas Leonard B.Sc. PhD

Acknowledgements

First and foremost, I would like to thank my supervisor, Thomas. I could not have asked for a more supportive and enthusiastic mentor. You have taught me the importance of careful and honest science, while also fostering a collaborative and fun lab environment. Your approach to research has shaped my way of thinking as a scientist and is something I will carry with me throughout my career.

To all lab members, particularly my fellow PhDs Ronja, Lucas, Eva, Magda, and Felix – thank you for the unforgettable memories. You have been my second family in Vienna, and I couldn't have done this without your constant encouragement through the highs and lows. Thank you also to our neighbours in the Falk lab, especially Virginia and Toni. I could always count on you for a pep talk in the change room.

I would like to thank our collaborators, Dave Keays and Patrick Heisterkamp. It's been a real pleasure exploring the MAST project together, and I thoroughly enjoyed our mini-symposium meet-ups. I am also grateful to my TAC members, Dave Keays and Clemens Plaschka. Thank you for your thoughtful guidance and your confidence in me to overcome the many challenges. A big thank you to the mass spectrometry facility – Markus, Dorothea, and WeiQiang – my project simply would not have been possible without your outstanding help. You are truly the best mass spec facility the world has ever seen!

To my mum, dad, and brother, the hardest part of my PhD was being so far away from all of you. Thank you for always being there for me despite the distance and time zones. No one has ever believed in me as much as you guys. And finally, Jamie, what an adventure this has been! Thank you from the bottom of my heart for your love, support, and for sharing this crazy experience with me. Every moment was made better with you by my side.

Abstract

The process of cortical development is essential and extremely delicate, requiring the precise spatial and temporal control of molecular programs. A wide range of neurodevelopmental disorders (NDDs) can arise from the dysregulation of this process and affect approximately a tenth of our population. A rare NDD termed mega-corpus callosum syndrome (MCC) is characterised by an enlargement of the corpus callosum and global developmental delay. The only known cause of MCC is the mutation of a gene called microtubule-associated serine/threonine kinase 1 (MAST1). Recently, MAST1, as well as other members of the MAST kinase family, have frequently been reported to be linked to multiple NDDs and neurological disorders including autism, intellectual disability, epilepsy, and cerebral palsy. Despite this, very little is known about the biological roles and mechanism of action of the MAST kinases.

This work investigates the largely unexplored field of MAST kinase biology by examining its substrates, interaction partners, and mechanisms of regulation. We show that 14-3-3η is an interaction partner of MAST1, binding to S90 and S161 of MAST1 in a phosphorylation-dependent manner. We identify p21-activated protein kinase (PAK) as an upstream kinase of MAST1, phosphorylating it on S90, and demonstrate the ability of MAST1 to autophosphorylate on S161. Using *in vivo* phosphoproteomics with MAST1 mutant mouse models, we propose the microtubule-associated protein tau (MAPT, Tau) as a substrate of MAST1. Finally, we show that the disease-associated MAST1 mutations either cause misfolding of the protein or perturb kinase activity. Taken together, we suggest a model where MAST1 bridges PAK, a known regulator of the actin cytoskeleton, to microtubule remodelling via Tau. Our findings contribute to the emerging field of the MAST kinases, and provide a foundation for future studies to clarify their functions and regulatory mechanisms.

Table of contents

1 Introduction

1.1 Development of the human brain

All organisms with a nervous system must undergo the process of neurodevelopment. The earliest organisms to evolve a nervous system are the Cnidarians (jellyfish and corals), roughly 700 million years ago [1]. Around 150 million years later, the Planarians (flatworms) were the first animals to evolve a bilobal, whole-body controlling brain, thought to be the ancestor of the vertebrate brain [2]. As the control centre of the body, the development of the brain is an extremely complicated and tightly regulated process, referred to as neurodevelopment. The precise proliferation, migration, and differentiation of neurons with the correct localisation and timing is essential to form specialised brain compartments and neural connections. Dysregulation of this process can cause defects in these structures, potentially resulting in neurodevelopmental disorders (NDDs).

In humans, neurodevelopment begins early in gestation and continues well into postnatal life, often extending into adolescence or early adulthood [3]. The process begins with the formation of the neural tube, known as neurulation, when precursor cells are set aside to give rise to the central nervous system. A significant portion of gestation is dedicated to neurogenesis, involving the rapid proliferation of neurons and their expansion into multiple distinct layers of brain tissue. These neurons migrate and differentiate into organised brain structures, and the general brain architecture is complete at birth. Several processes occur postnatally such as synaptogenesis, myelination, and maturation of glial cells like astrocytes and oligodendrocytes, and are crucial for cognitive and motor development.

1.1.1 Neurogenesis and the formation of the cerebral cortex

During neurulation, the neural tube exists in a three-vesicle stage comprising the prosencephalon (forebrain), mesencephalon (midbrain), and rhombencephalon (hindbrain). With the expansion of neurons in neurogenesis, these vesicles split and specialise into specific brain structures; for example, the forebrain gives rise to the telencephalon, forming the cerebral cortex and hippocampus, and the diencephalon, forming the thalamus and hypothalamus. The walls of the neural tube are made up of a

single-cell layer of neuroepithelial cells, also known as neural stem cells, with their elongated shape allowing them to contact both the lumen of the tube and the extracellular matrix (Figure 1). Capable of both symmetric and asymmetric cell division, neural stem cells give rise to nearly all cell types in the developing brain, such as neurons, glial cells, and ependymal cells [4,5].

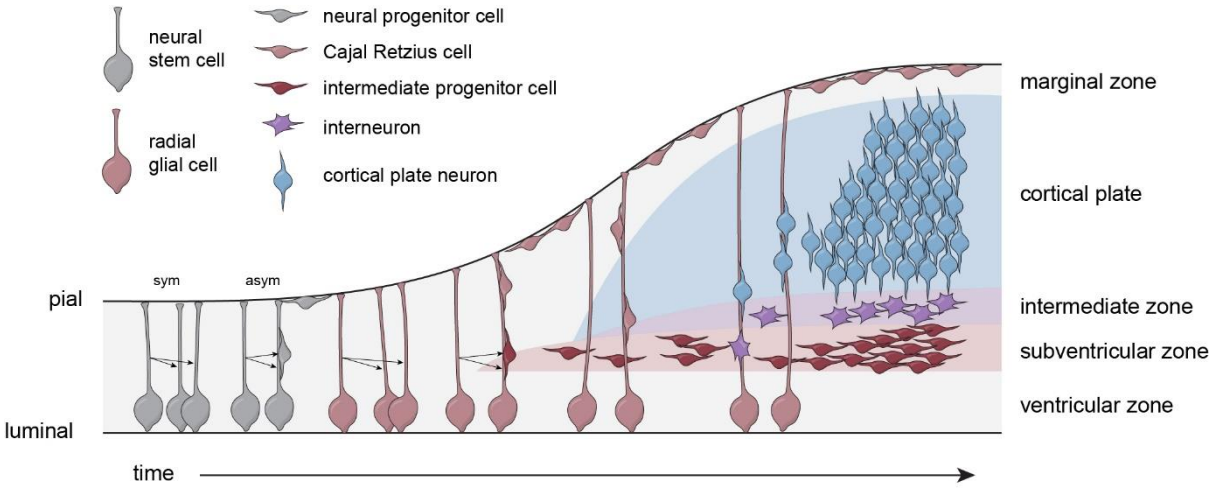

Figure 1. The process of neurogenesis.

At the start of neurogenesis, the neural tube wall is lined with one layer of neural stem cells (grey), which span the width from the apical (luminal) to the basal (pial) side. Neural stem cells undergo interkinetic nuclear migration to divide symmetrically (sym) and asymmetrically (asym). Eventually, neural stem cells transition to radial glial cells (pink), producing a higher complexity of daughter cells. These cells subsequently migrate and give rise to new layers of brain tissue, such as the cortical plate, intermediate zone, and subventricular zone. Figure adapted from Jiang et al (2016) [6].

Neural stem cells divide through a process called interkinetic nuclear migration (INM) [7]. The nucleus first migrates from the luminal side of the neural tube wall to the extracellular (pial) side, during which it undergoes DNA replication, and subsequently travels back to the luminal side. In symmetric division, the cell divides vertically, producing two identical daughter neural stem cells [8,9]. In asymmetric division, the division plane is horizontal, producing one daughter neural stem cell and one neural progenitor cell [8,9]. The new neural progenitor migrates along its sister cell towards the pial surface and differentiates into a neuron (Figure 1).

The repetition of asymmetric division gradually increases the thickness of the neural tube walls, and a layered structure begins to form, with developing neurons in the outer layers (called the marginal zone) and neural stem cells closer to the lumen (called

the ventricular zone) [10] (Figure 1). Over time, the neural stem cells start to express different markers and transition to a new cell population called radial glial cells (RGCs) [11]. While RGCs continue to undergo INM and asymmetric division, they give rise to one self-renewing RGC and a daughter cell called an intermediate progenitor cell. Similarly to neural progenitor cells, intermediate progenitors also migrate along their sister RGC and differentiate into neurons, however they establish a new zone between the ventricular and marginal zone, called the subventricular zone [12–14] (Figure 1).

As RGCs continue to divide, the expansion and migration of intermediate progenitor cells diversifies to form two new layers; the cortical plate, located immediately beneath the marginal zone and containing the youngest neurons [15,16], and the intermediate zone, one layer deeper and home to neurons destined for the formation of white matter [17] (Figure 1). In this fashion, the brain develops from the inside out, where the earliest neurons are found deep in the ventricular zone.

In the final phase of neurogenesis, RGCs split into two distinct subpopulations – outer RGCs and inner RGCs. Outer RGCs span the subventricular zone to the marginal zone, continuing asymmetric division and giving rise to glial cells such as astrocytes and oligodendrocytes [18,19]. Inner RGCs reside only in the ventricular zone and can differentiate into ependymal cells [20]. This specialisation of RGC populations marks the transition from neurogenesis to gliogenesis, and the mature brain begins to take shape.

1.1.2 Development of the corpus callosum

Brain tissue can be categorised into two types: grey matter and white matter. Grey matter, such as that found in the cerebral cortex, is primarily composed of neuronal cell bodies and dendrites and is responsible for processing and integrating information. In contrast, white matter gets its pale appearance from its high density of myelinated axons. The insulating properties of myelin allows it to increase the speed of electrical signal conduction along axons, enabling white matter to facilitate rapid communication between brain regions.

The largest white matter structure of the brain is the corpus callosum. The corpus callosum is evolutionarily the youngest brain structure, first appearing in placental mammals [21], and serves to coordinate communication between the left and the right hemispheres of the brain. Many NDDs are associated with agenesis of the corpus callosum

such as autism spectrum disorder (ASD), intellectual disability, and epilepsy [22–24], highlighting the importance of this structure in proper brain function.

During neurogenesis, a subset of intermediate progenitor cells is designated to form the corpus callosum, termed callosal projection neurons [25]. After asymmetric division from RGCs, the new neuron initially resides in the subventricular zone, and develops multiple small neurites [26]. In response to specification cues, the cell migrates up to the intermediate zone, and undergoes neuronal polarisation [26,27]. This involves the extension of two neurites into an axon and a leading process, on opposite ends of the cell. The soma continues to migrate upwards, towards the leading process, until it passes into the cortical plate and settles there (Figure 2).

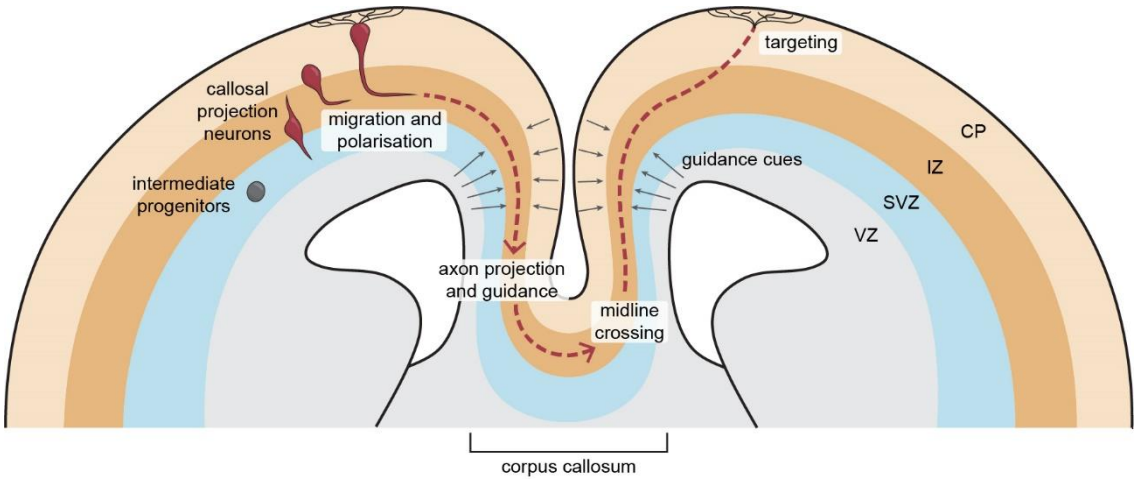

Figure 2. Axon navigation in corpus callosum genesis.

A subset of intermediate progenitor cells (grey) residing in the subventricular zone (SVZ) differentiate into callosal projection neurons (red). As they migrate into the intermediate zone (IZ), they become polarised, extending two neurites in opposite directions – the leading process, and the axon. The soma continues migrating towards the leading process, moving into the cortical plate (CP), and establishes connections with local neurons. The axon projects longer, towards attractive cues, and traverses towards the midline, eventually crossing over and continuing to grow into the contralateral hemisphere. Repulsive cues ensure the axon never crosses into the ventricular zone (VZ) or CP, until it reaches its destination, where it establishes connections in the CP of the opposite hemisphere.

On the other end, the growing axon associates into bundles with neighbouring axons and continues to project further. Using molecular guidance cues from the surrounding environment, axon bundles navigate through the intermediate zone and subventricular zone, never crossing into the cortical plate or ventricular zone (Figure 2). They extend towards attractive cues at the midline of the developing brain, and

eventually grow long enough to cross the midline [28–31]. Once crossed, axons face a sudden shift to repulsive cues, and by adapting their molecular program, they continue extending away from the midline and into the contralateral hemisphere [30,32,33]. This dynamic cue change is essential to ensure axons successfully exit the midline and prevent aberrant recrossing [34].

Axon bundles continue to traverse the contralateral hemisphere in a symmetrical fashion, until they enter the opposite cortical plate. Here, they form synapses with the surrounding neurons, establishing interhemispheric communication [34] (Figure 2).

1.1.3 The cellular cytoskeleton in axon growth

The cellular cytoskeleton serves multiple critical functions, such as modulating cell shape and migration, and is particularly important in the growth and steering of neuronal axons. The three primary components of the cytoskeleton are actin filaments, microtubules, and intermediate filaments, all of which are protein-based structures. Microtubules are composed of a highly dynamic polymer of α- and β-tubulin, continuously undergoing cycles of polymerisation and depolymerisation, a process known as dynamic instability [35]. Microtubules are also subjected to various post-translational modifications (PTMs) and associate with numerous microtubule-associated proteins (MAPs), conferring distinct properties and functionalities. Actin filaments (F-actin), made up of globular actin (G-actin) subunits, similarly cycle between polymerisation and depolymerisation, and are also regulated by a wide array of actin-binding proteins and PTMs.

In callosal axons, both microtubules and actin are heavily involved in axon growth and guidance, allowing axons to travel long distances with high accuracy [36,37]. The tip of a growing axon, termed the growth cone, is a fan-like structure responsible for sampling surrounding molecular cues as it navigates through the developing neural environment. These cues, such as attractive or repulsive cues, are detected by receptor complexes in the membrane of the growth cone. Transduction of these signals then triggers cytoskeletal rearrangements that steer the growth cone towards or away from the source of the cue.

The growth cone is divided into three zones; the central domain, in the centre of the structure, the transition zone, surrounding the central domain, and the peripheral

domain, comprising the outermost space and splaying outwards [38] (Figure 3). The central domain is largely occupied by stable, acetylated microtubules. Actin contractile arcs present in the transition zone exert forces that can bend incoming microtubules, providing the flexibility necessary for the growth cone to change direction [39]. Actin is most abundant in the peripheral domain, and exerts outward forces causing protrusions from the growth cone called filopodia and lamellipodia [37] (Figure 3). This has the effect of increasing the surface area subjected to environmental cues. Microtubules are also present in the peripheral domain, where they are more dynamic than those in the central domain due to their proximity to the membrane and subsequent need to rapidly respond to environmental cues [40,41]. However, the dense population of actin largely regulates the ability for microtubules to intrude into the peripheral domain [40,41]. The precise coupling of these two cytoskeletal components is crucial for productive axonal growth and steering.

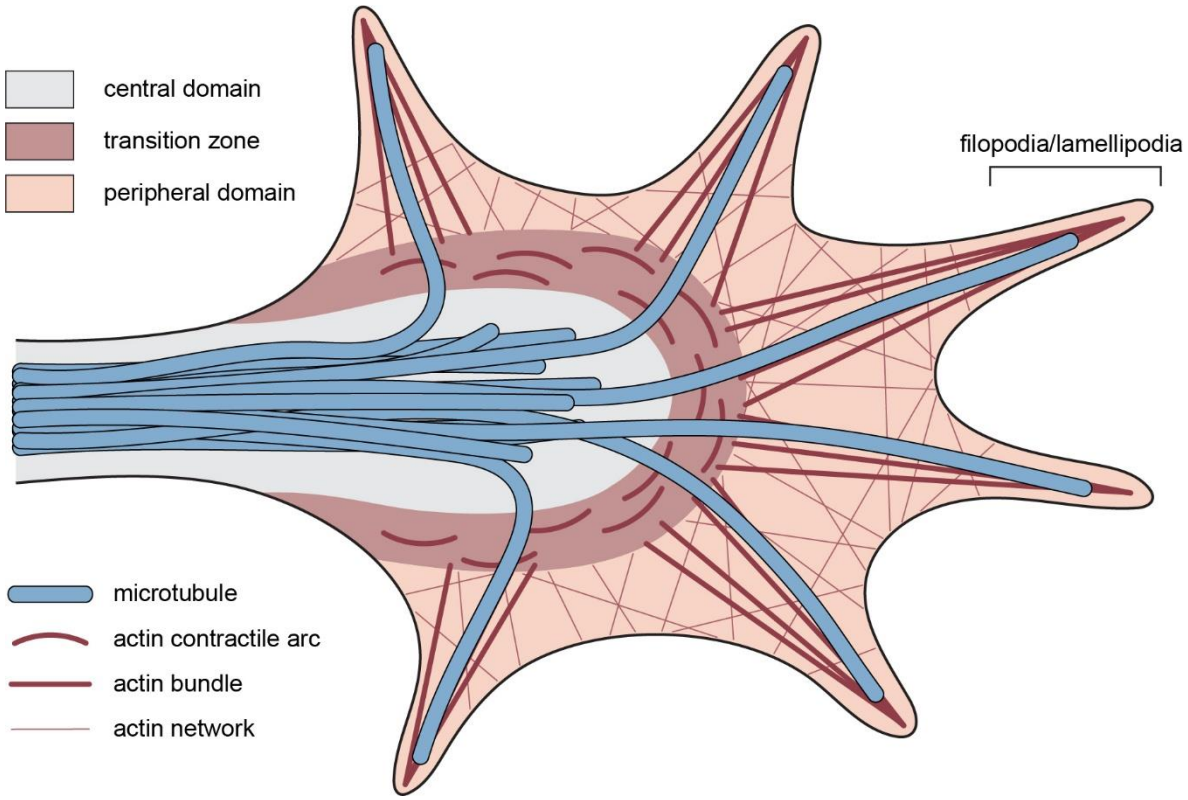

Figure 3. The cellular cytoskeleton in the growth cone.

The growth cone is a fan like structure at the tip of growing axons, and is divided into three areas – the central domain (grey), the transition zone (dark pink), and the peripheral domain (light pink). The central domain consists of stable microtubules, some of which pass through into the transition zone and peripheral domain. The presence of actin contractile arcs in the transition zone induces dynamic bends in the microtubules. The peripheral domain predominantly consists of a network of actin, creating protrusions called filopodia and lamellipodia to increase the surface area of the growth cone and aid sampling of the external environment.

The binding of MAPs to microtubules also plays a role in the response of microtubules to attractive or repulsive cues. MAP1B localises to the growth cones of axons, and is known to regulate the growth of microtubules in response to the chemoattractant Netrin-1 [42]. Furthermore, loss of function mutations in MAP1B results in agenesis of the corpus callosum [43]. The microtubule-associated protein Tau (MAPT, Tau) has been shown to directly interact with F-actin, and can coordinate the simultaneous polymerisation of microtubules and actin [44]. Since the phosphorylation state of MAPs influences their binding capacity to microtubules [45], upstream kinases are heavily involved in the regulation of microtubule dynamics via MAPs.

Clearly, the cellular cytoskeleton and its interacting components must be tightly orchestrated for precise neuronal polarisation and axonal growth, and by extension, successful neurodevelopment.

1.1.4 Neurodevelopmental disorders

The intricate nature of neurodevelopment creates numerous points of vulnerability, where dysregulation can lead to the emergence of NDDs. The severity of NDDs can vary widely, depending on the nature and timing of the underlying disruption. Affected individuals typically suffer cognitive, motor, social, and/or emotional disabilities, and often developmental milestones are delayed or never reached. It is thought that approximately 5-15% of the population live with NDDs, with children and teenagers representing the majority of patients [46–48].

According to the Diagnostic and Statistical Manual of Mental Disorders (Fifth Edition) (DSM-5), NDDs can be classified into six distinct categories; intellectual disability, autism spectrum disorder, attention-deficit/hyperactivity disorder, communication disorders, specific learning disorders, and motor disorders [49]. Comorbidity of two or more NDDs also occurs frequently as the affected neural circuits and developmental processes often overlap.

NDDs can arise from both environmental and genetic causes. Several environmental factors are known to negatively affect neurodevelopment, including drug and alcohol misuse during pregnancy, exposure to toxins or pollution, and early childhood experiences such as neglect or abuse. Genetic causes, ranging from single nucleotide polymorphisms to large chromosomal deletions, as well as epigenetic

alterations, can interfere with all molecular processes from protein function to gene expression, contributing to the broad spectrum of disease phenotypes and severities observed. Although genetic mutations causing NDDs can be inherited, many arise *de novo*, particularly in severe cases, likely due to the reduced reproductive fitness associated with strongly deleterious mutations [50].

Currently, the most commonly used technique to identify mutations associated with NDDs in patients is whole-exome sequencing (WES). 85% of known disease-causing mutations occur within protein-coding regions of the genome, allowing WES to capture the majority of pathogenic mutations in an efficient and cost-effective way [51]. Since defects in neurodevelopment often lead to morphological abnormalities in key brain structures, such as the cortex, corpus callosum, and cerebellum, brain imaging techniques such as magnetic resonance imaging (MRI) are also commonly used in diagnosis [52]. These structural differences can reflect disruptions in processes such as neuronal migration, axonal growth, or synapse formation, and may underlie the cognitive, motor, or behavioural symptoms observed in various NDDs.

1.1.5 Mega Corpus Callosum Syndrome

Many NDDs are associated with an abnormality of the corpus callosum. Corpus callosum agenesis, in which this structure is either absent or significantly thinner, has commonly been observed in patients with microcephaly, lissencephaly, or ASD [53]. On the other hand, enlargement of the corpus callosum, termed mega-corpus callosum syndrome (MCC), is less prevalent. There are several potential causes for enlargement, such as an increased number of axons crossing the midline, a greater axonal diameter, or thicker myelin sheaths surrounding the axons, all of which are tightly regulated under normal conditions.

The genetic causes underlying MCC are not deeply understood yet. Patients with megalencephaly-polymicrogyria-polydactyly-hydrocephalus (MPPH), a condition characterised by megalencephaly and frequently associated with MCC, have been found to carry mutations in protein kinase B3 (AKT3), phosphatidylinositol-3-kinase regulatory subunit 2 (PIK3R2), phosphatidylinositol-3-kinase catalytic subunit alpha (PIK3CA), and cyclin D2 (CCND2) [54,55]. The microtubule network and tubulinopathies have also been implicated in MCC. Three individuals with different mutations in tubulin gamma 1

(TUBG1) presented with cortical malformations and a thickened corpus callosum [56], and another case of MCC in combination with microcephaly was recently reported in a patient with a tubulin gamma complex component 2 (TUBGCP2) mutation [57]. However, it remains unclear whether these mutations are specifically responsible for the enlarged corpus callosum.

A study by Tripathy *et al* further investigated the genetic reasons for MCC by performing WES on a cohort of seven patients, all presenting with mega-corpus callosum with cerebellar hypoplasia and cortical malformations (MCC-CH-CM), but without megalencephaly [58]. These patients suffer severe symptoms such as intellectual disability, global developmental delay, hypotonia, seizures, and an inability to walk, stand, or talk. Six out of the seven individuals were all found to carry *de novo* mutations in a gene called microtubule-associated serine/threonine kinase 1 (MAST1) [58].

Since then, several other cases of MAST1-associated MCC were reported. One patient with MCC and cortical malformations, but without cerebellar hypoplasia, suffers from developmental delay, epilepsy, poor verbal communication, and hypotonia [59]. Another patient with congenital bilateral perisylvian syndrome (CBPS), a condition characterised by abnormal gyri in the cortex, also presented with corpus callosum hyperplasia [60]. In a recent study, brain abnormalities including MCC, lissencephaly, and cortical dysplasia were identified in a 25-week-old foetus [61]. In all three cases, *de novo* mutations in MAST1 were present.

The following chapter will explore the current literature on the MAST kinases, examining their biological roles and emerging significance in human disease.

1.2 The MAST family of kinases

The MAST kinases are eukaryotic protein kinases. There are four closely related paralogs of the MAST kinases: MAST1, MAST2, MAST3, and MAST4, and another more distantly related paralog MAST-like (MASTL), also known as Greatwall kinase (GWL). MAST1-4 are ~200 kDa, multi-domain proteins, while MASTL comprises only the catalytic kinase domain. Due to its structural and functional divergence, MASTL will not be discussed further, and all subsequent mentions of the MAST kinases refer to MAST1-4 only.

1.2.1 Background of the MAST kinases

Evolution and conservation

The MAST kinases first appeared approximately 600 million years ago in early-diverging animals such as Cnidaria and Ctenophora, coinciding with the emergence of primitive nervous systems. In invertebrate model organisms, the sole MAST homolog is known as Kin-4 in *C. elegans* and Dop in *D. melanogaster*. Among the vertebrate paralogs, MAST2 is most similar to the ancestral gene, with subsequent gene duplication events giving rise to MAST1, 3, and 4.

MAST1-4, sharing 30-45% sequence identity, display high levels of conservation within their three folded domains. The unstructured N- and C-terminal extensions lack conservation and largely differ in length, albeit with short segments of invariance, implying functional roles, possibly as short linear motifs, within those particular regions.

Domain architecture and structure

The MAST kinases are made up of three distinct domains; a domain of unknown function (DUF), a catalytic kinase domain, and a PSD-95, Gld, ZO-1 (PDZ) domain (Figure 4A). The DUF, the most N-terminal domain, is partially disordered, hence its amino acid boundaries are based off conservation and not strictly defined. The DUF harbours a folded sub-domain termed the four-helix bundle (4HB). The structure of the 4HB of MAST1, consisting of four closely packed α-helices, has been experimentally determined by NMR [62] (Figure 4B). MAST's kinase domain starts shortly after the DUF. Roughly 350 amino acids in length, the kinase domain is the only domain in MAST with catalytic activity. The PDZ domain is situated C-terminal to the kinase domain, with approximately 200-250 amino acids of unstructured linker between them. PDZ domains are prevalent across many proteins, and are known to facilitate protein/protein interactions by binding to specific PDZ-binding motifs at the C-terminus of proteins. Crystal structures of the PDZ domain have been determined for MAST1-3 [63–65] (Figure 4C).

Excluding the three domains, the MAST kinases are otherwise largely disordered, particularly the N-terminus before the DUF and the long C-terminal extension following the PDZ domain (Figure 4D). The high degree of intrinsic disorder in MAST proteins complicates purification of constructs containing these regions and makes structure determination particularly difficult. Therefore, the orientation of each domain with

respect to each other and any interaction interfaces they may share are not yet known. Although AlphaFold [66] enables structural prediction of the full-length protein (Figure 4E), the interfaces between domains are predicted with low confidence (Figure 4F).

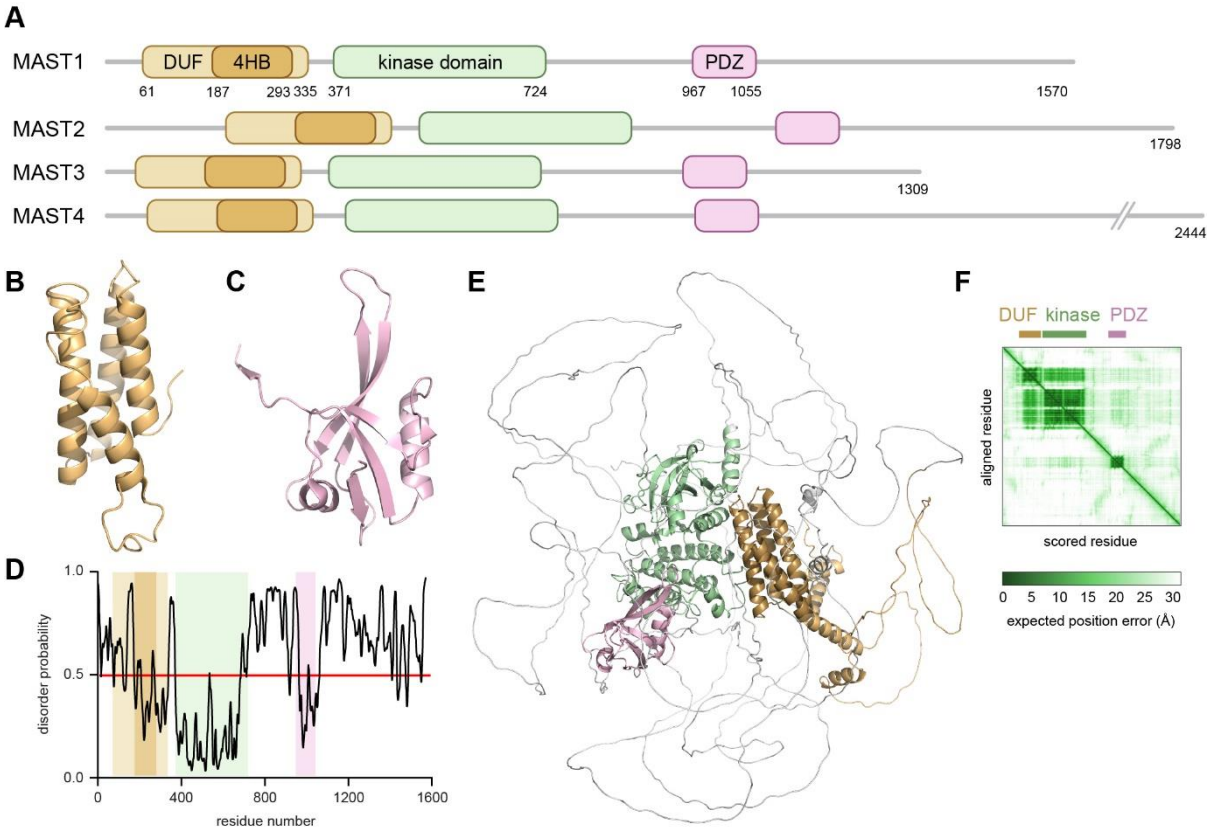

Figure 4. Domains and structure of the MAST kinases.

A. The MAST kinases comprise three folded domains: the domain of unknown function (DUF, yellow), which harbours a four-helix bundle domain (4HB, orange), a catalytic kinase domain (green), and a PDZ domain (pink). **B.** Structure of the 4HB of MAST1, determined by NMR (PDB: 2M9X). **C.** Structure of the PDZ domain of MAST1, determined by X-ray crystallography (PDB: 3PS4). **D.** Disorder probability of MAST1 predicted by PrDOS [67], scores between 0.0-0.5 are predicted disordered, scores between 0.5-1.0 are predicted ordered. **E.** AlphaFold2 [66] structure prediction of full length, human MAST1. **F.** Predicted aligned error plot of AlphaFold2 structure prediction in (E).

Classification

Eukaryotic protein kinases are classified into eight families. Based on homology of the kinase domain, the MAST kinases belong to the AGC family. Named after protein kinase A (PKA), protein kinase G (PKG), and protein kinase C (PKC), the AGC kinase family includes well-studied members such as AKT and phosphoinositide-dependent kinase 1 (PDK1). The family's defining feature is a regulatory C-terminal tail (C-tail) that extends from the kinase domain [68]. Evolutionarily, the MAST kinases diverged from the majority of the AGC

kinases relatively early, together with another branch including the dystonia myotonica protein kinases (DMPKs), nuclear Dbf2-related (NDR) kinases, and large tumour suppressor (LATS) kinases. It is therefore likely that the MASTs share similar features and mechanisms of action to the DPMKs, NDR and LATS kinases.

Protein kinases confer specificity for their substrates by using residues within their substrate-binding pockets to recognise the sequence around the target phosphorylation site. AGC kinases typically recognise and phosphorylate the sequence motif RXRXX(S/T*)φ, where S/T* is the target site and φ represents a large hydrophobic residue [69]. To date, the exact substrate recognition motif for the MAST kinases has not been experimentally determined. However, as the MAST kinases possess the key substrate binding residues of AGC kinases within their kinase domain, they likely recognise a similar motif.

Expression pattern and localisation

At an organ level, all four MAST kinases are highly expressed in the brain. For MAST1, 3, and 4, expression is mostly limited to the brain, but low levels have also been detected in the liver, spleen, lungs, and testes [58,70,71]. MAST2 appears in high levels across the brain, heart, and testes [70,71]. RNA sequencing and exome microarray data of the developing human brain revealed that MAST1-3 are expressed throughout most brain structures, while MAST4 shows specificity to the dorsal thalamus [72]. Additionally, single-cell RNA sequencing of the developing mouse brain found MAST1 exclusively in neurons, while MAST2-4 were widespread across neurons, glial cells, and astrocytes [73]. Another mouse study found MAST1 to be enriched in the cortical plate and intermediate zone of the brain, specifically in post-mitotic neurons and corpus callosal fibres but not progenitors or intermediate progenitors [58]. As their name suggests, the MAST kinases localise to the microtubule network, and MAST1 and MAST2 have been shown to bind to microtubules *in vitro*, though only in the presence of MAPs [58,74].

On a temporal scale, all four MAST kinases show clear expression during embryonic development, though they differ in the timing of expression onset and duration. In humans and mice, MAST1 expression is first detected at 12 weeks post conception and E12.5 respectively, and in both cases increases over the course of development, and drops postnatally [58,72]. MAST2 shares similar temporal patterns to

MAST1, while MAST3 expression begins later in development and persists well into adulthood [72]. Taken together, the MAST kinases are predominantly expressed in the developing brain but differ slightly in their temporal expression and localisation across brain regions and cell types.

1.2.2 Proposed substrates of MAST kinases

A few candidate substrates of the MAST kinases have been proposed. One candidate, phosphatase and tensin homolog (PTEN), was first identified as an interactor of MAST1-3 (but not MAST4), via the PDZ domain of MAST and the PDZ-binding motif of PTEN [75]. It was subsequently shown that an affinity-purified construct of the MAST1-3 kinase domain was capable of phosphorylating PTEN in a radiometric kinase assay [75]. This phosphorylation was dependent on the presence of PTEN's PDZ-binding motif, suggesting the PDZ-mediated interaction of the proteins is required for phosphorylation. However, the residue in PTEN targeted by MAST was not explored.

By utilising 1318 site-specific antibodies to profile the phosphorylation pattern of wild-type (WT) and MAST1 knock-out (KO) cells, S221 of mitogen-activated protein kinase kinase 1 (MEK1) was identified as a differentially phosphorylated site [76]. The reduction of MEK1 S221 phosphorylation in MAST1 knockdown cells was rescued with overexpression of MAST1, but not a kinase-dead mutant, suggesting that MEK1 phosphorylation occurs downstream of MAST1 activity. MEK1 was further characterised as a direct substrate of MAST1 *in vitro* as phosphorylation of S221 was detected by western blot following incubation with affinity-purified WT MAST1, but not kinase dead MAST1.

cAMP-regulated phosphoprotein of 16 kDa (ARPP-16) has also been reported as a MAST3 substrate [77,78]. Upon overexpression of MAST3 in HEK293 cells, an increase in phosphorylation on S46 of ARPP-16 was detected by western blot. Affinity-purified MAST3 also demonstrated an ability to phosphorylate ARPP-16 *in vitro*, but since a kinase-dead control was lacking, the contribution of a contaminating kinase cannot be ruled out.

In all cases, it remains difficult to definitively establish these proposed proteins as bona fide MAST substrates. Many of the performed experiments either cannot distinguish between the direct and indirect effects of MAST activity or are missing crucial kinase-

dead controls for proteins that were purified with a single affinity step. Additionally, none of the reported substrate sequences conform to a canonical AGC kinase substrate motif, and may instead reflect off-target phosphorylation events, common in *in vitro* kinase assays. Further research will be required to identify bona fide MAST substrates, with an emphasis on establishing a functional link between MAST and neurodevelopment.

1.2.3 MAST kinases in neurodevelopment

MAST1 in MCC

As discussed in chapter 1.1.5, mutations in MAST1 have been linked to MCC. The original paper describing MCC-CH-CM reported a cohort of seven patients with an enlarged corpus callosum, of which six harbour *de novo* mutations in MAST1 [58]. Three patients have trinucleotide deletion mutations, resulting in the loss of a single amino acid, occurring within helices of the 4HB domain: E194del, K276del, and L278del (Figure 5). Since the loss of a residue in an α-helix causes a register shift, and given that the 4HB is composed of four α-helices tightly packed together, these mutations were hypothesised to alter the surface properties of the affected helix and subsequently destabilise the whole domain. The remaining three patients all share the same G517S substitution mutation (Figure 5). The affected glycine resides in the kinase domain of MAST1, and is part of the highly conserved Asp-Phe-Gly (DFG) motif, critical for ATP binding and catalysis.

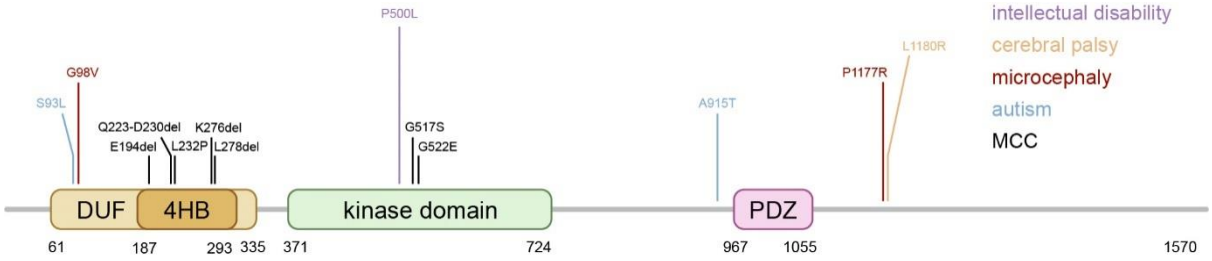

Figure 5. Reported NDD-associated mutations in MAST1.

Mutations in MAST1 have been linked to Mega-Corpus Callosum Syndrome (MCC, black), autism (blue), microcephaly (red), cerebral palsy (yellow), and intellectual disability (purple).

To probe whether the MAST1 mutations are causative of MCC, a mouse model harbouring the patient-derived L278del mutation was generated [58]. While L278del homozygous mice died shortly after birth, the heterozygous mice were viable and recapitulated the enlarged corpus callosum phenotype. Both the thickness and the

volume of the corpus callosum of MAST1$^{L278del/+}$ mice were significantly greater than WT littermate controls. A simultaneous reduction in the thickness and volume of the cortex was observed in the mutant mice.

Interestingly, a MAST1 KO mouse model displayed no significant change to its brain morphology and had no other observable phenotype, compared to the WT [58]. Hence, the MCC patient mutations must exert a dominant-negative mode of pathogenicity. A clue to the mechanism behind this was revealed when comparing the abundances of the other MAST kinases in the cortices of MAST1 WT, L278del, and KO mice. Both MAST2 and MAST3 protein levels were observed to increase significantly in response to the complete loss of MAST1 protein in the KO background, compared to WT. This implies redundancy between the MAST kinases, and an ability for compensation between paralogs. On the other hand, while MAST1 protein levels decreased in the L278del background, both MAST2 and MAST3 abundances also dropped significantly, and is likely the dominant-negative consequence of mutation. Since transcript levels of all three MAST kinase remained unchanged, it was hypothesised that the proteins were degraded post-translationally.

Three additional studies have since detected MAST1 mutations associated with MCC, as discussed in chapter 1.1.5, including G522E [59], Q223-D230del [60], and L232P [61] (Figure 5). While these studies did not explore the molecular consequences of the mutations, they may have analogous effects to those of the original study, given these mutations affect similar regions of MAST1. The G522E mutation sits in the activation loop of the kinase domain, five amino-acids downstream of the G517S mutation. The affected glycine is evolutionarily invariant across MAST1 orthologs, and may be important for activation loop flexibility, given the unrestricted backbone angles of glycine. Its mutation to glutamate could therefore change the conformational landscape that the activation loop can sample, and would potentially affect the catalytic activity or substrate binding capacity of MAST1. The remaining two mutations both affect the second α-helix of the 4HB domain. The Q223-D230del mutant is missing seven amino acids from the centre of the helix, shortening it significantly and breaking its interactions with the surrounding helices. Since prolines lack a backbone amide hydrogen, they are incapable of making the necessary hydrogen bonds to form an α-helix; hence the L232P mutation would result in

unfolding of the affected helix. Both instances would almost certainly destabilise the whole 4HB domain, similarly to the E194del, K276del, and L278del mutations.

MAST kinases in other neurodevelopmental disorders

The involvement of the MAST kinases in NDDs is not limited to MCC. Mutations in all four MAST kinases, most of them *de novo*, have been linked to a wide variety of neurodevelopmental and neurological disorders.

Alongside the original cohort of MCC patients, Tripathy *et al* assessed four more patients carrying MAST1 mutations but without MCC [58]. Two (G98V and P1177R) presented with both microcephaly and motor deficits, and two (S93L and A915T) have ASD (Figure 5). Unlike the MCC-associated variants, these all affect unstructured regions of MAST1. In separate studies, two other mutations, P500L and L1180R, were identified in patients suffering cerebral palsy and intellectual disability, respectively [79,80] (Figure 5). Intellectual disability in combination with ASD was also linked to MAST3 mutations in four cases, affecting either the DUF or the kinase domain (S101P, S104L, L516P, and G515S) [81].

A considerable number of individuals with epilepsy have been reported to harbour MAST mutations. The previously identified, MCC-associated MAST1 G517S mutation was found in a patient suffering epilepsy, along with central hypogonadism [82]. In a cohort of 11 epilepsy patients, all had mutations within the kinase domain of MAST3 [83]. Notably, five of these patients shared the recurrent G510S variant, which aligns to the G517S mutation in MAST1. Among six MAST4 mutations linked to epilepsy across two studies [84,85], one patient carrying an I898T mutation in the C-tail of the kinase domain also exhibited corpus callosum dysgenesis [85].

In unpublished work (Keays' lab, LMU, Munich), MAST2 mutations have been associated with several conditions and symptoms such as microcephaly, macrocephaly, ASD, intellectual disability, epilepsy, speech and motor impairments, and developmental delay. Taken together, there is a clear link between mutations in the MAST family and NDDs. However, these studies only establish correlations and do not decipher the causative link between MAST mutations and NDDs.

1.2.4 MAST kinases in cancer

In addition to their emerging role in neurodevelopment, the MAST kinases have also been implicated in various types of cancer and in treatment resistance. As discussed in chapter 1.2.2, MAST1 has been proposed to modulate the anti-apoptotic MEK/ERK pathway, by phosphorylating and activating MEK, which subsequently activates extracellular signal-regulated kinase (ERK), decreasing Bcl-2 interacting mediator of cell death (BIM) protein levels and inhibiting apoptosis [76]. In the context of several human cancer lines such as human carcinoma line KB-3-1 and lung cancer line A549, the activation of this pathway by MAST1 was shown to confer resistance to cisplatin-induced cell death. In contrast, a MAST1 KO cell line was more susceptible to cisplatin-induced cell death. In a follow-up study, carboxy terminus of hsc70-interacting protein (CHIP) was shown to ubiquitinate and target MAST1 for degradation, promoting cisplatin sensitisation, while heat shock protein 90 B (Hsp90B) antagonises CHIP by protecting MAST1 from degradation [86]. This work was continued by another group, showing that the deubiquitinases ubiquitin specific peptidase 1 (USP1) and USP28 inhibit MAST1 degradation, hence promoting cisplatin resistance [87,88]. The identification of multiple regulators of MAST1 has led to the suggestion that combinatorial therapy may help tackle cisplatin resistance.

Several studies have linked the MAST kinases to breast cancer. Both MAST1 and MAST2 are frequently involved in gene fusions driving breast cancer, in most cases including their kinase and PDZ domain, but the mechanistic implications of these fusions are not yet understood [89,90]. MAST4 has also been identified as a potential breast cancer biomarker in urine, as its abundance was significantly enriched in the urine of breast cancer patients compared to control subjects [91]. Conversely, MAST3 levels were significantly reduced in breast cancer, and it was labelled a tumour suppressor as its overexpression inhibited breast cancer cell proliferation. The study further reported that low MAST3 expression correlated with inactivation of the Hippo pathway, a known driver of breast cancer [92]. Beyond this, MAST1 has also been implicated in lung cancer [93], and MAST2 in both liver cancer [94] and prostate cancer [95].

1.2.5 MAST kinases in other biological processes

The MAST kinases have been proposed to play a role in spermatogenesis. Indeed, aside from the brain, MAST kinase expression is elevated in the testis, particularly MAST2

[70,71,74]. MAST2-associated kinase activity was shown to fluctuate throughout different stages of spermatid maturation [96], and three cases of MAST2 gene duplication were linked to nonobstructive azoospermia [97]. Expression of MAST4 was also detected at several stages of testicular development, and MAST4 KO mice exhibited smaller testes with a significant decrease in sperm count [98]. Further investigation of the MAST4 KO revealed an increase in the cell cycle time of spermatogonial stem cells compared to WT, due to a downregulation of cyclin-dependent kinase 2 (CDK2) [99].

A number of neuronal functions have been reported for MAST1 and 2. The first study to characterise MAST1, originally named SAST, demonstrated an interaction between the PDZ domain of MAST1 and β2-syntrophin at post-synaptic densities [70]. It was proposed that MAST1 bridges the microtubule network to the dystrophin and utrophin network via β2-syntrophin. In the neuroblastoma cell line SH-SY5Y, MAST1 knockdown impaired neuronal differentiation and promoted cell cycle progression, suggesting a role for MAST1 in the transition from proliferation to differentiation [100]. MAST2 was shown to negatively regulate neurite outgrowth in SH-SY5Y cells [101,102], an effect also observed for PTEN [103,104]. Given the previously reported interaction between MAST2 and PTEN [75], it was suggested they perform this function in synergy.

The studies discussed in Chapter 1.2 have provided initial insights into MAST kinase function. Despite this, a full picture of the biological roles of MAST, and the mechanics of its kinase activity and regulation, has not yet been determined.

1.3 Molecular regulation of kinases

The efficient transduction of cellular signals is essential for cells to respond to stimuli in a specific and timely manner. To facilitate this, PTMs are utilised by cells to rapidly modulate protein function and trigger appropriate signalling pathways. One of the most common PTMs employed by cells for signal transduction is protein phosphorylation. The addition of a phosphate to a protein substrate can induce various effects such as enabling molecular interactions, triggering allosteric changes, or increasing solubility. This modification is catalysed by protein kinases, while its removal is mediated by protein phosphatases. These enzymes allow the efficient transmission of messages via

phosphorylation, and are tightly regulated to ensure signalling fidelity in both space and time.

The human proteome contains a repertoire of more than 500 protein kinases, each with their own specific substrates and mode of action. The majority of kinases phosphorylate the hydroxyl group of either serine/threonine residues or tyrosine residues. To permit control of their catalytic activity, protein kinases adopt different conformations that are either compatible or incompatible with phospho-transfer, working in a switch-like on/off manner. This ensures signals are only transduced when needed, with precise processes in place to regulate the switch between these states. This chapter will explore the molecular mechanics of protein kinases, simply referred to from here on as "kinases".

1.3.1 Anatomy of a kinase

A kinase domain is typically ~290 amino acids in length and consists of two folded lobes; the N-terminal and C-terminal lobe (N-lobe and C-lobe) [105] (Figure 6A). The N-lobe is made up of a β-sheet (β1- β5) and at least one α-helix (αC), and contains several catalytically relevant structures such as the αC helix and the glycine-rich loop between β1 and β2. The C-lobe is mostly α-helical and harbours many important motifs including the catalytic loop motif His-Arg-Asp (HRD), the ATP-binding activation loop motif Asp-Phe-Gly (DFG), and the Ala-Pro-Glu (APE) motif that delineates the end of the activation loop. The activation loop sits between the DFG and APE motif, playing a crucial role in substrate binding, and is commonly phosphorylated as a means to regulate kinase activity [106]. The N- and C-lobes of the kinase are held together by a short linker called the hinge.

A kinase's active site is located in between the N- and C-lobe, where the features mentioned above are precisely arranged to position the components of the phospho-transfer reaction in place (Figure 6B). These components, including one molecule of ATP, two Mg^{2+} ions, and the hydroxyl group of the accepting residue of the substrate, are the minimum required components for a phospho-transfer reaction. To ensure specificity of the reaction between a particular kinase and its substrate, the substrate binding cleft of the kinase is typically lined with residues that recognise the sequence surrounding its substrate's phosphorylation site.

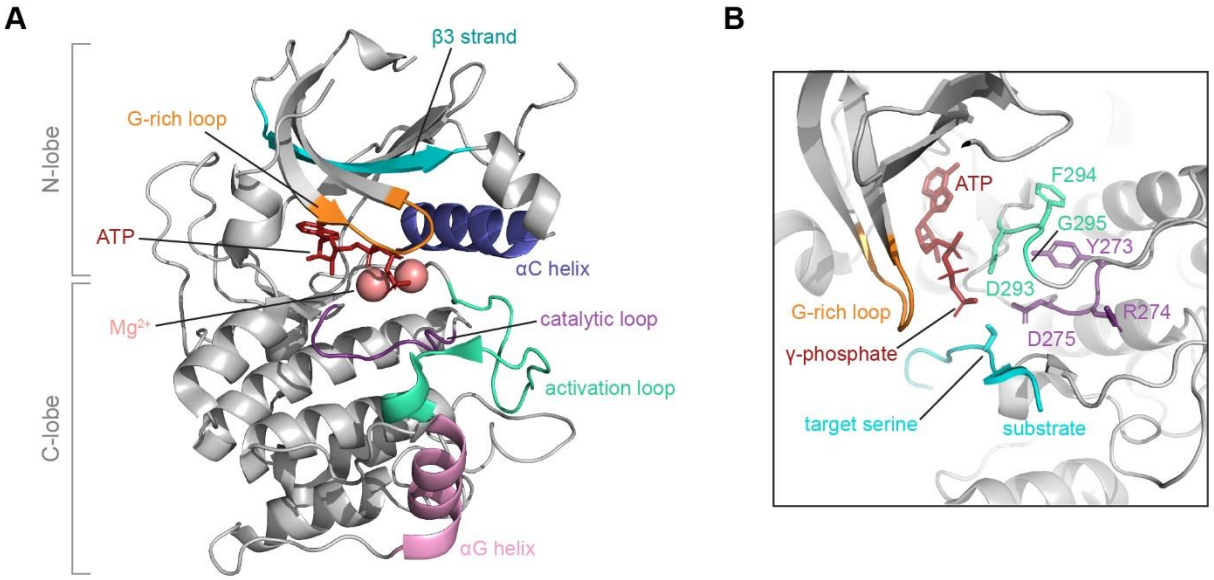

Figure 6. The protein kinase domain.

A crystal structure of AKT2 in complex with a substrate peptide (GSK3) and ANP-PNP (PDB: 1O6K [107]) is shown as a representative kinase domain. **A.** Kinase domains are made up of two globular lobes: the N-lobe and the C-lobe. The important elements of kinase domains are highlighted: the αC helix (dark blue), the glycine-rich loop (G-rich loop, orange), the β3 strand (teal), the activation loop (green), the catalytic loop (purple), the αG helix (pink), ATP (ANP-PNP in the representative image, red), and Mg^{2+} ions (salmon). **B.** The target phospho-acceptor (serine depicted, cyan) is aligned and in close proximity to the γ-phosphate of ATP (red). Several motifs and residues of the kinase domain is essential to coordinate this, such as the DFG motif (D293, F294, and G295 with AKT2 numbering, green), the (H/Y)RD motif (Y273, R274, and D275 with AKT2 numbering, purple), and the G-rich loop (orange).

While the core motifs and structures required for catalysis display high conservation across all kinases, some variation in sequence is necessary to accommodate many different kinase/substrate pairs within the active site. Kinase domains also vary through the addition of other features such as insertion loops, longer activation loops, and C-terminal extensions, allowing for unique binding surfaces and modes of regulation.

1.3.2 Conformational requirements for an active kinase

The structural differences between an active and inactive kinase was first introduced by comparing the solved structures of PKA and CDK2, in their active and inactive conformations respectively [108,109].

Kinases orchestrate phospho-transfer by holding their substrates in the optimal configuration and providing the chemical environment that promotes transfer. In the active site, the γ-phosphate of the ATP molecule and the accepting hydroxyl group of the

substrate must be brought into close proximity and aligned collinearly. Their placement and orientation relative to the catalytic residues of the active site must also be precisely coordinated, and is achieved by a network of interactions (Figure 7). The adenine of the ATP is held in place by forming two hydrogen bonds with the peptide backbone of the kinase hinge, as well as numerous van der Waals interactions between the planar base and surrounding residues. The two positively charged Mg^{2+} ions also aid the binding of ATP into the catalytic cleft by stabilising its highly negatively charged phosphates. Coordination of the Mg^{2+} ions involves the aspartate residue of the DFG motif, which chelates both ions, and an asparagine located five residues downstream of the HRD motif, which contributes to the chelation of one ion. Here, the orientation of the DFG motif is a defining feature of a kinase's active state. In the active conformation, the phenylalanine of the DFG points away from the catalytic cleft (Figure 6B). However, an inward-facing phenylalanine is characteristic of the inactive conformation, as it disrupts the interaction between the DFG aspartate and the Mg^{2+} ions [110].

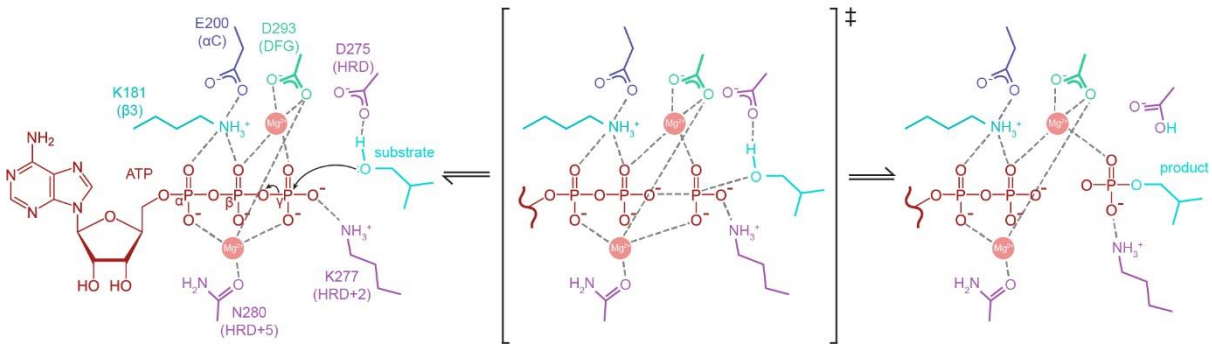

Figure 7. The kinase-catalysed phospho-transfer reaction.

The depicted kinase residues are labelled with the AKT2 numbering as well as its position within the kinase in brackets. The phospho-transfer reaction requires one molecule of ATP (red), two molecules of Mg^{2+} (salmon), the hydroxyl group of the acceptor site (cyan), and a network of interactions within the active site of the kinase. The Mg2+ ions are coordinated by the aspartate of the DFG (D293, green) and an asparagine five residues downstream of the HRD motif (N280, purple), and helps to stabilise the negatively charged phosphates of the ATP. The αC glutamate (E200, dark blue) forms a salt bridge with the β3 lysine (K181, teal), which in turn bind and positions the α- and β-phosphate. The aspartate of the HRD motif (D275, purple) initiates the phospho-transfer reaction by deprotonating the hydroxyl group of the substrate, inducing its nucleophilic attack on the γ-phosphate (left). A transition state is formed (centre) where the substrate is partially bonded to both the γ-phosphate and the catalytic aspartate. When the new bond is formed (right), the resultant product and ADP dissociate from the active site. Figure adapted from Endicott et al (2012) [105].

Several contacts are made between the active site and the phosphates of the ATP, in order to poise the γ-phosphate collinearly to the substrate (Figure 7). A glutamate

residue in the αC helix forms a salt bridge with a lysine in the β3 strand, which in turn holds the α- and β-phosphates in place via hydrogen bonds. For these interactions to occur, the αC helix must rotate inwards towards the N-lobe, another distinguishing structural feature of a kinase's active conformation. Another lysine found two residues downstream of the HRD motif similarly binds and positions the γ-phosphate. Together with the magnesium cations, these surrounding positively-charged lysines also function to neutralise the strong negative charge of the ATP, particularly upon breakage of the β to γ phospho-ester bond. An additional feature involved in ATP binding and positioning is the glycine-rich loop, which makes contacts to the β- and γ-phosphates of ATP.

The key catalytic residue of kinases is the aspartate of the HRD motif. Its negatively-charged side chain initiates the phospho-transfer reaction by deprotonating the hydroxyl group of the substrate, inducing the nucleophilic attack of the accepting oxygen to the phosphorus of the γ-phosphate [111] (Figure 7). The phospho-ester bond between the β- and γ-phosphate is subsequently broken. The local negative charges of the product and ADP leaving groups results in dissociation of the product.

Another feature essential for the formation of the active conformation is the activation loop. Lacking defined secondary structure features, the activation loop is disordered in the inactive conformation, unable to facilitate substrate binding. However, upon certain triggers, it becomes ordered and adopts a conformation compatible with substrate binding [105]. The typical activating trigger is phosphorylation of a key residue within the activation loop, either by the kinase itself (autophosphorylation) or by an upstream kinase. The added phosphate forms a network of hydrogen bonds to several key residues: the arginine of the HRD motif, a histidine on the αC helix (which pulls the αC helix towards the N-lobe), and a lysine within the activation loop itself (Figure 8). This not only stabilises the activation loop for substrate binding, but also draws the N- and C-lobes of the kinase closer together, aligning all essential residues for catalysis.

1.3.3 Regulation mechanisms

Kinases have evolved a large variety of regulatory mechanisms to switch between their on and off states to ensure that signals are only transduced upon the appropriate trigger. These include phosphorylation, binding of accessory proteins, dimerisation, and localisation.

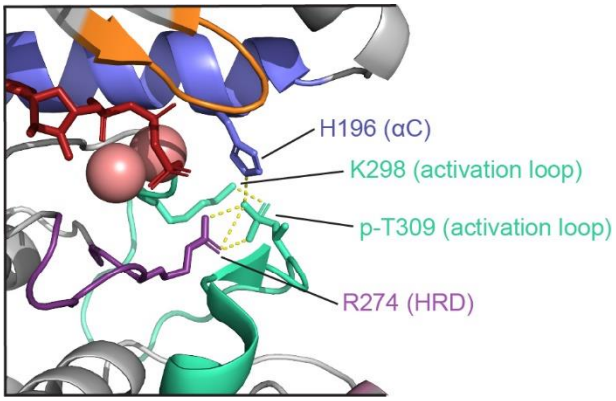

Figure 8. Interactions of the phosphorylated activation loop.

The phosphorylated regulatory residue of activation loop (p-T309, green) forms a network of hydrogen bonds, with the αC histidine (H196, dark blue), the arginine of the HRD (R274, purple), and another lysine in the activation loop (K298, green) (AKT2 depicted, PDB: 1O6K) [107].

Phosphorylation

In many cases, the protein substrate of a kinase is itself (autophosphorylation), or another kinase. Phosphorylation of a kinase often serves an important regulatory function, such as activating or inactivating the kinase, or allowing it to bind to other proteins.

As mentioned previously, a typical example of this is activation loop phosphorylation (Figure 9A). This can be achieved in three ways: either a kinase phosphorylates a different kinase's activation loop, or autophosphorylates its own activation loop, which it can perform either in *cis* (within the same molecule) or in *trans* (one molecule to another). Activation loop phosphorylation from one to another kinase is described within signalling cascades such as the RAF-MEK-ERK pathway [112–114], or with PDK1 [115], which is reported to phosphorylate a wide array of substrate kinases [116]. Until recently, autophosphorylation of the activation loop was generally understood to occur in *trans*, as also described for PDK1 [115]. However, a recent study on protein kinase D1 (PKD1) demonstrated that its autophosphorylation occurs in *cis*, prompting further exploration into the prevalence of *cis*-autophosphorylation among kinases [117].

The AGC family of kinases also possess two other regulatory phosphorylation sites within their C-tail, allowing additional control of their active states. These sites will be discussed further in Chapter 1.3.4.

Phosphorylation of kinases can also be employed to enable their interactions with other proteins (Figure 9A), such as 14-3-3 proteins. A family of highly abundant and constitutively dimeric proteins, the 14-3-3's specifically bind to protein motifs containing phosphorylated serines [118,119]. Numerous kinases have been reported to bind to 14-3-3

proteins, in many cases for the purpose of kinase activity regulation. For instance, B-Raf proto-oncogene serine/threonine kinase (BRAF) possesses two regulatory serines which can either be singly or doubly phosphorylated, allowing BRAF to form either a tetrameric or trimeric complex respectively with a 14-3-3 dimer [120,121]. Only the formation of the tetrameric complex serves to switch on BRAF kinase activity, as the 14-3-3 dimer facilitates the back-to-back dimerisation of BRAF, which in turn allosterically triggers its active conformation [122,123].

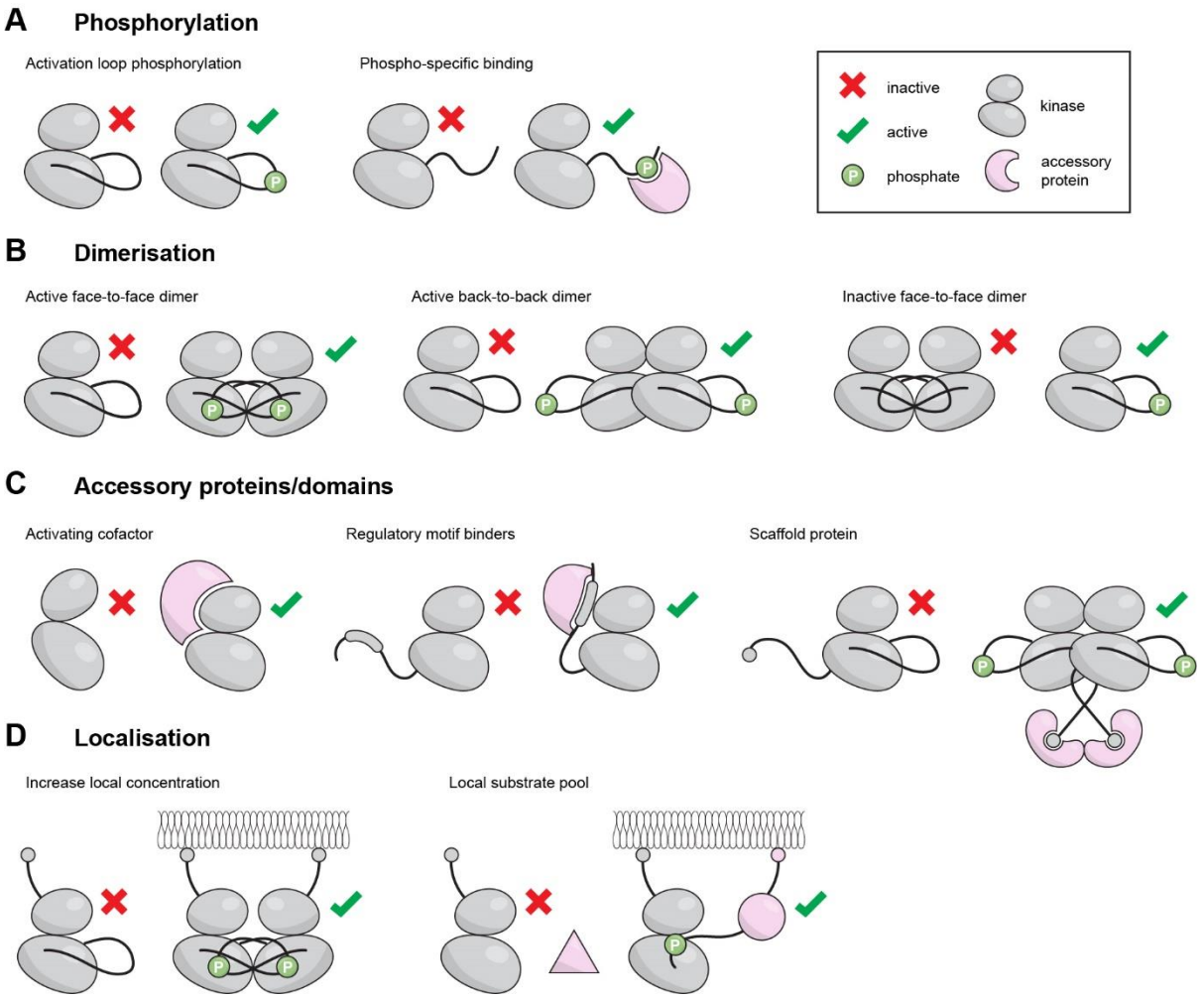

Figure 9. Modes of regulation of kinase activity.

A. Phosphorylation of a kinase itself can modulate its activity, for example by ordering its activation loop or promoting its interaction with an accessory protein. **B.** Various forms of kinase dimerisation, such as active face-to-face, active back-to-back, and inactive face-to-face have been reported. **C.** Many mechanisms of regulation are possible with accessory proteins or domains, such as direct or allosteric activation by binding, binding of regulatory motifs, or scaffolding. **D.** Localisation of a kinase to certain cellular compartments can either increase its local concentration, aiding other regulatory mechanisms such as dimerisation, or promote its access to a particular pool of substrates.

Dimerisation

Kinases have frequently been observed to use dimerisation as a means of activity regulation. The most commonly studied example of kinase dimerisation is in the context of *trans*-autophosphorylation of the activation loop (Figure 9B). First reported for receptor tyrosine kinases [124], the formation of a transient face-to-face dimer allows the activation loops from each protomer to reach into the opposing protomer's active site, subsequently undergoing autophosphorylation and resulting in active monomers. Meanwhile, a number of kinases rely on back-to-back dimerisation to allosterically induce the active conformation (Figure 9B), as mentioned above for BRAF [120–123]. Conversely, a recent study on PKD1 reported its formation of inactive face-to-face dimers [125] (Figure 9B). Stabilised by accessory domains, these dimers are maintained in an inactive conformation. The binding of PKD1 to diacylglycerol has been proposed to induce dissociation of the inactive dimer, enabling *cis*-autophosphorylation and activation of the kinase.

Accessory proteins or domains

Additional domains, subunits, or protein cofactors can also serve as regulatory inputs for kinase activity. These accessory binders commonly regulate function by directly or allosterically triggering a conformational change in the kinase (Figure 9C). Several kinases rely on cofactors to press their αC helix towards the N-lobe, such as CDK2, which requires the association of a cyclin subunit for salt bridge formation between the αC glutamate and the β3 lysine [126]. The catalytic activity of the NDR kinases also depends on an external protein cofactor, Mps one binder homolog 1 (MOB1), as it binds to NDR's N-terminal domain and releases its autoinhibition [127–129]. PKA ensures inhibition of catalytic activity with its own regulatory subunit, which contains a pseudosubstrate motif that occupies and blocks the substrate binding cleft of its catalytic subunit. Autoinhibition is released due to a conformational change upon association of cAMP, allowing the catalytic subunit to autophosphorylate its activation loop and proceed with downstream substrate phosphorylation [130].

Accessory proteins or domains can control the docking of regulatory motifs to a kinase, by either holding them in place or pulling them away (Figure 9C). This is observed in the DMPK family, which includes the Rho-associated coiled-coil kinases (ROCK),

myotonic dystrophy kinase-related CDC42-binding protein kinases (MRCK), Citron Rho-interacting kinase (CRIK) and DMPK itself. These kinases employ a dimerization-competent capped-helix bundle (CHB) domain at the N-terminus of their kinase domain to sandwich the regulatory C-tail in the active conformation [131–135]. Scaffold proteins also play a key role in kinase regulation by assembling the necessary components and positioning them in the correct spatial arrangement (Figure 9C), as described for 14-3-3 and BRAF.

Localisation

Aside from catalytic regulation at a structural and molecular level, the organisation of proteins into different cellular locations provides an additional layer of control. The probability of two interaction partners coming into contact by random diffusion in the crowded environment of a cell is very unlikely. To enhance interaction efficiency, cells shuttle proteins into distinct compartments, thereby increasing the local concentration of potential interactors (Figure 9D). As a result, kinase activity can be temporally controlled, by only initiating its localisation upon certain signals. This mechanism is demonstrated by PDK1, which undergoes dimerisation from an increase in its local concentration that is triggered by binding to the lipid second messenger phosphatidylinositol (3,4,5)-triphosphate (PIP3) at the plasma membrane [115].

Cellular localisation can also be employed to restrict a kinase's catalytic activity to a particular compartment (Figure 9D). The DMPK family consists of seven kinases with an AGC kinase domain and a membrane-binding domain, separated by rigid coiled-coils of conserved lengths. With the membrane-binding domain anchored at the plasma membrane, the elongated coiled-coil functions as a molecular ruler by restricting the zone of kinase activity at a fixed distance from the membrane [136,137]. As each member of the DMPK family has a conserved, but different length of its coiled coil domain, they each have access to potentially unique substrate pools.

1.3.4 AGC kinases

The AGC kinases are one of the eight protein kinase families and comprise 63 serine/threonine kinases [69] (Figure 10A). As discussed in Chapter 1.2.1, AGC kinases are characterised by the presence of a ~50 amino acid long regulatory C-tail at the end of the kinase domain [68]. The C-tail can be divided into three segments; the C-lobe tether (CLT),

the active-site tether (AST), and the N-lobe tether (NLT), which together describe how the C-tail docks into various locations around the surface of the kinase [68]. C-tail docking induces conformational changes that activate the kinase, and is accomplished by several regulatory motifs along the tail.

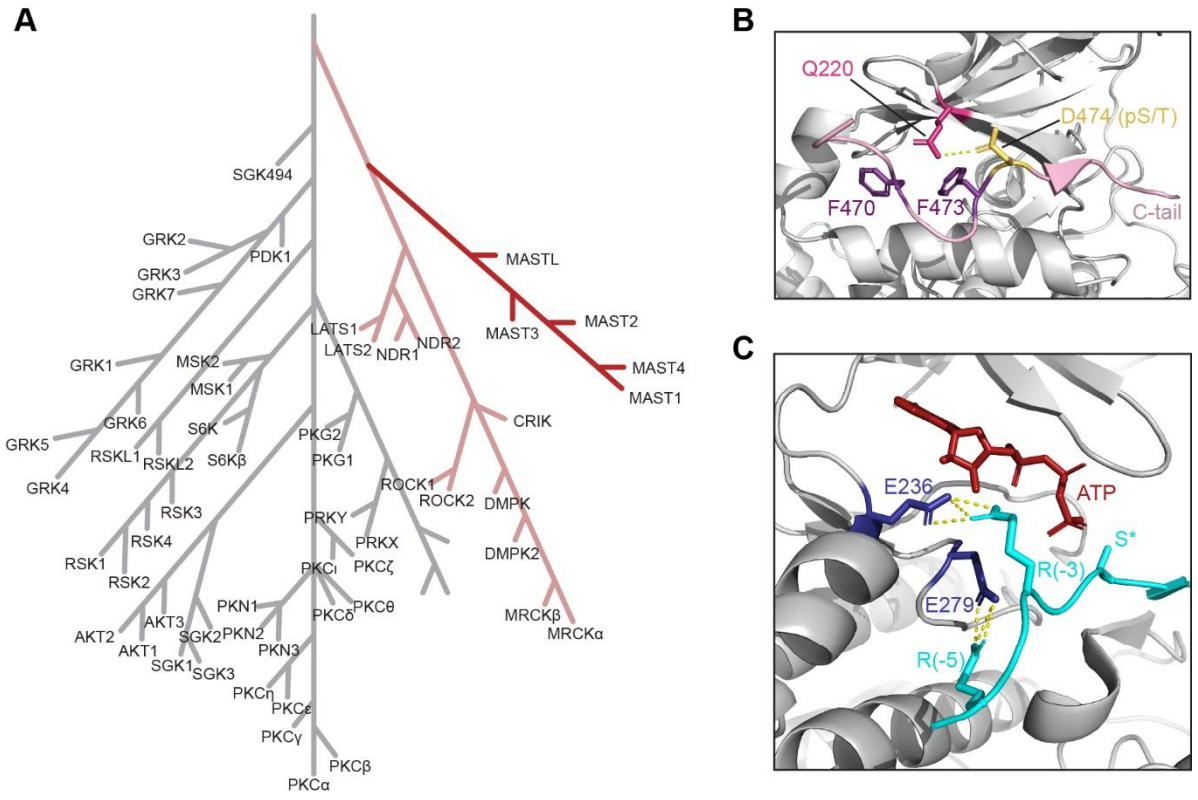

Figure 10. AGC kinases.

A. Family tree of all AGC kinases. The MAST family (red) and the DMPK family (pink) diverged together from the rest of the AGC family, early in evolution. **B.** AGC kinases are characterised by their regulatory C-tail (light pink), which harbours the hydrophobic motif FXXF(S/T) (F470 and F473, purple) (AKT2 depicted, PDB: 1O6K). The aromatic rings of the phenylalanines are buried into a hydrophobic pocket of the N-lobe. The phosphorylated serine or threonine residue succeeding the second phenylalanine (replaced in this structure with a phosphomimetic aspartate, D474, yellow), makes a hydrogen bond with a glutamine residue in the β4 strand (Q220, dark pink). **C.** AGC kinases recognise the substrate motif RXRXX(S/T) by forming hydrogen bonds between two acidic amino acids in its active site (E236 and E279, dark blue) and the -3 and -5 arginines of the substrate (cyan), respectively (AKT2 depicted, PDB: 1O6K). S* represents the phosphosite.

One such motif, called the hydrophobic motif (HM), is found in the NLT. The motif sequence typically conforms to FXXF(S/T), with some variants incorporating alternative hydrophobic residues in place of the first phenylalanine. Phosphorylation of the serine or threonine succeeding the HM allows it to hydrogen bond with a glutamine residue in the β4 strand. This promotes insertion of the phenylalanine's aromatic rings into a

hydrophobic pocket of the kinase's N-lobe (Figure 10B), which in turn stabilises the αC helix in its active conformation [138]. Some AGC kinases harbour an additional regulatory phosphorylation site in the C-tail, slightly upstream of the HM, called the turn motif (TM). When phosphorylated, the TM docks into a positively charged pocket in the N-lobe, acting as a tether mid-way through the C-tail to aid engagement of the HM into the hydrophobic pocket [139].

The canonical AGC kinase substrate motif, RXRXX(S*)φ, is recognised by specific acidic residues within the core of the kinase domain. Based on the residue numbering of AKT2, the arginine in the -3 position forms a hydrogen bond with E236, as does the arginine in the -5 position with E279 (Figure 10C), though many AGC kinases employ an aspartate at these positions. Deviations to the canonical recognition motif are also reported, with the NDR and LATS kinases preferring a histidine in the -5 position instead of an arginine [140].

While activation loop phosphorylation is typically involved in the activation of AGC kinases, members of the DMPK family function independently of this. MRCK displays full kinase activity despite harbouring a valine in the canonical phosphorylatable position in its activation loop [137,141]. Furthermore, while ROCK possesses a threonine in this position, its mutation to either a non-phosphorylatable alanine or phospho-mimetic glutamate had no effect on kinase activity [136]. Although not explored yet, the MAST kinases similarly lack a phosphorylatable residue in this position, and are likely not regulated by activation loop phosphorylation. Instead, MAST1 harbours an aspartate in the canonical position, which has the potential to act as a phosphomimetic and form a similar network of hydrogen bonds as the typically phosphorylated serine or threonine. If so, an alternative regulatory mechanism may be necessary to control the formation of that network.

1.3.5 Phosphatases – the kinase antagonist

The transduction of cellular signals via phosphorylation must be reversible in order to counterbalance signalling pathways and maintain homeostasis. While kinases catalyse the transfer of a phosphate onto a substrate, phosphatases catalyse the opposite reaction. The active site of a protein phosphatase accommodates a phosphorylated serine, threonine, or tyrosine residue from a substrate, along with a water molecule that acts as

a nucleophile. Hydrolysis of the phosphoester bond results in the release of an inorganic phosphate and the dephosphorylated substrate.

Dephosphorylation is a classic mechanism for regulating the catalytic activity of kinases. Kinases that rely on phosphorylation of their activation loop or hydrophobic motif for activity must be appropriately switched off by dephosphorylation. This applies for the pro-growth kinase AKT, which is frequently hyperactivated in human cancers and overgrowth disorders [142,143]. The phosphatase responsible for dephosphorylating AKT's activation loop is established as protein phosphatase 2A (PP2A) [144,145], while PH domain leucine-rich repeat protein phosphatase 1-2 (PHLPP1-2) has been proposed to dephosphorylate AKT's hydrophobic motif [146,147]. However, a recent study revealed that the PHLPPs are pseudophosphatases, having lost their catalytic activity in the last metazoan ancestor [148].

While phosphatases are relatively understudied in comparison to kinases, their importance is highlighted by the many human diseases associated with phosphatase mutations. For example, mutations affecting several subunits of PP2A have been linked to various neurodevelopmental and neurological disorders. Mutations in PPP2CA, a catalytic subunit of PP2A, have been identified in cases of intellectual disability, ASD, epilepsy, corpus callosum agenesis, and severe language delay [149]. Similarly, disruption of the regulatory or scaffolding subunits of PP2A has similar outcomes: mutations in PPP2R5D, a regulatory subunit, and PPP2R1A, a scaffolding subunit, were found in individuals with intellectual disability, epilepsy, hypotonia, and corpus callosum agenesis [150]. Numerous studies have also implicated the lipid and protein phosphatase PTEN in ASD, particularly in combination with macrocephaly and developmental delay [151–154].

Taken together, it is clear that phosphorylation-based signal transduction must be tightly regulated by kinases, phosphatases, and their associated mechanisms, to coordinate the sensitive process of neurodevelopment. In this work, we investigate how the kinase MAST1 contributes to this regulation through structural, biochemical, and *in vivo* characterisation.

2 Aims

This work aims to shed light on the biological function and molecular mechanisms of MAST1, using a broad range of approaches such as *in vitro* biochemistry, cellular studies, and mouse models. The following three specific aims will be addressed in this work.

1. **What is the substrate of MAST1?**

   While a handful of studies have proposed candidate substrates of the MAST kinases, none so far conform to the canonical AGC kinase recognition motif, nor establish a functional link to neurodevelopment. We aim to use both unbiased *in vivo* and targeted *in vitro* approaches to determine the bona fide substrate of MAST1. Identification of the substrate will shed light on the biological pathways MAST1 acts in and the cellular processes it regulates.

2. **How is MAST1 activity regulated?**

   Almost nothing is currently known about the molecular mechanism by which MAST kinases fulfil their biological role. With an *in vitro* biochemical and structural approach, we will investigate the molecular regulation of MAST1 kinase activity. We will explore questions such as what is required for full kinase activity, how the switch between active and inactive states occurs, and what regulatory motifs, domains, and interaction partners are involved.

3. **How do the MCC patient mutations cause disease?**

   To date, seven MAST1 mutations have been associated with MCC. In order to understand the pathogenicity of these MAST1 mutations, we aim to investigate their molecular consequences. We would like to understand how the mutations affect MAST1 structurally, how they affect its catalytic activity, and how this can be extrapolated to explain the observed phenotype of the enlarged corpus callosum.

3 Results

3.1 A complex of MAST1 and 14-3-3η regulates Tau phosphorylation in the developing cortex

3.1.1 Preamble

The MAST kinases have recently emerged as candidate genes for several neurodevelopmental disorders. Despite this, almost nothing is understood about their substrates, the pathways they act in, and the molecular mechanisms governing their kinase activity. Using *in vitro* biochemistry, cellular studies, and mouse models, we have identified 14-3-3η an interaction partner of MAST1, p21-activated kinase 4 (PAK4) as an upstream kinase of MAST1, and Tau as a potential MAST1 substrate. We also investigate the molecular consequences of disease-associated MAST1 mutations, and show that they result in misfolding of the protein or perturbation of MAST1 kinase activity. Our findings shed light on the pathways MAST1 may be involved in and its biological role during cortical development.

This work has been deposited on bioRxiv and is currently under review at PNAS (as of 27.01.2026).

3.1.2 Contribution statement

This publication is my main, first author publication from my PhD. I performed all experiments in the publication with the exception of the mouse line generation and characterisation, preparation of phosphoproteomics samples, and proteomics and phosphoproteomics experiments. I was also involved in the design of the experiments and writing of the manuscript.

3.1.3 Publication

Antonioli S., Heisterkamp P., Chen W., Anrather D., Hartl M., Martinez-Reza M.F., Tripathy R., Schutzbier M., Mechtler K., Keays D.A., Leonard T.A. (2025) A complex of MAST1 and 14-3-3η regulates Tau phosphorylation in the developing cortex. *bioRxiv,* doi: https://doi.org/10.1101/2025.07.09.663707.

A complex of MAST1 and 14-3-3η regulates Tau phosphorylation in the developing cortex

Sumire Antonioli[1,2,§], Patrick Heisterkamp[3,§], Weiqiang Chen[4], Dorothea Anrather[4], Markus Hartl[4,5], Maria-Fernanda Martinez-Reza[6], Ratna Tripathy[7], Michael Schutzbier[7,] Karl Mechtler[7], David A. Keays[3,7] and Thomas A. Leonard[1*]

[1]Max Perutz Labs, Medical University of Vienna, Dr. Bohr-Gasse 9, 1030, Vienna, Austria.

[2]Vienna BioCenter PhD Program, a Doctoral School of the University of Vienna and the Medical University of Vienna, A-1030 Vienna, Austria.

[3]Division of Neurobiology, Department of Biology, Ludwig-Maximilians-University Munich, Grosshaderner Str. 2, 82152 Planegg-Martinsried, Germany

[4]Max Perutz Labs, Mass Spectrometry Facility, Vienna Biocenter Campus (VBC), Dr. Bohr-Gasse 9, 1030, Vienna, Austria.

[5]University of Vienna, Center for Molecular Biology, Department of Biochemistry and Cell Biology, Dr. Bohr-Gasse 9, 1030, Vienna, Austria.

[6]Faculty of Medicine, Ludwig-Maximilians-University Munich, Grosshaderner Str. 9, 82152 Planegg-Martinsried, Germany

[7] Institute of Molecular Pathology (IMP), Dr-Bohr Gasse 7, Vienna 1030, Vienna Biocentre (VBC), Austria.

[§]These authors contributed equally to this work.

[*]Correspondence: thomas.leonard@meduniwien.ac.at

Summary

The MAST family of serine/threonine kinases has been implicated in a spectrum of human neurodevelopmental disorders. However, little is known about their biological function or regulation. Seeking to fill these gaps in our knowledge, we have identified upstream and downstream partners of MAST1. 14-3-3η, a neuronal 14-3-3 paralog, specifically interacts with MAST1 at two regulatory serines, S90 and S161. PAK, a neuronal regulator of the actin cytoskeleton, phosphorylates MAST1 to regulate its interaction with 14-3-3η. Exploiting mouse models of human Mega Corpus Callosum Syndrome (MCC) and whole brain phosphoproteomics, we identify the microtubule-associated protein Tau as a substrate of MAST1. We show that pathogenic MAST1 mutations perturb protein function either through misfolding or attenuation of kinase activity. Our data is consistent with a model in which the MAST kinases couple PAK, a neuronal regulator of the actin cytoskeleton, to microtubule remodeling during the differentiation and specification of cortical neurons.

Keywords

Serine/threonine kinase, phosphorylation, microtubules, corpus callosum, neurodevelopment.

Introduction

The differentiation of cortical neurons is an essential and tightly regulated process, dysregulation of which is associated with a variety of neurodevelopmental disorders (NDDs). A rare NDD called Mega-Corpus-Callosum Syndrome with Cerebellar Hypoplasia and Cortical Malformations (MCC-CH-CM) is characterized by enlargement of the corpus callosum, epilepsy, and severe cognitive and motor impairment [1]. Whole exome sequencing of a cohort of seven patients revealed that six harbored *de novo* mutations in a gene called Microtubule Associated Serine/Threonine Kinase 1 (MAST1). A mouse model that recapitulates a heterozygous trinucleotide deletion (L278del) identified in an MCC-CH-CM patient mirrors multiple aspects of the disease, including the enlarged corpus callosum. The identification of additional MCC patients bearing mutations in MAST1, as well as *de novo* mutations in MAST1, MAST3, and MAST4 associated with epilepsy, autism, cerebral palsy, and intellectual disability [2–9] has provided further evidence for the involvement of the MAST kinases in neurodevelopment. Despite their association with human NDDs, very little is known about the biological function, structure, or regulation of any MAST kinase.

The MAST kinases are large, ~200 kDa proteins that first arose ~600 million years ago in Cnidaria and Ctenophora, the first organisms with a primitive nervous system [10]. They contain three domains; an N-terminal domain of unknown function (DUF) which harbors a four-helix bundle (4HB), a catalytic Ser/Thr kinase domain, and a C-terminal PDZ domain. The kinase domain belongs to the AGC family of protein kinases, characterized by the presence of a regulatory C-terminal tail [11]. Although many eukaryotic protein kinases are regulated by activation loop phosphorylation [12], the MAST kinases possess a glutamine in place of the canonical serine or threonine.

MAST1 is expressed in post mitotic cortical neurons throughout neurodevelopment [1,13,14], associating with the microtubule cytoskeleton via unknown microtubule associated proteins (MAPs) [1]. It has been reported that the PDZ domain of MAST1 interacts with the adaptor protein β2-syntrophin, bridging it to the dystrophin/utrophin network at postsynaptic densities [13]. Little is known about MAST substrates. MAST1/2/3 and KIN-4 (the sole homolog of MAST kinases in *C. elegans*) reportedly phosphorylate the C-terminus of PTEN in a PDZ domain-dependent manner, however, this interaction has not been confirmed *in vivo* [15–17]. In addition, Mitogen-

Activated Protein Kinase Kinase (MEK) [18] and cAMP-regulated phosphoprotein of 16 kDa (ARPP-16) [19] are also reported substrates. However, these findings are largely based on immunoprecipitated proteins and lack kinase-dead controls, while the substrates neither conform to canonical AGC kinase substrate motifs, nor establish a functional link to development of the corpus callosum.

Here, we identify 14-3-3η as an interaction partner of MAST1. We show that 14-3-3η binds specifically to two conserved phosphorylation sites in MAST1, S90 and S161. We identify p21-activated kinase (PAK) as the upstream kinase that phosphorylates MAST1 on S90, and S161 as a regulatory autophosphorylation site. We demonstrate that MAST1 phosphorylated on either S90 or S161 forms a stable complex with 14-3-3η *in vitro*. Using two mouse models of patient-derived MCC-CH-CM mutations, we identify the microtubule-associated protein Tau as a substrate of MAST1 and demonstrate that MAST1 phosphorylates Tau *in vitro*. Finally, we show that MCC-CH-CM-associated disease mutations perturb MAST1 kinase activity either through misfolding of its 4HB domain or disruption of its catalytic site.

Results

MAST1 interacts with 14-3-3 proteins via S90 and S161

To shed light on the function and regulation of the MAST kinases, we first sought to identify MAST1 interactors by affinity-purification mass spectrometry (AP-MS) in HEK293 cells. All MAST1 constructs employed in this study are depicted in Figure 1A. MAST1^{DKP}, which includes all three folded domains, was N-terminally tagged with EGFP and overexpressed in HEK293 cells (Figure 1B). Comparison of the EGFP-MAST1-bound proteins with an EGFP-only control revealed a MAST1-dependent 6- to 30-fold enrichment of six 14-3-3 paralogs (η, γ, ε, β, ζ, and θ) (Figure 1C, Supplementary Files 1-2). 14-3-3 proteins are known to bind specifically to phosphorylated serines [20]. Analysis of MAST1's amino acid sequence by 14-3-3Pred [21] revealed two putative 14-3-3 binding motifs [22,23] surrounding S90 and S161. Both sites exhibit near-invariant sequence conservation over 600 million years. To visualize a potential interaction between MAST1 and 14-3-3, we predicted the structure of MAST1^{D} and the seven mammalian 14-3-3 isoforms, with a 2:2 stoichiometry implied by the dimeric nature of 14-3-3 proteins. AlphaFold [24,25] generated five near-identical models for each prediction with an RMSD ranging between 0.439 and 4.286, placing the unstructured N-terminal region of MAST1 in the cradle of 14-3-3 (Figure 1D-E; 14-3-3η shown as representative). Superposition of the resulting structure with an experimentally determined structure of 14-3-3η in complex with a bound phospho-peptide [26] revealed that either residue S90 (Figure 1D) or S161 (Figure 1E) of MAST1 was consistently placed in the same position as the bound phospho-serine of the ligand.

To probe whether the N-terminal region of MAST1 binds to 14-3-3, we compared truncation constructs of MAST1 lacking S90, or both S90 and S161 (Figure 1B). By performing pairwise comparison of the interactomes of the truncation constructs, we observed significant enrichment of six 14-3-3 paralogs by MAST1^{DKP} when compared to either MAST1^{DKP} ΔS90 (Figure S1A) or MAST1^{DKP} ΔS90 ΔS161 (Figure S1B). To determine the site specificity of the interaction, we next performed AP-MS comparisons between MAST1^{DKP} WT and S90A or S161A point mutants. Mutation of either S90 or S161 resulted in a significant loss of 14-3-3 binding to MAST1 (Figure 1F-G), while double mutation of both residues resulted in an apparently synergistic loss of 14-3-3 proteins (Figure 1H). The absence of 14-3-3 enrichment in MAST1^{DKP} ΔS90, which

includes S161 but not S90 (Figure 1I), suggests that 14-3-3 binding to S161 is dependent on 14-3-3 first binding to S90. 14-3-3η was reproducibly the most highly enriched paralog of the six, despite having the lowest abundance in HEK293 cells [27] (Figure S1C).

We further confirmed the interaction between purified 14-3-3η to MAST1 by determining its binding affinity to phosphorylated peptides corresponding to the S90 and S161 motifs *in vitro* (Figure 1J). We confirmed the correct mass of all recombinant proteins and derivatives thereof employed in this study by mass spectrometry (Figure S2). Consistent with the AP-MS results, 14-3-3η bound to both phospho-S90 (p-S90) and phospho-S161 (p-S161) peptides, but neither to their unphosphorylated counterparts nor a phosphopeptide with a scrambled amino acid sequence. 14-3-3θ, which exhibited the lowest enrichment by AP-MS, bound MAST1 phosphopeptides with a correspondingly lower affinity.

Finally, single cell sequencing has shown that MAST1 and 14-3-3η are expressed simultaneously in developing cortical neurons in mice [28] (Figure S3A-D). In summary, 14-3-3η binds to MAST1 phosphorylated on either S90 or S161.

PAK4 phosphorylates MAST1 on S90

The phosphorylation-dependent interaction of MAST1 with 14-3-3η immediately begs the question of which kinase(s) phosphorylate S90 and S161. To identify candidate upstream kinases for the conserved S90 site (Figure 2A), we employed the ScoreSite prediction algorithm [29], which identified PAK4-6 as the highest ranked kinases (Figure 2B). Curiously, we observed significant enrichment of PAK4 in all AP-MS experiments involving MAST1 S90A (Figure 1F, 1H), suggesting that endogenous PAK4 may have been trapped on a non-phosphorylatable substrate. While PAK4 is relatively abundant in HEK293 cells (280 nM), PAK5 and PAK6 are not detected [30] (Figure S4A). PAK4-6 are group II PAKs with a consensus motif that differs from group I PAKs (PAK1-3) at positions P+2 and P+3 (Figure S4B). PAK4-6 recognize an alanine at the P+2 position, in contrast to the tyrosine or phospho-tyrosine favored by PAK1-3, and PAK4 has a strong preference for a serine at the P+3 position [31]. The S90 motif of MAST1 encodes alanine and serine in the P+2 and P+3 positions respectively (Figure 2A). Consistent with PAK4

being the upstream kinase of MAST1 in HEK293 cells, we observed that purified, recombinant PAK4 phosphorylates MAST1^{D} in an *in vitro* radiometric kinase assay while a kinase-dead mutant did not (Figure 2C). Mass spectrometry analysis revealed that S90 was phosphorylated with the highest spectral count (Figure 2D-E, Supplementary File 3). We also observed S77 to be phosphorylated, likely due to the similarity in the surrounding amino acid sequence. Single cell RNA sequencing data of the developing mouse brain shows a significant overlap in the transcripts of MAST1 and PAK6, whereas PAK4 is barely detected and PAK5 is not detected at all (Figure S4C-H). These findings imply that a group II PAK is an upstream regulator of MAST1 signaling in the developing cortex, with PAK6 being the strongest candidate.

MAST1 S161 is an autoregulatory motif

Having identified the upstream kinase for S90, we next sought to identify the kinase that phosphorylates S161. Inspection of the conserved motif surrounding S161 (Figure 3A) revealed the presence of a canonical AGC kinase consensus sequence, characterized by arginine in the P-5 and P-3 positions, as well as a large hydrophobic residue in the P+1 position (Figure 3B) [11]. This motif is near invariant in all MAST kinases (Figure 3C), implying an evolutionarily conserved function. Since MAST kinases are, themselves, members of the AGC family, this observation suggested that S161 may represent an autoregulatory phosphorylation site. AlphaFold predictions of a complex between the MAST1 kinase domain and the DUF reproducibly converged on a model that places S161 in the substrate-binding cleft of the kinase domain, canonically poised for phospho-transfer (Figure 3D, S5A). In an *in vitro* kinase assay, recombinant MAST1^{DK} ΔS90 (Figure S5B-C) incubated with ATP was able to autophosphorylate, while a kinase-dead MAST1 was completely inactive (Figure 3E-F). To determine the site-specificity of the reaction, we performed tandem mass spectrometry, which revealed phosphorylation of S161 (Figure 3G, Supplementary File 3). However, the reaction was inefficient and resulted in multiple phosphorylated sites, suggesting that unknown factors may be required for full and specific MAST1 activity. Finally, we measured the binding affinity of MAST1^{DK} ΔS90 ΔS161 (Figure S5D-E) for a peptide corresponding to the S161 motif (Figure 3H). A peptide bearing the native sequence of MAST1 bound to the kinase with a low affinity consistent with the known strength of kinase-substrate interactions [32].

Mutation of the arginines at P-3 and P-5 reduced the binding affinity, which was further reduced by mutation of the leucine in the P+1 position (Figure 3H). These findings are consistent with a specific interaction of the conserved S161 motif with the MAST1 kinase domain. In summary, MAST1 undergoes autophosphorylation at S161, but the factors which control the rate and specificity of the reaction are unknown.

MAST1 phosphorylated on S90 or S161 forms a complex with 14-3-3η *in vitro*

Having established that MAST1 interacts specifically with 14-3-3η in a phosphorylation-dependent manner both in cells and *in vitro*, we sought to reconstitute stable complexes of the purified proteins *in vitro*. To first reconstitute S90-phosphorylated MAST1:14-3-3η, we co-expressed MAST1^{DK} with 14-3-3η and PAK4^{FL} in baculovirus-infected Sf9 insect cells. Affinity purification of the GST-tagged 14-3-3η yielded a complex with MAST1 which was stable by size-exclusion chromatography (SEC) (Figure 4A-B). Unexpectedly, however, MAST1 was found to be phosphorylated not only on S90 but also on S161 and S163 by tandem mass spectrometry, with higher spectral counts for p-S161 and p-S163 than p-S90 (Figure 4C, Supplementary File 3). The origin and significance of MAST1 phosphorylation on S163 in the insect cells is unclear, but a phospho-peptide corresponding to the S163 motif is incapable of binding to 14-3-3η (Figure S6A). Therefore, the complex of MAST1 and 14-3-3η isolated from insect cells co-expressing PAK4 is mediated by phosphorylation of S90, S161, or a combination of both. This suggests that PAK4-mediated MAST1 phosphorylation on S90 promotes the acquisition of p-S161, presumably by autophosphorylation, but this will require further investigation. To determine the stoichiometry of the complex, we measured the mass of the particles by mass photometry [33]. Unfortunately, at the concentrations required for mass photometry, the complex dissociated into its constituent components (Figure S6B). We therefore employed glutaraldehyde cross-linking to stabilize the complex (Figure S6C) and measure its stoichiometry. Particles of MAST1 and 14-3-3η were observed to have an average mass of 132 kDa, which corresponds to a 1:2 complex (Figure 4D, Figure S6D-F). The 1:2 stoichiometry was further supported by gel densitometry analysis of the complex in Figure 4B.

Since efforts to obtain S90-phosphorylated MAST1 in complex with 14-3-3η by co-expression with PAK4 yielded complexes with a mixture of S90- and S161-

phosphorylated MAST1, we reconstituted the S90-phosphorylated MAST1:14-3-3η complex *in vitro* to assess its stoichiometry. Purified MAST1^{D}, phosphorylated with PAK4^{FL} and subsequently incubated with 14-3-3η at a 1:1 stoichiometry, was purified by analytical SEC (Figure 4E). Complex formation was evidenced by the increase in hydrodynamic radius of MAST1 and the co-elution of the two proteins. Gel densitometry of the co-eluting peak again indicated a 1:2 complex (Figure 4F). This was confirmed by glutaraldehyde cross-linking mass photometry, where particles of S90-phosphorylated MAST1 crosslinked to 14-3-3η were observed to have an average mass of 90 kDa, corresponding to a 1:2 complex (Figure 4G, Figure S6D, G-H). In summary, we could reconstitute MAST1:14-3-3η complexes *in vitro*, mediated by either S90 and S161 phosphorylation, and both assemble with a stoichiometry of 1:2.

MAST1 G519S mice exhibit an enlarged corpus callosum

To investigate the mechanisms of MCC-CH-CM pathogenicity, we next focused on the molecular consequences of patient-derived MAST1 mutations. MCC-CH-CM patients with heterozygous mutations in MAST1 exhibit gross morphological alterations in their brain structure, with a significantly enlarged corpus callosum [1]. Curiously, MAST1 knock-out mice are phenotypically normal [1], implying that the disease is driven by a dominant negative effect of the mutant MAST1 and not by haploinsufficiency. Three of these mutations are triplet deletions in the coding sequence of the 4HB domain and one is a missense mutation in the activation loop of the kinase domain that replaces an invariant glycine in the DFG motif with a serine (Figure 5A). A MAST1$^{L278del/+}$ mouse model has previously been generated and exhibits an enlarged corpus callosum and thinner cortex [1]. The G517S patient mutation (G519S in mice) has, as yet, not been phenotypically characterized in a mouse model. Using CRISPR-Cas9 genome editing, we generated MAST1$^{G519S/+}$ and MAST1$^{G519S/G519S}$ mice. Following pronuclear injection with guides targeting exon 14 (Supplementary Table 1), founder animals were identified by Sanger sequencing (Figure 5B-C) and backcrossed for 10 generations to C57Bl/6J. G519S homozygotes died shortly after birth, whereas heterozygotes survived into adulthood. Analysis of adult G519S/+ mouse brains by Nissl staining confirmed the presence of an enlarged corpus callosum with a reduction in cortical thickness (Figure 5D-F) consistent with the disease state and the L278del mouse model. It is worth noting

that while the phenotypes of the G519S/+ mouse and the previously described L278del/+ mouse are qualitatively similar, the L278del/+ line displays a more pronounced enlargement of the corpus callosum, hinting towards a more severe molecular disruption caused by the L278del mutation. Analysis of MAST protein levels in P0 cortical samples revealed a dose dependent decrease in the levels of MAST1, MAST2 and MAST3 in the G519S/+ mouse compared to +/+ (Figure 5G-H) consistent with a dominant negative mechanism. This implies that the disease phenotype stems from a perturbation of MAST signaling in the developing brain.

Tau is a MAST1 substrate

To identify candidate substrates of MAST1, we exploited the previously published MAST1$^{L278del/L278del}$ mouse model and the MAST1$^{G519S/G519S}$ model generated in this study. To explore how the mutations alter the phosphoproteome in the developing brain we extracted protein lysates from P0 cortices from both controls and homozygotes for the L278del and G519S lines. This time point was selected because the callosal projection neurons are already specified and are extending axons to the contralateral hemisphere [35]. Following protein isolation, denaturation, reduction and alkylation, isobaric labels were added and samples were enriched for phosphopeptides using titanium dioxide (TiO2) resin. This resulted in the identification by mass spectrometry of 50601 phosophopeptides in the L278del mouse line and 22192 phosphopeptides in the G519S line, of which 1608 and 610 passed the 5% FDR threshold respectively. A comparative analysis identified 70 phosphopeptides, from 38 proteins, that were observed to be differentially phosphorylated in both L278del and G519S mice when compared to littermate controls (Figure 6A, Supplementary File 4). By filtering for hypo-phosphorylated proteins for which the phosphorylated residue was embedded in an AGC kinase consensus motif, we reduced the list of candidate proteins to four (Figure 6B). Of the four candidates, phosphorylation of microtubule-associated protein Tau (MAPT) on S214 was most notable. Tau is a microtubule-associated protein that, like MAST1, is highly expressed in neurons of the developing mouse brain (Figure S7A-B) and the phosphorylation state of S214 is considered to be a biomarker for Alzheimer's Disease (AD) [34,36]. Inspection of the amino acid sequence surrounding S214 revealed that it is near-identical to the S161 autophosphorylation site in MAST1 (Figure 6C).

Phosphorylation of Tau on S214 was reduced in both L278del and G519S mice compared to littermate controls (Figure 6D-E).

To assess whether MAST1 can phosphorylate Tau *in vitro*, we performed a kinase assay with purified, recombinant Tau (mouse isoform F). The purity and monodispersity of Tau^{FL} was confirmed by SEC and mass photometry (Figure S7C-D). Wild-type $MAST1^{DK}$ ΔS90 phosphorylated Tau, and a kinase-dead mutant of MAST1 was completely inactive against Tau (Figure 6F). However, the speed of the reaction was lower than what would be expected of a fully active AGC kinase. To benchmark this quantitatively, we compared MAST1 phosphorylation of Tau to the catalytic activity of the closely related AGC kinase Myotonic Dystrophy Kinase-Related Cdc42-binding Kinase α (MRCKα), on its substrate myosin light chain 2 (MLC2). MRCKα exhibited a 50-fold higher catalytic efficiency than MAST1 (Figure 6G). The post-translational modification profile of Tau exhibited multiple phosphorylation sites including S214, as well as three known Tau phosphorylation sites [37–39] within its repeat domains (Figure 6H, Supplementary File 3). This phosphorylation pattern is reminiscent of MAST1 autophosphorylation (Figure 3F-G), implying that other factors govern the site-specificity of the reaction. To test whether the catalytic activity of MAST1 is increased when in complex with 14-3-3η, we compared Tau phosphorylation by $MAST1^{DK}$ alone or in complex with 14-3-3η, but observed no significant increase (Figure S7E).

Tau phosphorylated on S214 has previously been reported to bind 14-3-3 proteins [40,41]. Given the similarity of the S214 motif in Tau to the S161 motif in MAST1 and the observation that MAST1 phosphorylated on S161 interacts with 14-3-3η, this is not surprising. We confirmed that purified 14-3-3η binds a phosphorylated peptide of the Tau S214 motif by fluorescence anisotropy (Figure 6I). As previously observed for p-S161, the binding was phosphorylation-dependent and 14-3-3η exhibited a higher affinity than 14-3-3θ. Taken together, these findings support a model in which MAST1 activity plays a role in the regulation of the microtubule cytoskeleton of neurons, via Tau.

MCC-CH-CM mutations perturb MAST1 folding and kinase activity

MAST1 proteins in mouse models of patient-derived MCC-CH-CM mutations exert a dominant negative effect by depleting MAST1, 2, and 3 (Figure 5H and Tripathy *et al.* [1]). To investigate the molecular basis of pathogenicity, we characterized the effect of the four patient-derived mutations from the original cohort [1] *in vitro* (Figure 5A). Since E194, K276 and L278 are all located in α-helices of the 4HB domain (Figure 7A), their deletion would be predicted to induce a register shift in the alpha helix that is incompatible with folding of the 4HB domain. We confirmed that deletion of either E194, K276 or L278 leads to misfolding of MAST1^{D} ΔS90 and the formation of insoluble inclusion bodies in *E. coli* (Figure 7B). By contrast, the WT MAST1^{D} ΔS90 is almost entirely soluble (Figure 7B, S8A). Consistently, expression of a longer construct of MAST1 K276del (MAST1^{DK} ΔS90) in Sf9 insect cells resulted in aggregated protein with low yields (Figure 7C, S8B).

Multiple patients have now been identified with a G517S mutation (mouse G519S), in the kinase domain. Although MAST1^{DK} ΔS90 bearing the G519S mutation was properly folded and monomeric by SEC (Figure 7D, S8C), it exhibited significantly lower kinase activity against Tau *in vitro*, albeit not completely inactive (Figure 7E). Taken together, these observations show that MCC-CH-CM mutations disrupt the folding and/or catalytic activity of MAST1.

Discussion

We have discovered that MAST1 interacts with 14-3-3η in a phosphorylation-specific manner, mediated by S90 and S161. We also identified a group II PAK as the upstream kinase for MAST1 S90 phosphorylation, and S161 as a MAST1 autophosphorylation site. Finally, we provide evidence, both *in vitro* and *in vivo*, that the microtubule-associated protein Tau is a MAST1 substrate.

Our finding that PAK phosphorylates MAST1 sheds light on the broader biological pathways that MAST1 may be involved in. Like MAST1, PAK4 is highly expressed during embryogenesis, and is crucial in neurodevelopment, where it regulates the proliferation of neural progenitor cells [42], neuronal differentiation, and migration [43]. This stems from PAK4's role in the Cdc42-dependent reorganization of the actin cytoskeleton [44–48]. Depletion of either Cdc42 or PAK4 results in cell polarity defects in a number of cell types [49], while knockout of PAK4 is embryonic lethal [43]. PAK6 activity has been correlated with neurite outgrowth [50], and while PAK5/PAK6 double knockout mice are viable, they exhibit locomotor, learning and memory defects [51]. Coordination of the actin cytoskeleton is crucial for axonal growth and steering. Actin and microtubule dynamics are coupled in the peripheral domain of the growth cone, together driving accurate axon navigation [52,53]. Importantly, dysregulation of the growth cone can cause axonal rerouting, resulting in the disruption of axonal fiber tracts such as the corpus callosum [54]. Here, Cdc42-activated group II PAKs may link actin polymerization and MAST1-mediated microtubule reorganization. However, the mechanisms that mediate the co-localization of MAST1 and PAK will require further investigation.

We have identified S214 of Tau as a MAST1 substrate. Tau binds to microtubules via its microtubule binding domain, encompassing the proline-rich domain (which contains S214) and the repeat domains, allowing Tau to rigidify and stabilize microtubules. Several studies have demonstrated the decreased microtubule binding capacity of Tau p-S214, reducing the stability of axonal microtubules [36,55,56]. This effect is a combination of a decrease in microtubule binding affinity when Tau is phosphorylated [55], and the sequestration of Tau p-S214 by 14-3-3, which we and others [40,41] have observed. Interestingly, S214 has previously been identified as a cAMP-dependent protein kinase (PKA) phosphorylation site [34,36,40,41,58]. Both PKA and the MAST kinases are AGC kinases, which recognize a conserved substrate consensus motif. It is therefore

possible that MAST1 and PKA converge on the same substrate under different cellular conditions. It is also worth noting that, since MAST1 S161 and Tau S214 motifs are near-identical, it is perhaps not surprising that 14-3-3η is a common component in the signaling pathway. Curiously, hyperphosphorylation of S214 is also a marker of Alzheimer's disease [34,36], though the significance of the connection to neurodevelopment is unclear. Our data also demonstrates that, at least *in vitro*, MAST1 is capable of phosphorylating Tau on S262, S324 and S356, all of which are reported phosphosites that inhibit microtubule binding [37–39]. Nevertheless, these sites deviate from canonical AGC recognition motifs, so whether MAST1 is the physiologically relevant kinase *in vivo* will require further investigation. Whilst we have not yet explored the implications of MAST1-mediated Tau phosphorylation in the context of neurodevelopment, we hypothesize that MAST1 may negatively regulate microtubule polymerization in neuronal axons to ensure proper formation of the corpus callosum. Indeed, while the loss of Tau alone appears to have little impact on corpus callosum formation, a Tau and MAB1B double-knockout in mice causes a severe reduction in callosal size [57], beyond the more moderate agenesis phenotype observed in MAB1B-only knockout animals [57,59]. This suggests a potential role of Tau in corpus callosum development, which may be partially redundant with MAP1B.

By combining these cellular insights with mechanistic insights into the molecular regulation of MAST1, we propose a model for MAST1 signaling (Figure 8). Activated Cdc42 recruits a group II PAK to the plasma membrane, whereupon it phosphorylates MAST1 on S90. MAST1 p-S90 specifically recruits 14-3-3η, expression of which is highly enriched in the brain and ubiquitously expressed in all brain structures [60–63], forming a complex with 1:2 stoichiometry. Since deletion of the S90 motif results in a loss of 14-3-3 binding to S161, we hypothesize that recruitment of 14-3-3η via p-S90 is required prior to S161 autophosphorylation and subsequent 14-3-3η binding. PAK-mediated phosphorylation of MAST1 S90 could therefore serve to pre-assemble a MAST1:14-3-3η complex. We hypothesize that the p-S90-bound complex is inactive, primed for activation by an unknown cofactor. The binding of a stimulatory cofactor to either MAST1 or the MAST1:14-3-3η complex would trigger MAST1 autophosphorylation at S161, thereby relieving autoinhibition. The consequences of p-S161 displacement from the kinase domain are two-fold: activation of the kinase, and sequestration of p-S161 by 14-3-3η, the latter of which may serve to both prevent reassociation of S161 and protect

it from dephosphorylation. Activated MAST1 phosphorylates Tau on S214, causing the dissociation of Tau from microtubules. In short, Cdc42 signaling at the plasma membrane is transduced, through MAST1, to microtubule reorganization and changes in cell morphology.

While our findings imply a PAK-dependent coupling between actin and microtubule reorganization via MAST1, there are still many unanswered questions, particularly regarding the mechanism of activation of MAST1. Our data currently do not support a direct role for 14-3-3η in kinase activation, and MAST1 exhibits low activity *in vitro*. These observations beg the obvious question of precisely what role 14-3-3η plays in MAST1 regulation. Like MAST1, the oncoprotein BRAF possesses two regulatory phosphoserines, which simultaneously occupy the binding grooves of a 14-3-3 dimer. This trimeric complex maintains BRAF in an inactive conformation [64,65], which, upon RAS binding, is converted into an active complex with 2:2 stoichiometry [64]. Whilst it is easy to envisage a similar mode of regulation for MAST1, both p-S90 and p-S161-mediated MAST1:14-3-3η complexes were observed to be trimeric, and a tetrameric complex has, so far, not been observed.

While the involvement of 14-3-3η in MAST1 signaling is clear, we speculate that there is another, as yet unidentified, factor that drives its activation. AGC kinases, such as MAST, are defined by a ~50 amino acid C-terminal tail containing multiple regulatory motifs, including a hydrophobic motif that allosterically promotes the active conformation [11]. In the closely related Dystrophia Myotonica Protein Kinase (DMPK) kinases, the hydrophobic motif is sandwiched in place by dimerization of the N-terminal capped helix bundle domain [66–69], while the Nuclear Dbf2-related (NDR) kinases are known to depend on MOB1 for activation via a similar mechanism [70–73]. Currently, neither a MAST1-intrinsic domain nor a co-factor has been identified that could fulfil an analogous function. Although inspection of the MAST1 interactome in HEK293s (Figure 1C) failed to reveal any candidate activators by AlphaFold screening, identification of such a factor may depend on the correct cellular context, possibly in differentiated neurons.

Finally, this study provides important insights into the molecular consequences of MCC-CH-CM disease-associated mutations. We show that pathogenic mutations in MAST1 perturb folding and/or catalytic activity of the protein. Similar to the L278del

mouse mutant, we report that the G519S mutation causes a notable decrease in the protein levels of MAST2, MAST3 and MAST4. Since MAST1 knock-out mice are phenotypically normal, this implies that MCC-CH-CM is the consequence of a dominant negative effect. As 14-3-3 proteins are obligate homodimers, the integration of mutant MAST1 has the potential to poison wild-type MAST complexes, though this would depend on hetero-tetramers of MAST and 14-3-3. Alternatively, the localization of mutant MAST1 to microtubules or titration of essential co-factors may inhibit signaling by wild-type MAST1.

In summary, MAST1 is a key regulator of neurodevelopment that potentially links group II PAKs, neuronal regulators of the actin cytoskeleton, to microtubule dynamics. However, several questions surrounding the precise mechanism of MAST1 activation, the origin of the dominant negative effect, and the stoichiometry of 14-3-3η binding remain. Answers to these questions are undoubtedly required to elucidate the physiological role of MAST1 in neurodevelopment as well as its pathological role in MCC-CH-CM.

Acknowledgements

Proteomics analyses were performed on instruments of the Vienna BioCenter Core Facilities (VBCF). We acknowledge members of the Leonard lab for constructive feedback on the manuscript. This work was funded by Austrian Science Fund (FWF) grants P33066, P6212, P36724, and W1261 to T.A.L. We thank Boehringer Ingelheim for funding basic research and the core facilities at the Institute for Molecular Pathology, and Ludwig-Maximilians-University. P.H is supported by the Studienstiftung des deutschen Volkes.

Author Contributions

S.A., P.H., D.A.K. and T.A.L. designed the experiments. S.A. performed all experiments reported in this manuscript with the exception of: proteomics analyses (W.C., D.A., M.H., K.M., G.D.); generation of mouse lines (P.H., R.T., M.F.M.R.); preparation of mouse brain samples for phosphoproteomics (P.H., R.T., M.F.M.R.); analysis of G519S mouse line (P.H.). D.A.K. and T.A.L. obtained funding for the project. S.A., P.H. D.A.K., and T.A.L. wrote the manuscript. All authors commented on the manuscript.

Materials and Methods

EGFP-MAST1 AP-MS

N-terminally EGFP-tagged MAST1^{DKP} constructs (WT, ΔS90, ΔS90 ΔS161, S90A, S161A, S90A S161A) were cloned into the pEGFP-C1 vector for expression in HEK293 cells and were transfected using Lipofectamine 3000 (Invitrogen). Media on the cells was exchanged 24 h post-transfection and cells were harvested by trypsinization 48 h post-transfection. Cells were lysed with three freeze/thaw cycles in liquid nitrogen, resuspended in lysis buffer (10 mM monosodium phosphate, 40 mM disodium phosphate, 10 mM NaCl, 50 mM NaF, 1 mM TCEP, 10 U Denarase, 1x protease inhibitor cocktail (Sigma P8849), 2 mM benzamidine, 2 mM MgCl2, 0.25% CHAPS, 10 mM betaglycerophosphate, 2 mM sodium pyrophosphate, 1 mM sodium orthovanadate, 1 mM EDTA), and incubated at 4°C for 30 min with rotation. Cleared lysates were obtained by centrifuging at 21,000 g, 4°C, for 15 min. Cleared lysates were incubated with GFP-Trap Magnetic beads (Chromotek), incubated at 4°C for 2 h while rotating, washed five times with wash buffer (10 mM monosodium phosphate, 40 mM disodium phosphate, 10 mM NaCl, 50 mM NaF, 1 mM TCEP), and the dry beads were snap-frozen in liquid nitrogen and stored at -80°C, for analysis by mass spectrometry.

Fluorescence anisotropy

A 2x serial dilution series was made with purified protein (14-3-3η, 14-3-3θ, or MAST1^{DK} ΔS90 ΔS161) and mixed with 50 nM of N-terminally FITC-conjugated peptide and incubated at room temperature for 15 min. The following peptides were used in this study: DGRRWSLASLPSS (MAST1$^{85-97}$), DGRRW{pS}LASLPSS (MAST1$^{85-97}$ p-S90), RPRSRSLSPGRSP (MAST1$^{156-168}$), RPRSR{pS}LSPGRSP (MAST1$^{156-168}$ p-S161), PLGDP{pS}GRWARLS (MAST1 p-Scramble), RSRSL{pS}PGRSPSS (MAST1$^{158-170}$ p-S163), PAVRPRSRSLSPGR (MAST1$^{153-166}$ WT), PAVEPESRSLSPGR (MAST1$^{153-166}$ R156E R158E), PAVEPESRSDSPGR (MAST1$^{153-166}$ R156E R158E L162D), RSRTPSLPTPPTR (Tau$^{209-221}$), and RSRTP{pS}LPTPPTR (Tau$^{209-221}$ p-S214). Anisotropy was measured in a 384-well black polystyrene plate on the TECAN Spark Multi-Mode Microplate Reader.

Radiometric kinase assay

For substrate phosphorylation assays, 100 nM of kinase was mixed with 25 μM of substrate in assay buffer (50 mM HEPES pH 7.4, 150 mM NaCl, 1 mM TCEP, 2 mM $MgCl_2$,

2 mM ATP, 0.25% CHAPS, spiked with 1 µL [γ-32P] ATP/100 µL reaction) and incubated at 23°C for up to 2 h. Aliquots were taken from the reaction volume and quenched with 80 mM EDTA over a time course, then equal volumes of each sample were subjected to SDS-PAGE. The gels were washed three times in dH_20, dried, exposed to a phosphor screen for 4 h, and imaged with an Amersham Typhoon imager (Cytiva). Densitometry was performed using ImageJ to quantify the bands of phosphorylated substrate. An internal standard was made by spotting 0.5, 1, 5, and 20 pmol of ATP from the reaction onto a strip of Whatman paper. The standards were also measured with densitometry and used to calculate the total mol of phosphorylated substrate in each sample.

For autophosphorylation assays, 50 nM, 150 nM, and 500 nM of $MAST1^{DK}$ ΔS90 (WT and D499N) was incubated in assay buffer (50 mM HEPES pH 7.4, 150 mM NaCl, 1 mM TCEP, 2 mM $MgCl_2$, 2 mM ATP, 0.25% CHAPS, spiked with 1 µL [γ-32P] ATP/100 µL reaction) at 23°C for up to 2 h. Aliquots were taken from the reaction volume and quenched with 80 mM EDTA over a time course, then equal volumes of each sample were spotted onto a 0.45 µm nitrocellulose membrane. The membrane was washed five times with 20 mL of 75 mM H_3PO_4, and exposed and imaged as described above. An internal standard and densitometry were performed as described above.

Analytical size exclusion chromatography

A Superdex 200 Increase 3.2/300 size exclusion column (Cytiva) was connected to an Äkta Pure with a Micro configuration (Cytiva) and equilibrated in buffer (50 mM HEPES pH 7.4, 150 mM NaCl, 1 mM TCEP) at 4°C. 50 µL of 30 µM protein samples were centrifuged at 21,000 g for 5 min prior to injection onto the column. For the $MAST1^{D}$ p-S90 and 14-3-3η complex formed *in vitro*, equimolar concentrations of each protein were mixed and incubated for 30 min at room temperature prior to injection. 50 µL fractions were collected from each run for analysis by Coomassie-stained SDS-PAGE.

Mass photometry

Purified protein samples were clarified after thawing by centrifugation at 21,000 g, 4°C for 5 min and diluted to 0.5 µM in freshly filtered buffer (50 mM HEPES pH 7.4, 150 mM NaCl, 1mM TCEP). Measurements of 60 s duration were recorded at a final concentration of 25-50 nM on microscopy coverslips that were cleaned by sonication in water and isopropanol. All measurements were recorded using a Two^{MP} mass

photometer (Refeyn) and analyzed using Discover MP (Refeyn). Protein mass was calculated using a contrast-to-mass calibration with NativeMark Protein Standard (Invitrogen).

Histological analysis of mice

Adult brains were isolated after transcardial perfusion with 0.9% NaCl followed by 4% PFA for 5 min at a flow rate of approx. 6 mL per minute. Brains were dissected and post-fixed in 4% PFA overnight at 4°C. Brains were washed with PBS and cryoprotected in 30% Sucrose in PBS. For sectioning, brains were embedded in Neg-50™ Medium (Richard-Allan Scientific) and sectioned into 40 µM-thick coronal brain sections using a sledge microtome. Nissl stainings were carried out via incubation in a 0.25% solution of Cresyl Violet acetate (Sigma, #C5042), followed by dehydration in a graded ethanol series (30%, 70%, 95%, 100%; 3 min, 2 min, 30 s, 10 s) and xylol (2 x 2 min) and mounted using DPX mountant (Fluka, #44581). Slides were left to solidify overnight at RT and images were acquired using a Mirax slide scanner (Zeiss). The thickness of the corpus callosum was measured at Bregma + 0.86 mm by performing 3 parallel measurements near the midline position using ImageJ. The cortical thickness was measured at Bregma -1.82 mm through bilateral measurements of the somatosensory cortex at 3 matched positions. Averages were taken and used for analysis.

References

1. Tripathy, R., Leca, I., van Dijk, T., Weiss, J., van Bon, B.W., Sergaki, M.C., Gstrein, T., Breuss, M., Tian, G., Bahi-Buisson, N., et al. (2018). Mutations in MAST1 Cause Mega-Corpus-Callosum Syndrome with Cerebellar Hypoplasia and Cortical Malformations. Neuron *0*. https://doi.org/10.1016/j.neuron.2018.10.044.

2. Rodríguez-García, M.E., Cotrina-Vinagre, F.J., Gómez-Cano, M. de L.Á., Martínez de Aragón, A., Martín-Hernández, E., and Martínez-Azorín, F. (2020). MAST1 variant causes mega-corpus-callosum syndrome with cortical malformations but without cerebellar hypoplasia. Am. J. Med. Genet. A *182*, 1483–1490.

3. McMichael, G., Bainbridge, M.N., Haan, E., Corbett, M., Gardner, A., Thompson, S., van Bon, B.W.M., van Eyk, C.L., Broadbent, J., Reynolds, C., et al. (2015). Whole-exome sequencing points to considerable genetic heterogeneity of cerebral palsy. Mol. Psychiatry *20*, 176–182.

4. Ben-Mahmoud, A., Al-Shamsi, A.M., Ali, B.R., and Al-Gazali, L. (2020). Evaluating the Role of MAST1 as an Intellectual Disability Disease Gene: Identification of a Novel De Novo Variant in a Patient with Developmental Disabilities. J. Mol. Neurosci. *70*, 320–327.

5. Hecher, L., Johannsen, J., Bierhals, T., Buhk, J.-H., Hempel, M., and Denecke, J. (2020). The Clinical Picture of a Bilateral Perisylvian Syndrome as the Initial Symptom of Mega-Corpus-Callosum Syndrome due to a MAST1-Gene Mutation. Neuropediatrics *51*, 435–439.

6. Spinelli, E., Christensen, K.R., Bryant, E., Schneider, A., Rakotomamonjy, J., Muir, A.M., Giannelli, J., Littlejohn, R.O., Roeder, E.R., Schmidt, B., et al. (2021). Pathogenic MAST3 Variants in the STK Domain Are Associated with Epilepsy. Ann. Neurol. *90*, 274–284.

7. Shu, L., Xiao, N., Qin, J., Tian, Q., Zhang, Y., Li, H., Liu, J., Li, Q., Gu, W., Wang, P., et al. (2022). The Role of Microtubule Associated Serine/Threonine Kinase 3 Variants in Neurodevelopmental Diseases: Genotype-Phenotype Association. Front. Mol. Neurosci. *14*, 326.

8. Zhang, X., Xiao, N., Cao, Y., Peng, Y., Lian, A., Chen, Y., Wang, P., Gu, W., Xiao, B., Yu, J., et al. (2023). De novo variants in MAST4 related to neurodevelopmental disorders with developmental delay and infantile spasms: Genotype-phenotype association. Front. Mol. Neurosci. *16*, 1097553.

9. Landoulsi, Z., Laatar, F., Noé, E., Mrabet, S., Ben Djebara, M., Achaz, G., Nava, C., Baulac, S., Kacem, I., Gargouri-Berrechid, A., et al. (2018). Clinical and genetic study of Tunisian families with genetic generalized epilepsy: contribution of CACNA1H and MAST4 genes. Neurogenetics *19*, 165–178.

10. Martín-Durán, J.M., and Hejnol, A. (2021). A developmental perspective on the evolution of the nervous system. Dev. Biol. *475*, 181–192.

11. Pearce, L.R., Komander, D., and Alessi, D.R. (2010). The nuts and bolts of AGC protein kinases. Nat. Rev. Mol. Cell Biol. *11*, 9–22.

12. Reinhardt, R., and Leonard, T.A. (2023). A critical evaluation of protein kinase regulation by activation loop autophosphorylation. Elife *12*. https://doi.org/10.7554/eLife.88210.

13. Lumeng, C., Phelps, S., Crawford, G.E., Walden, P.D., Barald, K., and Chamberlain, J.S. (1999). Interactions between β2-syntrophin and a family of microtubule-associated serine/threonine kinases. Nat. Neurosci. *2*, 611–617.

14. Garland, P., Quraishe, S., French, P., and O'Connor, V. (2008). Expression of the MAST family of serine/threonine kinases. Brain Res. *1195*, 12–19.

15. Delhommel, F., Chaffotte, A., Terrien, E., Raynal, B., Buc, H., Delepierre, M., Cordier, F., and Wolff, N. (2015). Deciphering the unconventional peptide binding to the PDZ domain of MAST2. Biochem. J. *469*, 159–168.

16. Terrien, E., Chaffotte, A., Lafage, M., Khan, Z., Préhaud, C., Cordier, F., Simenel, C., Delepierre, M., Buc, H., Lafon, M., et al. (2012). Interference with the PTEN-MAST2 interaction by a viral protein leads to cellular relocalization of PTEN. Sci. Signal. *5*, ra58.

17. Valiente, M., Andrés-Pons, A., Gomar, B., Torres, J., Gil, A., Tapparel, C., Antonarakis, S.E., and Pulido, R. (2005). Binding of PTEN to specific PDZ domains contributes to PTEN protein stability and phosphorylation by microtubule-associated serine/threonine kinases. J. Biol. Chem. *280*, 28936–28943.

18. Jin, L., Chun, J., Pan, C., Li, D., Lin, R., Alesi, G.N., Wang, X., Kang, H.-B., Song, L., Wang, D., et al. (2018). MAST1 Drives Cisplatin Resistance in Human Cancers by Rewiring cRaf-Independent MEK Activation. Cancer Cell *34*, 315-330.e7.

19. Andrade, E.C., Musante, V., Horiuchi, A., Matsuzaki, H., Brody, A.H., Wu, T., Greengard, P., Taylor, J.R., and Nairn, A.C. (2017). ARPP-16 Is a Striatal-Enriched Inhibitor of Protein Phosphatase 2A Regulated by Microtubule-Associated Serine/Threonine Kinase 3 (Mast 3 Kinase). J. Neurosci. *37*, 2709–2722.

20. Muslin, A.J., Tanner, J.W., Allen, P.M., and Shaw, A.S. (1996). Interaction of 14-3-3 with signaling proteins is mediated by the recognition of phosphoserine. Cell *84*, 889–897.

21. Madeira, F., Tinti, M., Murugesan, G., Berrett, E., Stafford, M., Toth, R., Cole, C., MacKintosh, C., and Barton, G.J. (2015). 14-3-3-Pred: improved methods to predict 14-3-3-binding phosphopeptides. Bioinformatics *31*, 2276–2283.

22. Yaffe, M.B., Rittinger, K., Volinia, S., Caron, P.R., Aitken, A., Leffers, H., Gamblin, S.J., Smerdon, S.J., and Cantley, L.C. (1997). The structural basis for 14-3-3:phosphopeptide binding specificity. Cell *91*, 961–971.

23. Johnson, C., Crowther, S., Stafford, M.J., Campbell, D.G., Toth, R., and MacKintosh, C. (2010). Bioinformatic and experimental survey of 14-3-3-binding sites. Biochem. J *427*, 69–78.

24. Jumper, J., Evans, R., Pritzel, A., Green, T., Figurnov, M., Ronneberger, O., Tunyasuvunakool, K., Bates, R., Žídek, A., Potapenko, A., et al. (2021). Highly accurate protein structure prediction with AlphaFold. Nature, 1–7.

25. Abramson, J., Adler, J., Dunger, J., Evans, R., Green, T., Pritzel, A., Ronneberger, O., Willmore, L., Ballard, A.J., Bambrick, J., et al. (2024). Accurate structure prediction of biomolecular interactions with AlphaFold 3. Nature *630*, 493–500.

26. Yang, X., Lee, W.H., Sobott, F., Papagrigoriou, E., Robinson, C.V., Grossmann, J.G., Sundström, M., Doyle, D.A., and Elkins, J.M. (2006). Structural basis for protein-protein interactions in the 14-3-3 protein family. Proc. Natl. Acad. Sci. U. S. A. *103*, 17237–17242.

27. Cho, N.H., Cheveralls, K.C., Brunner, A.-D., Kim, K., Michaelis, A.C., Raghavan, P., Kobayashi, H., Savy, L., Li, J.Y., Canaj, H., et al. (2022). OpenCell: Endogenous tagging for the cartography of human cellular organization. Science *375*. https://doi.org/10.1126/science.abi6983.

28. La Manno, G., Siletti, K., Furlan, A., Gyllborg, D., Vinsland, E., Mossi Albiach, A., Mattsson Langseth, C., Khven, I., Lederer, A.R., Dratva, L.M., et al. (2021). Molecular architecture of the developing mouse brain. Nature *596*, 92–96.

29. Johnson, J.L., Yaron, T.M., Huntsman, E.M., Kerelsky, A., Song, J., Regev, A., Lin, T.-Y., Liberatore, K., Cizin, D.M., Cohen, B.M., et al. (2023). An atlas of substrate specificities for the human serine/threonine kinome. Nature *613*, 759–766.

30. Hein, M.Y., Hubner, N.C., Poser, I., Cox, J., Nagaraj, N., Toyoda, Y., Gak, I.A., Weisswange, I., Mansfeld, J., Buchholz, F., et al. (2015). A human interactome in three quantitative dimensions organized by stoichiometries and abundances. Cell *163*, 712–723.

31. Rennefahrt, U.E.E., Deacon, S.W., Parker, S.A., Devarajan, K., Beeser, A., Chernoff, J., Knapp, S., Turk, B.E., and Peterson, J.R. (2007). Specificity profiling of Pak kinases allows identification of novel phosphorylation sites. J. Biol. Chem. *282*, 15667–15678.

32. Endicott, J.A., Noble, M.E.M., and Johnson, L.N. (2012). The structural basis for control of eukaryotic protein kinases. Annu. Rev. Biochem. *81*, 587–613.

33. Young, G., Hundt, N., Cole, D., Fineberg, A., Andrecka, J., Tyler, A., Olerinyova, A., Ansari, A., Marklund, E.G., Collier, M.P., et al. (2018). Quantitative mass imaging of single biological macromolecules. Science *360*, 423–427.

34. Fenlon, L.R., and Richards, L.J. (2015). Contralateral targeting of the corpus callosum in normal and pathological brain function. Trends Neurosci. *38*, 264–272.

35. Jicha, G.A., Weaver, C., Lane, E., Vianna, C., Kress, Y., Rockwood, J., and Davies, P. (1999). cAMP-dependent protein kinase phosphorylations on tau in Alzheimer's disease. J. Neurosci. *19*, 7486–7494.

36. Yoshida, H., and Goedert, M. (2006). Sequential phosphorylation of tau protein by cAMP-dependent protein kinase and SAPK4/p38delta or JNK2 in the presence of heparin generates the AT100 epitope. J. Neurochem. *99*, 154–164.

37. Biernat, J., Gustke, N., Drewes, G., Mandelkow, E.M., and Mandelkow, E. (1993). Phosphorylation of Ser262 strongly reduces binding of tau to microtubules: distinction between PHF-like immunoreactivity and microtubule binding. Neuron *11*, 153–163.

38. Schneider, A., Biernat, J., von Bergen, M., Mandelkow, E., and Mandelkow, E.M. (1999). Phosphorylation that detaches tau protein from microtubules (Ser262, Ser214) also protects it against aggregation into Alzheimer paired helical filaments. Biochemistry *38*, 3549–3558.

39. Carlomagno, Y., Chung, D.-E.C., Yue, M., Castanedes-Casey, M., Madden, B.J., Dunmore, J., Tong, J., DeTure, M., Dickson, D.W., Petrucelli, L., et al. (2017). An acetylation-phosphorylation switch that regulates tau aggregation propensity and function. J. Biol. Chem. *292*, 15277–15286.

40. Sadik, G., Tanaka, T., Kato, K., Yamamori, H., Nessa, B.N., Morihara, T., and Takeda, M. (2009). Phosphorylation of tau at Ser214 mediates its interaction with 14-3-3 protein: implications for the mechanism of tau aggregation. J. Neurochem. *108*, 33–43.

41. Neves, J.F., Petrvalská, O., Bosica, F., Cantrelle, F.-X., Merzougui, H., O'Mahony, G., Hanoulle, X., Obšil, T., and Landrieu, I. (2021). Phosphorylated full-length Tau interacts with 14-3-3 proteins via two short phosphorylated sequences, each occupying a binding groove of 14-3-3 dimer. FEBS J. *288*, 1918–1934.

42. Tian, Y., Lei, L., and Minden, A. (2011). A key role for Pak4 in proliferation and differentiation of neural progenitor cells. Dev. Biol. *353*, 206–216.

43. Qu, J., Li, X., Novitch, B.G., Zheng, Y., Kohn, M., Xie, J.-M., Kozinn, S., Bronson, R., Beg, A.A., and Minden, A. (2003). PAK4 kinase is essential for embryonic viability and for proper neuronal development. Mol. Cell. Biol. *23*, 7122–7133.

44. Abo, A., Qu, J., Cammarano, M.S., Dan, C., Fritsch, A., Baud, V., Belisle, B., and Minden, A. (1998). PAK4, a novel effector for Cdc42Hs, is implicated in the reorganization of the actin cytoskeleton and in the formation of filopodia. EMBO J. *17*, 6527–6540.

45. Baskaran, Y., Ng, Y.-W., Selamat, W., Ling, F.T.P., and Manser, E. (2012). Group I and II mammalian PAKs have different modes of activation by Cdc42. EMBO Rep. *13*, 653–659.

46. Ha, B.H., and Boggon, T.J. (2018). CDC42 binds PAK4 via an extended GTPase-effector interface. Proc. Natl. Acad. Sci. U. S. A. *115*, 531–536.

47. Dan, C., Kelly, A., Bernard, O., and Minden, A. (2001). Cytoskeletal changes regulated by the PAK4 Serine/threonine kinase are mediated by LIM kinase 1 and cofilin. J. Biol. Chem. *276*, 32115–32121.

48. Etienne-Manneville, S. (2004). Cdc42--the centre of polarity. J. Cell Sci. *117*, 1291–1300.

49. Selamat, W., Tay, P.-L.F., Baskaran, Y., and Manser, E. (2015). The Cdc42 effector kinase PAK4 localizes to cell-cell junctions and contributes to establishing cell polarity. PLoS One *10*, e0129634.

50. Civiero, L., Cirnaru, M.D., Beilina, A., Rodella, U., Russo, I., Belluzzi, E., Lobbestael, E., Reyniers, L., Hondhamuni, G., Lewis, P.A., et al. (2015). Leucine-rich repeat kinase 2 interacts with p21-activated kinase 6 to control neurite complexity in mammalian brain. J. Neurochem. *135*, 1242–1256.

51. Nekrasova, T., Jobes, M.L., Ting, J.H., Wagner, G.C., and Minden, A. (2008). Targeted disruption of the Pak5 and Pak6 genes in mice leads to deficits in learning and locomotion. Dev. Biol. *322*, 95–108.

52. Schaefer, A.W., Kabir, N., and Forscher, P. (2002). Filopodia and actin arcs guide the assembly and transport of two populations of microtubules with unique dynamic parameters in neuronal growth cones. J. Cell Biol. *158*, 139–152.

53. Gomez, T.M., and Letourneau, P.C. (2014). Actin dynamics in growth cone motility and navigation. J. Neurochem. *129*, 221–234.

54. Lanier, L.M., Gates, M.A., Witke, W., Menzies, A.S., Wehman, A.M., Macklis, J.D., Kwiatkowski, D., Soriano, P., and Gertler, F.B. (1999). Mena is required for neurulation and commissure formation. Neuron *22*, 313–325.

55. Illenberger, S., Zheng-Fischhöfer, Q., Preuss, U., Stamer, K., Baumann, K., Trinczek, B., Biernat, J., Godemann, R., Mandelkow, E.M., and Mandelkow, E. (1998). The endogenous and cell cycle-dependent phosphorylation of tau protein in living cells: implications for Alzheimer's disease. Mol. Biol. Cell *9*, 1495–1512.

56. Hong, Y., Chan, C.B., Kwon, I.-S., Li, X., Song, M., Lee, H.-P., Liu, X., Sompol, P., Jin, P., Lee, H.-G., et al. (2012). SRPK2 phosphorylates tau and mediates the cognitive defects in Alzheimer's disease. J. Neurosci. *32*, 17262–17272.

57. Liu, S.J., Zhang, J.Y., Li, H.L., Fang, Z.Y., Wang, Q., Deng, H.M., Gong, C.X., Grundke-Iqbal, I., Iqbal, K., and Wang, J.Z. (2004). Tau becomes a more favorable substrate for GSK-3 when it is prephosphorylated by PKA in rat brain. J. Biol. Chem. *279*, 50078–50088.

58. Takei, Y., Teng, J., Harada, A., and Hirokawa, N. (2000). Defects in axonal elongation and neuronal migration in mice with disrupted tau and map1b genes. J. Cell Biol. *150*, 989–1000.

59. Meixner, A., Haverkamp, S., Wässle, H., Führer, S., Thalhammer, J., Kropf, N., Bittner, R.E., Lassmann, H., Wiche, G., and Propst, F. (2000). MAP1B is required for axon guidance and Is involved in the development of the central and peripheral nervous system. J. Cell Biol. *151*, 1169–1178.

60. Takahashi, H., Lassmann, T., Murata, M., and Carninci, P. (2012). 5' end-centered expression profiling using cap-analysis gene expression and next-generation sequencing. Nat. Protoc. *7*, 542–561.

61. Edfors, F., Danielsson, F., Hallström, B.M., Käll, L., Lundberg, E., Pontén, F., Forsström, B., and Uhlén, M. (2016). Gene-specific correlation of RNA and protein levels in human cells and tissues. Mol. Syst. Biol. *12*, 883.

62. Pontén, F., Gry, M., Fagerberg, L., Lundberg, E., Asplund, A., Berglund, L., Oksvold, P., Björling, E., Hober, S., Kampf, C., et al. (2009). A global view of protein expression in human cells, tissues, and organs. Mol. Syst. Biol. *5*, 337.

63. Uhlén, M., Fagerberg, L., Hallström, B.M., Lindskog, C., Oksvold, P., Mardinoglu, A., Sivertsson, Å., Kampf, C., Sjöstedt, E., Asplund, A., et al. (2015). Tissue-based map of the human proteome. Science *347*, 1260419.

64. Park, E., Rawson, S., Li, K., Kim, B.-W., Ficarro, S.B., Pino, G.G.-D., Sharif, H., Marto, J.A., Jeon, H., and Eck, M.J. (2019). Architecture of autoinhibited and active BRAF-MEK1-14-3-3 complexes. Nature, 1–5.

65. Kondo, Y., Ognjenović, J., Banerjee, S., Karandur, D., Merk, A., Kulhanek, K., Wong, K., Roose, J.P., Subramaniam, S., and Kuriyan, J. (2019). Cryo-EM structure of a dimeric B-Raf:14-3-3 complex reveals asymmetry in the active sites of B-Raf kinases. Science *366*, 109–115.

66. Yamaguchi, H., Kasa, M., Amano, M., Kaibuchi, K., and Hakoshima, T. (2006). Molecular mechanism for the regulation of rho-kinase by dimerization and its inhibition by fasudil. Structure *14*, 589–600.

67. Heikkila, T., Wheatley, E., Crighton, D., Schroder, E., Boakes, A., Kaye, S.J., Mezna, M., Pang, L., Rushbrooke, M., Turnbull, A., et al. (2011). Co-Crystal Structures of Inhibitors with MRCKβ, a Key Regulator of Tumor Cell Invasion. PLoS One *6*, e24825.

68. Komander, D., Garg, R., Wan, P.T.C., Ridley, A.J., and Barford, D. (2008). Mechanism of multi-site phosphorylation from a ROCK-I:RhoE complex structure. EMBO J. *27*, 3175–3185.

69. Couzens, A.L., Saridakis, V., and Scheid, M.P. (2009). The hydrophobic motif of ROCK2 requires association with the N-terminal extension for kinase activity. Biochem. J. *419*, 141–148.

70. Devroe, E., Erdjument-Bromage, H., Tempst, P., and Silver, P.A. (2004). Human Mob proteins regulate the NDR1 and NDR2 serine-threonine kinases. J. Biol. Chem. *279*, 24444–24451.

71. Bichsel, S.J., Tamaskovic, R., Stegert, M.R., and Hemmings, B.A. (2004). Mechanism of activation of NDR (nuclear Dbf2-related) protein kinase by the hMOB1 protein. J. Biol. Chem. *279*, 35228–35235.

72. Parker, B.W., Gogl, G., Bálint, M., Hetényi, C., Reményi, A., and Weiss, E.L. (2020). Ndr/Lats Kinases Bind Specific Mob-Family Coactivators through a Conserved and Modular Interface. Biochemistry *59*, 1688–1700.

73. Gógl, G., Schneider, K.D., Yeh, B.J., Alam, N., Nguyen Ba, A.N., Moses, A.M., Hetényi, C., Reményi, A., and Weiss, E.L. (2015). The Structure of an NDR/LATS Kinase–Mob Complex Reveals a Novel Kinase–Coactivator System and Substrate Docking Mechanism. PLoS Biol. *13*, e1002146.

74. Yang, J., Cron, P., Good, V.M., Thompson, V., Hemmings, B.A., and Barford, D. (2002). Crystal structure of an activated Akt/Protein Kinase B ternary complex with GSK3-peptide and AMP-PNP. Nat. Struct. Biol. *9*, 940–944.

Figure Legends

Figure 1. MAST1 interacts with 14-3-3 proteins via S90 and S161.

A. Domain architecture of *Mus musculus* MAST1. Construct boundaries and nomenclature for all constructs used in this study are defined. DUF = domain of unknown function, 4HB = four-helix bundle, PDZ = postsynaptic density protein (PDS95) Drosophila disc large tumor suppressor (DlgA) and Zonula occludens-1 protein (zo-1). Right: schematic representation of MAST1 to be employed throughout the figures.

B. Construct boundaries and experimental setup for EGFP-MAST1^{DKP} AP-MS in HEK293 cells.

C. Volcano plot displaying the enriched interactome of EGFP-MAST1^{DKP} (right) vs EGFP (left) from AP-MS, n = 3.

D. AlphaFold3 [25] model and pair alignment error (PAE) plot of 14-3-3η dimer (red) and MAST1^{D} dimer (gold), when region spanning MAST1 S90 (light blue bubble) interacts with 14-3-3 cradle.

E. AlphaFold3 [25] model and PAE plot of 14-3-3η dimer (red) and MAST1^{D} dimer (gold), when region spanning MAST1 S161 (dark blue bubble) interacts with 14-3-3 cradle.

F. Volcano plot displaying the enriched interactome of EGFP-MAST1^{DKP} WT (right) vs EGFP-MAST1^{DKP} S90A (left) from AP-MS, n = 3.

G. Volcano plot displaying the enriched interactome of EGFP-MAST1^{DKP} WT (right) vs EGFP-MAST1^{DKP} S161A (left) from AP-MS, n = 3.

H. Volcano plot displaying the enriched interactome of EGFP-MAST1^{DKP} WT (right) vs EGFP-MAST1^{DKP} S90A S161A (left) from AP-MS, n = 3.

I. Volcano plot displaying the enriched interactome of EGFP-MAST1^{DKP} ΔS90 (right) vs EGFP-MAST1^{DKP} ΔS90 ΔS161 (left) from AP-MS, n = 3.

J. Binding curves for 14-3-3η or θ and MAST1 peptides spanning S90 or S161, measured by fluorescence anisotropy. Data are presented as mean values ± S.E., n = 3. Data were fit with a one-site binding model and the K_d derived from curve fitting.

Figure 2. PAK4 phosphorylates MAST1 on S90.

A. Multiple sequence alignment of MAST1 residues surrounding S90 from *Nematoda* to *Mammalia*. S90 residue highlighted above, sequence used for ScoreSite prediction outlined in black box.

B. ScoreSite [29] prediction results using input sequence GRRWs*LASLP (s* represents S90 phosphosite). Top five hits shown in table, PAK4 highlighted in turquoise.

C. Radiometric kinase assay by PAK4 WT or PAK4 kinase dead (D442N) on $MAST1^{D}$. Data are presented as mean values ± S.E., $n = 3$. Representative phosphorimage shown in inset.

D. Intact MS analysis of $MAST1^{D}$ before (black) and after (red) phosphorylation by PAK4 WT shown in panel C. Intensity of both samples were normalized to a scale of 0 to 1. Addition of phosphate (1P, 2P etc.) detected by each 80 Da shift.

E. Tandem MS analysis of $MAST1^{D}$ after phosphorylation by PAK4 WT shown in panel C. Phosphorylated serines are indicated in red. Top three sites (by spectral count) shown in table, S90 highlighted in light blue. See Supplemental File 3 for full data.

Figure 3. MAST1 S161 is an autoregulatory motif.

A. Multiple sequence alignment of MAST1 residues surrounding S161 from *Nematoda* to *Mammalia*. S161 residue highlighted above, AGC kinase recognition region outlined in black box.

B. Alignment of canonical AGC kinase substrate motif with $MAST1^{156\text{-}162}$, where S161 is the phosphorylatable residue (red) and R156 (-5), R158 (-3), and L162 (+1) are in positions specifically involved in substrate recognition (black).

C. Consensus sequence of $MAST1^{156\text{-}162}$ from sequence alignment in panel A.

D. AlphaFold2 [24] model of MAST1 DUF (gold) and kinase domain (green), with region spanning S161 (dark blue) positioned in the catalytic site of MAST1. AMP-

PNP molecule (pink) was incorporated into the model by superposition of MAST1 kinase domain with X-ray structure of Akt (PDB ID 1O6K) [77].

E. Radiometric autophosphorylation assay with various concentrations of MAST1^{DK} ΔS90 WT or kinase dead (D499N). Data are presented as mean values ± S.E., *n* = 3.

F. Intact MS analysis of MAST1^{DK} ΔS90 WT (red) and kinase dead (D499N) (black) after autophosphorylation shown in panel E. Intensity of both samples were normalized to a scale of 0 to 1. Addition of phosphate in WT sample (1P, 2P etc.) detected by each 80 Da shift.

G. Tandem MS analysis of MAST1^{DK} ΔS90 WT after autophosphorylation shown in panel E. Phosphorylated serines are indicated in red and residues involved in AGC kinase binding (-5, -3, +1) are in black. Top six serine sites (by spectral count) shown in table, S161 highlighted in dark blue. See Supplemental File 3 for full data.

H. Binding curves for MAST1^{DK} ΔS90 ΔS161 and MAST1 peptides spanning S161, measured by fluorescence anisotropy. Data are presented as mean values ± S.E., *n* = 3. Data were fit with a one-site binding model and the K_d derived from curve fitting.

Figure 4. MAST1 p-S90 or p-S161 forms a complex with 14-3-3η *in vitro*.

A. Analytical size exclusion chromatography (SEC) elution profiles of purified MAST1^{DK} (yellow), purified 14-3-3η (red), and a co-purified complex of MAST1^{DK} and 14-3-3η (dark blue).

B. Coomassie-stained SDS-PAGE gel of SEC fractions spanning elution peaks in panel A. Theoretical masses of each protein/complex shown in parentheses.

C. Tandem MS analysis of co-purified MAST1^{DK} and 14-3-3η complex to determine phosphorylation state of MAST1 in the complex. Phosphorylated serines are indicated in red. S90, S161 (highlighted in dark blue), and S163 sites shown in table. See Supplemental File 3 for full data.

D. Gaussian fits from mass photometry of purified MAST1^{DK} (yellow), purified 14-3-3η (red), and a co-purified complex of MAST1^{DK} and 14-3-3η (dark blue). Experimentally measured masses of each protein/complex indicated above the Gaussian fit.

E. Analytical SEC elution profiles of purified MAST1^{D} p-S90 (yellow), purified 14-3-3η (red), and an *in vitro*-formed complex of MAST1^{D} p-S90 and 14-3-3η (light blue).

F. Coomassie-stained SDS-PAGE gel of SEC fractions spanning elution peaks in panel E. Theoretical masses of each protein/complex shown in parentheses.

G. Gaussian fits from mass photometry of purified MAST1^{D} p-S90 (yellow), purified 14-3-3η (red), and an *in vitro*-formed complex of MAST1^{D} p-S90 and 14-3-3η (light blue). Experimentally measured masses of each protein/complex indicated above the Gaussian fit.

Figure 5. MAST1 G519S mice exhibit an enlarged corpus callosum.

A. Schematic of MCC-CH-CM patient-derived mutations in MAST1 protein. G519S (mouse numbering) corresponds to G517S in humans. Mouse models have been generated for the highlighted L278del and G519S variants.

B. G519S animals were generated by injection of a single strand DNA repair template and Cas9/guide RNA into the pronucleus of mouse zygotes. Founder animals were identified by Sanger sequencing and backcrossed to C57Bl/6J animals for 10 generations.

C. Sequencing traces of MAST1 allele for control (+/+), heterozygous (G519S/+), and homozygous animals (G519S/G519S).

D. Nissl stain of coronal 8-week-old control (+/+) and heterozygous brains (G519S/+) shows an enlargement of the corpus callosum in mutants. Bregma = 0.86 mm.

E. Quantification of corpus callosal thickness in control (+/+) and heterozygous brains (G519S/+) (n = 5, $P < 0.05$, paired, two-sided t-test with Bonferroni correction). Data are presented as mean values ± S.E.

F. Quantification of cortical thickness in control (+/+) and heterozygous brains (G519S/+) (n = 5, P < 0.05, paired, two-sided t-test with Bonferroni correction). Data are presented as mean values ± S.E.

G. Western blot analysis on P0 cortical lysates for MAST1, MAST2, and MAST3 in control (+/+), heterozygous (G519S/+) and homozygous (G519S/G519S) animals.

H. Quantification of western blot in panel F (n = 3, * p < 0.05; ** p < 0.01; ***, p < 0.001; **** p < 0.0001, two-way ANOVA with Dunnet's multiple comparisons test). Intensity of bands for MAST family members was normalized to corresponding GAPDH band. Data are presented as mean values ± S.E.

Figure 6. Tau is a MAST1 substrate.

A. Schematic of MAST1 WT vs L278del vs G519S phosphoproteomics experiment. Number of significantly differentially phosphorylated peptides obtained in each comparison, and shared in both comparisons, shown in Venn diagram (n = 5 WT and homozygous litter-matched P0 mice, LIMMA test with 5% FDR threshold described in Hein *et al* [30] was applied).

B. Table displaying data from four of the 70 shared phosphosite hits in panel A. The four phosphosites listed all conform to the canonical AGC kinase substrate motif (phosphorylated serines indicated in red). MAPT (Tau) is highlighted in purple.

C. Sequence alignment of $Tau^{209\text{-}215}$ and $MAST1^{156\text{-}162}$, where Tau S214 (substrate) and MAST1 S161 (autophosphorylation site) are aligned.

D. Volcano plot of phosphoproteomics analysis showing hyperphosphorylated sites (right) and hypophosphorylated sites (left) for L278del when compared to WT. Tau S214 highlighted in purple.

E. Volcano plot of phosphoproteomics analysis showing hyperphosphorylated sites (right) and hypophosphorylated sites (left) for G519S when compared to WT. Tau S214 highlighted in purple.

F. Radiometric kinase assay by MAST1^{DK} ΔS90 WT or kinase dead (D499N) on Tau. Data are presented as mean values ± S.E., n = 10 for WT, 3 for D499N. Representative phosphorimage shown in inset.

G. Radiometric kinase assay by MRCKα on MLC2, overlaid on assay shown in E.

H. Tandem MS analysis of Tau after phosphorylation by MAST1^{DK} ΔS90 WT shown in panel E. Phosphorylated serines are indicated in red and residues involved in AGC kinase binding (-5, -3, +1) are in black. S214 site (highlighted in purple) as well as three known Tau phosphorylation sites in its repeat domains shown in table. See Supplemental File 3 for full data.

I. Binding curves for 14-3-3η or θ and Tau peptides spanning S214, measured by fluorescence anisotropy. Data are presented as mean values ± S.E., n = 3. Data were fit with a one-site binding model and the K_d derived from curve fitting.

Figure 7. MCC-CH-CM mutations perturb MAST1 folding and kinase activity.

A. Structure of MAST1 4HB determined by NMR (PDB ID 2M9X). Patient mutations residing in 4HB highlighted in red and labelled.

B. Coomassie-stained SDS-PAGE gel of MAST1^{D} ΔS90 WT, E194del, K276del, or L278del, expressed in *E. coli*. WCL = whole cell lysate, P = pellet, S = supernatant.

C. SEC elution profile of purified MAST1^{DK} ΔS90 WT and K276del from Sf9 insect cells, void volume = 9 mL.

D. SEC elution profile of purified MAST1^{DK} ΔS90 WT and G519S from Sf9 insect cells.

E. Radiometric kinase assay by MAST1^{DK} ΔS90 WT, kinase dead (D499N), or G519S on Tau. Data are presented as mean values ± S.E., n = 3.

Figure 8. Model of MAST1 regulation.

A group II PAK (PAK4-6) is activated by Cdc42 and phosphorylates MAST1 on S90. MAST1 p-S90 recruits 14-3-3η, forming an inactive trimeric complex, with S161 blocking MAST1's substrate binding site. Upon binding of an unknown cofactor, the kinase domain of MAST1 adopts the active conformation and autophosphorylates S161, expelling it from the substrate binding site. p-S161 is sequestered by 14-3-3η,

preventing dephosphorylation and reassembly with the kinase domain. Active MAST1 phosphorylates Tau on S214, resulting in its dissociation from microtubules, sequestration by 14-3-3η, and subsequent microtubule depolymerization.

Figure 1. MAST1 interacts with 14-3-3 proteins via S90 and S161.

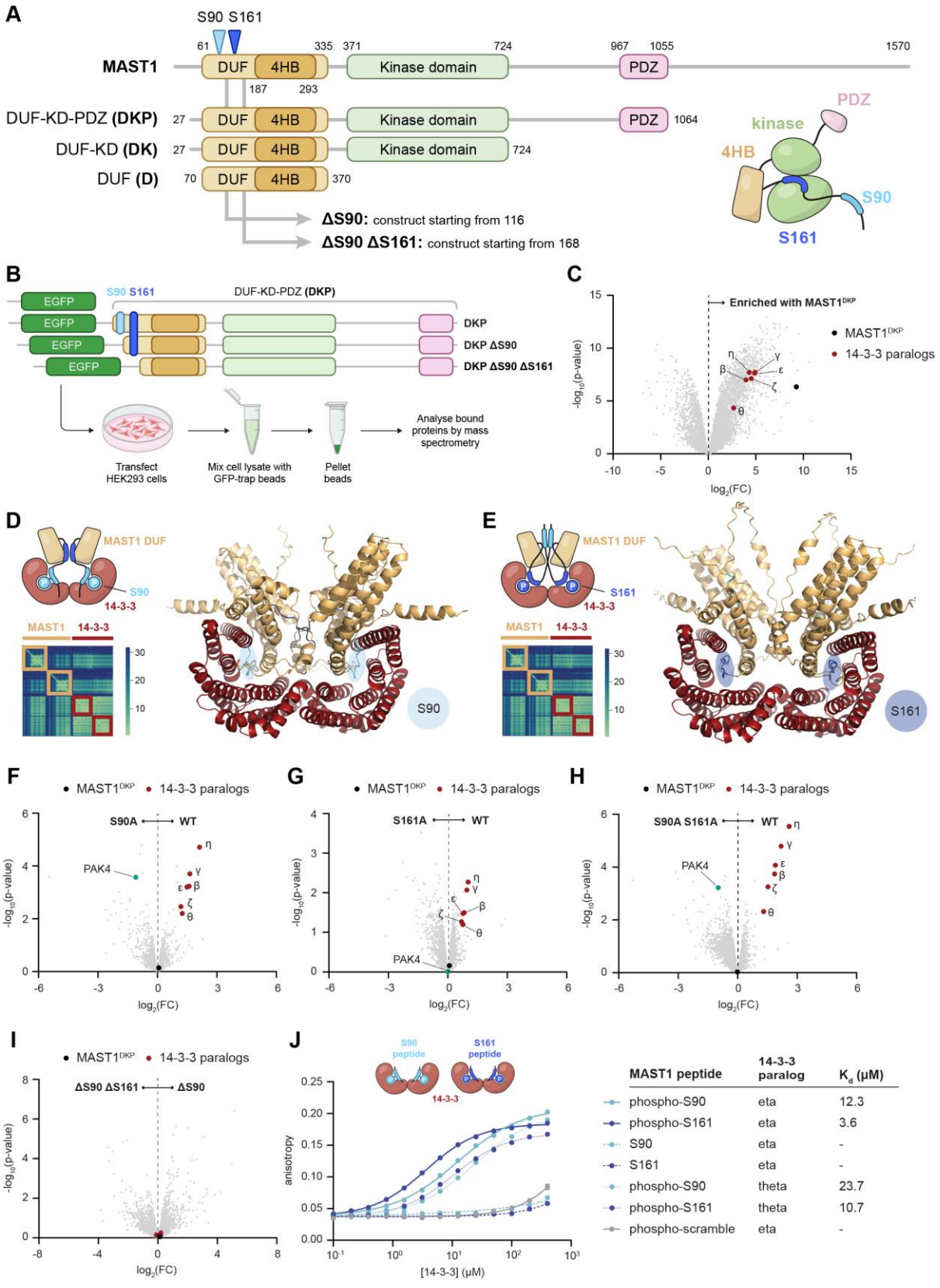

MAST1 peptide	14-3-3 paralog	K_d (μM)
phospho-S90	eta	12.3
phospho-S161	eta	3.6
S90	eta	-
S161	eta	-
phospho-S90	theta	23.7
phospho-S161	theta	10.7
phospho-scramble	eta	-

Figure 2. PAK4 phosphorylates MAST1 on S90.

A

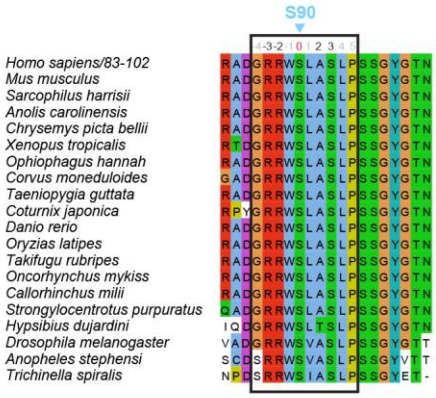

B

Kinase	Kinase group	Log_2(score)	Site percentile	Percentile rank
PAK4	STE	8.254	99.96 %	1
PAK6	STE	7.071	99.90 %	2
PAK5	STE	7.155	99.89 %	3
AURA	Other	5.550	99.25 %	4
PGK1	AGC	5.426	99.22 %	5

C

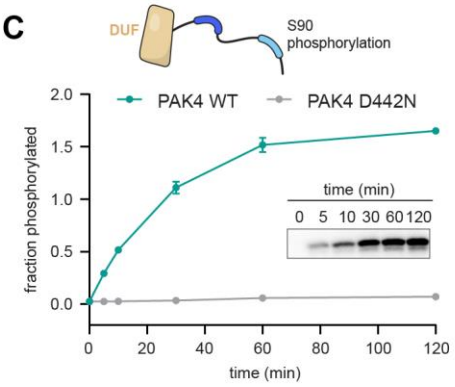

D

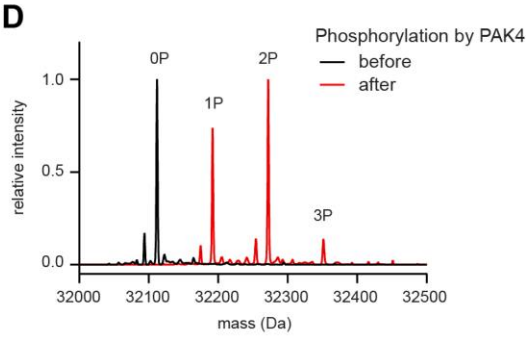

E

Residue	Sequence window	Localisation probability	Spectral count
S90	D G R R W S L A S L P	93.1 %	56
S77	T P A H F S F A S S R	91.3 %	35
T72	A M G P N S P A H F S	93.7 %	8

Figure 3. MAST1 S161 is an autoregulatory motif.

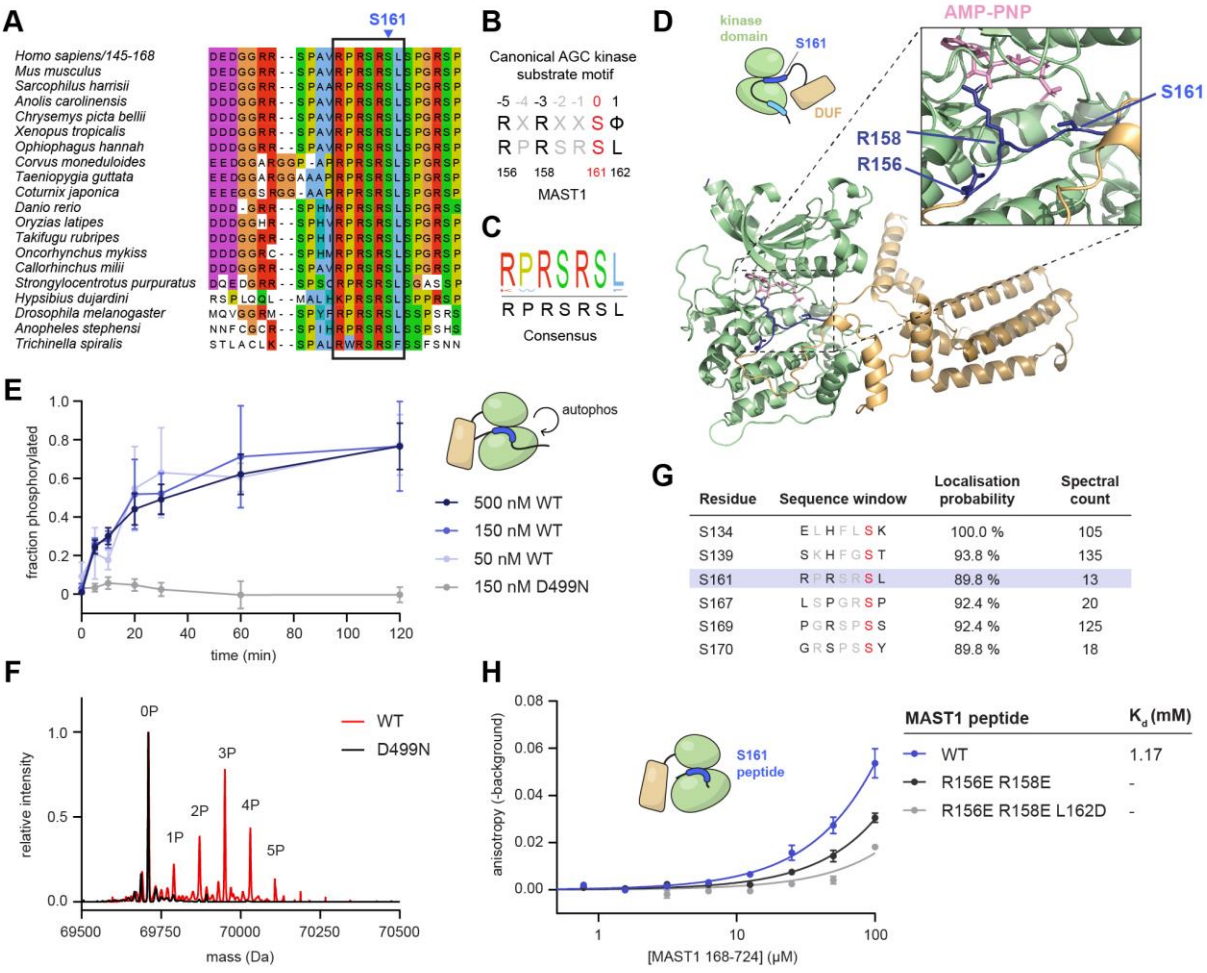

Residue	Sequence window	Localisation probability	Spectral count
S134	E L H F L S K	100.0 %	105
S139	S K H F G S T	93.8 %	135
S161	R P R S R S L	89.8 %	13
S167	L S P G R S P	92.4 %	20
S169	P G R S P S S	92.4 %	125
S170	G R S P S S Y	89.8 %	18

Figure 4. MAST1 p-S90 or p-S161 forms a complex with 14-3-3η *in vitro*.

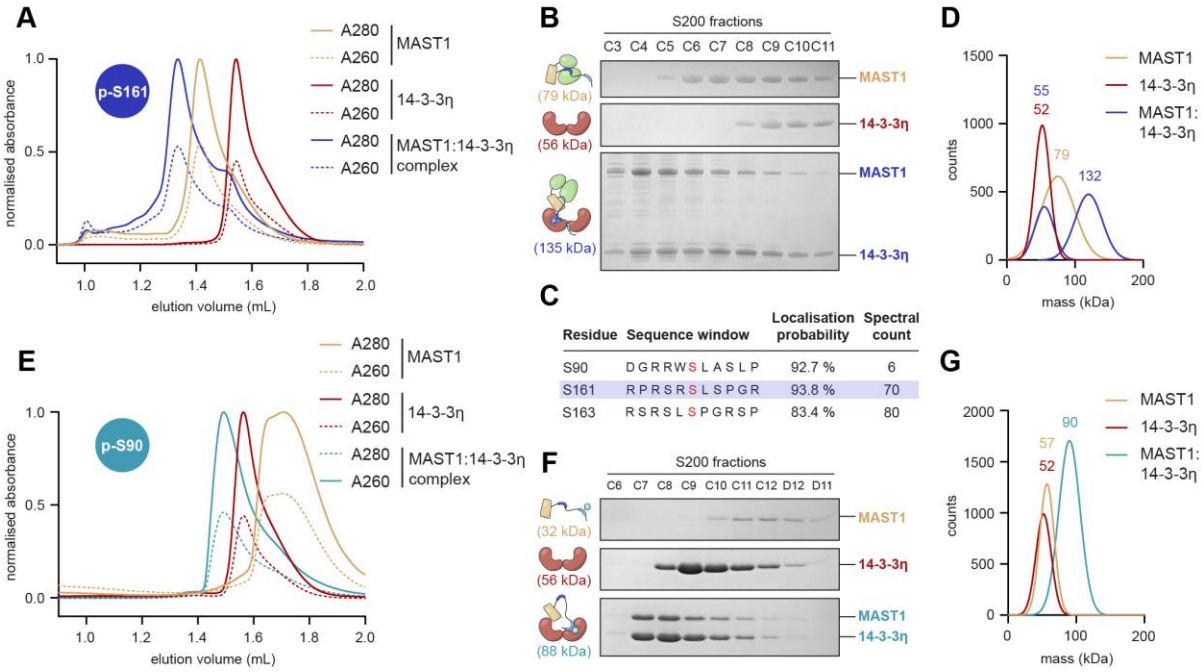

Figure 5. MAST1 G519S mice exhibit an enlarged corpus callosum.

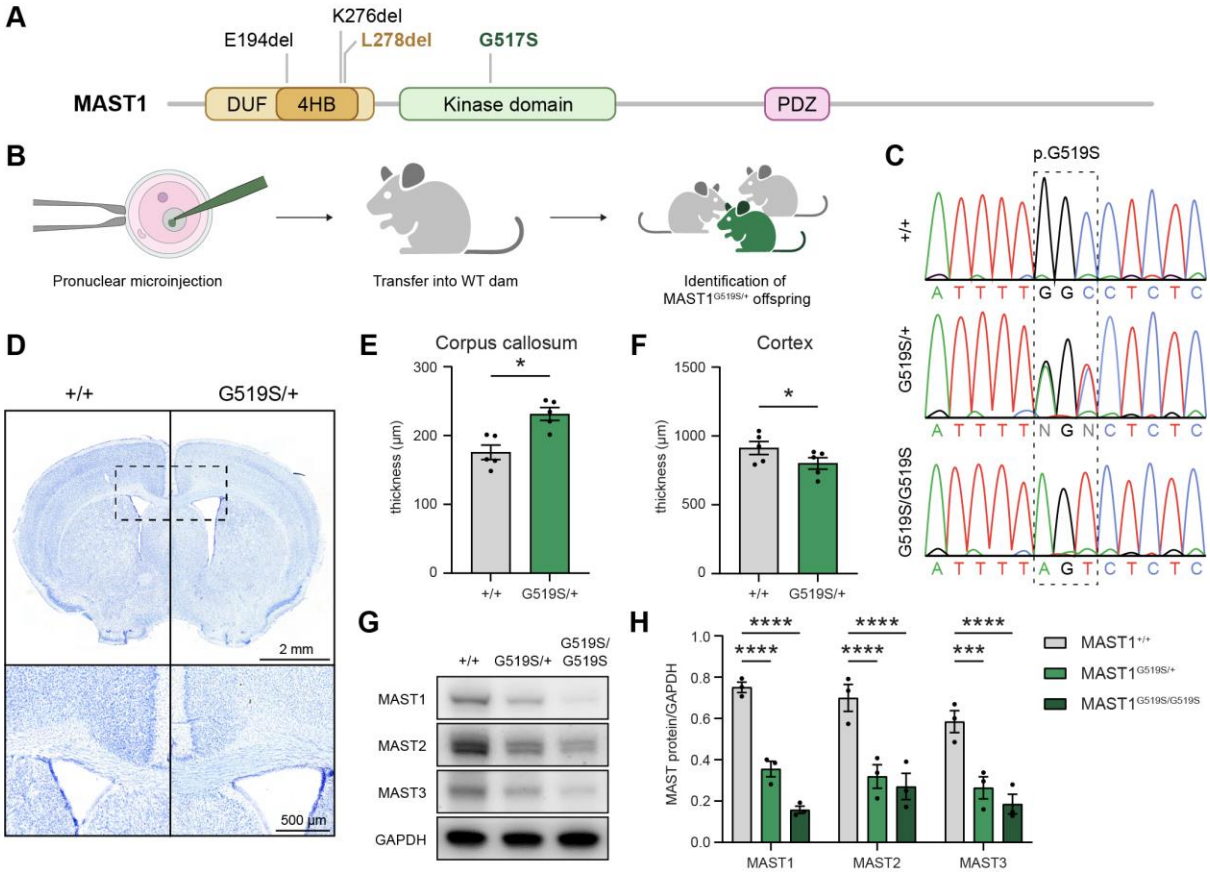

Figure 6. Tau is a MAST1 substrate.

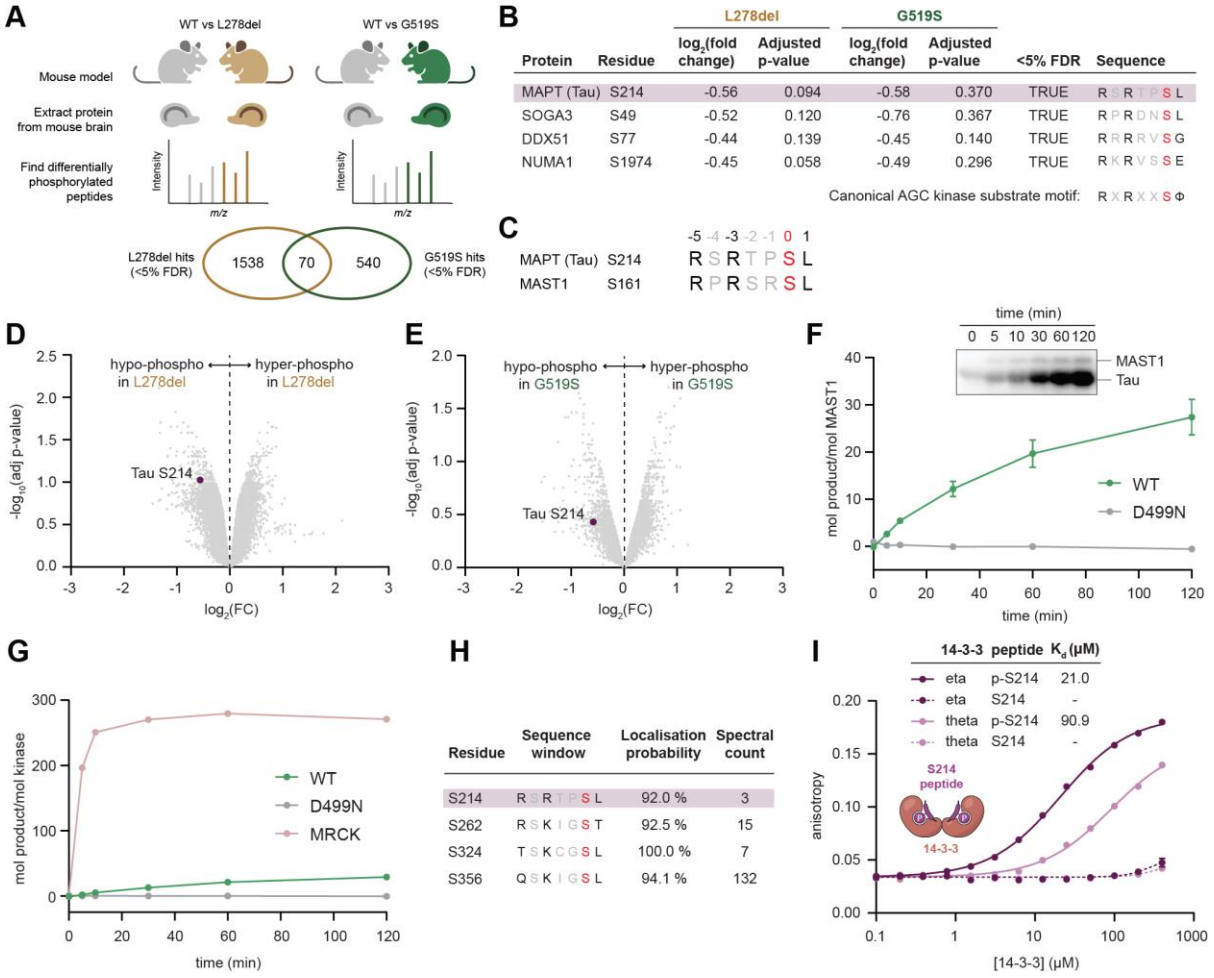

Figure 7. MCC-CH-CM mutations perturb MAST1 folding and kinase activity.

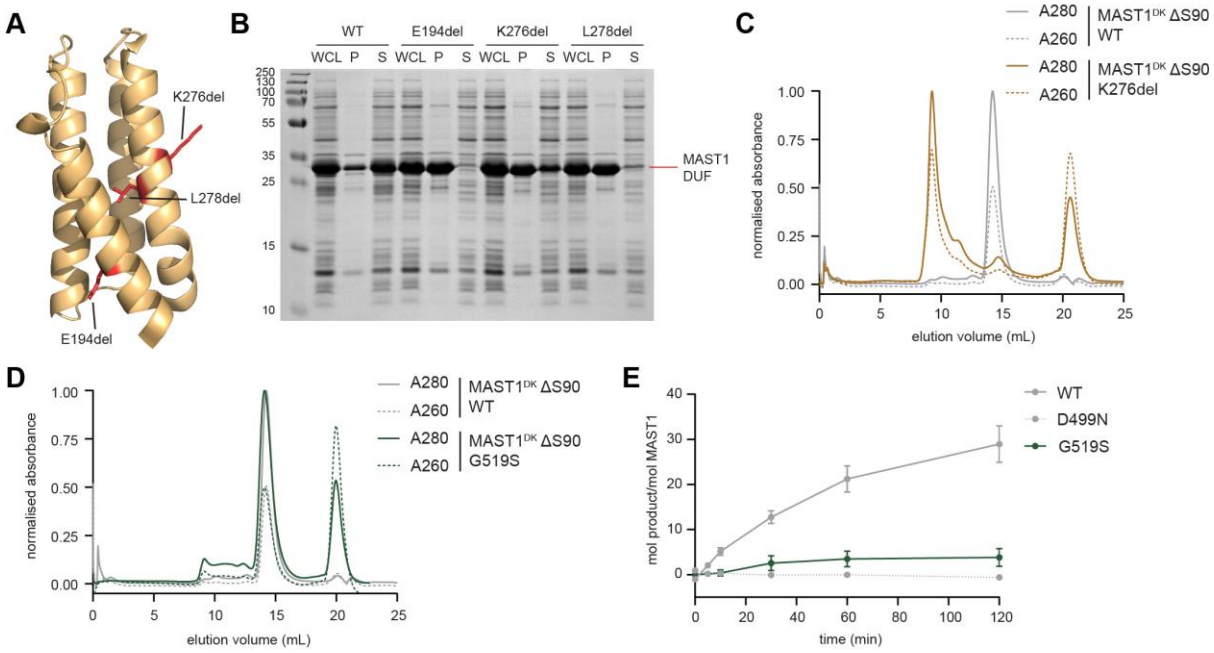

Figure 8. Model of MAST activation.

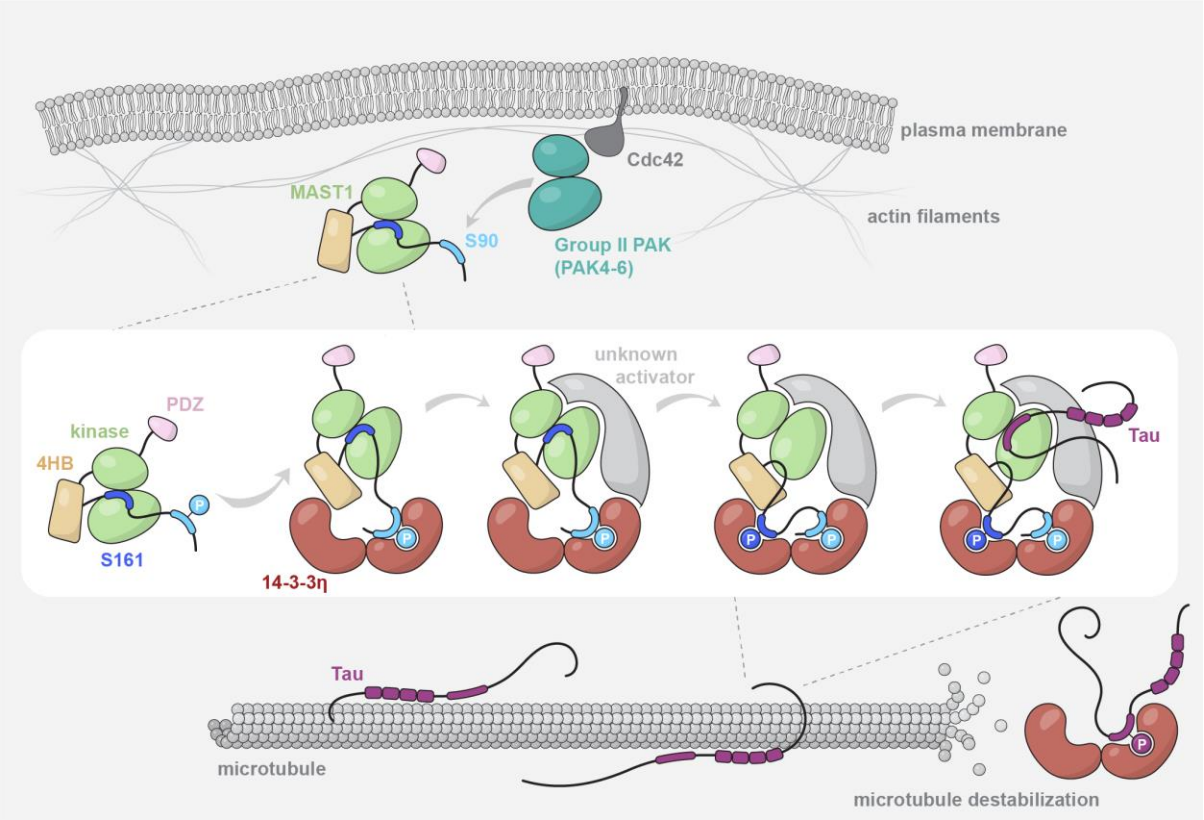

Supplementary Information

A complex of MAST1 and 14-3-3η regulates Tau phosphorylation in the developing cortex

Sumire Antonioli[1,2,§], Patrick Heisterkamp[3,§], Weiqiang Chen[4], Dorothea Anrather[4], Markus Hartl[4,5], Maria-Fernanda Martinez-Reza[6], Ratna Tripathy[7], Michael Schutzbier[7,] Karl Mechtler[7], David A. Keays[3,7] and Thomas A. Leonard[1*]

[1]Max Perutz Labs, Medical University of Vienna, Dr. Bohr-Gasse 9, 1030, Vienna, Austria.

[2]Vienna BioCenter PhD Program, a Doctoral School of the University of Vienna and the Medical University of Vienna, A-1030 Vienna, Austria.

[3]Division of Neurobiology, Department of Biology, Ludwig-Maximilians-University Munich, Grosshaderner Str. 2, 82152 Planegg-Martinsried, Germany

[4]Max Perutz Labs, Mass Spectrometry Facility, Vienna Biocenter Campus (VBC), Dr. Bohr-Gasse 9, 1030, Vienna, Austria.

[5]University of Vienna, Center for Molecular Biology, Department of Biochemistry and Cell Biology, Dr. Bohr-Gasse 9, 1030, Vienna, Austria.

[6]Faculty of Medicine, Ludwig-Maximilians-University Munich, Grosshaderner Str. 9, 82152 Planegg-Martinsried, Germany

[7] Institute of Molecular Pathology (IMP), Dr-Bohr Gasse 7, Vienna 1030, Vienna Biocentre (VBC), Austria.

[§]These authors contributed equally to this work.

[*]Correspondence: thomas.leonard@meduniwien.ac.at

Contains: Supplementary Figures 1-8

Supplementary Table 1

Supplementary Methods

Supplementary References

Supplementary Figures

Supplementary Figure 1. MAST1 interacts with 14-3-3 proteins via S90 and S161.

Figure S1. MAST1 interacts with 14-3-3 proteins via S90 and S161.

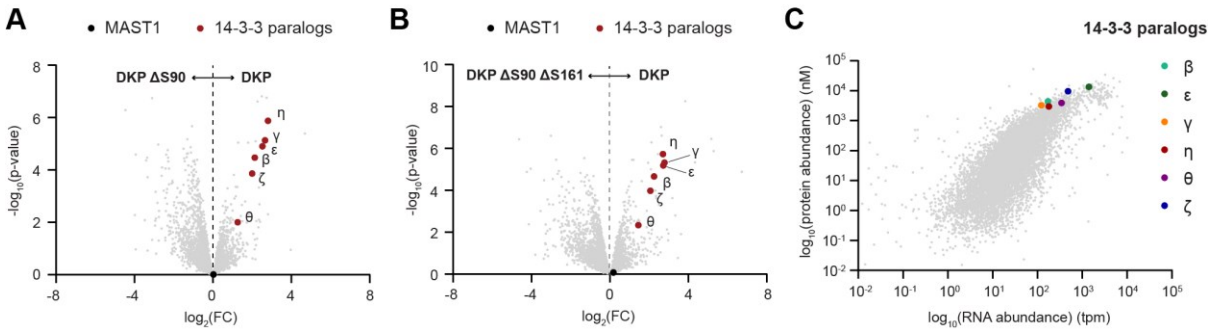

A. IP-MS for EGFP-MAST1^{DKP} (right) vs EGFP-MAST1^{DKP} ΔS90 (left), *n* = 3.

B. IP-MS for EGFP-MAST1^{DKP} (right) vs EGFP-MAST1^{DKP} ΔS90 ΔS161 (left), *n* = 3.

C. Scatter plot showing RNA and protein abundance of all six 14-3-3 paralogs identified in Figure 1C (highlighted by large colored dots) overlayed on all detected RNA/protein, in HEK293 cells [12].

Supplementary Figure 2. Mass spectra of all protein constructs employed in this study.

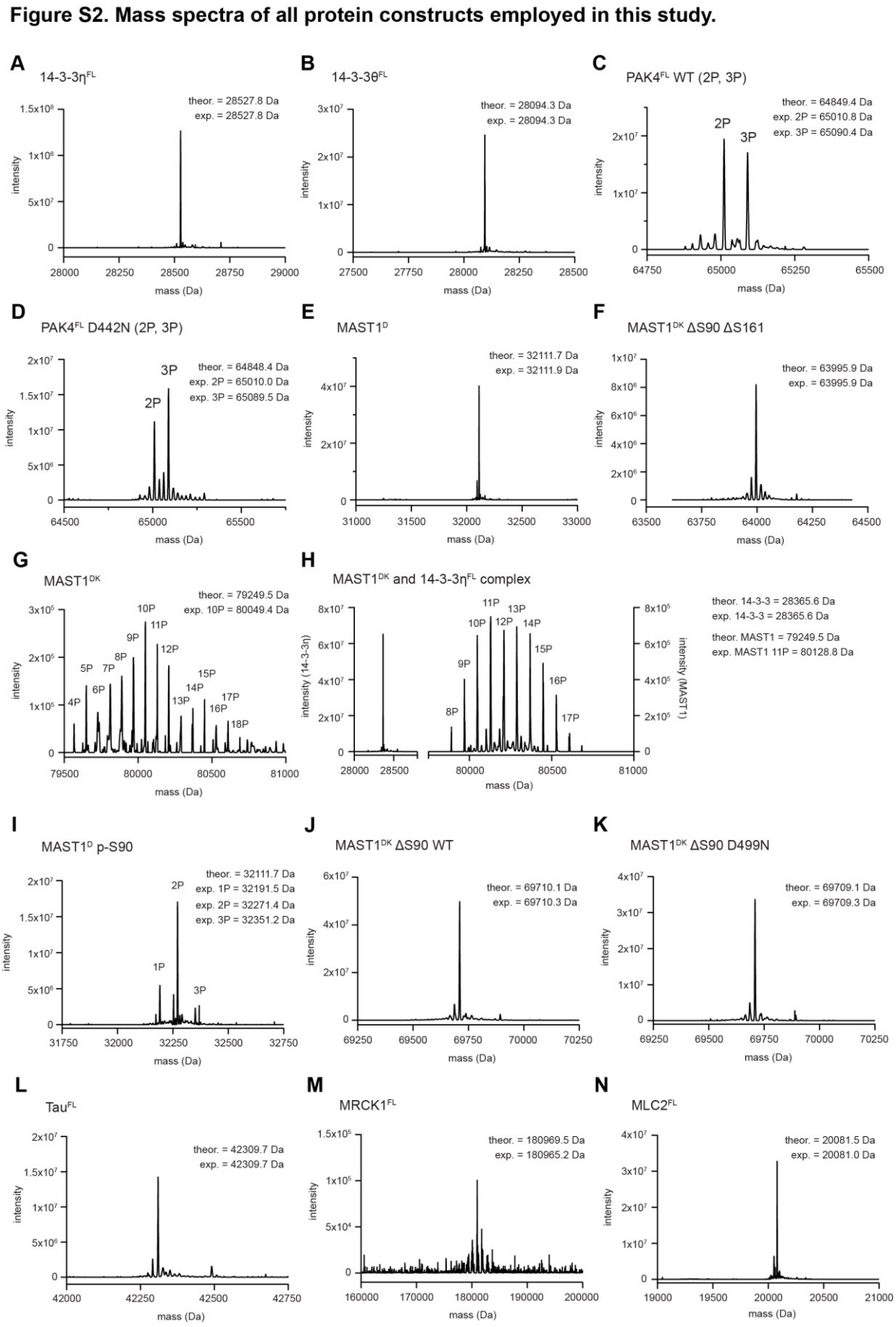

O

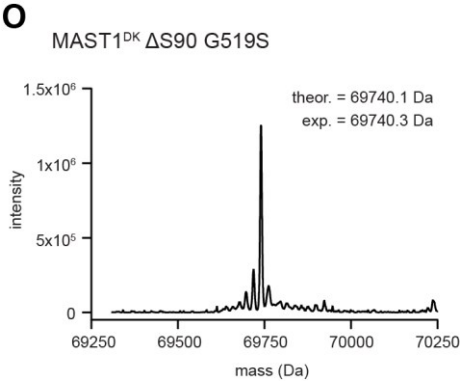

A. Mass spectrum of purified 14-3-3η^{FL}.

B. Mass spectrum of purified 14-3-3θ^{FL}.

C. Mass spectrum of purified PAK4^{FL} WT.

D. Mass spectrum of purified PAK4^{FL} D442N.

E. Mass spectrum of purified MAST1^{D}.

F. Mass spectrum of purified and dephosphorylated MAST1^{DK} ΔS90 ΔS161.

G. Mass spectrum of purified MAST1^{DK}.

H. Mass spectrum of co-purified MAST1^{DK} and 14-3-3η^{FL} complex.

I. Mass spectrum of purified MAST1^{D} after phosphorylation by PAK4^{FL} WT.

J. Mass spectrum of purified and dephosphorylated MAST1^{DK} ΔS90 WT.

K. Mass spectrum of purified and dephosphorylated MAST1^{DK} ΔS90 D499N.

L. Mass spectrum of purified Tau^{FL}.

M. Mass spectrum of purified MRCK1^{FL}.

N. Mass spectrum of purified MLC2^{FL}.

O. Mass spectrum of purified and dephosphorylated MAST1^{DK} ΔS90 G519S.

Supplementary Figure 3. MAST1 interacts with 14-3-3 proteins via S90 and S161.

Figure S3. MAST1 interacts with 14-3-3 proteins via S90 and S161.

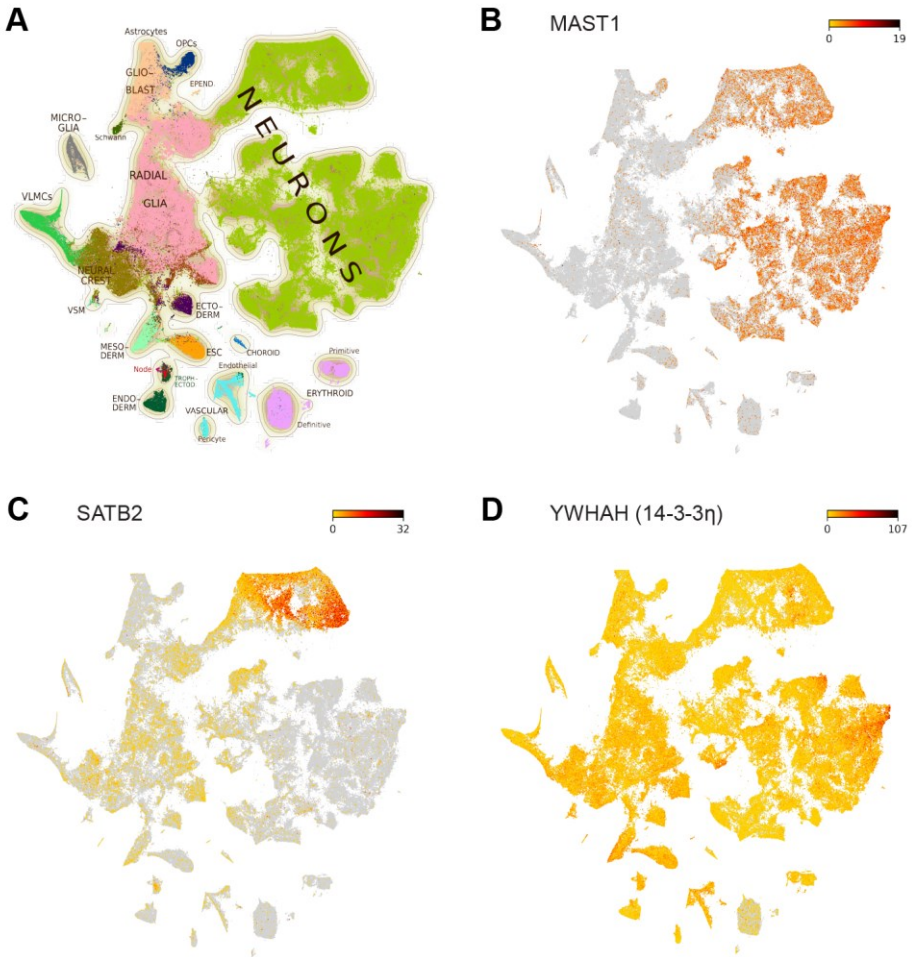

A. t-SNE plot of single-cell RNA sequencing data from embryonic mouse brains between embryonic stage E7-E18, colored by major cell types [14].

B. MAST1 expression levels overlayed on t-SNE plot from panel A.

C. SATB2 expression levels overlayed on t-SNE plot from panel A.

D. YWHAH (14-3-3η) expression levels overlayed on t-SNE plot from panel A.

Supplementary Figure 4. PAK4 phosphorylates MAST1 on S90.

Figure S4. PAK4 phosphorylates MAST1 on S90.

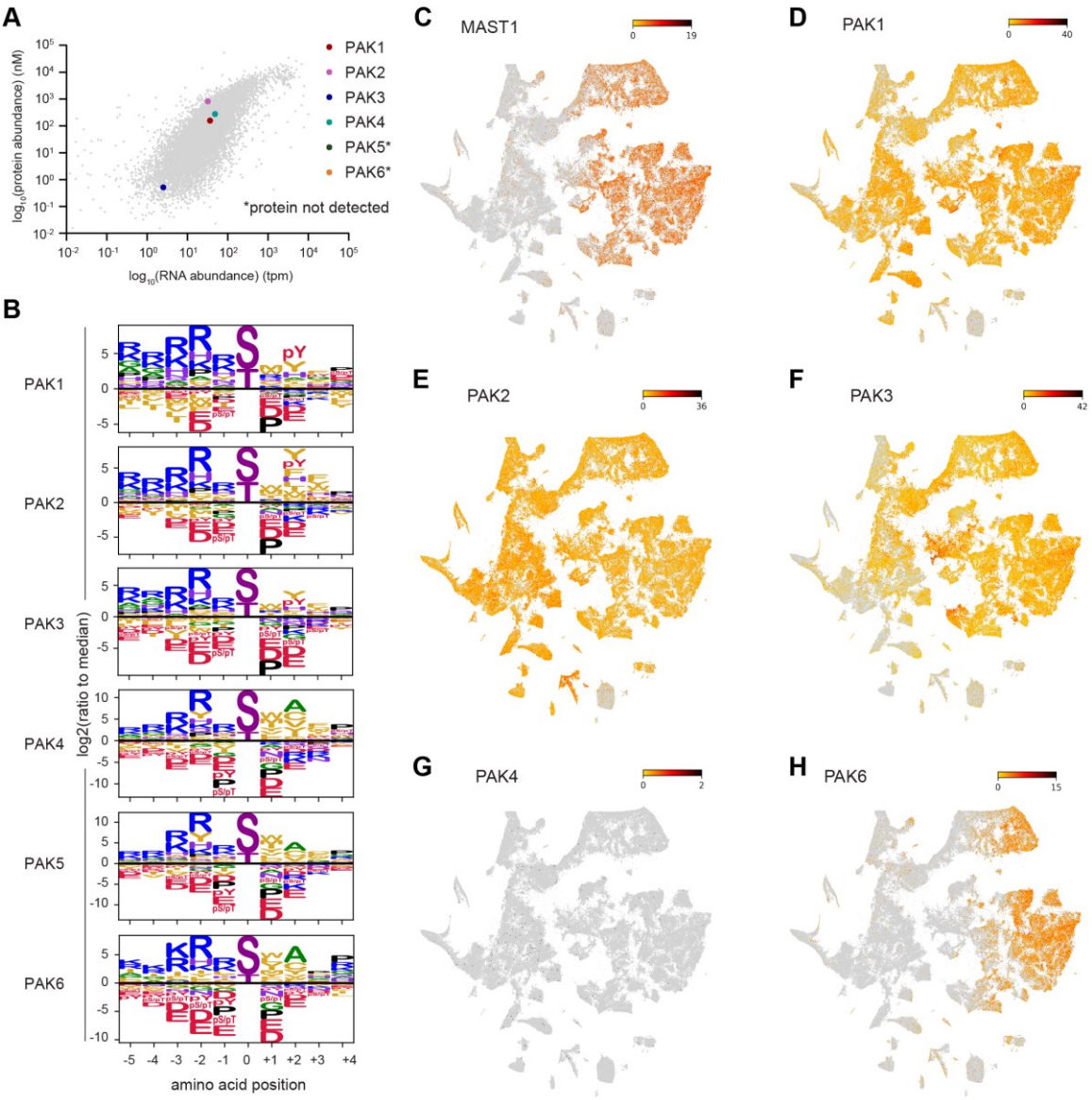

A. Scatter plot showing RNA and protein abundance of all PAKs (highlighted by large colored dots) overlayed on all detected RNA/protein, in HEK293 cells [12]. Both PAK5 and PAK6 protein was not detected, and are not plotted.

B. Substrate motif sequence logos of PAK1-6 from P-5 to P+4, where position 0 is the phosphorylatable residue [15].

C. MAST1 expression levels overlayed on t-SNE plot from Figure S3A.

D. PAK1 expression levels overlayed on t-SNE plot from Figure S3A.

E. PAK2 expression levels overlayed on t-SNE plot from Figure S3A.

F. PAK3 expression levels overlayed on t-SNE plot from Figure S3A.

G. PAK4 expression levels overlayed on t-SNE plot from Figure S3A.

H. PAK6 expression levels overlayed on t-SNE plot from Figure S3A.

Supplementary Figure 5. MAST1 S161 is an autoregulatory motif.

Figure S5. MAST1 S161 is an autoregulatory motif.

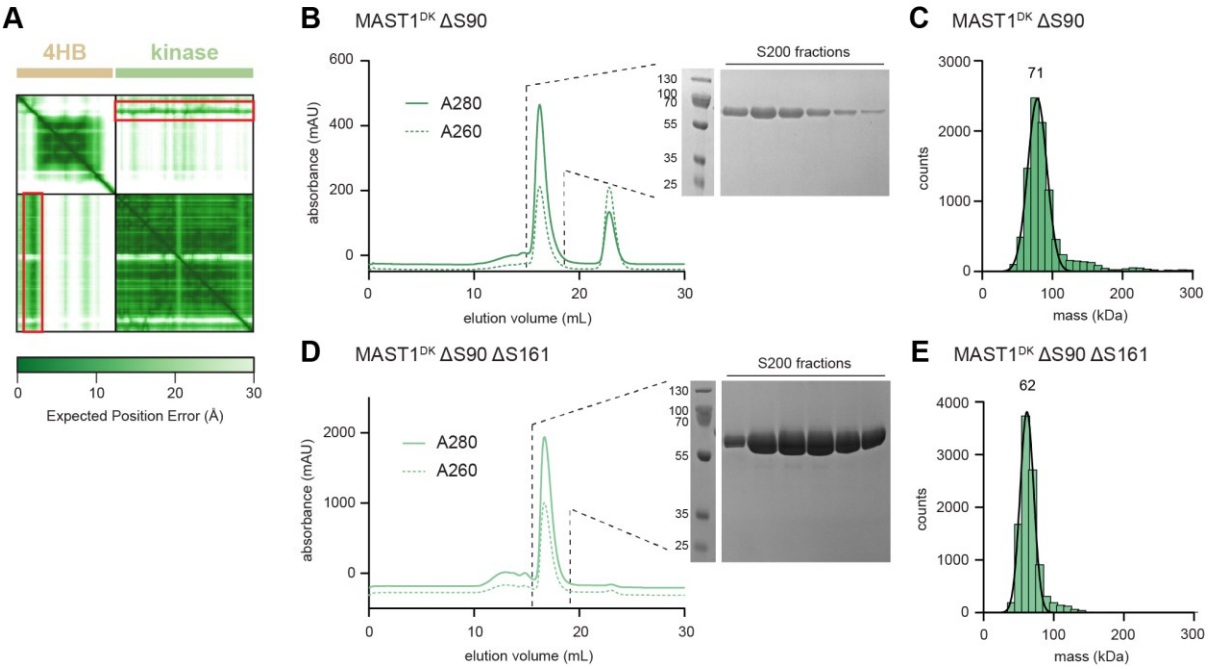

A. Pair alignment error (PAE) plot of MAST1 kinase domain and DUF. Region spanning the S161 sequence motif outlined in red box.

B. Size exclusion chromatography (SEC) elution profile of purified MAST1^{DK} ΔS90. Coomassie-stained SDS-PAGE gel of SEC fractions spanning elution peak shown in inset.

C. Mass photometry of purified MAST1^{DK} ΔS90. Theoretical mass = 70 kDa, observed mass = 71 kDa.

D. SEC elution profile of purified MAST1^{DK} ΔS90 ΔS161. Coomassie-stained SDS-PAGE gel of SEC fractions spanning elution peak shown in inset.

E. Mass photometry of purified MAST1^{DK} ΔS90 ΔS161. Theoretical mass = 64 kDa, observed mass = 62 kDa.

Supplementary Figure 6. MAST1 p-S90 or p-S161 forms a complex with 14-3-3η *in vitro*.

Figure S6. MAST1 p-S90 or p-S161 forms a complex with 14-3-3η *in vitro*.

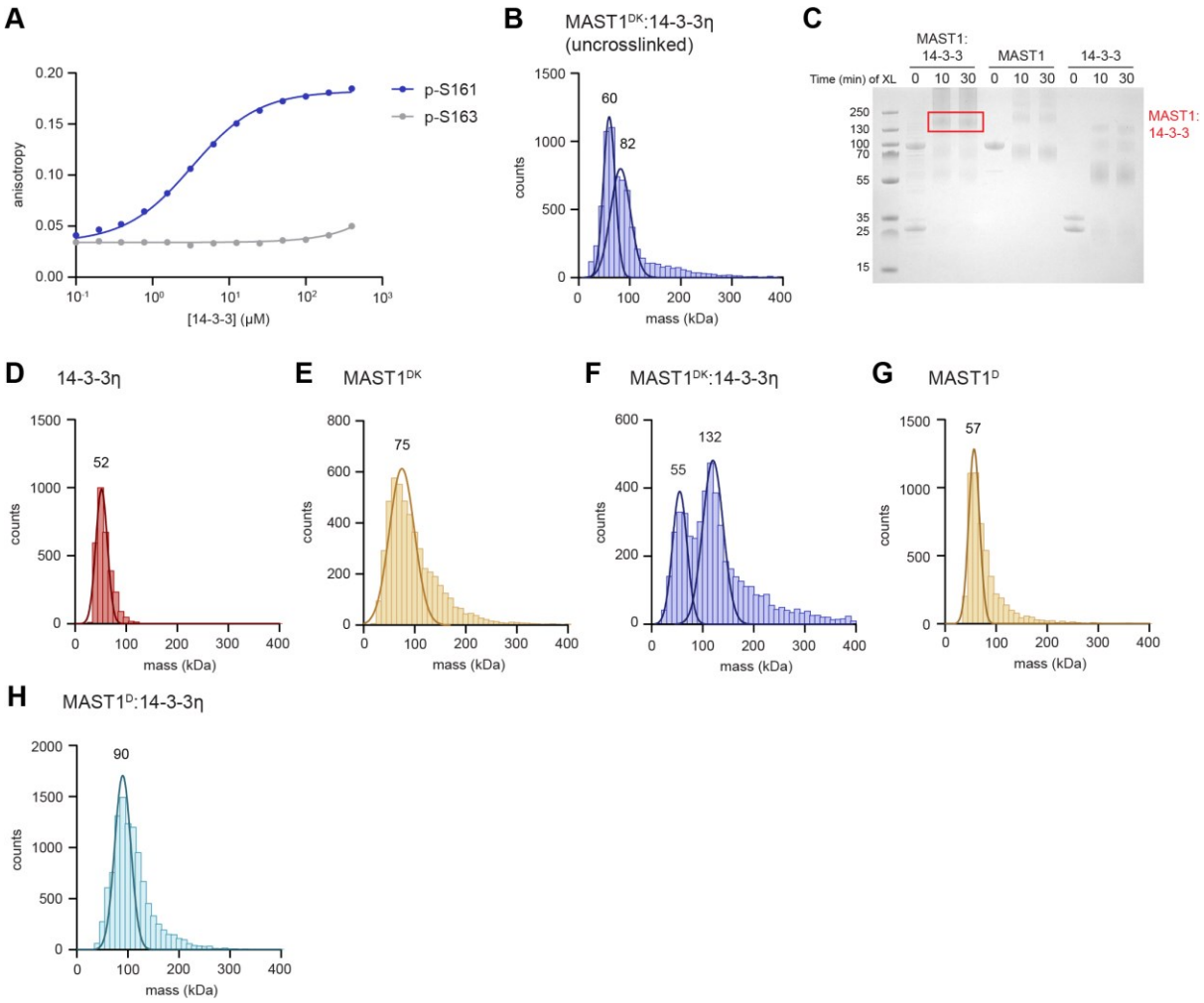

A. Binding curves for 14-3-3η and MAST1 peptides spanning S161 or S163, measured by fluorescence anisotropy. Data are presented as mean values ± S.E., *n* = 3. Data were fit with a one-site binding model and the K_d derived from curve fitting.

B. Mass photometry of co-purified MAST1^{DK} and 14-3-3η complex.

C. Coomassie-stained SDS-PAGE gel of MAST1^{DK} and 14-3-3η complex, MAST1^{DK} and 14-3-3η after 0, 10, and 30 min of glutaraldehyde crosslinking. Crosslinked trimeric complex outlined in red box.

D. Mass photometry of purified 14-3-3η after 10 min of glutaraldehyde crosslinking.

E. Mass photometry of purified MAST1^{DK} after 10 min of glutaraldehyde crosslinking.

F. Mass photometry of co-purified MAST1^{DK} and 14-3-3η complex after 10 min of glutaraldehyde crosslinking.

G. Mass photometry of purified MAST1^{D} p-S90.

H. Mass photometry of *in vitro*-formed MAST1^{D} p-S90 and 14-3-3η complex after 10 min of glutaraldehyde crosslinking.

Supplementary Figure 7. Tau is a MAST1 substrate.

Figure S7. Tau is a MAST1 substrate.

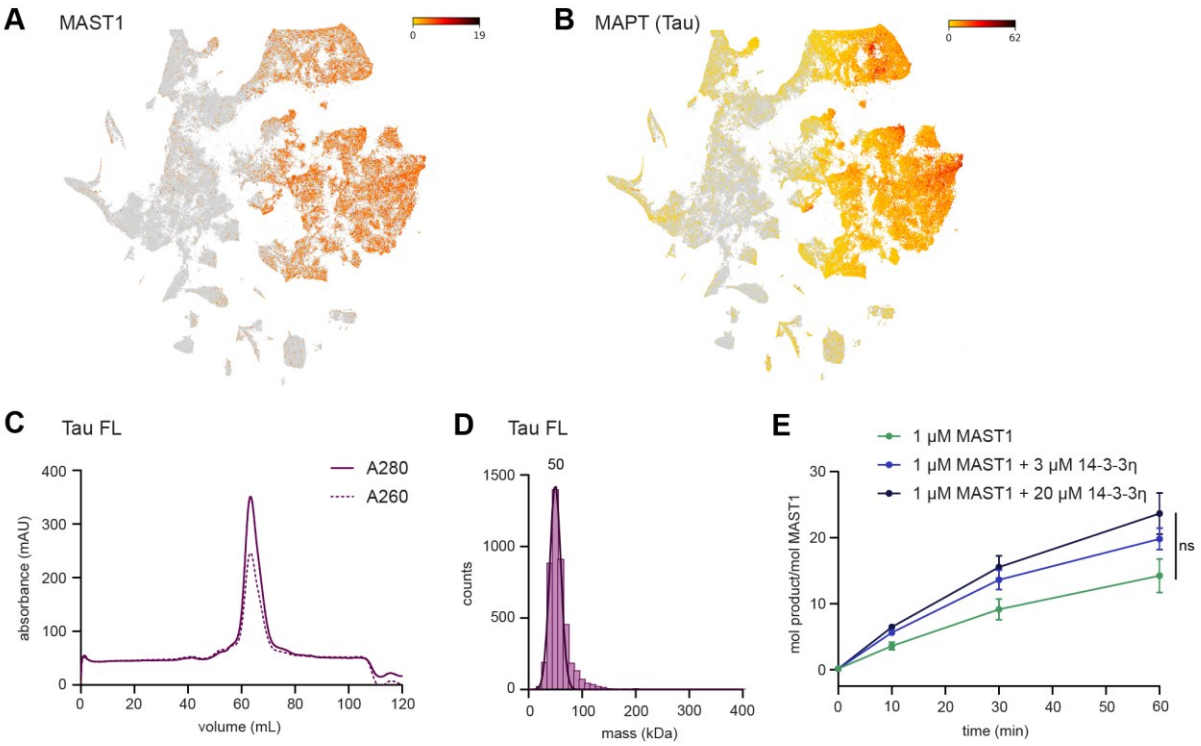

A. MAST1 expression levels overlayed on t-SNE plot from Figure S3A.

B. MAPT (Tau) expression levels overlayed on t-SNE plot from Figure S3A.

C. SEC elution profile of purified Tau.

D. Mass photometry of purified Tau. Theoretical mass = 42 kDa, observed mass = 50 kDa.

E. Radiometric kinase assay by $MAST1^{DK}$, $MAST1^{DK}$ and 14-3-3η complex, or $MAST1^{DK}$ and 14-3-3η complex supplemented with excess of purified 14-3-3η, on Tau (n = 3, p = 0.0642, two-way repeated-measures ANOVA). Data are presented as mean values ± S.E.

Supplementary Figure 8. MCC-CH-CM mutations perturb MAST1 folding and kinase activity.

Figure S8. MCC-CH-CM mutations perturb MAST1 folding and kinase activity.

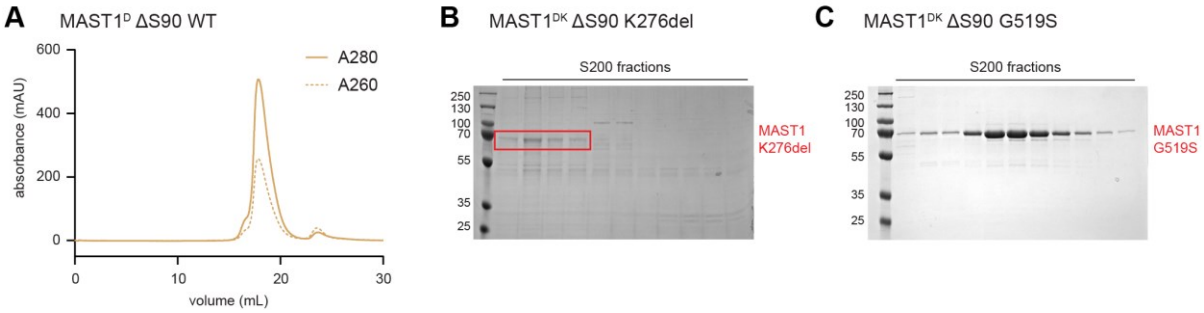

A. SEC elution profile of purified MAST1^{D} ΔS90 WT.

B. Coomassie-stained SDS-PAGE gel of SEC fractions spanning elution peak of MAST1^{DK} ΔS90 K276del. Bands representing MAST1 outlined in red box.

C. Coomassie-stained SDS-PAGE gel of SEC fractions spanning elution peak of MAST1^{DK} ΔS90 G519S.

Supplementary Tables

Supplementary Table 1. Oligonucleotide sequences for generation of G519S mouse model

mMAST1-G517S sgRNA target sequence	CACATCAAGCTCACGGATTTTGG
mMAST1-G517S ssDNA repair template	CCTGAGATCCCCACCTGTGCCTACAGCCTCCTTATCACCTCCATGGGTCACA TCAAGCTCACAGATTTCGGCCTCTCCAAGATGGGGCTCATGAGCCTCACCAC CAACTTATATGAAGGCCACATCGAGAAGGACGCCCC
mMAST1-G517S genotyping primer fw	CTCAAGCCAGACAAGTGAG
mMAST1-G517S genotyping primer rv	CCTGTTTGTCCAGGAACTC

Supplementary Methods

Protein expression and purification

Sf9 expression

All proteins expressed are derived from *Mus musculus* sequence unless otherwise stated. TEV-cleavable N-terminal 10xHis-tagged constructs of MAST1^{DK}, MAST1^{DK} ΔS90, MAST1^{DK} ΔS90 ΔS161, and PAK4^{FL}, 3C-cleavable N-terminal GST-tagged constructs of 14-3-3η, and a TEV-cleavable N-terminal StrepII-tagged construct of *Homo sapeins* MRCKα^{FL} were cloned into the pFastBacDual vector and expressed in baculovirus-infected *Spodoptera frugiperda* (Sf9) insect cells. Mutant constructs were cloned using site-directed mutagenesis. Sf9 cell pellets from 1 L of expression culture were lysed in 100 mL lysis buffer (50 mM HEPES pH 7.4, 150 mM NaCl, 1 mM TCEP, 2 mM benzamidine, 2 mM $MgCl_2$, 1x protease inhibitor cocktail (Sigma P8849), 1 kU Denarase (c-LEcta)). 20 mM imidazole was added for constructs purified by Ni-NTA affinity chromatography, 0.25% CHAPS was added for constructs purified by GST-beads, and phosphatase inhibitors (50 mM NaF, 10 mM betaglycerophosphate, 2 mM sodium pyrophosphate, 1 mM sodium orthovanadate) was added for MAST1^{DK}/14-3-3η co-purification to retain phosphates. Cleared lysates were obtained by centrifugation (38,000 g, 4°C, 30 min).

BL21 expression

All proteins expressed are derived from *Mus musculus* sequence unless otherwise stated. TEV-cleavable N-terminal 6xHis-tagged constructs of MAST1^{D}, 14-3-3η, and 14-3-3θ were cloned into the pHisII vector, an N-terminal 6xHis-tagged construct of Tau^{FL} (isoform F) was cloned into the pET28b vector, and a TEV-cleavable N-terminal GST-tagged construct of *Homo sapiens* MLC2^{FL} was cloned into the pGST2 vector, for expression in BL21 Star *E. coli*. The cells were grown at 37°C to an OD of 0.7 before induction with 250 µM IPTG and overnight expression at 18°C. BL21 cell pellets from 1 L of expression culture were lysed in 50 mL lysis buffer (50 mM HEPES pH 7.4, 150 mM NaCl, 1 mM TCEP, 2 mM benzamidine, 2 mM $MgCl_2$, 1x protease inhibitor cocktail (Sigma P8849), 0.5 kU Denarase (c-LEcta), 5 mg lysozyme). 20 mM imidazole and 0.25% CHAPS

was added as described above. Lysates were sonicated three times for 3 min at 50% amplitude and cleared lysates were obtained by centrifugation (38,000 g, 4°C, 20 min).

Purification

For Ni-NTA affinity purification, cleared lysates were run over a HisTrap FF column (Cytiva), washed with buffer A (50 mM HEPES pH 7.4, 150 mM NaCl, 1 mM TCEP) followed by buffer A with 2% buffer B (buffer A + 1 M imidazole), and eluted with buffer A with 30% buffer B. The eluate was cleaved and dialyzed overnight at 4°C with 8.8 nmol TEV protease (purified in house) in 50 mM HEPES pH 7.4, 50 mM NaCl, and 1 mM TCEP. Constructs requiring dephosphorylation were treated with 2.3 nmol of lambda-phosphatase (purified in house) and 0.1 mM $MnCl_2$.

For GST affinity purification, cleared lysates were incubated with 3 mL glutathione sepharose beads (Cytiva) for 3 hours at 4°C. The beads were washed three times with buffer A (50 mM HEPES pH 7.4, 150 mM NaCl, 1 mM TCEP, 0.25% CHAPS) and the construct was cleaved off the beads overnight at 4°C with either 8.8 nmol TEV protease (purified in house) or 11.1 nmol 3C protease (purified in house).

For StrepII affinity purification, cleared lysates were run over a StrepTrap HP column (Cytiva), washed with buffer A (50 mM HEPES pH 7.4, 150 mM NaCl, 1 mM TCEP), and eluted with buffer B (buffer A + 2.5 mM d-desthiobiotin). The eluate was cleaved overnight at 4°C with 8.8 nmol TEV protease (purified in house).

Following affinity purification, constructs underwent ion-exchange purification. Proteins that were not dialyzed to 50 mM NaCl were first diluted to make a final concentration of 50 mM NaCl, then run over either a HiTrap Q HP or HiTrap SP HP column (Cytiva), washed with buffer A (50 mM HEPES pH 7.4, 1 mM TCEP), and eluted with a gradient of buffer B (50 mM HEPES pH 7.4, 1 M NaCl, 1 mM TCEP). The peak fractions were pooled, concentrated, and injected onto a size exclusion column (Cytiva) equilibrated in 50 mM HEPES pH 7.4, 150 mM NaCl, 1 mM TCEP. S200 and S75 columns were used for constructs >30 kDa and <30 kDa respectively, and 10/300 and 16/600 columns were used for yields >5 mg and <5 mg respectively. For $MAST1^{D}$ requiring phosphorylation on S90, it was incubated with purified $PAK4^{FL}$ at room temperature for 2 hours prior to injection on the size exclusion column. The peak fractions were pooled, concentrated, and stored at -80°C.

Cell culture

HEK293 cells were maintained in DMEM supplemented with 10% FBS. Cells were tested negative for *Mycoplasma* contamination using Eurofins Genomics Mycoplasmacheck service.

Intact mass spectrometry

Protein sample was diluted in dH2O to 4 ng/µL and dithiothreitol was added to a final concentration of 25 mM. 8 ng (2 µL) of protein was loaded on an XBridge Protein BEH C4 column (2.5 µm particle size, dimensions 2.1 mm x 150 mm; Waters) using a Vanquish™ Horizon UHPLC system (Thermo Scientific) with a working temperature of 50 °C, 0.1% formic acid (FA) as solvent A, 100% acetonitrile, 0.08% FA as solvent B. Proteins were separated on a 6 min step gradient from 12 to 72% solvent B at a flow rate of 250 µL/min and analyzed on a Synapt G2-Si coupled via a ZSpray ESI source (Waters). Data were recorded with MassLynx V 4.2 (Waters) and analyzed using the MaxEnt 1 process to reconstruct the uncharged average protein mass.

Tandem mass spectrometry

Sample preparation

For MAST1^{D}, MAST1^{DK} ΔS90, and MAST1^{DK}:14-3-3η, ~5 µg protein in 1.5 µL was diluted with 8.5 µL of 8 M urea, 50 mM ammonium bicarbonate (ABC). For Tau^{FL}, ~5 µg of protein in 2.5 µL was mixed with 10% sodium deoxycholate (SDC) and 50 mM ABC to reach 2% SDC. Proteins were reduced with 0.4 µL of 250 mM dithiothreitol (DTT) for 30 min at room temperature (50°C for Tau^{FL}) and alkylated by adding 0.4 µL of 500 mM IAA and incubating for 30 min at room temperature in the dark. The remaining iodoacetamide (IAA) was quenched by adding 0.2 µL of 250 mM DTT for 10 min. For MAST1^{D}, MAST1^{DK} ΔS90, and MAST1^{DK}:14-3-3η, the sample was diluted to below 1 M urea with 70 µL of 50 mM ABC. For Tau^{FL}, the sample was diluted to 1% SDC with 10 µL of 100 mM ABC. Proteins were digested by adding ~160 ng trypsin (Trypsin Gold, Promega) and incubated at 37°C overnight. The digest was stopped by the addition of 10% trifluoroacetic acid to a final concentration of 0.5% (1% for Tau^{FL}). For Tau^{FL}, samples were centrifuged at 18,500 x g for 10 min to remove the SDC, the supernatant was transferred to a new tube, 10% TFA was added to reach a final concentration of 2%, and the sample was centrifuged again at 18,500 x g for 10 min. The resulting supernatant was desalted using C18 Stagetips [1].

For EGFP-MAST1 AP-MS bead samples, the beads were resuspended in 30 µL of 2 M urea and 50 mM ammonium bicarbonate. Disulfide bonds were reduced with 1.2 µL of 250 mM DTT for 30 min at room temperature before adding 1.2 µL of 500 mM IAA and incubating for 30 min at room temperature in the dark. The remaining iodoacetamide was quenched with 0.6 µL of 250 mM DTT for 10 min. Proteins were digested with 150 ng LysC (mass spectrometry grade, FUJIFILM Wako chemicals) and trypsin (Trypsin Gold, Promega) mix at room temperature for 90 min. The supernatant was transferred to a new tube and the beads were rinsed with 30 µL of 2 M urea and 50 mM ammonium bicarbonate. 60 µL of 50 mM ammonium bicarbonate was added to the tube, before digestion with 150 ng LysC/trypsin mix at 37°C for 5 h. The digest was stopped by the addition of TFA to a final concentration of 0.5%, and the peptides were desalted using C18 Stagetips [1].

Liquid chromatography-mass spectrometry analysis

For MAST1^{D}, MAST1^{DK} ΔS90, MAST1^{DK}:14-3-3η, and Tau^{FL}, LC-MS analysis was performed on a Vanquish Neo UHPLC system (Thermo Scientific) coupled to an Orbitrap Exploris 480 mass spectrometer (Thermo Scientific). The system was equipped with a Nanospray Flex ion source (Thermo Scientific), coated emitter tips (PepSep, MSWil), and a Butterfly Portfolio Heater (Phoenix S&T). Peptides were loaded onto a trap column (Acclaim PepMap 100 C18 HPLC Column, 20 mm × 0.1 mm, 5 µm particle size, Thermo Scientific) using 0.1% TFA as mobile phase, and separated on an analytical column (Acclaim PepMap 100 C18 HPLC Column, 50 cm × 75 µm, 2 µm particle size, Thermo Scientific), applying a linear gradient starting with a mobile phase of 98% solvent A (0.1% FA) and 2% solvent B (80% acetonitrile, 0.08% FA), increasing to 35% solvent B over 60 min at a flow rate of 230 nL/min. The analytical column was heated to 30°C.

The mass spectrometer was operated in data-dependent acquisition (DDA) mode, with 2 s MS1 cycle time. For MAST1^{D}, MAST1^{DK} ΔS90, and MAST1^{DK}:14-3-3η, survey scans were acquired from 375-2000 m/z with lock mass enabled, normalized AGC target of 300%, resolution of 120,000. For Tau^{FL}, survey scans were acquired from 340-1500 m/z with lock mass enabled, normalized AGC target of 300%, resolution of 60,000. The most intense precursor ions (charge states +2 to +6) were selected for fragmentation using an isolation window of 1.2-1.4 m/z. Selected ions were analyzed with a maximum fill time of 100 ms, normalized AGC target of 200%, and resolution of 30,000 after HCD

fragmentation with normalized collision energy of 28-30%. Monoisotopic precursor selection (MIPS) was set to "peptide" mode, the intensity threshold to 2.5 x 10^4 (1 x 10^4 for Tau^{FL}), and selected precursors were dynamically excluded for 20 seconds with isotope exclusion enabled.

For EGFP-MAST1 AP-MS samples, LC-MS analysis was performed on an UltiMate 3000 RSLCnano LC system (Thermo Scientific) coupled to a timsTOF HT (Bruker). The system was equipped with a CaptiveSpray ion source (Bruker), and a Butterfly Portfolio Heater (Phoenix S&T). Peptides were loaded onto a trap column (Acclaim PepMap 100 C18 HPLC Column, 20 mm × 0.1 mm, 5 µm particle size, Thermo Scientific) using 0.1% TFA as mobile phase, and separated on an analytical column (Aurora Ultimate XT C18, 25 cm × 75 µm, 1.7 µm particle size, IonOpticks), applying a linear gradient starting with a mobile phase of 98% solvent A (0.1% FA) and 2% solvent B (80% acetonitrile, 0.08% FA), increasing to 35% solvent B over 60 min at a flow rate of 300 nL/min. The analytical column was heated to 50°C.

The mass spectrometer was operated in data-independent acquisition (DIA) parallel accumulation serial fragmentation (PASEF) mode. MS2 data were acquired with eight PASEF scans per duty cycle, each containing three m/z windows. The m/z window widths were adjusted based on the expected precursor density, covering a total range of 300–1200 m/z. The ion mobility range was set to 0.64-1.42 V*s/cm, and the accumulation and ramp time was set to 100 ms. TIMS elution voltages were calibrated linearly to obtain the reduced ion mobility coefficients (1/K0) using three Agilent ESI-L Tuning Mix ions (m/z 622, 922 and 1,222). Collision energy for fragmentation was scaled linearly with precursor mobility (1/K0), ranging from 20 eV (at 1/K0 = 0.6 V*s/cm) to 59 eV at (at 1/K0 = 1.6 V*s/cm).

Mass spectrometry data analysis

For $MAST1^{D}$, $MAST1^{DK}$ ΔS90, $MAST1^{DK}$:14-3-3η, and Tau^{FL}, MS raw data were analyzed with FragPipe (22.0), using MSFragger (4.1) [2], IonQuant (1.10.27) [3], and Philosopher (5.1.1) [4]. The default FragPipe workflow for label free quantification (LFQ-MBR) was used, except "Normalize intensity across runs" was turned off. Cleavage specificity was set to Trypsin/P, with two missed cleavages allowed. The protein FDR was set to 1%. Carbamidomethyl was used as fixed cysteine modification; methionine oxidation, phosphorylation at STY and protein N-terminal acetylation were specified as variable

modifications. PTMProphet was used for the PTM site localization. MS2 spectra were searched against the *Spodoptera frugiperda* protein sequences from Uniprot (Taxon ID: 7108, release 2024_01), concatenated with a database of 379 common laboratory contaminants (release 2023.03, https://github.com/maxperutzlabs-ms/perutz-ms-contaminants), and protein sequences for the constructs.

For EGFP-MAST1 AP-MS samples, MS raw data were processed with Spectronaut (19.0 or 19.2, Biognosys). The library-free DirectDIA+ workflow was employed for analysis of the raw files, the *H. sapiens* 1 protein per gene reference proteome from Uniprot (Proteome ID: UP000005640, release 2024_01), concatenated with a database of 379 common laboratory contaminants (release 2023.03, https://github.com/maxperutzlabs-ms/perutz-ms-contaminants), and sequences for the constructs. The cleavage specificity was set to full trypsin specificity (Trypsin/P), with two missed cleavages allowed. Carbamidomethyl was used as fixed cysteine modification; methionine oxidation and protein N-terminal acetylation were specified as variable modifications. Cross-run normalization was disabled, and all other settings were used at their default values.

Post-processing with in-house pipeline

Computational analysis was performed using Python and the in-house developed Python library MsReport (0.0.26) [5]. Only non-contaminant proteins identified with a minimum of two peptides and being quantified once were considered for further analysis. LFQ protein intensities were log2-transformed and normalized across samples using the ModeNormalizer from MsReport. The ModeNormalizer method involves calculating log2 protein ratios for all pairs of samples and determining normalization factors based on the modes of all ratio distributions. Missing values were imputed by drawing random values from a normal distribution. Sigma and mu of this distribution were calculated per sample from the standard deviation and median of the observed log2 protein intensities (μ = median sample LFQ intensity – 1.8 standard deviations of the sample LFQ intensities, σ = 0.3 × standard deviation of the sample LFQ intensities). iBAQ intensities were calculated by dividing protein intensities by the number of theoretically observable tryptic peptides between 6 and 30 amino acids. To estimate the relative protein abundances within each sample, the iBAQ intensities were normalized by dividing them by the total sum of iBAQ intensities for all proteins in the sample. For

the EGFP-MAST1 AP-MS samples, statistical analysis was performed using the linear models for microarray analysis (limma) v.3.54.2 [6] package in R. Moderated t-statistics were calculated using the limma-trend method, and multiple testing correction was applied using the Benjamini–Hochberg method. The Python library XlsxReport (0.1.1) [7] was used to create formatted Excel files summarizing the results of the proteomics experiments.

Data availability

The mass spectrometry proteomics data have been deposited to the ProteomeXchange Consortium via the PRIDE [8] partner repository with the data set identifiers PXD063727, PXD063803, PXD063802, PXD063795, and PXD063731.

Phosphoproteomics

Methanol/Chloroform precipitation and proteolytic digest

Cortical P0 samples were extracted from n = 5 WT and homozygous litter-matched P0 animals of both the MAST1 L278del and the MAST1 G519S mouse line and flash-frozen for storage. The cortices were dissolved in 500 µL methanol and then protein was precipitated by adding 1 mL chloroform. After centrifugation (10 min, 10,000 g) the supernatant was removed. The pellets were lysed in a solution of 10 M urea and 50 mM HCl and then 1 M Triethylammoniumbicarbonate (TEAB) was added to a final concentration of 100 mM.

The lysates were supplemented with 5 mM DTT and incubated at 37°C for 1 h. The alkylation was performed by adding 10 mM Iodoacetamide and incubating for 30 min in the dark. The reaction was quenched by addition of 7.5 mM DTT and incubation at room temperature for 30 min. The samples were diluted to 6 M urea by addition of 100 mM TEAB and the proteins were digested with lysyl endopeptidase (Lys-C, Fujifilm Wako Pure Chemical Corporation) at an enzyme to protein ration of 1:50 for 3 h at 37°C. Subsequently, the samples were further diluted with 100 mM TEAB Buffer to 2 M urea, and trypsin (Trypsin Gold, Promega) was added at an enzyme to protein ratio of 1:50 and the samples were incubated overnight at 37°C.

The samples were acidified to a pH below 2 with 10% TFA and were desalted using C18 cartridges (Sep-Pak Vac 1cc (200 mg), Waters). Peptides were eluted with 2 x 600 µL 80% Acetonitrile (ACN) and 0.1% Formic Acid (FA), followed by freeze-drying.

TMT labelling

1.5 mg of lyophilized peptides were dissolved in 240 µL of 100 mM Triethylammonium bicarbonate. TMT10-plex labelling reagents (3 vials per label) were dissolved in 41 µL of anhydrous acetonitrile. 3 vials per label (2.4 mg of reagent) were added to the peptide samples and incubated for 1 h. After quenching with 5% hydroxylamine, the samples were mixed in several steps to achieve a correct mixing ratio of 1:1:1:1:1:1:1:1:1:1. (median of Top 500 proteins)

Following labelling, peptides were again freeze-dried, dissolved in TFA 0.1% and split in two aliquots: one containing 500 µg for measurement of the unmodified peptides and proteome quantification and one containing 13 mg for enrichment of phosphopeptides and phosphoproteome quantification. Both were desalted using C18 cartridges (Sep-Pak, Waters). Peptides were eluted with 70% ACN and 0.1% FA, followed by freeze-drying.

Phosphopeptide enrichment

Phosphopeptides were enriched using TiO_2 by first dissolving the dried peptide mixture in 4 mL of TiO_2 loading buffer (300 mg/mL lactic acid (Sigma-Aldrich), 80% ACN, 0.1% TFA) and incubating them with 120 mg of TiO_2 resin (Titansphere bulk media, 5 µm, GL Science) for 60 min at room temperature with over end rotation. For washing and elution the bead suspension was split and transferred to 8 Mobicol (MoBiTec) spin columns with a 10 µm pore filter at the outlet.

The TiO_2 beads in each spin column were washed with 8 x 500 µL of TiO_2 loading buffer, 8 x 500 µL of 80% ACN, 0.1% TFA, 4 x 500 µL of 1% ACN, 0.1% TFA, 4 x 500 µL of 1% ACN, 0.1% FA. Bound peptides were eluted from the resin by addition of 3 x 200 µL 0.3 M NH_4OH, 2 x 200 µL 0.7 M NH_4OH and 2 x 150 µL 0.4 M NH_4OH and 40% ACN, eluates were unified and freeze-dried.

Fractionation of total peptides and enriched phosphopeptides by SCX

The lyophilized peptide samples were dissolved in SCX buffer A (5 mM phosphate buffer pH 2.7, 15% ACN). 200 µg of the unmodified peptides and the total amount of the enriched phosphopeptides were loaded on the SCX column. The SCX fractionation was performed on an Ultimate system (Thermo Fisher Scientific) using a TSKgel SP-25W (ToSOH) column (5 µm particles, 1 mm i.d. x 300 mm) at a flow rate of 40 µL/min.

For the separation a ternary gradient was used, starting with 100% buffer A for 10 min, followed by a linear increase to 10% buffer B (5 mM phosphate buffer pH 2.7, 1 M NaCl, 15% ACN) and 50% buffer C (5 mM phosphate buffer pH 6.0, 15% ACN) in 15 min (for proteome) or 30 min (for phosphoproteome), to 25% buffer B and 50% buffer C in next 5 min (for proteome) or 10 min (for phosphoproteome), to 50% buffer B and 50% buffer C in next 5 min and an isocratic elution for further 15 min.

The flow-through was collected as a single fraction, along the gradient fractions were collected every minute and stored before analysis.

LC-MS/MS

The nano HPLC system used was an UltiMate 3000 HPLC RSLC nano system (Thermo Scientific) coupled to a Q Exactive HF-X mass spectrometer (Thermo Scientific), equipped with a Proxeon nanospray source (Thermo Scientific). Peptides were loaded onto a trap column (Thermo Scientific, PepMap C18, 5 mm × 300 µm ID, 5 µm particles, 100 Å pore size) at a flow rate of 25 µL/min using 0.1% TFA as mobile phase. After 10 min, the trap column was switched in line with the analytical column (Thermo Scientific, PepMap C18, 500 mm × 75 µm ID, 2 µm, 100 Å). Peptides were eluted using a flow rate of 230 nL/min and a binary 120 min gradient. The two-step gradient started with the mobile phases: 98% A (water/formic acid, 99.9/0.1, v/v) and 2% B (water/acetonitrile/formic acid, 19.92/80/0.08, v/v/v) increased to 40% B over the next 120 min, followed by a gradient in 5 min to 95% B, stayed there for 5 min and decreased in 2 min back to 98% A and 2% B for equilibration at 30°C.

The Q Exactive HF-X mass spectrometer was operated in data-dependent mode, using a full scan (m/z range 380-1650, nominal resolution of 120,000, target value 3E6) followed by MS/MS scans of the 10 most abundant ions. MS/MS spectra were acquired using normalized collision energy of 35, isolation width of 0.7 m/z, resolution of 45,000, a target value of 1E5 and maximum fill time of 250 ms. For the detection of the TMT reporter ions a fixed first mass of 110 m/z was set for the MS/MS scans. Precursor ions selected for fragmentation (exclude charge state 1, 7, 8, >8) were put on a dynamic exclusion list for 30 s. Additionally, the minimum AGC target was set to 1E4 and intensity threshold was 4E4. The peptide match feature was set to preferred and the exclude isotopes feature was enabled.

Data processing

For peptide identification, the RAW-files were loaded into Proteome Discoverer (version 2.3.0.523, Thermo Scientific). All hereby created MS/MS spectra were searched using MSAmanda v2.3.0.12368, engine version 2.0.0.12368 [9]. The RAW-files were searched against the Uniprot reference database, using mouse as sub-organism (21,963 sequences; 11,719,000 residues). The following search parameters were used: Iodoacetamide derivative on cysteine, 11-plex tandem mass tag® (TMT) on lysine were set as fixed modifications, deamidation on asparagine and glutamine, oxidation on methionine, phosphorylation on serine, threonine and tyrosine as well as Carbamylation and 11-plex TMT on peptide-N-term were set as variable modifications. Monoisotopic masses were searched within unrestricted protein masses for tryptic enzymatic specificity. The peptide mass tolerance was set to ±5 ppm and the fragment mass tolerance to ±15 ppm. The maximal number of missed cleavages was set to 2. The result was filtered to 1% FDR on protein level using Percolator algorithm integrated in Thermo Proteome Discoverer. The localization of the modification sites within the peptides was performed with the tool ptmRS, which is based on phosphoRS [10]. Peptides were quantified based on Reporter Ion intensities extracted by the "Reporter Ions Quantifier"-node implemented in Proteome Discoverer. Proteins were quantified by summing unique peptides.

To distinguish regulated phospho-peptides that are altered due to regulation of the phosphorylation site from changes due to regulation of the underlying protein, PSMs were separated into those acquired from phospho-enriched samples and others acquired from the input before enrichment to capture changes on the proteome level. Therefore, proteins were quantified by summing unique and razor peptides detected and quantified in the input fractions. Resulting values were sum normalized across samples. Fractions of the phospho-enrichment were grouped and summarized on the peptide isoform level.

Subsequently, phosphopeptide regulations determined in the enriched fractions were corrected by regulation of the corresponding protein in the input fractions to correct for changes observed due to regulation on the proteome level. Statistical significance of differentially expressed phosphopeptides was determined using LIMMA [6] and FDR curves determined in Hein *et al* [12] were applied to extract significantly regulated

phosphopeptides. MS/MS spectra assigned to the Tau peptide phosphorylated on residue S214 were validated manually. Most of them showed a mix of different isoforms, mainly of phosphorylated T212 and S214, while some spectra did not contain fragments that allowed for the unambiguous distinction between the possible isoforms.

Data availability

The phosphoproteomics data have been deposited to the ProteomeXchange Consortium via the PRIDE [10] partner repository with the data set identifier PXD065759.

Glutaraldehyde crosslinking

Purified MAST1^{DK,} MAST1^{D} p-S90, 14-3-3η, and co-purified MAST1^{DK}:14-3-3η complex was incubated either alone or in combination, at a final concentration of 20 µM, with 0.01% glutaraldehyde in buffer (50 mM HEPES pH 7.4, 150 mM NaCl, 1 mM TCEP), at room temperature for up to 30 min. The reaction was quenched with 20 mM Tris pH 7.5.

Generation of MAST1 G519S mouse model

Animals used in this study were housed at the IMP/IMBA animal facility under a 12:12 light-dark cycle. Food was provided ad-libitum. G519S MAST1 transgenic mice were generated by CRISPR/Cas9 editing through pronuclear microinjection using Cas9 mRNA, sgRNA, and a single-stranded DNA repair template [11]. See supplementary table 1 for gRNA and repair template sequences. The gRNA target sequence was cloned into PX458 plasmid as described previously [13] and sgRNA was expressed using the MEGAshortscript™ T7 Transcription kit (Thermo Fisher Scientific, AM1354). The ssDNA repair template was ordered from Integrated DNA Technologies (Alt-R™ HDR Donor Oligo). Injections were performed on BL6/CBA F1 zygotes. Successfully edited mice were identified using Sanger sequencing and backcrossed using C57BL/6J mice for at least 10 generations. All procedures were carried out in accordance with the legal requirements under an approved license (M58/006093/2011/14).

Solubility analysis of MAST1 mutants

MAST1^{D} ΔS90WT, E194del, K276del, and L278del were transformed into BL21 Star *E. coli* and grown at 37°C to an OD of 0.7, before induction with 100 µM IPTG and

overnight expression at 18°C. Cell pellets from 10 mL of expression culture were lysed in 2 mL of lysis buffer (50 mM HEPES pH 7.4, 150 mM NaCl, 1 mM TCEP, 2 mM benzamidine, 2 mM $MgCl_2$, 1x protease inhibitor cocktail (Sigma P8849), 0.2 kU Denarase, 2 mg lysozyme). Lysates were sonicated three times for 30 sec at 20% amplitude. A sample was taken for SDS-PAGE (whole cell lysate). The lysate was centrifuged at 38,397 g, 4°C, for 15 min, and a sample of the cleared lysate was taken for SDS-PAGE (supernatant). The pellet was resuspended in the same volume of buffer (50 mM HEPES pH 7.4, 150 mM NaCl, 1 mM TCEP, 0.25% CHAPS) by vigorously vortexing, and a sample was taken for SDS-PAGE (pellet).

Western blot

Mouse P0 cortical lysates were prepared using lysis buffer (20 mM Tris pH 7.5, 100 mM NaCl, 10% Glycerol, 1% Triton-X100) and 1:100 Halt™ Protease & Phosphatase Inhibitor Cocktail (Thermo Fisher Scientific, #78444). Brains were lysed by addition of 10 µL lysis buffer per mg of sample, addition of a Tungsten carbide bead and shaking using a TissueLyser II machine (Qiagen; 20 Hz, 2 x 60 s, RT) followed by further incubation on a rotating tube holder (60 min, 4°C). Protein concentrations were determined using a Pierce™ BCA Protein Assay Kit (Thermo Fisher Scientific, #23225). 30 µg of protein lysate was prepared in Laemmli loading buffer + 2% β-Mercaptoethanol and boiled for 5 min at 95°C. Gel electrophoresis was carried out using Novex™ WedgeWell™ 8-16% Tris-Glycine gel (Thermo Fisher Scientific, # XP08160BOX) and Tris-Glycine SDS running buffer (25 mM Tris, 240 mM glycine, 0.1% SDS, pH 8.3) for 2 h at 120 V. Blotting was done on activated PVDF membranes via wet transfer in transfer buffer (31 mM Tris, 240 mM Glycine, 0.025% SDS, 20% Methanol) for 16 h at 20 V. Membranes were blocked used 5% skimmed milk in TBS-T for 1 h @ RT. Incubation with primary antibody was performed overnight, 4°C in blocking solution. The following primary antibodies were used: Anti-MAST1 (ProteinTech, 13305-1-AP, 1:1000), Anti-MAST2 (SantaCruz, sc-377198, 1:300), Anti-MAST3 (Novus Biologicals, NBP1-82993, 1:500), Anti-GAPDH (Millipore, MAB374, 1:2000). Membranes were washed with TBST and incubated for 1 h, RT with the following secondary antibodies: Goat anti-mouse HRP (Abcam, ab6823, 1:5000), Goat anti-rabbit HRP (Abcam, ab6721, 1:10000). Chemiluminescent imaging was carried out using the ECL™ Western blotting reagent (Sigma Aldrich, #

GERPN2109) on a Chemidoc-MP Bioimaging system (Bio-Rad). Quantification was performed using ImageJ.

Supplementary References

1. Rappsilber, J., Mann, M., and Ishihama, Y. (2007). Protocol for micro-purification, enrichment, pre-fractionation and storage of peptides for proteomics using StageTips. Nat. Protoc. *2*, 1896–1906.

2. Kong, A.T., Leprevost, F.V., Avtonomov, D.M., Mellacheruvu, D., and Nesvizhskii, A.I. (2017). MSFragger: ultrafast and comprehensive peptide identification in mass spectrometry-based proteomics. Nat. Methods *14*, 513–520.

3. Yu, F., Haynes, S.E., and Nesvizhskii, A.I. (2021). IonQuant enables accurate and sensitive label-free quantification with FDR-controlled match-between-runs. Mol. Cell. Proteomics *20*, 100077.

4. da Veiga Leprevost, F., Haynes, S.E., Avtonomov, D.M., Chang, H.-Y., Shanmugam, A.K., Mellacheruvu, D., Kong, A.T., and Nesvizhskii, A.I. (2020). Philosopher: a versatile toolkit for shotgun proteomics data analysis. Nat. Methods *17*, 869–870.

5. Hollenstein, D., and Hartl, M. (2025). MsReport. Preprint.

6. Ritchie, M.E., Phipson, B., Wu, D., Hu, Y., Law, C.W., Shi, W., and Smyth, G.K. (2015). limma powers differential expression analyses for RNA-sequencing and microarray studies. Nucleic Acids Res. *43*, e47.

7. Hollenstein, D., and Hartl, M. (2025). XlsxReport. Preprint.

8. Perez-Riverol, Y., Bai, J., Bandla, C., García-Seisdedos, D., Hewapathirana, S., Kamatchinathan, S., Kundu, D.J., Prakash, A., Frericks-Zipper, A., Eisenacher, M., et al. (2022). The PRIDE database resources in 2022: a hub for mass spectrometry-based proteomics evidences. Nucleic Acids Res. *50*, D543–D552.

9. Dorfer, V., Pichler, P., Stranzl, T., Stadlmann, J., Taus, T., Winkler, S., and Mechtler, K. (2014). MS Amanda, a universal identification algorithm optimized for high accuracy tandem mass spectra. J. Proteome Res. *13*, 3679–3684.

10. Taus, T., Köcher, T., Pichler, P., Paschke, C., Schmidt, A., Henrich, C., and Mechtler, K. (2011). Universal and confident phosphorylation site localization using phosphoRS. J. Proteome Res. *10*, 5354–5362.

11. Wang, H., Yang, H., Shivalila, C.S., Dawlaty, M.M., Cheng, A.W., Zhang, F., and Jaenisch, R. (2013). One-step generation of mice carrying mutations in multiple genes by CRISPR/Cas-mediated genome engineering. Cell *153*, 910–918.

12. Hein, M.Y., Hubner, N.C., Poser, I., Cox, J., Nagaraj, N., Toyoda, Y., Gak, I.A., Weisswange, I., Mansfeld, J., Buchholz, F., et al. (2015). A human interactome in three quantitative dimensions organized by stoichiometries and abundances. Cell *163*, 712–723.

13. Ran, F.A., Hsu, P.D., Wright, J., Agarwala, V., Scott, D.A., and Zhang, F. (2013). Genome engineering using the CRISPR-Cas9 system. Nat. Protoc. *8*, 2281–2308.

14. La Manno, G., Siletti, K., Furlan, A., Gyllborg, D., Vinsland, E., Mossi Albiach, A., Mattsson Langseth, C., Khven, I., Lederer, A.R., Dratva, L.M., et al. (2021). Molecular architecture of the developing mouse brain. Nature *596*, 92–96.

15. Johnson, J.L., Yaron, T.M., Huntsman, E.M., Kerelsky, A., Song, J., Regev, A., Lin, T.-Y., Liberatore, K., Cizin, D.M., Cohen, B.M., et al. (2023). An atlas of substrate specificities for the human serine/threonine kinome. Nature *613*, 759–766.

3.2 Establishing human brain organoids as a model to study MAST1

3.2.1 Preamble

MAST1 is known to have a restricted expression pattern, being predominantly expressed in post-mitotic neurons during mid-embryonic brain development. This presents a major challenge for MAST1 research, as neuronal cells are notoriously difficult to culture and manipulate. Moreover, since other protein interactors of MAST1, such as an activating cofactor, are likely to share similar expression patterns, the ability to perform future experiments in a relevant cellular context will be crucial.

One suitable *in vitro* model is human brain organoids. Brain organoids not only contain post-mitotic neurons but also model the embryonic developmental stages relevant to MAST1. First developed in 2013 [155], brain organoids have since been increasingly utilised in basic research, with protocols and technologies continually advancing to improve their usability [156].

To identify new MAST1 interactors in brain organoids, an AP-MS experiment similar to that described in Chapter 3.1.3 (Figure 1) could be performed. Since an activating cofactor may interact with MAST1's C-tail, binders of this region could be specifically probed by comparing proteins enriched with WT MAST1 and a C-tail truncation. However, expression of the desired constructs via plasmid transfection is largely ineffective in post-mitotic neurons, as plasmid DNA cannot traverse the nuclear envelope. This limitation can be circumvented by transfecting mature mRNA encoding the constructs. This chapter presents results from preliminary experiments to transfect organoids with *in vitro* transcribed mRNA.

3.2.2 Materials and Methods

Western blot

H9 dorsal organoids used for western blot were generously provided by the Knoblich lab. An organoid grown to day 80 and 1 million Neuro2A cells were snap-frozen and resuspended in lysis buffer (10 mM Tris pH 7.5, 150 mM NaCl, 0.1% SDS, 0.1% Triton X-100, 1% w/v sodium deoxycholate, 1x Sigma Protease Inhibitor Cocktail (P8849), 10 mM beta-glycerophosphate, 2 mM sodium pyrophosphate, 1 mM sodium orthovanadate, 50 mM NaF). Lysates were passed through a 25-gauge syringe and sonicated with three

pulses at low amplitude. Protein concentrations were determined with Qubit Protein Broad Range Assay Kit (A50669). 30 μg of lysate was prepared in loading dye (50 mM Tris pH 6.8, 2% SDS, 6% glycerol, 1% β-mercaptoethanol, 0.004% w/v bromophenol blue) and boiled at 95°C for 5 min. Samples were run on a 12% SDS-PAGE gel in Tris-Glycine SDS running buffer (25 mM Tris, 192 mM glycine, 0.1% SDS, pH 8.3) at 200 V for 55 min. The gel was blotted onto a 0.22 μm nitrocellulose membrane via wet transfer in transfer buffer (25 mM Tris, 192 mM glycine, 20% methanol) for 16 h at 30 V. The membrane was blocked with 5% w/v BSA in TBS-T for 1 h at RT. The membrane was incubated with primary antibody for 2 h at RT. The following antibodies were used: anti-SATB2 (Abcam, ab34735, 1:1000), anti-Tau (CST, #4019, 1:1000), anti-phospho-Tau (S214) (CST, #77348, 1:1000), and anti-ACTB (CST, #3700, 1:1000). The membrane was washed 3x with TBS-T and incubated with secondary antibody for 1 h at RT. The following secondary antibodies were used: 800CW goat anti-rabbit (LiCor, 926-32211, 1:15000), and 680RD goat anti-mouse (LiCor, 926-68070, 1:15000). The membrane was washed 3x with TBS-T and imaged on a LiCor Odyssey CLx fluorescent imager.

In vitro *transcription (IVT)*

The MAST1 sequence (residue 27-1064) was cloned into a pEGFP-C1 plasmid to make N-terminally tagged EGFP-MAST1 under a CMV promoter. IVT primers were designed to amplify EGFP alone or EGFP-MAST1 with the addition of 5' overhangs including a T7 promoter sequence followed by an AG initiation sequence and 5' UTR (Xenopus globin) sequence on the forward primer and 50x T's followed by a minimal 3' UTR (Xenopus globin) on the reverse primer. The full sequence of the primers are as follows, with lower case denoting the overhang and uppercase denoting binding nucleotides: T7AG_5'UTR_pEGFP_FWD: taatacgactcactataagcttgttctttttgcagaagctcagaataaacgctcaacttt-ggcagaTCGCCACCATGGTGAGCAAG, polyA_stop_MAST1_RVS: ttttttttttttttttttttttttttttttttt-tttttttttttttttttactttctttttattaggagcagatacgatggctacTTACCCAATCCGGATGGAAGTG, polyA_stop_EGFP_RVS: ttttttttttttttttttttttttttttttttttttttttttttttttttactttctttttattaggagcagata-cgatggctacTTACTTGTACAGCTCGTCCATGC.

EGFP-MAST1 was PCR amplified with Q5 polymerase (NEB #M0491) for 20 cycles and products were purified. 1 μg of the purified PCR products were used as a template for IVT. IVT was performed with HiScribe T7 mRNA Kit with CleanCap Reagent AG (NEB #E2080) according to manufacturer's instructions. Product mRNA was purified with

Monarch Spin RNA Cleanup Kit (NEB #T2040). A longer polyA tail was enzymatically added by mixing *E. coli* Poly(A) Polymerase (NEB #M0276) with 50 µg of purified mRNA according to manufacturer's instructions. Product mRNA was again purified with Monarch Spin RNA Cleanup Kit (NEB #T2040), then aliquoted and stored at -80°C. The mRNA was checked to be the correct length by mixing ~500 ng of mRNA with RNA loading dye (NEB #B0363) in a 1:1 ratio, denaturing it at 70°C for 10 min, and running it on a 1% agarose gel at 120 V for 20 min.

Transfection

H9 dorsal organoids to be transfected were generously provided by the Knoblich lab. Organoids grown to day 120 were cut into smaller pieces using a scalpel to increase the surface area to volume ratio (~8 small pieces from one organoid). Cut organoids were recovered for a week in fresh differentiation medium without shaking. Transfection was carried out in a 48-well plate with 4 organoid pieces per plate. Lipofectamine MessengerMax Transfection Reagent (Invitrogen #LMRNA) was used for transfection according to manufacturer's instructions, with 5 µg of mRNA in a total volume of 100 µL per transfection. Organoid pieces were transfected for 10 h then harvested for analysis.

Flow cytometry

One organoid piece from each transfection were transferred into tubes with a sterile glass bead and incubated on a thermoshaker (37°C, 1000 rpm) to dissociate them into single cell suspensions. The cells were spun at 300 g for 3 min, the supernatant removed, and cells resuspended in PBS. The cells were filtered through a 70 µm filter and analysed on the NovoCyte Penteon Flow Cytometer. Cells were gated for live cells, then single cells, then GFP positive cells using the mock-transfected cells to determine the gate boundary.

3.2.3 Results

Brain organoids can be grown from various starting cell lines and cultured under different conditions in order to model specific brain regions. To identify the protocol that produces organoids most optimal for MAST1 expression, we utilised the Vienna Brain Organoid Explorer, a web explorer allowing access to single-cell transcriptomics data of brain organoids grown from seven pluripotent cell lines, four protocols, and sampled over six time points [157]. MAST1 was found to be expressed widely across all cell types and

protocols, exhibiting a gradual increase in expression over time for the dorsal and striatum protocols while peaking in expression at day 40-80 for midbrain and ventral protocols (Figure 11A). Single-cell transcriptomics analysis revealed a widespread presence of MAST1, such as in regions representative of the dorsal and ventral forebrain, hindbrain, and striatum (Figure 11B-C).

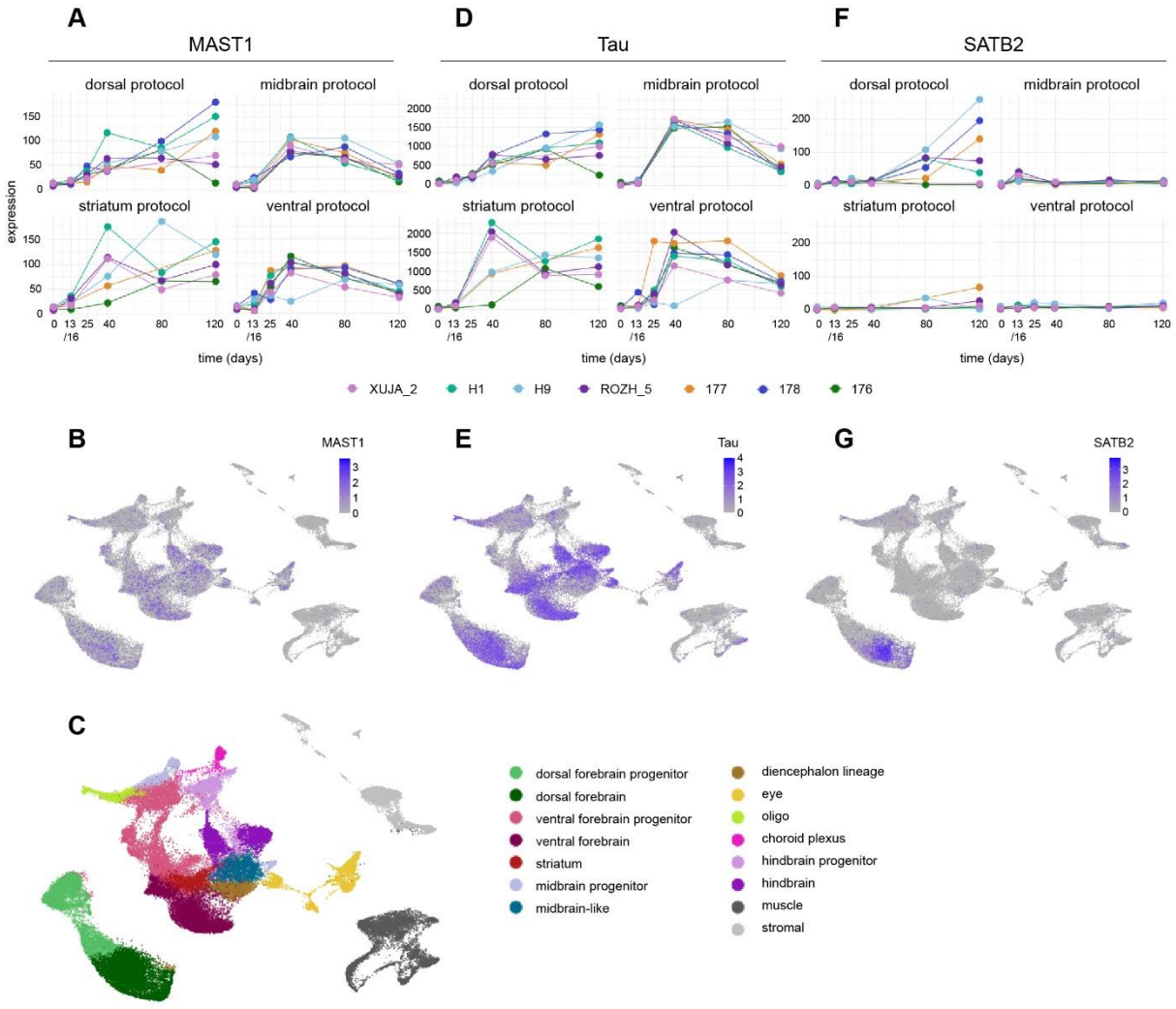

Figure 11. MAST1, Tau, and SATB2 exhibit overlapping expression in human brain organoids.

A-G. All figures are adapted from https://vienna-brain-organoid-explorer.vbc.ac.at/, all data from Naas et al., 2025 [157]. **A.** Relative expression levels of MAST1 in human brain organoids grown from seven cell lines with four protocols. **B.** MAST1 expression overlayed on UMAP of single-cell transcriptomics analysis of human brain organoids. **C.** UMAP of single-cell transcriptomics analysis of human brain organoids with cell type annotation for each cluster. **D.** Relative expression levels of Tau (MAPT) in human brain organoids grown from seven cell lines with four protocols. **E.** Tau (MAPT) expression overlayed on UMAP of single-cell transcriptomics analysis of human brain organoids. **F.** Relative expression levels of SATB2 in human brain organoids grown from seven cell lines with four protocols. **G.** SATB2 expression overlayed on UMAP of single-cell transcriptomics analysis of human brain organoids.

A proposed substrate for MAST1, Tau (Chapter 3.1.3, Figure 6), displays an almost identical temporal and cellular expression pattern across protocols (Figure 11D-E). SATB2, a marker for projection neurons destined to form the corpus callosum, was almost exclusively expressed in organoids grown under the dorsal protocol (Figure 11F-G). Similarly to MAST1 and Tau under the dorsal protocol, SATB2 expression increased over time with the highest expression at day 120 in H9 cells. Due to the relevance of MAST1 in corpus callosum development [58–61], we chose to continue with day 80-120 H9 dorsal organoids for further experiments.

To confirm the expression of SATB2 and Tau in these organoids, we assessed the lysate of day 80 H9 dorsal organoids by western blot. We additionally tested the lysate of Neuro2A cells, a neuroblastoma cell line commonly employed to model neurodevelopment. SATB2, which typically runs just below the 100 kDa marker, was detected in the organoid but not Neuro2A cells (Figure 12A), with the double band potentially representing different PTM states of SATB2 or antibody cross-reactivity with SATB1. Tau was strongly expressed in the organoid sample, while also not detected in Neuro2A cells (Figure 12A). Furthermore, Tau expressed in the organoids was found to be phosphorylated on S214 (Figure 12A), the candidate site of MAST1 phosphorylation (Chapter 3.1.3, Figure 6). MAST1 expression could not be confirmed due to a lack of a suitable antibody.

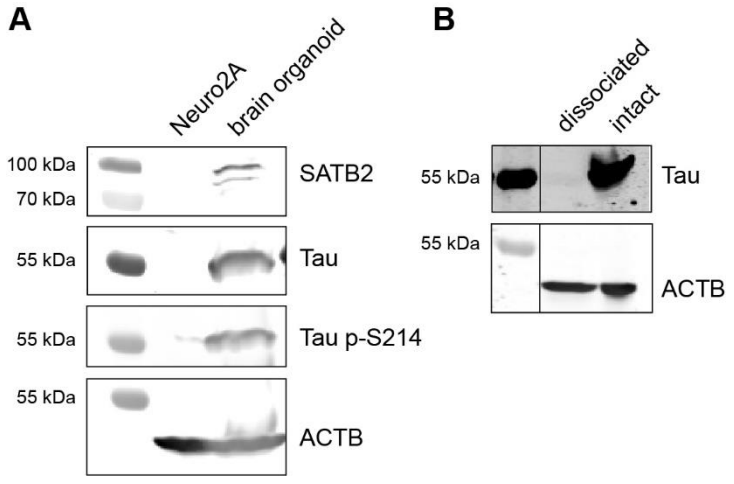

Figure 12. Intact human brain organoids express Tau phosphorylated on S214.

A. Western blot of Neuro2A and human brain organoid lysate, stained with antibodies against SATB2, Tau, phospho-Tau (S214), and ACTB. **B.** Western blot of dissociated and intact human brain organoids, stained with antibodies against Tau and ACTB.

We originally intended to dissociate the organoids into a single cell suspension, plate them, and transfect the 2D culture, to maximise the surface area of cells to be transfected. However, Tau expression was surprisingly lost following organoid

dissociation and plating (Figure 12B). Further transfection experiments were therefore carried out in intact organoids cut into smaller sections, to increase the surface area to volume ratio.

Four constructs were tested for day 120 H9 dorsal organoid transfection: EGFP alone (Figure 13A), EGFP-MAST1$^{27\text{-}1064}$ WT (Figure 13B), EGFP-MAST1$^{27\text{-}1064}$ D499N (kinase dead mutant) (Figure 13C), and EGFP-MAST1$^{27\text{-}1064}$ ΔC-tail (truncation construct lacking residues 691-742) (Figure 13D). Residue 27-1064 of MAST1 spans all three of its folded domains.

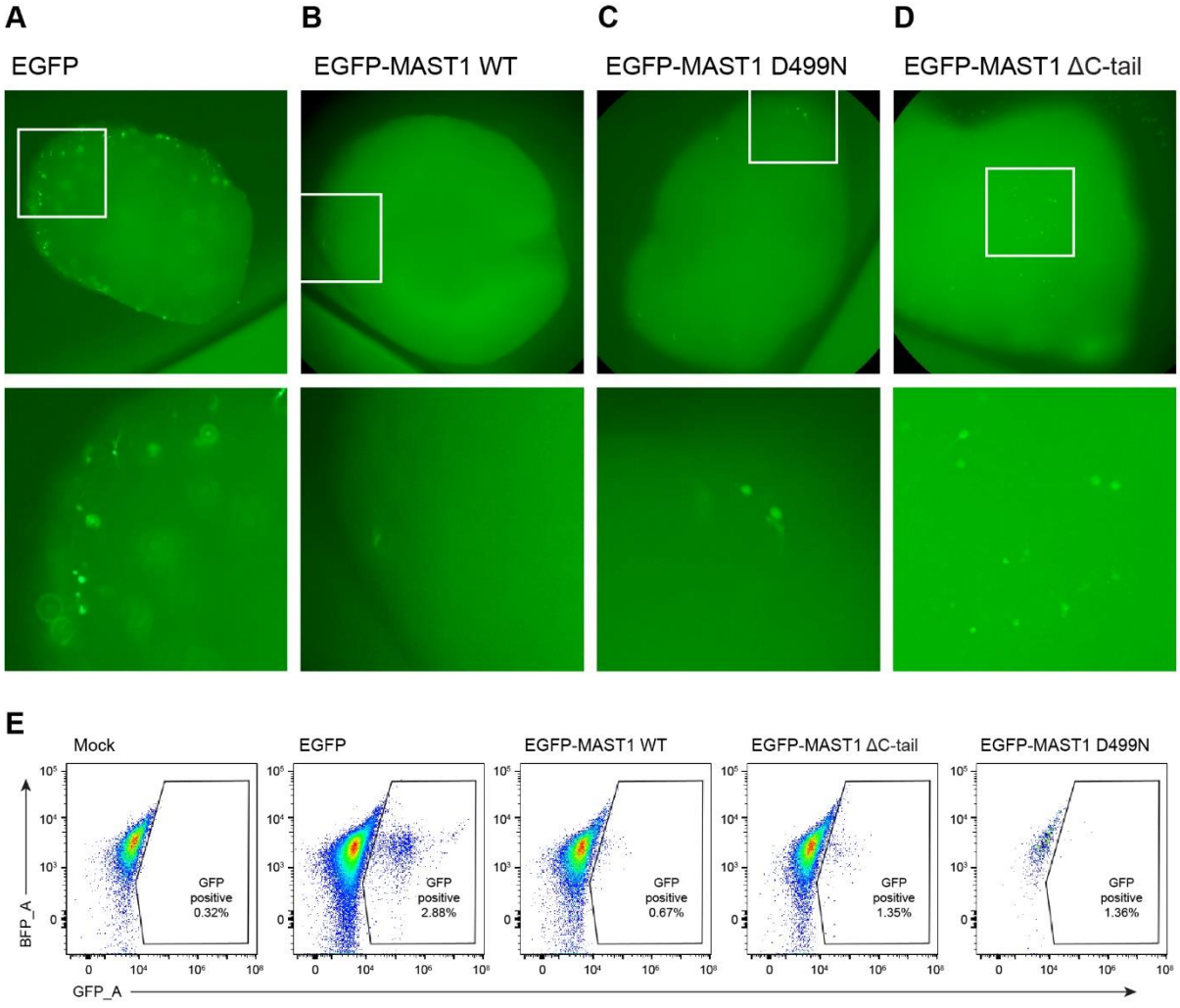

Figure 13. Intact human brain organoids can be transfected with EGFP-MAST1 with low efficiency.

A-D. Fluorescent images of human brain organoids transfected with EGFP alone (**A**), EGFP-MAST1$^{27\text{-}1064}$ WT (**B**), EGFP-MAST1$^{27\text{-}1064}$ D499N (**C**), and EGFP-MAST1$^{27\text{-}1064}$ ΔC tail (**D**). Region in white square is shown as a close-up below. **E.** Flow cytometry analysis of transfected organoids to measure percentage of GFP positive cells.

The transfected organoids were dissociated after 10 hours, and the transfection efficiency, measured as a percentage of GFP positive cells, was analysed by flow cytometry. EGFP alone achieved the highest transfection efficiency of approximately 2.9%, while all EGFP-MAST1 constructs had much lower efficiencies ranging from 0.7-1.4% (Figure 13E). Notably, both the D499N and ΔC-tail constructs resulted in a higher percentage of GFP-positive cells than the WT construct. Since the D499N mutation and ΔC-tail truncation both render the MAST1 kinase inactive, we hypothesise that MAST1 kinase activity may be causing protein turnover of the WT construct. While significant improvements to the transfection efficiency must be made to produce enough bait material for AP-MS, the higher efficiencies observed for both kinase dead constructs is a promising indication that the organoids provide a cellular environment permissive of MAST1 activity. Alternatively, a cell-free pull down could be performed to avoid transfection altogether, by mixing the lysate of organoids with immobilised, purified MAST1 as the bait, although this approach lacks the native subcellular organisation and compartmentalisation present in intact cells.

In short, we have found that intact H9 dorsal organoids, grown for 80-120 days, possess the ideal cellular context for further MAST1 studies. While intact organoids can be transfected with mature IVT mRNA, the efficiency is currently too low to produce enough material for downstream applications. Efforts to improve the transfection of organoids would hugely benefit the future of MAST1 research.

3.3 Structure and regulation of the myotonic dystrophy kinase-related Cdc42-binding kinase

3.3.1 Preamble

The DMPK family are key regulators of the actin cytoskeleton. They are known to phosphorylate both myosin light chain 2 (MLC2), a component of non-muscle myosin II, and myosin phosphatase target subunit 1 (MYPT1). The DMPK kinases are associated with numerous biological processes such as cell protrusion, neurite outgrowth, and cytokinesis. One member of the DMPK family, MRCK, plays a key role in apical constriction in *C. elegans* during gastrulation, and localises via GTP-bound cell division control protein 42 (Cdc42) to the plasma membrane. However, the regulation of MRCK kinase activity and its membrane-binding properties are not fully understood.

In this study, the crystal structure of the regulatory domains of *C. elegans* MRCK1, as well as the low-resolution structure of full length MRCK1 was determined, where it exhibited an elongated conformation of its coiled-coil domain with its kinase and regulatory domains on either end. MRCK1's ability to bind various membrane lipids as well as active Cdc42 was assessed *in vitro*. We propose that MRCK1's coiled-coil domain acts as a molecular ruler, positioning its kinase domain at a fixed distance from the membrane and restricting MRCK activity to a specific local pool of substrates in the actin cortex.

This work has been published by Structure in 2023.

3.3.2 Contribution statement

I contributed to this publication by performing all revision experiments after the initial submission. This includes purification of recombinant proteins, kinase assays, mass photometry, and liposome pelleting experiments.

3.3.3 Publication

Truebestein L., Antonioli S., Waltenberger E., Gehin C., Gavin A.C., Leonard T.A. (2023) Structure and regulation of the myotonic dystrophy kinase-related Cdc42-binding kinase. *Structure* 31 (4): 435-446.

Article

Structure

Structure and regulation of the myotonic dystrophy kinase-related Cdc42-binding kinase

Graphical abstract

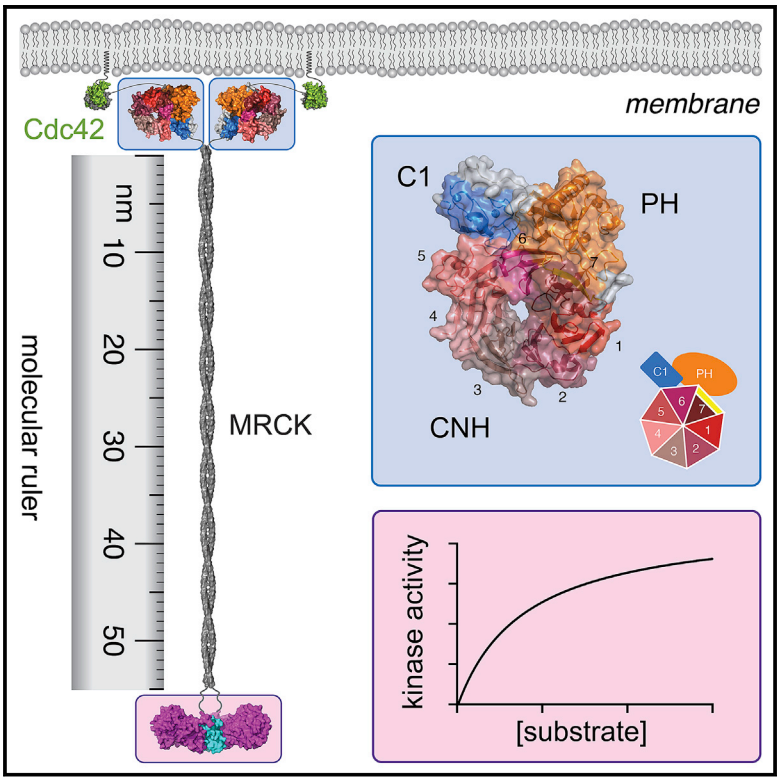

Highlights

- Electron microscopy of recombinant MRCK1 reveals an extended conformation
- Structure of membrane-binding domains reveals a composite tripartite architecture
- Coiled-coil domains of DMPK kinases act as molecular rulers to restrict activity

Authors

Linda Truebestein, Sumire Antonioli, Elisabeth Waltenberger, Charlotte Gehin, Anne-Claude Gavin, Thomas A. Leonard

Correspondence

thomas.leonard@meduniwien.ac.at

In brief

Truebestein et al. determined structures of full-length MRCK1 and its membrane-binding domains by electron microscopy and X-ray crystallography, respectively. They characterized the binding of MRCK1 to model membranes and Cdc42 *in vitro*. They propose a model by which the DMPK kinases, which also include ROCK, CRIK, and DMPK, are regulated.

Truebestein et al., 2023, Structure *31*, 435–446
April 6, 2023
https://doi.org/10.1016/j.str.2023.02.002

CellPress

Structure

CellPress
OPEN ACCESS

Article

Structure and regulation of the myotonic dystrophy kinase-related Cdc42-binding kinase

Linda Truebestein,[1,2] Sumire Antonioli,[1,2,3] Elisabeth Waltenberger,[1,2] Charlotte Gehin,[4,5] Anne-Claude Gavin,[4,6] and Thomas A. Leonard[1,2,7,*]

[1]Department of Structural and Computational Biology, Max Perutz Labs, Campus Vienna Biocenter 5, 1030 Vienna, Austria
[2]Department of Medical Biochemistry, Medical University of Vienna, 1090 Vienna, Austria
[3]Vienna BioCenter PhD Program, Doctoral School of the University of Vienna and Medical University of Vienna, 1030 Vienna, Austria
[4]European Molecular Biology Laboratory, EMBL, Meyerhofstrasse 1, 69117 Heidelberg, Germany
[5]École Polytechnique Fédérale de Lausanne (EPFL), AI 1108, Station 19, 1015 Lausanne, Switzerland
[6]University of Geneva, Department of Cell Physiology and Metabolism, CMU Rue Michel-Servet 1, 1211 Genève 4, Switzerland
[7]Lead contact
*Correspondence: thomas.leonard@meduniwien.ac.at
https://doi.org/10.1016/j.str.2023.02.002

SUMMARY

Protein kinases of the dystonia myotonica protein kinase (DMPK) family are critical regulators of actomyosin contractility in cells. The DMPK kinase MRCK1 is required for the activation of myosin, leading to the development of cortical tension, apical constriction, and early gastrulation. Here, we present the structure, conformation, and membrane-binding properties of *Caenorhabditis elegans* MRCK1. MRCK1 forms a homodimer with N-terminal kinase domains, a parallel coiled coil of 55 nm, and a C-terminal tripartite module of C1, pleckstrin homology (PH), and citron homology (CNH) domains. We report the high-resolution structure of the membrane-binding C1-PH-CNH module of MRCK1 and, using high-throughput and conventional liposome-binding assays, determine its binding to specific phospholipids. We further characterize the interaction of the C-terminal CRIB motif with Cdc42. The length of the coiled-coil domain of DMPK kinases is remarkably conserved over millions of years of evolution, suggesting that they may function as molecular rulers to position kinase activity at a fixed distance from the membrane.

INTRODUCTION

Cell shape remodeling and cell movement are necessary for physiological processes such as fertilization, cell division, and the morphogenesis and motility of intracellular organelles, as well as pathophysiological processes such as the phagocytosis of invading pathogens, cancer cell invasion, and metastasis. These changes in cell shape and motility are accomplished primarily by the contraction of actomyosin filaments within the actin cytoskeleton.[1]

In order for cells to adopt defined shapes and be capable of directed movement, the contractile machinery must be exquisitely regulated. At the heart of this regulation is the control of myosin II activity by phosphorylation of its regulatory light chain (RMLC/MLC2). Phosphorylation of two conserved residues in the N terminus of MLC2 stimulates the ATPase activity of myosin, leading to actomyosin contraction.[2] MLC2 is phosphorylated by myosin light-chain kinase (MLCK)[3] and dephosphorylated by myosin light-chain phosphatase (MLCP).[4–6]

The dystonia myotonica protein kinase (DMPK) family, comprising citron Rho-interacting kinase (CRIK), myotonic dystrophy protein kinase (DMPK), myotonic dystrophy kinase-related Cdc42-binding kinase (MRCK), and Rho-associated coiled-coil kinase (ROCK), are known regulators of MLC2 phosphorylation. *In vitro*, ROCK and MRCK are capable of directly phosphorylating MLC2[7–9] but primarily exert their effects *in vivo* via the inhibitory phosphorylation of MLCP.[10–12] As such, they play key roles in cytoskeletal remodeling and have been implicated in diverse cellular processes from cell protrusion,[9] neurite outgrowth,[13] and cytokinesis[14] to embryonic elongation,[15,16] nuclear positioning,[17] and establishment of epithelial polarity.[18,19] Triplet expansion of the DMPK1 gene is causative of autosomal dominant muscular dystrophy 1,[20–22] while ROCK and MRCK have been shown to play essential roles in neural tube closure during embryonic development,[23] as well as cancer cell invasion and metastasis.[10,24,25]

The DMPK kinases are members of the AGC kinase family with a conserved domain architecture of N-terminal kinase domains followed by a predicted coiled-coil domain and C-terminal regulatory domains that mediate a variety of protein-protein and protein-membrane interactions. While many AGC kinases are regulated by phosphorylation of motifs in their activation loop or C-terminal tail,[26] the DMPK kinases are not. Instead, their N-terminal capped-helix bundle (CHB) domain cooperates with the C-terminal tail to maintain the kinase domain in a homodimeric, active conformation with an ordered activation

loop.[27–29] Plasma membrane localization of ROCK and CRIK is reported to be driven by RhoA,[14,30] while Cdc42 mediates the recruitment of MRCK.[9] DMPK1, which is almost exclusively expressed in skeletal and cardiac muscle,[31] is presumably anchored to the membrane via its predicted C-terminal transmembrane domain. While a recent study of ROCK2 suggested that its activity is regulated by a combination of its subcellular localization and the length of its coiled-coil domain,[7] the mechanisms by which other DMPK kinases are regulated are still largely unknown.

The nematode worm *Caenorhabditis elegans* encodes a single *mrck* gene (*mrck-1*), with closest homology to human MRCKα. MRCK1 has been shown to be essential for apical constriction during gastrulation in *C. elegans*[15] and is localized to the apical membrane by activated, GTP-bound Cdc42, where it drives actomyosin contractility via increased phosphorylation of MLC2. Conversely, Cdc42 is locally inactivated on the basolateral membrane, thereby inhibiting the recruitment of MRCK. To better understand how MRCK1 is localized and how its activity is regulated, we have determined the low-resolution structure and conformation of full-length MRCK1 as well as the high-resolution structure of its regulatory domains. Using diverse membrane-binding assays, we have determined which lipids can be recognized by MRCK1 at the membrane surface. Finally, we have quantified MRCK1 binding to active Cdc42 *in vitro*. We propose a model in which MRCK1 is recruited to the apical membrane by the coincident recognition of membrane lipids and active Cdc42, which serve to position its kinase domains at the end of its coiled-coil domain at a fixed distance from the membrane. Bioinformatic analysis reveals remarkable conservation of the lengths of the coiled coils of all DMPK kinase family members, thereby extending the concept of the coiled-coil domain as a "molecular ruler" capable of governing protein kinase signaling and actomyosin contraction at precise subcellular locations.

RESULTS

Full-length MRCK1 adopts a ROCK-like extended, active conformation

C. elegans MRCK1 consists of an N-terminal CHB domain that mediates kinase domain dimerization,[28] followed by a region of predicted coiled-coil and C-terminal C1, pleckstrin homology (PH), and citron homology (CNH) domains of unknown structure and function (Figure 1A). A Cdc42 and Rac-interactive binding (CRIB) motif is encoded C-terminally to the CNH domain. Bioinformatic analysis of the coiled-coil domain revealed that, despite variation in the length of the sequence between the N-terminal kinase domain and C-terminal regulatory domains (Figure 1B), the length of the predicted coiled-coil domain is remarkably well conserved (Figure S1A), reminiscent of the strict length conservation in the related ROCK kinases.[7,32] To investigate the structure and conformation of a full-length MRCK protein, we purified recombinant *C. elegans* MRCK1 from baculovirus-infected Sf9 insect cells to homogeneity. We confirmed the correct mass of the purified protein by mass spectrometry (Figure S1B) and the mass and dimeric stoichiometry of MRCK1 particles by mass photometry (Figure S1C). MRCK1 exhibited robust kinase activity against recombinant myosin light chain 2 (MLC2), the regulatory subunit of myosin (Figure 1C). Purified MRCK1 was imaged by rotary shadowing electron microscopy, revealing an extended particle, 70–85 nm in length, comprising globular regions of electron density at either end of a long, semi-rigid coiled-coil domain with an average length of 55.0 ± 7.2 nm (Figure 1D). Dimeric ROCK2 particles exhibit comparable barbell-shaped structures with a length of 106.7 ± 3.5 nm (Figure 1E), corresponding to the length of predicted coiled-coil between its N-terminal kinase and C-terminal regulatory domains.[7] The length of the coiled-coil domain of ROCK2 is highly conserved over 650 million years of evolution and has been shown to be important for stress fiber formation in cells.[7] While the number of intervening amino acids in MRCK1 would predict a canonical, uninterrupted coiled coil of 78.1 nm, we observed a shorter mean distribution of particle lengths and a bigger fluctuation from the mean than in ROCK2 (Figure 1F). *In silico* prediction of the coiled-coil propensity of the intervening amino acids revealed four segments of coiled coil with a total predicted length of 54.6 nm (Figure S1A). The structural explanation for why full-length MRCK1 dimers are considerably shorter than expected (taking into account regions of predicted disorder) is not obvious and will likely require further investigation, though the predicted coiled-coil length of ~55 nm (Figure S1A) is conserved over 650 million years and corresponds to the mean length observed.

Structure and properties of the C1-PH-CNH module of MRCK1

The C terminus of MRCK contains predicted C1, PH, and CNH domains of unknown structure and function. To shed light on the function of this regulatory module, we determined the structure of a construct of MRCK1 comprising residues 955–1,534 by X-ray crystallography. The protein crystallized in space group P1 with 5 molecules per asymmetric unit and crystals diffracted to 2.14 Å. Efforts to determine the structure either by molecular replacement, multiple isomorphous replacement, or anomalous dispersion were unsuccessful. The structure was eventually solved by molecular replacement with residues 955–1,534 of the AlphaFold structure prediction for MRCK1.[33] The final, experimentally determined model of MRCK1 955–1,534 exhibits a root-mean-square deviation from the AlphaFold prediction of just 0.906 Å over all atoms (Figure S2A). This demonstrates the power of AlphaFold to predict not just protein structures but intramolecular assemblies of domains from pure co-evolutionary variance.[34]

The structure of the C-terminal module of MRCK1 (Figure 2A) reveals an intimate association of the C1, PH, and CNH domains. The 5 copies in the asymmetric unit are near identical, exhibiting root-mean-square deviations of 0.249–0.494 Å over all main-chain C_α atoms. The C1 domain is held together by two zinc ions and makes extensive contacts with both the PH and CNH domains. The assignment of zinc ions was made on the basis of the known tetrahedral coordination of zinc by the two C3H1 zinc finger motifs of homologous C1 domains,[35,36] and refinement of these sites perfectly accounts for the observed scattering. The PH domain is distinguished from homologous PH domains by a loop insertion between strands β6 and β7 that packs against the CNH domain (Figure S2B). The CNH domain forms a 7-bladed beta propeller with strongest homology to the CNH domain of yeast Rho1.[37] The CNH domain is

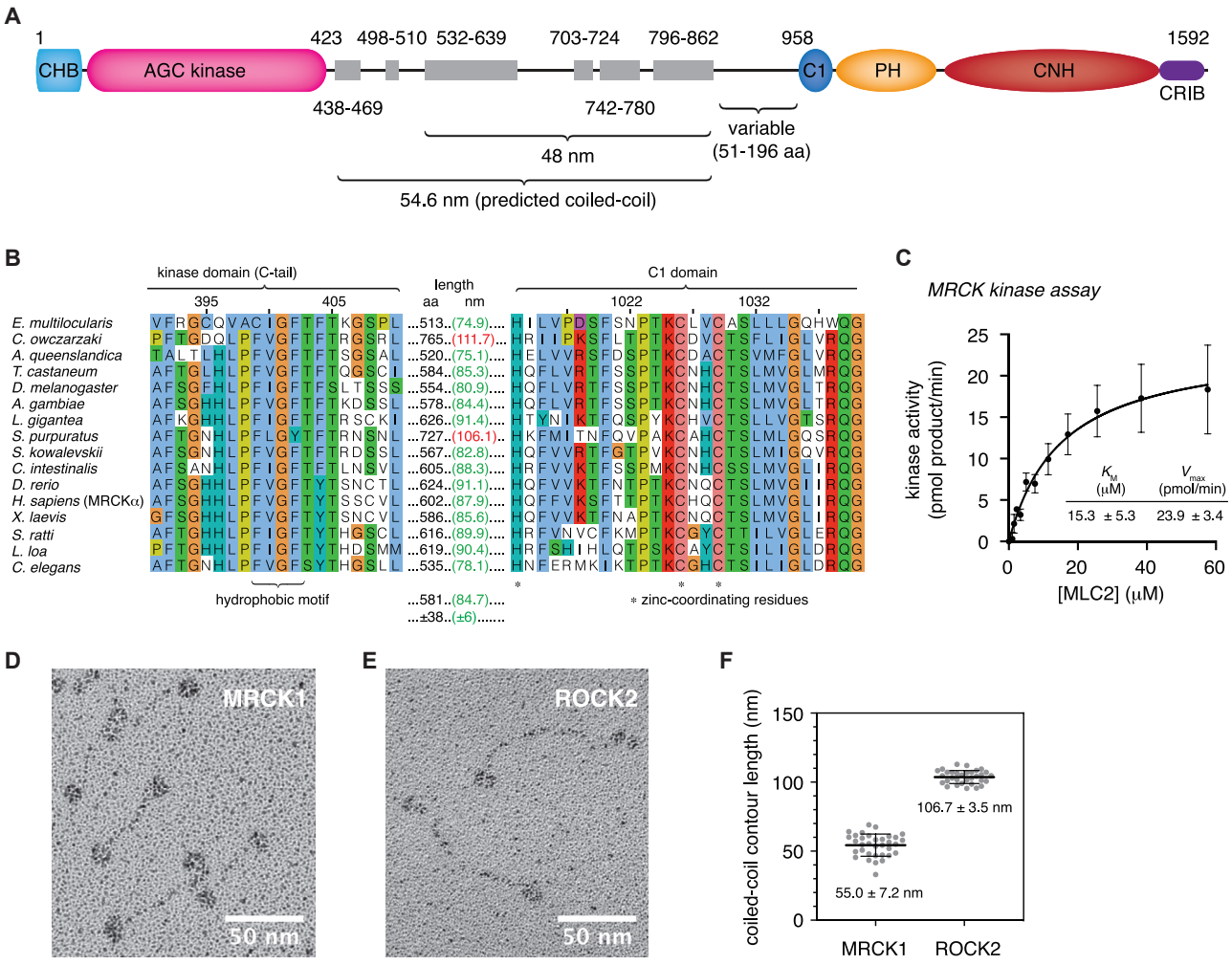

Figure 1. Full-length MRCK1 adopts a ROCK-like extended, active conformation

(A) Domain architecture of *C. elegans* MRCK1 (CHB, capped helix bundle domain; C1, protein kinase C conserved domain 1; PH, pleckstrin homology domain; CNH, citron homology domain; CRIB, Cdc42 and Rac-interactive binding domain).

(B) Partial sequence alignment of MRCK orthologs. The length of the intervening sequence between the end of the kinase domain and the beginning of the C1 domain is indicated as number of amino acids (black) and predicted length of a canonical parallel coiled-coil (green) (assuming continuous parallel coiled coil with a pitch of 1.48 Å/residue).

(C) MRCK1 kinase activity against recombinant MLC2. Data are fitted with the Michaelis-Menten equation (n = 3). Data are represented as mean ± SEM.

(D) Rotary shadowing electron microscopy of full-length *C. elegans* MRCK1. Scale bar: 50 nm.

(E) Rotary shadowing electron microscopy of full-length *Homo sapiens* ROCK2. Scale bar: 50 nm.

(F) Contour length distribution of the coiled-coil domain of MRCK1 and ROCK2. Data are represented as mean ± SEM.

held together by a beta strand contributed by the linker between the PH domain and blade 1 of the beta propeller (Figure 2B, yellow) and the C terminus of the construct (Figure 2A, dark brown), which together form blade 7. The buried surface area in the interface between the C1-PH and CNH modules of the complex is 1,998 Å^2, with a solvation free energy of −14.9 kcal/mol,[38] indicating that this is a stable association of the three domains. This is also consistent with failed efforts to purify the isolated CNH domain.

Surface conservation analysis revealed that the C1-PH-CNH module exhibits conservation on the composite surface formed by the C1 and PH domains but surprisingly little elsewhere (Figure S2C, top view). Surface electrostatic potential analysis[39] revealed that this surface is predominantly hydrophobic in nature (Figure S2D), perhaps indicative of a role in a hereto uncharacterized protein-protein or protein-membrane interaction. Analysis of the structure with PDBePISA (Proteins, Interfaces, Structures and Assemblies)[40,41] revealed no predicted quaternary assemblies of the C1-PH-CNH module in the crystal lattice.

C1 domains are so called due to their homology to the first conserved domain of protein kinase C (PKC) and are divided into two groups: typical C1 domains that bind the neutral lipid diacylglycerol (DAG) and atypical C1 domains that do not.[42] Those C1 domains that bind DAG do so via a cleft formed by unzipped beta strands in which a hydrogen bond network

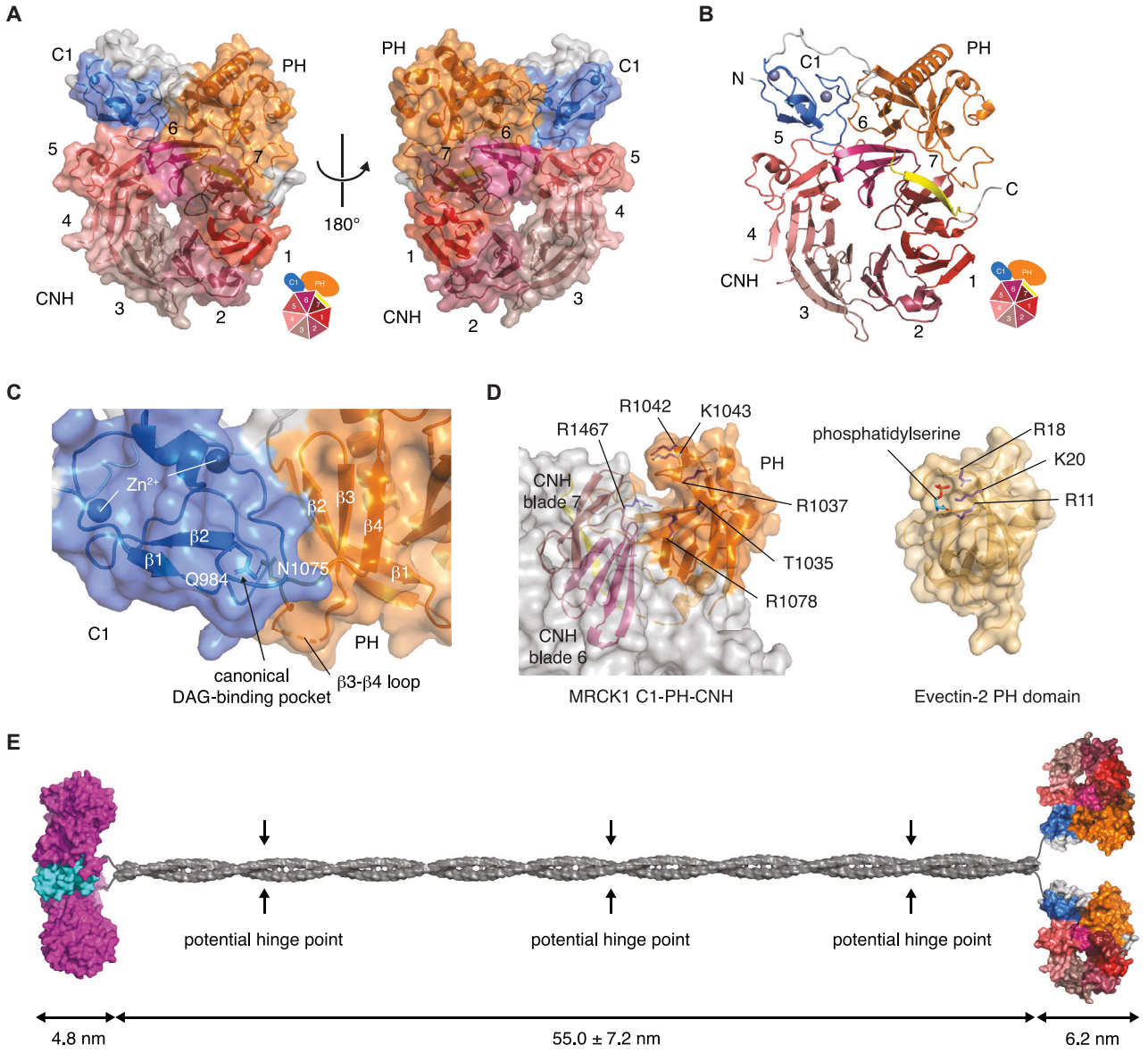

Figure 2. Structure and properties of the C1-PH-CNH module of MRCK1

(A) Structure of the C1-PH-CNH module of *C. elegans* MRCK1 (C1, blue; PH, orange; CNH, shades of red). The seven blades of the CNH domain beta propeller are indicated in order.

(B) Topology of the CNH domain beta propeller. The last beta strand of blade 7 (yellow) is contributed by the linker between the PH domain and blade 1 of the CNH domain. The remaining beta strands of blade 7 are contributed by the C terminus of the CNH domain.

(C) Occlusion of the DAG binding pocket of the C1 domain by the β3-β4 loop of the PH domain.

(D) Side-by-side comparison of the PH domain of Evectin-2 (PDB: 3AJ4) bound to phosphatidylserine (PS) with the C1-PH-CNH domains of MRCK1. Conserved basic residues in the β1-β2 loop of the MRCK1 PH domain are shown in blue sticks. Basic residues coordinating PS in the Evectin-2 PH domain are also shown in blue sticks.

(E) Composite model of MRCK1 based on the coordinates of the kinase domain of MRCKα, a canonical coiled coil of 55 nm (modeled on the basis of the electron microscopy analysis of MRCK1), and the structure of the C1-PH-CNH module reported in this study. Arrows indicate predicted discontinuities/breaks in the coiled-coil domain that may permit some structural flexibility.

involving conserved glycine and glutamine residues in the cleft is critical for binding the 3′ hydroxyl head group of DAG.[43] While MRCK and CRIK orthologs all exhibit conservation of this glutamine (Gln984), the putative DAG binding cleft is obscured by a loop between strands β3 and β4 of the PH domain in the structure of MRCK1 (Figure 2C). Within this loop, Asn1075 inserts its side chain into the cleft and makes a hydrogen bond with Gln984. B-factor analysis of the tripartite interface between the C1 domain, the linker between blades 5 and 6 of the CNH domain, and the PH domain indicates a well-ordered interface (Figure S2E), although sequence conservation in the β3-β4 loop of the PH domain is poor (Figure S2C). This raises obvious

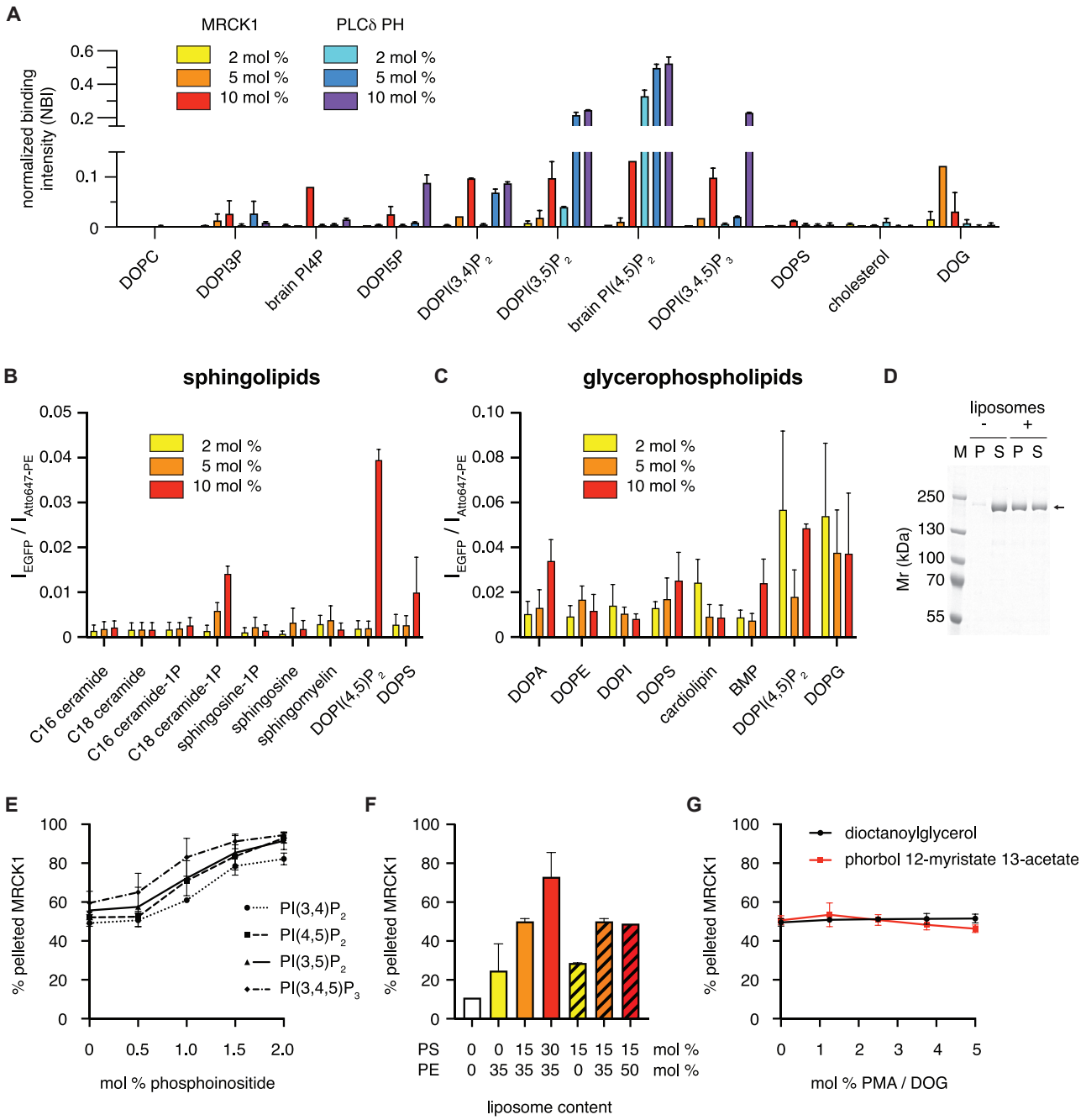

Figure 3. Membrane-binding properties of the C1-PH-CNH module of MRCK1

(A) Normalized binding of MRCK1$^{955-1534}$-EGFP (C1-PH-CNH) to liposomes containing the indicated lipid species in a high-throughput LiMA assay. Binding was quantified as the ratio of MRCK1$^{955-1534}$-EGFP to Atto647-conjugated phosphatidylethanolamine incorporated into the liposomes. MRCK1 binding to each lipid was evaluated with three different concentrations of signaling lipid, yellow (2 mol %), orange (5 mol %), and red (10 mol %), and compared with the PH domain of PLCδ, which binds specifically to PI(4,5)P_2 and was used as a positive control, cyan (2 mol %), blue (5 mol %), and purple (10 mol %). Data are represented as mean ± SEM.

(B) Normalized binding of MRCK1$^{955-1534}$-EGFP to sphingolipids. Data are derived from LiMA assay. Note that the scale on the y axis is not the same as in (A). Data are represented as mean ± SEM.

(C) Normalized binding of MRCK1$^{955-1534}$-EGFP to glycerophospholipids. Data are derived from LiMA assay. Note that the scale on the y axis is not the same as in (A). Data are represented as mean ± SEM.

(D) MRCK1^{FL} pelleting assay with and without liposomes. P, pellet; S, supernatant. Arrow indicates 180.7 kDa MRCK1 protein. MRCK1 exhibited approximately 50% binding to liposomes at 1 mM total lipid concentration.

(legend continued on next page)

questions regarding the conformation of the loop in solution and whether the cleft of the C1 domain is accessible.[44]

Since MRCK has been heavily implicated in the regulation of cytoskeletal processes beneath the plasma membrane and interacts with the membrane-associated small GTPase Cdc42, it is conceivable that its PH domain might be a membrane-interacting domain with specificity for phospholipids. While superposition of the PH domain of Akt1 bound to inositol-1,3,4,5-tetrakisphosphate (IP_4) reveals steric clashes with all four phosphate groups of the ligand, superposition of the PH domain of Evectin-2 bound to phosphatidylserine (PS) reveals fewer clashes (Figure 2D). Interestingly, loop residues 1,037–1,045 between strands β1 and β2 of the MRCK PH domain, which exhibit high B-factors, show remarkable sequence conservation among MRCK orthologs, including four basic residues (Figures 2D and S2F). Blade 7 of the CNH domain contributes an additional basic residue (Arg1467) at the base of the pocket (Figure 2D). While the β1-β2 loop corresponds to residues 11–19 of the Evectin-2 PH domain, which participate in specific interactions with the head group of PS,[44] none of the basic residues involved in coordinating the phosphate group are conserved in their 3-dimensional positions. It is perhaps interesting to note, however, that while Arg11 of Evectin-2 corresponds to Thr1035 in MRCK1, Arg1078 from the β3-β4 loop of the PH domain projects its guanidinium head group into almost precisely the same position (Figure 2D). Finally, it is worth noting that the β3-β4 loop of the PH domain that inserts Asn1075 into the cleft of the C1 domain forms a surface immediately adjacent to the putative phospholipid binding β1-β2 loop. As such, binding of a ligand to the C1 domain would necessarily displace the β3-β4 loop of the PH domain and potentially impact the properties of the phospholipid-binding pocket.

In summary, the C1-PH-CNH module of MRCK1 forms a globular structure in which the putative membrane-binding surfaces of the C1 and PH domains are co-aligned. The role of the CNH domain is not clear from the structure but presumably facilitates additional protein-protein interactions or protein-membrane interactions that localize MRCK activity to the appropriate subcellular compartment. By combining the electron microscopy images of full-length MRCK1 (Figure 1D) and the high-resolution structure of the regulatory domains (Figure 2A) with the structure of the dimeric kinase domains of human MRCKα (PDB: 4AW2; unpublished data), we propose a composite high-resolution model of MRCK1 in which the kinase and regulatory domains are linked by a coiled coil of 55 nm (Figure 2E). While the model depicts a continuous coiled coil and the electron micrographs depict a semi-rigid, extended coiled-coil domain, predicted discontinuities in the coiled coil (Figure S1A) may introduce "hinges" that could permit some flexibility.

Membrane-binding properties of the C1-PH-CNH module of MRCK1

To investigate the membrane lipids specifically recognized by MRCK1, we probed the interaction of its regulatory module C1-PH-CNH with membrane surrogates containing various combinations of lipids in a systematic manner using the high-throughput liposome microarray assay (LiMA).[45,46] In parallel, we probed the binding of the PH domain of phospholipase C (PLC) δ as a control of membrane binding specificity.[47] Membrane binding was quantified by determining the ratio of fluorescent protein to that of Atto647-conjugated phosphatidylethanolamine (Atto647-PE) contained in liposomes. In this context, we observed that $MRCK1^{955-1534}$-EGFP bound preferentially to di- and tris-phosphorylated phosphoinositides (PIPs) over mono-phosphorylated PIPs in a dose-dependent manner, as well as to C18 ceramide-1-phosphate, but to a lesser extent (Figures 3A–3C).

To validate the LiMA assay, we performed conventional liposome pelleting assays using a lipid composition that mimics the plasma membrane and was previously optimized for the binding of Akt1 to $PI(3,4,5)P_3$.[48] The lipid mixture contains 15 mol % PS, previously reported to be important for MRCKα/β binding to DAG and phorbol esters.[49] We supplemented these liposomes with increasing concentrations of di- and tris-phosphorylated PIPs at the expense of PC and measured the binding of full-length MRCK1 by sedimentation. We confirmed that MRCK1 binds to liposomes and does not sediment in their absence (Figure 3D). We reproducibly observed increased MRCK1 binding to $PI(3,4)P_2$, $PI(4,5)P_2$, $PI(3,5)P_2$, and $PI(3,4,5)P_3$ but no significant difference in the strength of binding (Figure 3E). Since PIPs modified with two phosphate groups project those groups on different sides of the inositol ring, this implied a lack of specificity in binding. Therefore, to explore whether the increased binding was due to an increase in negative charge density, we measured the binding of MRCK1 to liposomes containing increasing concentrations of PS. MRCK1 binding was increased from 25% to 75% by the inclusion of up to 30 mol % PS (Figure 3F), suggesting that MRCK1 may recognize PS. Finally, we probed the binding of MRCK1 to DAG and the DAG-mimetic phorbol 12-myristate, 13-acetate (PMA). We could not detect any significant binding of MRCK1 to liposomes containing 0–5 mol % of either DAG or PMA (Figure 3G) above the baseline binding of ~50% (Figure 3D).

In vivo, the specific targeting of MRCK1 to apical membranes may be explained by two additional factors: while $MRCK1^{955-1534}$ is monomeric in solution, full-length MRCK1 is a dimer, which doubles the membrane interacting surface; secondly, MRCK1, like all MRCK orthologs, encodes a CRIB domain C-terminal to its CNH domain (Figures 1A and 4A). It is therefore likely that membrane-associated MRCK is tethered via a set of polyvalent interactions, including binding to two copies of membrane-anchored Cdc42. To determine the affinity of MRCK1 for Cdc42, we expressed a C-terminally truncated Cdc42 lacking its geranylgeranylation motif in *Escherichia coli* and purified it to homogeneity. The mass of the recombinant protein was confirmed by intact, denaturing mass spectrometry (Figure S3A). Using the same protocol as we previously reported for RhoA,[7] we loaded Cdc42 with either guanosine 5′-diphosphate (GDP) or the non-hydrolyzable GTP analog guanosine 5'-[(β,γ)-imido]

(E) Binding of $MRCK1^{FL}$ to liposomes with 0%–2% di- and tris-phosphorylated phosphoinositides, quantified by densitometry, n = 2. Data are represented as mean ± SEM.
(F) Binding of $MRCK1^{FL}$ to liposomes with increasing concentrations of PS and PE, quantified by densitometry, n = 2. Data are represented as mean ± SEM.
(G) Binding of $MRCK1^{FL}$ to liposomes with 0%–5% DOG and PMA, quantified by densitometry, n = 3. Data are represented as mean ± SEM.

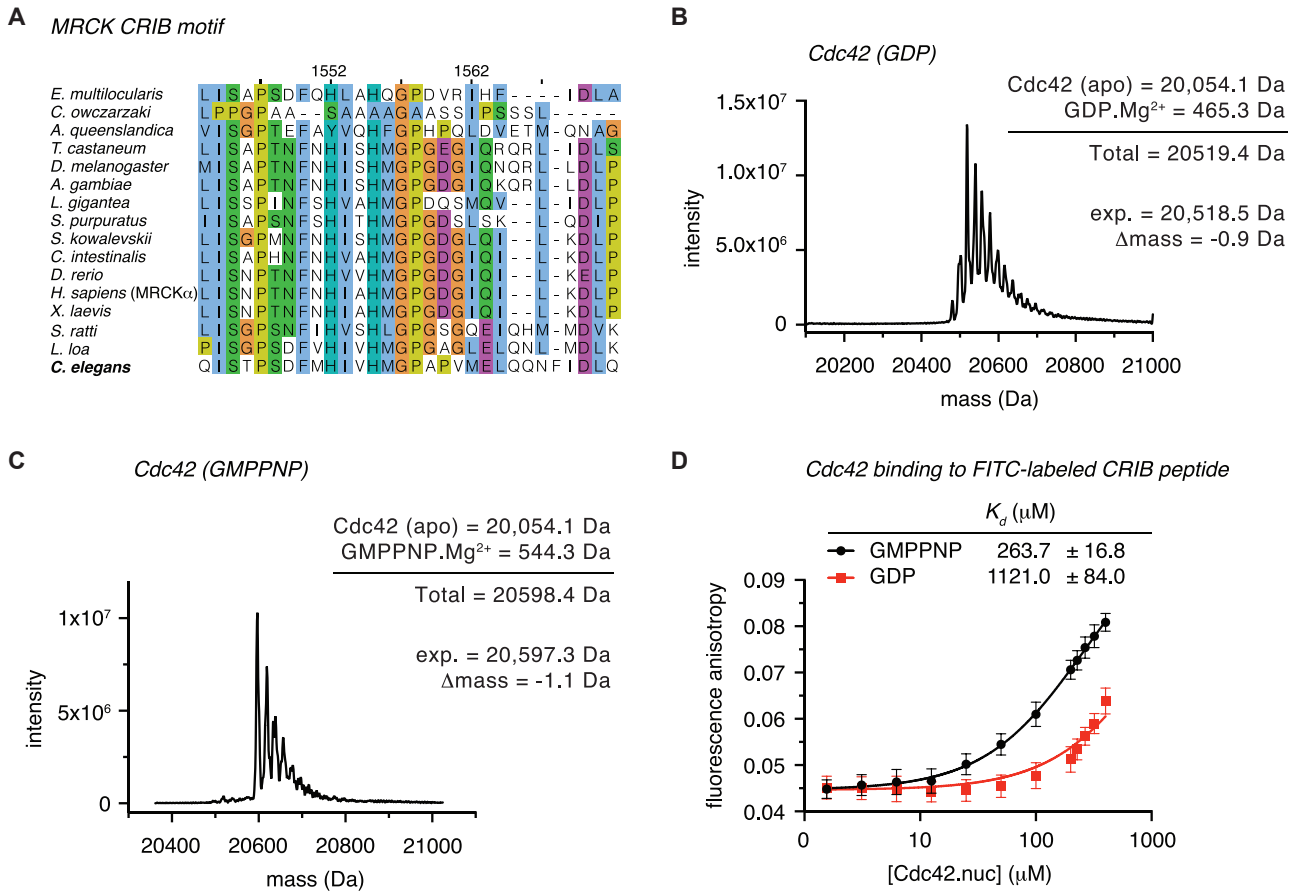

Figure 4. C1-PH-CNH module binds to activated Cdc42

(A) Sequence alignment of the CRIB domain of MRCK orthologs. The CRIB domain of *C. elegans* MRCK1 is highlighted in bold.

(B) Native mass spectrometry of GDP-loaded Cdc42.

(C) Native mass spectrometry of GMPPNP-loaded Cdc42.

(D) Binding of Cdc42 to a FITC-labeled CRIB peptide corresponding to the *C. elegans* CRIB motif sequence shown in (C), determined by fluorescence anisotropy. Data are fitted with a one-site binding model to determine the affinity of interaction. Data are represented as mean ± SEM.

triphosphate (GMP-PNP). Stoichiometric loading of Cdc42 with either GDP or GMP-PNP was confirmed by native mass spectrometry (Figures 4B and 4C, respectively).

We measured the binding affinity of Cdc42 to a peptide comprising the CRIB motif of MRCK1 (residues 1,543–1,572) by fluorescence anisotropy. While Cdc42 bound to GDP exhibited an estimated K_d in the millimolar range, the binding to Cdc42 loaded with GMP-PNP was 5-fold stronger (Figure 4D). The binding of MRCK1 to two molecules of membrane-anchored Cdc42 is therefore likely to be in the low-mid nanomolar range; if additional specific interactions with lipids are factored in, this will be even tighter.

DISCUSSION

We have determined that full-length MRCK1 adopts a highly extended conformation *in vitro*, with dimeric kinase domains at its N terminus and monomeric membrane- and Cdc42-binding domains at its C terminus, joined by a coiled coil of approximately 55 nm in length. MRCK1 binds specifically to active, GTP-bound Cdc42 via its CRIB motif and weakly to membranes, with a preference for di-phosphorylated PIPs. While the structural basis for these protein-lipid interactions will require further investigation, the combination of membrane-anchoring regulatory domains at one end of a highly extended particle with kinase domains at the other suggests that the coiled-coil domain of MRCK, like in ROCK, may act as a molecular ruler to position its kinase domains at a fixed distance from a membrane scaffold.

The defining members of the DMPK subfamily of AGC kinases (DMPK, CRIK, MRCK, and ROCK) exhibit a conserved domain architecture, with the principal difference being the length of their coiled-coil domains. The coiled-coil domains of each family member are evolutionarily conserved in length, much less so in sequence. Each member has been reported to associate with the plasma membrane either directly, via their C-terminal regulatory domains or a transmembrane helix, or indirectly, via binding to a membrane-anchored small GTPase. Structures of the kinase domains of ROCK1, ROCK2, MRCKα (PDB: 4AW2; unpublished data), MRCKβ, and DMPK1 all reveal a dimeric, head-to-head conformation mediated by the CHB domains, which clamp the C-terminal extension of the kinase domains, thereby maintaining an active conformation.[27–29] Deletion or

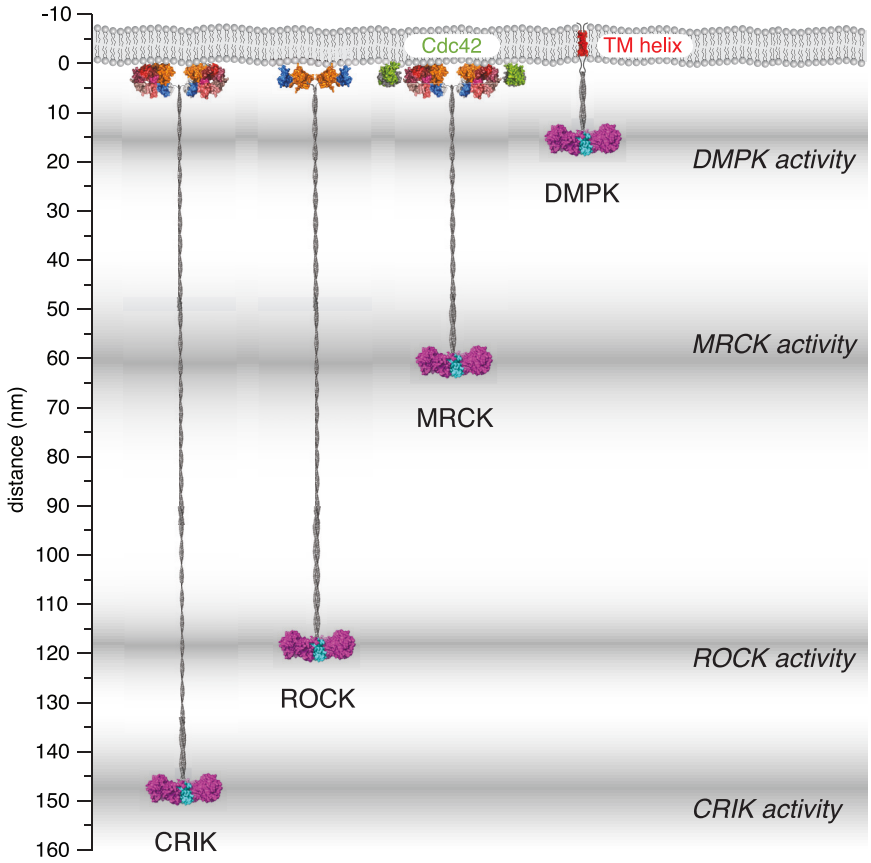

Figure 5. Model of DMPK kinases as molecular rulers

The four DMPK family members (CRIK, DMPK, MRCK, and ROCK) are depicted bound to a hypothetical membrane. Specific membrane anchors are indicated where known. The coiled-coil domains are depicted at their maximum extensions based on experimental analysis of DMPK, MRCK1, and ROCK2 together with bioinformatic analysis of all four family members. A ruler indicates the distance that they are capable of spanning between the membrane and a hypothetical position in the actin cortex.

mutation of the hydrophobic motif in the C-terminal tail of ROCK leads to abrogation of dimerization and a corresponding loss of kinase activity.[50] The unphosphorylated activation loops of these AGC kinases adopt a stable conformation compatible with substrate binding, and each has been reported to exhibit robust kinase activity *in vitro*. MRCK, DMPK, and CRIK do not possess a phosphorylatable residue at the canonical position in their activation loops, while substitution of the activation loop threonine for alanine or a phosphomimetic glutamate in ROCK does not change its specific activity.[7] Allosteric regulation of kinase activity by phosphorylation, protein co-factors, membrane binding, or intramolecular autoinhibition has either not been reported or early reports, particularly in the case of ROCK,[30,51–53] have not been further substantiated with purified recombinant full-length protein.[7] While an early report claimed autoinhibition of MRCKα activity by a distal region of the coiled-coil domain and modest (2-fold) activation by phorbol esters,[54] we could not detect any evidence for a physical association between the C-terminal regulatory domains and the kinase domain in full-length MRCK1. Previous work has also shown that overexpression of active Cdc42 did not influence the activity of immunoprecipitated MRCK,[9] which is consistent with the C-terminal location of the flexibly linked CRIB motif, ~60 nm away from the kinase domains.

Taken together, these observations hint at other, cellular mechanisms that likely regulate signaling via these kinases. One such mechanism, which we have previously proposed for ROCK, is the concept of a molecular ruler, in which the length of the coiled-coil domain fixes the kinase domains at a precise molecular location with respect to the membrane. Truncation mutants, in which the coiled coil of ROCK was shortened while preserving catalytic activity, elicited a defect in stress fiber formation when expressed in cells, indicating that the length of the coiled coil is important for ROCK function.[7] Such a mechanism necessarily relies on the precise positioning of enzyme and substrate within a non-diffusive framework, which could be argued to be the case in the context of the regulation of actomyosin contractility beneath the plasma membrane.

Within the actin cortex, which microscopic studies have measured to span a distance of approximately 20–200 nm beneath the plasma membrane in various mammalian cells,[55] actomyosin fibers are precisely arranged in order to effect changes in cell shape and motility. MLC2, phosphorylation of which regulates this contractility, is bound to myosin II, while MLCP must also be recruited to MLC2 in order to affect its dephosphorylation. Experimental characterization of DMPK, MRCK, and ROCK, together with bioinformatic analysis of CRIK, suggests that the four DMPK family members could, in principle, span distances from as short as 15 nm to as far as 145 nm from the plasma membrane (Figure 5), thereby differentially controlling actomyosin contractility within the actin cortex. The integration of multiple membrane-based signals, including protein-lipid and protein-protein interactions, likely specify the target membrane to which these kinases are localized. Both ROCK and MRCK exhibit subcellular localization to the apical plasma membrane,[56,57] where they play roles in the establishment of epithelial cell polarity and apical constriction. The specificity of signaling is further orchestrated by a variety of adaptor proteins that physically link ROCK, MRCK, and CRIK to components of the actin cytoskeleton. These adaptors include Shroom, an actin-binding protein that binds to the coiled-coil domain of ROCK via its SD2 domain and has been shown to be essential for apical constriction,[23,58,59] and leucine repeat adaptor proteins 25 (LRAP25) and LRAP35a, which link MRCK to LIM kinase (LIMK)[60] and MYO18A,[61] respectively. While the interaction site of LRAP35a was mapped to a so-called kinase-inhibitory motif (KIM) in the coiled-coil domain of MRCKα[61] previously determined to be an autoinhibitory domain,[54,62] we observed no

evidence of a physical association of the coiled-coil domain with either end of MRCK1 in the electron micrographs.

The membrane localization of all members of the DMPK family is by now quite well established, though there is much still to learn about the specificity of the interactions that control their precise subcellular localization. Overexpression of the regulatory domains of ROCK and MRCK is sufficient to induce the dominant negative inhibition of stress fiber formation[52,63] and neurite outgrowth,[13] presumably by the displacement of the endogenous kinase. In the case of MRCK, ectopic expression of a regulatory domain construct lacking its CRIB motif is sufficient to impair neurite outgrowth,[13] indicating that, in addition to its recruitment by Cdc42, specific membrane interactions most likely contribute to its localization. However, while binding of the C1 domain of MRCKα to phorbol esters has previously been described,[49,54] we could not detect robust, concentration-dependent binding to liposomes containing either DOG or phorbol ester (Figure 3G). The putative lipid-binding pocket of the C1 domain of MRCK1 is sequestered in the assembly with the PH and CNH domains, which suggests that membrane binding by the C1 domain would necessitate a conformational change in the regulatory domains. However, it is not obvious whether such a conformational change is possible or what might trigger it. The absence of any binding at PMA concentrations 5,000× the reported K_d[49] suggests that this is unlikely. The precise nature of the membrane lipids that MRCK1 binds to will, therefore, require further investigation.

Although full-length CRIK and DMPK1 have, as yet, not been characterized, they also exhibit conservation of the length of their coiled coils. DMPK orthologs are found only in tetrapods, where they have been implicated primarily in muscle-specific functions. DMPK1 contains an N-terminal kinase domain with the same CHB domain-mediated dimeric arrangement as found in ROCK and MRCK[29] followed by a short coiled-coil and a C-terminal transmembrane helix. While X-ray crystallographic analysis of the isolated coiled-coil domain of DMPK has revealed a trimeric arrangement, constructs encompassing both the kinase domains and the coiled-coil domain are exclusively dimeric in solution.[64] Bioinformatic analysis reveals that the predicted coiled coil of DMPK is invariant in length (8.9 nm), while the linker length between the N-terminal kinase domain and the coiled-coil domain varies between 49 and 118 aa (Figure S4A). Approximately 75 aa that lie between the coiled-coil domain and the transmembrane helix are conserved in both sequence and length but have no known function. The evolution of deuterostomes coincides with a remarkable conservation of the length of CRIK, with a predicted coiled-coil domain of 145.9 ± 1.4 nm (Figures S4B–S4D). CRIK orthologs are found in some, but not all, protostomes, where they exhibit more variable length in their coiled-coil domain.

In summary, our findings are compatible with a model in which the activity of DMPK kinases is governed by the precise positioning of their kinase domains with respect to the membrane scaffold (Figure 5). This, we argue, may be accomplished by a "molecular ruler" in the form of the coiled-coil domain. While the model depicted is clearly an oversimplification of the cellular architecture of the membrane and the actin cortex beneath the membrane, it provides a framework for future work that is required to understand why the length of these coiled-coil domains have been so strongly conserved during evolution and which molecular and cellular events are required to bring enzyme (kinase) and substrate into proximity, as well as the correct orientation required for catalysis.[65]

STAR★METHODS

Detailed methods are provided in the online version of this paper and include the following:

- KEY RESOURCES TABLE
- RESOURCE AVAILABILITY
  - Lead contact
  - Materials availability
  - Experimental model and subject details
  - Data and code availability
- METHOD DETAILS
  - Protein expression and purification
  - Rotary shadowing electron microscopy
  - Kinase assay
  - Crystallization and structure determination
  - Liposome microarray assay (LiMA)
  - Rhodamine-labeled sucrose-loaded vesicles (SLVs)
  - Liposome pelleting assay
  - Cdc42 nucleotide exchange
  - Mass spectrometry
  - Mass photometry
  - Fluorescence anisotropy
- QUANTIFICATION AND STATISTICAL ANALYSIS

SUPPLEMENTAL INFORMATION

Supplemental information can be found online at https://doi.org/10.1016/j.str.2023.02.002.

ACKNOWLEDGMENTS

We would like to thank Montserrat Soler Lopez for assistance in data collection on ID29 at the European Synchrotron Radiation Facility (ESRF), Grenoble, France. We would also like to thank Dorothea Anrather and Markus Hartl in the Max Perutz Labs Mass Spectrometry Facility for help with the acquisition of mass spectra using instruments of the Vienna BioCenter Core Facilities (VBCF). We are grateful to Marlene Brandstetter in the VBCF Electron Microscopy Facility for help with preparing rotary-shadowed samples of MRCK1. This work was supported by a Hertha Firnberg Postdoctoral Fellowship to L.T. and Austrian Science Fund (FWF) grants P28135, P30584, P33066, and W1261 to T.A.L. C.G. was supported by the EMBL Interdisciplinary Postdoc Program under Marie Curie COFUND Actions. A.-C.G. acknowledges the financial support of the Louis-Jeantet Foundation.

AUTHOR CONTRIBUTIONS

L.T. and S.A. purified all recombinant proteins reported in this study. S.A. performed kinase assays and mass photometry analysis. S.A. and E.W. performed liposome pelleting assays with MRCK1 *in vitro*. S.A. analyzed and quantified all liposome pelleting data reported. L.T. performed LiMA assays with the help of C.G. in the lab of A.-C.G. T.A.L. collected diffraction data on MRCK1 crystals grown by L.T. and solved the structure. L.T. built and refined the structure. L.T., A.-C.G., and T.A.L. obtained the funding to support the work.

DECLARATION OF INTERESTS

The authors declare no competing interests.

Received: March 24, 2022
Revised: December 16, 2022
Accepted: February 2, 2023
Published: February 27, 2023

REFERENCES

1. Svitkina, T. (2018). The actin cytoskeleton and actin-based motility. Cold Spring Harb. Perspect. Biol. *10*, a018267. https://doi.org/10.1101/cshperspect.a018267.
2. Adelstein, R.S., and Conti, M.A. (1975). Phosphorylation of platelet myosin increases actin-activated myosin ATPase activity. Nature *256*, 597–598. https://doi.org/10.1038/256597a0.
3. Pires, E.M., and Perry, S.V. (1977). Purification and properties of myosin light-chain kinase from fast skeletal muscle. Biochem. J. *167*, 137–146. https://doi.org/10.1042/bj1670137.
4. Shimizu, H., Ito, M., Miyahara, M., Ichikawa, K., Okubo, S., Konishi, T., Naka, M., Tanaka, T., Hirano, K., and Hartshorne, D.J. (1994). Characterization of the myosin-binding subunit of smooth muscle myosin phosphatase. J. Biol. Chem. *269*, 30407–30411. https://doi.org/10.1016/S0021-9258(18)43828-8.
5. Shirazi, A., Iizuka, K., Fadden, P., Mosse, C., Somlyo, A.P., Somlyo, A.V., and Haystead, T.A. (1994). Purification and characterization of the mammalian myosin light chain phosphatase holoenzyme. The differential effects of the holoenzyme and its subunits on smooth muscle. J. Biol. Chem. *269*, 31598–31606. https://doi.org/10.1016/S0021-9258(18)31736-8.
6. Alessi, D., MacDougall, L.K., Sola, M.M., Ikebe, M., and Cohen, P. (1992). The control of protein phosphatase-1 by targetting subunits. The major myosin phosphatase in avian smooth muscle is a novel form of protein phosphatase-1. Eur. J. Biochem. *210*, 1023–1035. https://doi.org/10.1111/j.1432-1033.1992.tb17508.x.
7. Truebestein, L., Elsner, D.J., Fuchs, E., and Leonard, T.A. (2015). A molecular ruler regulates cytoskeletal remodelling by the Rho kinases. Nat. Commun. *6*, 10029–10113. https://doi.org/10.1038/ncomms10029.
8. Amano, M., Ito, M., Kimura, K., Fukata, Y., Chihara, K., Nakano, T., Matsuura, Y., and Kaibuchi, K. (1996). Phosphorylation and activation of myosin by rho-associated kinase (Rho-kinase). J. Biol. Chem. *271*, 20246–20249. https://doi.org/10.1074/jbc.271.34.20246.
9. Leung, T., Chen, X.-Q., Tan, I., Manser, E., and Lim, L. (1998). Myotonic dystrophy kinase-related Cdc42-binding kinase acts as a Cdc42 effector in promoting cytoskeletal reorganization. Mol. Cell Biol. *18*, 130–140. https://doi.org/10.1128/MCB.18.1.130.
10. Wilkinson, S., Paterson, H.F., and Marshall, C.J. (2005). Cdc42–MRCK and Rho–ROCK signalling cooperate in myosin phosphorylation and cell invasion. Nat. Cell Biol. *7*, 255–261. https://doi.org/10.1038/ncb1230.
11. Kimura, K., Ito, M., Amano, M., Chihara, K., Fukata, Y., Nakafuku, M., Yamamori, B., Feng, J., Nakano, T., Okawa, K., et al. (1996). Regulation of myosin phosphatase by rho and rho-associated kinase (Rho-Kinase). Science *273*, 245–248. https://doi.org/10.1126/science.273.5272.245.
12. Tan, I., Ng, C.H., Lim, L., and Leung, T. (2001). Phosphorylation of a novel myosin binding subunit of protein phosphatase 1 reveals a conserved mechanism in the regulation of actin cytoskeleton. J. Biol. Chem. *276*, 21209–21216. https://doi.org/10.1074/jbc.M102615200.
13. Chen, X.-Q., Tan, I., Leung, T., and Lim, L. (1999). The myotonic dystrophy kinase-related Cdc42-binding kinase is involved in the regulation of neurite outgrowth in PC12 cells. J. Biol. Chem. *274*, 19901–19905. https://doi.org/10.1074/jbc.274.28.19901.
14. Madaule, P., Eda, M., Watanabe, N., Fujisawa, K., Matsuoka, T., Bito, H., Ishizaki, T., and Narumiya, S. (1998). Role of citron kinase as a target of the small GTPase Rho in cytokinesis. Nature *394*, 491–494. https://doi.org/10.1038/28873.
15. Marston, D.J., Higgins, C.D., Peters, K.A., Cupp, T.D., Dickinson, D.J., Pani, A.M., Moore, R.P., Cox, A.H., Kiehart, D.P., and Goldstein, B. (2016). MRCK-1 drives apical constriction in C. elegans by linking developmental patterning to force generation. Curr. Biol. *26*, 2079–2089. https://doi.org/10.1016/j.cub.2016.06.010.
16. Gally, C., Wissler, F., Zahreddine, H., Quintin, S., Landmann, F., and Labouesse, M. (2009). Myosin II regulation during *C. elegans* embryonic elongation:LET-502/ROCK, MRCK-1 and PAK-1, three kinases with different roles. Development *136*, 3109–3119. https://doi.org/10.1242/dev.039412.
17. Gomes, E.R., Jani, S., and Gundersen, G.G. (2005). Nuclear movement regulated by Cdc42, MRCK, myosin, and actin flow establishes MTOC polarization in migrating cells. Cell *121*, 451–463. https://doi.org/10.1016/j.cell.2005.02.022.
18. Winter, C.G., Wang, B., Ballew, A., Royou, A., Karess, R., Axelrod, J.D., and Luo, L. (2001). Drosophila Rho-associated kinase (Drok) links Frizzled-mediated planar cell polarity signaling to the actin cytoskeleton. Cell *105*, 81–91. https://doi.org/10.1016/s0092-8674(01)00298-7.
19. Zihni, C., Vlassaks, E., Terry, S., Carlton, J., Leung, T.K.C., Olson, M., Pichaud, F., Balda, M.S., and Matter, K. (2017). An apical MRCK-driven morphogenetic pathway controls epithelial polarity. Nat. Cell Biol. *19*, 1049–1060. https://doi.org/10.1038/ncb3592.
20. Brook, J.D., McCurrach, M.E., Harley, H.G., Buckler, A.J., Church, D., Aburatani, H., Hunter, K., Stanton, V.P., Thirion, J.P., and Hudson, T. (1992). Molecular basis of myotonic dystrophy: expansion of a trinucleotide (CTG) repeat at the 3' end of a transcript encoding a protein kinase family member. Cell *68*, 799–808. https://doi.org/10.1016/0092-8674(92)90154-5.
21. Mahadevan, M., Tsilfidis, C., Sabourin, L., Shutler, G., Amemiya, C., Jansen, G., Neville, C., Narang, M., Barceló, J., O'Hoy, K., et al. (1992). Myotonic dystrophy mutation: an unstable CTG repeat in the 3′ untranslated region of the gene. Science *255*, 1253–1255. https://doi.org/10.1126/science.1546325.
22. Fu, Y.H., Pizzuti, A., Fenwick, R.G., King, J., Rajnarayan, S., Dunne, P.W., Dubel, J., Nasser, G.A., Ashizawa, T., de Jong, P., et al. (1992). An unstable triplet repeat in a gene related to myotonic muscular dystrophy. Science *255*, 1256–1258. https://doi.org/10.1126/science.1546326.
23. Nishimura, T., and Takeichi, M. (2008). Shroom3-mediated recruitment of Rho kinases to the apical cell junctions regulates epithelial and neuroepithelial planar remodeling. Development *135*, 1493–1502. https://doi.org/10.1242/dev.019646.
24. Gaggioli, C., Hooper, S., Hidalgo-Carcedo, C., Grosse, R., Marshall, J.F., Harrington, K., and Sahai, E. (2007). Fibroblast-led collective invasion of carcinoma cells with differing roles for RhoGTPases in leading and following cells. Nat. Cell Biol. *9*, 1392–1400. https://doi.org/10.1038/ncb1658.
25. Unbekandt, M., and Olson, M.F. (2014). The actin-myosin regulatory MRCK kinases: regulation, biological functions and associations with human cancer. J. Mol. Med. *92*, 217–225. https://doi.org/10.1007/s00109-014-1133-6.
26. Pearce, L.R., Komander, D., and Alessi, D.R. (2010). The nuts and bolts of AGC protein kinases. Nat. Rev. Mol. Cell Biol. *11*, 9–22. https://doi.org/10.1038/nrm2822.
27. Yamaguchi, H., Kasa, M., Amano, M., Kaibuchi, K., and Hakoshima, T. (2006). Molecular mechanism for the regulation of rho-kinase by dimerization and its inhibition by fasudil. Structure *14*, 589–600. https://doi.org/10.1016/j.str.2005.11.024.
28. Heikkila, T., Wheatley, E., Crighton, D., Schroder, E., Boakes, A., Kaye, S.J., Mezna, M., Pang, L., Rushbrooke, M., Turnbull, A., and Olson, M.F. (2011). Co-crystal structures of inhibitors with MRCKβ, a key regulator of tumor cell invasion. PLoS One *6*, e24825. https://doi.org/10.1371/journal.pone.0024825.
29. Elkins, J.M., Amos, A., Niesen, F.H., Pike, A.C.W., Fedorov, O., and Knapp, S. (2009). Structure of dystrophia myotonica protein kinase. Protein Sci. *18*, 782–791. https://doi.org/10.1002/pro.82.
30. Matsui, T., Amano, M., Yamamoto, T., Chihara, K., Nakafuku, M., Ito, M., Nakano, T., Okawa, K., Iwamatsu, A., and Kaibuchi, K. (1996). Rho-associated kinase, a novel serine/threonine kinase, as a putative target for small GTP binding protein Rho. EMBO J. *15*, 2208–2216. https://doi.org/10.1002/j.1460-2075.1996.tb00574.x.

31. Lam, L.T., Pham, Y.C., Nguyen, T.M., and Morris, G.E. (2000). Characterization of a monoclonal antibody panel shows that the myotonic dystrophy protein kinase, DMPK, is expressed almost exclusively in muscle and heart. Hum. Mol. Genet. *9*, 2167–2173. https://doi.org/10.1093/hmg/9.14.2167.

32. Truebestein, L., Elsner, D.J., and Leonard, T.A. (2016). Made to measure – keeping Rho kinase at a distance. Small GTPases *7*, 82–92. https://doi.org/10.1080/21541248.2016.1173770.

33. Jumper, J., Evans, R., Pritzel, A., Green, T., Figurnov, M., Ronneberger, O., Tunyasuvunakool, K., Bates, R., Žídek, A., Potapenko, A., et al. (2021). Highly accurate protein structure prediction with AlphaFold. Nature *596*, 583–589. https://doi.org/10.1038/s41586-021-03819-2.

34. Senior, A.W., Evans, R., Jumper, J., Kirkpatrick, J., Sifre, L., Green, T., Qin, C., Žídek, A., Nelson, A.W.R., Bridgland, A., et al. (2020). Improved protein structure prediction using potentials from deep learning. Nature *577*, 706–710. https://doi.org/10.1038/s41586-019-1923-7.

35. Hubbard, S.R., Bishop, W.R., Kirschmeier, P., George, S.J., Cramer, S.P., and Hendrickson, W.A. (1991). Identification and characterization of zinc binding sites in protein kinase C. Science *254*, 1776–1779. https://doi.org/10.1126/science.1763327.

36. Hommel, U., Zurini, M., and Luyten, M. (1994). Solution structure of a cysteine rich domain of rat protein kinase C. Nat. Struct. Biol. *1*, 383–387. https://doi.org/10.1038/nsb0694-383.

37. Bartual, S.G., Wei, W., Zhou, Y., Pravata, V.M., Fang, W., Yan, K., Ferenbach, A.T., Lockhart, D.E.A., and van Aalten, D.M.F. (2021). The citron homology domain as a scaffold for Rho1 signaling. Proc. Natl. Acad. Sci. USA *118*. e2110298118. https://doi.org/10.1073/pnas.2110298118.

38. Krissinel, E., and Henrick, K. (2007). Inference of macromolecular assemblies from crystalline state. J. Mol. Biol. *372*, 774–797. https://doi.org/10.1016/j.jmb.2007.05.022.

39. Baker, N.A., Sept, D., Joseph, S., Holst, M.J., and McCammon, J.A. (2001). Electrostatics of nanosystems: Application to microtubules and the ribosome. Proc. Natl. Acad. Sci. USA *98*, 10037–10041. https://doi.org/10.1073/pnas.181342398.

40. Krissinel, E., and Henrick, K. (2005). Multiple alignment of protein structures in three dimensions. In Computational Life Sciences (Springer), pp. 67–78. https://doi.org/10.1007/11560500_7.

41. Krissinel, E., Henrick, K., and IUCr. (2004). Secondary-structure matching (SSM), a new tool for fast protein structure alignment in three dimensions. Acta Crystallogr. D Biol. Crystallogr. *60*, 2256–2268. https://doi.org/10.1107/S0907444904026460.

42. Das, J., and Rahman, G.M. (2014). C1 domains: structure and ligand-binding properties. Chem. Rev. *114*, 12108–12131. https://doi.org/10.1021/cr300481j.

43. Zhang, G., Kazanietz, M.G., Blumberg, P.M., and Hurley, J.H. (1995). Crystal structure of the cys2 activator-binding domain of protein kinase C delta in complex with phorbol ester. Cell *81*, 917–924. https://doi.org/10.1016/0092-8674(95)90011-x.

44. Okazaki, S., Kato, R., Uchida, Y., Taguchi, T., Arai, H., and Wakatsuki, S. (2012). Structural basis of the strict phospholipid binding specificity of the pleckstrin homology domain of human evectin-2. Acta Crystallogr. D Biol. Crystallogr. *68*, 117–123. https://doi.org/10.1107/S0907444911051626.

45. Saliba, A.-E., Vonkova, I., Ceschia, S., Findlay, G.M., Maeda, K., Tischer, C., Deghou, S., van Noort, V., Bork, P., Pawson, T., et al. (2014). A quantitative liposome microarray to systematically characterize protein-lipid interactions. Nat. Methods *11*, 47–50. https://doi.org/10.1038/nmeth.2734.

46. Saliba, A.-E., Vonkova, I., Deghou, S., Ceschia, S., Tischer, C., Kugler, K.G., Bork, P., Ellenberg, J., and Gavin, A.-C. (2016). A protocol for the systematic and quantitative measurement of protein–lipid interactions using the liposome-microarray-based assay. Nat. Protoc. *11*, 1021–1038. https://doi.org/10.1038/nprot.2016.059.

47. Ferguson, K.M., Lemmon, M.A., Schlessinger, J., and Sigler, P.B. (1995). Structure of the high affinity complex of inositol trisphosphate with a phospholipase C pleckstrin homology domain. Cell *83*, 1037–1046. https://doi.org/10.1016/0092-8674(95)90219-8.

48. Ebner, M., Lučić, I., Leonard, T.A., and Yudushkin, I. (2017). PI(3,4,5)P3 Engagement restricts Akt activity to cellular membranes. Mol. Cell *65*, 416–431.e6. https://doi.org/10.1016/j.molcel.2016.12.028.

49. Choi, S.H., Czifra, G., Kedei, N., Lewin, N.E., Lazar, J., Pu, Y., Marquez, V.E., and Blumberg, P.M. (2008). Characterization of the interaction of phorbol esters with the C1 domain of MRCK (myotonic dystrophy kinase-related Cdc42 binding kinase) alpha/beta. J. Biol. Chem. *283*, 10543–10549. https://doi.org/10.1074/jbc.M707463200.

50. Couzens, A.L., Saridakis, V., and Scheid, M.P. (2009). The hydrophobic motif of ROCK2 requires association with the N-terminal extension for kinase activity. Biochem. J. *419*, 141–148. https://doi.org/10.1042/BJ20081376.

51. Amano, M., Chihara, K., Nakamura, N., Kaneko, T., Matsuura, Y., and Kaibuchi, K. (1999). The COOH terminus of Rho-kinase negatively regulates rho-kinase activity. J. Biol. Chem. *274*, 32418–32424. https://doi.org/10.1074/JBC.274.45.32418.

52. Ishizaki, T., Naito, M., Fujisawa, K., Maekawa, M., Watanabe, N., Saito, Y., and Narumiya, S. (1997). p160ROCK, a Rho-associated coiled-coil forming protein kinase, works downstream of Rho and induces focal adhesions. FEBS Lett. *404*, 118–124. https://doi.org/10.1016/s0014-5793(97)00107-5.

53. Feng, J., Ito, M., Kureishi, Y., Ichikawa, K., Amano, M., Isaka, N., Okawa, K., Iwamatsu, A., Kaibuchi, K., Hartshorne, D.J., and Nakano, T. (1999). Rho-associated kinase of chicken gizzard smooth muscle. J. Biol. Chem. *274*, 3744–3752. https://doi.org/10.1074/jbc.274.6.3744.

54. Tan, I., Seow, K.T., Lim, L., and Leung, T. (2001). Intermolecular and intramolecular interactions regulate catalytic activity of myotonic dystrophy kinase-related Cdc42-binding kinase α. Mol. Cell Biol. *21*, 2767–2778. https://doi.org/10.1128/MCB.21.8.2767-2778.2001.

55. Chugh, P., and Paluch, E.K. (2018). The actin cortex at a glance. J. Cell Sci. *131*, jcs186254. https://doi.org/10.1242/jcs.186254.

56. Loo, C.-S., Chen, C.-W., Wang, P.-J., Chen, P.-Y., Lin, S.-Y., Khoo, K.-H., Fenton, R.A., Knepper, M.A., and Yu, M.-J. (2013). Quantitative apical membrane proteomics reveals vasopressin-induced actin dynamics in collecting duct cells. Proc. Natl. Acad. Sci. USA *110*, 17119–17124. https://doi.org/10.1073/pnas.1309219110.

57. Mason, F.M., Tworoger, M., and Martin, A.C. (2013). Apical domain polarization localizes actin–myosin activity to drive ratchet-like apical constriction. Nat. Cell Biol. *15*, 926–936. https://doi.org/10.1038/ncb2796.

58. Plageman, T.F., Chauhan, B.K., Yang, C., Jaudon, F., Shang, X., Zheng, Y., Lou, M., Debant, A., Hildebrand, J.D., and Lang, R.A. (2011). A Trio-RhoA-Shroom3 pathway is required for apical constriction and epithelial invagination. Development *138*, 5177–5188. https://doi.org/10.1242/dev.067868.

59. Mohan, S., Rizaldy, R., Das, D., Bauer, R.J., Heroux, A., Trakselis, M.A., Hildebrand, J.D., and VanDemark, A.P. (2012). Structure of Shroom domain 2 reveals a three-segmented coiled-coil required for dimerization, Rock binding, and apical constriction. Mol. Biol. Cell *23*, 2131–2142. https://doi.org/10.1091/mbc.e11-11-0937.

60. Lee, I.C.J., Leung, T., and Tan, I. (2014). Adaptor protein LRAP25 mediates myotonic dystrophy kinase-related Cdc42-binding kinase (MRCK) regulation of LIMK1 protein in lamellipodial F-actin dynamics. J. Biol. Chem. *289*, 26989–27003. https://doi.org/10.1074/jbc.M114.588079.

61. Tan, I., Yong, J., Dong, J.M., Lim, L., and Leung, T. (2008). A tripartite complex containing MRCK modulates lamellar actomyosin retrograde flow. Cell *135*, 123–136. https://doi.org/10.1016/j.cell.2008.09.018.

62. Ng, Y., Tan, I., Lim, L., and Leung, T. (2004). Expression of the human myotonic dystrophy kinase-related Cdc42-binding kinase gamma is regulated by promoter DNA methylation and Sp1 binding. J. Biol. Chem. *279*, 34156–34164. https://doi.org/10.1074/jbc.M405252200.

63. Leung, T., Chen, X.Q., Manser, E., and Lim, L. (1996). The p160 RhoA-binding kinase ROK alpha is a member of a kinase family and is involved

in the reorganization of the cytoskeleton. Mol. Cell Biol. *16*, 5313–5327. https://doi.org/10.1128/MCB.16.10.5313.

64. Garcia, P., Ucurum, Z., Bucher, R., Svergun, D.I., Huber, T., Lustig, A., Konarev, P.V., Marino, M., and Mayans, O. (2006). Molecular insights into the self-assembly mechanism of dystrophia myotonica kinase. FASEB J *20*, 1142–1151. https://doi.org/10.1096/fj.05-5262com.
65. Lassila, J.K., Zalatan, J.G., and Herschlag, D. (2011). Biological phosphoryl-transfer reactions: understanding mechanism and catalysis. Annu. Rev. Biochem. *80*, 669–702. https://doi.org/10.1146/annurev-biochem-060409-092741.
66. Afonine, P.v., Grosse-Kunstleve, R.W., Echols, N., Headd, J.J., Moriarty, N.W., Mustyakimov, M., Terwilliger, T.C., Urzhumtsev, A., Zwart, P.H., Adams, P.D., et al. (2012). Towards automated crystallographic structure refinement with *phenix.refine*. Acta Crystallogr. D Biol. Crystallogr. *68*, 352–367. https://doi.org/10.1107/S0907444912001308.
67. Emsley, P., Cowtan, K., and IUCr. (2004). *Coot* : model-building tools for molecular graphics. Acta Crystallogr. D Biol. Crystallogr. *60*, 2126–2132. https://doi.org/10.1107/S0907444904019158.
68. McCoy, A.J., Grosse-Kunstleve, R.W., Adams, P.D., Winn, M.D., Storoni, L.C., Read, R.J., and IUCr. (2007). *Phaser* crystallographic software. J. Appl. Crystallogr. *40*, 658–674. https://doi.org/10.1107/S0021889807021206.

STAR★METHODS

KEY RESOURCES TABLE

REAGENT or RESOURCE	SOURCE	IDENTIFIER
Bacterial and virus strains		
E. coli BL21 (DE3)	NEB	Cat# C2527
Chemicals, peptides, and recombinant proteins		
FITC-Ahx-QISTPSDFMHIVHMGPAPVMELQQNFIDLQ	GenScript	Custom synthesis
Guanosine diphosphate (GDP)	Sigma	Cat# G7127
Guanosine 5'[(β-γ)-imido]triphosphate (GMPPNP)	Sigma	Cat# M3509
Lissamine Rhodamine B 1,2-dihexadecanoyl-*sn*-Glycero-3-phosphatidylethanoline	Thermo Fisher	Cat# L1392
Cholesterol	Sigma	Cat# C3045
Dioleoylphosphatidylserine (DOPS)	Sigma	Cat# 840035C
Dioleoylphosphatidylcholine (DOPC)	Mobitec	Cat# L-1182-1-EC
Dioleoylphosphatidylethanolamine (DOPE)	Mobitec	Cat# L-2182-1-EC
Phosphatidylinositol-4,5-bisphosphate [PI(4,5)P_2]	Avanti	Cat# 850155P
Phosphatidylinositol-3,4-bisphosphate [PI(3,4)P_2]	Avanti	Cat# 850153P
Phosphatidylinositol-3,5-bisphosphate [PI(3,5)P_2]	Avanti	Cat# 850154P
Phosphatidylinositol-3,4,5-bisphosphate [PI(3,4,5)P_3]	Avanti	Cat# 850156P
Dioctanoylglycerol (DOG)	Sigma	Cat# 317505
Phorbol 12-myristate 13-acetate	Sigma	Cat# 524400
Critical commercial assays		
Promega ADP-Glo	Promega	V9101
Deposited data		
X-ray structure of *C. elegans* MRCK1$^{955-1534}$	This paper	7Z6E
Software and algorithms		
Phenix	Afonine et al.[66]	https://phenix-online.org/download/
Coot	Emsley et al.[67]	https://www2.mrc-lmb.cam.ac.uk/personal/pemsley/coot/
ImageJ (Fiji)	NIH	https://imagej.nih.gov/ij/
GraphPad Prism	GraphPad	https://www.graphpad.com/scientificsoftware/prism/
Other		
Spodoptera frugiperda (Sf9) insect cells	Expression Systems	94-001F

RESOURCE AVAILABILITY

Lead contact

Further information and requests for resources and reagents should be directed to and will be fulfilled by the lead contact, Thomas A. Leonard (thomas.leonard@meduniwien.ac.at).

Materials availability

This study did not generate new unique reagents.

Experimental model and subject details

Spodoptera frugiperda (Sf9) insect cells used for baculovirus-mediated recombinant protein expression were obtained from Expression Systems (California) and cultured in ESF921 medium (Expression Systems). *E. coli* BL21 (DE3) cells used for the expression of MLC2 and Cdc42 were obtained from New England Biolabs.

Data and code availability

- The structure of MRCK$^{955-1534}$ has been deposited at PDB and is publicly available as of the date of publication. Accession numbers are listed in the key resources table.
- This paper does not report original code.
- Any additional information required to re-analyze the data reported in this paper is available from the lead contact upon request.

METHOD DETAILS

Protein expression and purification

MRCK1$^{1-1592}$ (full length protein) and MRCK$^{955-1534}$ were expressed in Sf9 insect cells with an N-terminal His_{10}-StrepII tag. For MRCK1 full length purification cells were lysed in 30 mL lysis buffer (50 mM Tris pH 7.5, 140 mM KCl, 10 mM NaCl, 10 mM β-glycerophosphate, 2 mM sodium pyrophosphate, 1 mM TCEP, 2 mM benzamidine, 0.2 mM sodium orthovanadate, 40 mM NaF, 1 mM PMSF, 100 μM bestatin, 14 μM E−64, 10 μM pepstatin and 1 μM phosphoramidon). After one freeze/thaw cycle, 1 mM $MgCl_2$ and benzonase were added and samples were left on ice for 30 min. After centrifugation at 38,724 x g for 30 min at 4°C, samples were loaded to a HisTrap FF column, which was equilibrated in buffer A (50 mM Tris pH 7.5, 140 mM KCl, 1 mM TCEP, 50 mM NaF). Column was washed with 2% buffer B (50 mM Tris pH 7.5, 140 mM KCl, 1 mM TCEP, 50 mM NaF, 1 M imidazole) and 4% buffer B before gradient elution into 100% buffer B. Fraction were collected in tubes containing 50 mM Tris pH 7.5, 100 mM KCl, 1 mM TCEP to reduce the imidazole concentration by two-thirds. Peak fractions were pooled, diluted 1:3 in QA buffer (50 mM Tris pH 8.0, 1 mM TCEP) and TEV cleaved overnight at 4°C. The next day the sample was loaded onto a HiTrap Q column equilibrated in Q_A buffer and eluted with a gradient into 100% buffer Q_B (50 mM Tris pH 8.0, 1 mM TCEP, 1 M NaCl). Elution fractions were pooled and concentrated and buffer exchanged using an Amicon concentrator (30 kDa cutoff) into storage buffer (20 mM Tris pH 8.0, 1 mM TCEP, 100 mM KCl), frozen in liquid nitrogen and stored at −80°C.

For purification of MRCK$^{955-1534}$ Sf9 cell pellets were resuspended in lysis buffer (50 mM HEPES pH 8.0, 150 mM KCl, 1 mM TCEP) with 2 mM $MgCl_2$, 2 mM benzamidine, 50 μL 100x protease inhibitor mix (P8849 Sigma), 1 μL benzonase, and 1 mM PMSF. The resuspended cells were incubated on ice for 30 min, and then centrifuged for 30 min at 38,724 x g, 4°C. The supernatant was loaded onto a 5 mL HisTrap FF column (GE Healthcare Life Sciences) washed and equilibrated in buffer A (50 mM HEPES pH 8.0, 150 mM KCl, 1 mM TCEP). After washing the column with 2% buffer B (buffer A, 1 M imidazole) protein was eluted with a gradient into 100% buffer B. Peak fractions were pooled and 1:1 diluted with lysis buffer. 150 μL of TEV (2 mg/mL) were added and the cleavage reaction was incubated at 4°C over night. The sample was further diluted 1:4 with S_A buffer (50 mM Tris pH 8.0, 1 mM TCEP) to lower the salt concentration for binding to a cation exchange column. The sample was then loaded onto a 5 mL HiTrap SP FF column (GE Healthcare Life Sciences) followed by gradient elution with elution buffer S_B (50 mM Tris pH 8, 1 M NaCl, 1 mM TCEP). Peak fractions were pooled, concentrated and loaded to a HiLoad 10/300 Superdex 200 column (GE Healthcare Life Sciences) equilibrated with gel filtration buffer (20 mM Tris pH 7.5, 150 mM KCl, 1 mM TCEP, 1% glycerol). Peak fractions were pooled and concentrated to 4 mg/mL and the protein was frozen in liquid nitrogen and stored at −80°C.

MLC2 (MYL12B) was expressed in *E. coli* BL21 (DE3) cells as an N-terminal GST-fusion protein. Protein expression was induced with 250 μM IPTG at 18°C and grown overnight before harvesting. MLC2 was purified by affinity chromatography using glutathione Sepharose beads in 50 mM Tris pH 7.5, 150 mM NaCl and 1 mM TCEP. Beads were washed and GST-MLC2 was cleaved with TEV overnight at 4°C. MLC2 was concentrated and applied to a Superdex 75 gel filtration column equilibrated in 20 mM Tris pH 7.5, 150 mM NaCl and 1 mM TCEP. Peak fractions were pooled, concentrated, and stored at −80°C.

Cdc42 was expressed with an N-terminal GST-tag in *E. coli* BL21 (DE3) overnight at 22°C. Cells were harvested and pellets resuspended in 50 mL lysis buffer (50 mM Tris pH 7.4, 150 mM KCl, 2 mM $MgCl_2$, 1 mM TCEP, 2 mM benzamidine) and frozen at −80°C. After thawing, 10 mg lysozyme and 2 μL benzonase were added and the solution was incubated for 30 min on ice. After sonication and centrifugation for 15 min at 38,724 x g at 4°C the supernatant was incubated in 1 mL of lysis buffer equilibrated GST beads for 3 h at 4°C rotating. Beads were collected at 500 x g for 10 min and washed with buffer A (50 mM Tris pH 7.4, 150 mM KCl, 2 mM $MgCl_2$, 1 mM TCEP) and beads resuspended in 15 mL buffer A. The protein was incubated with TEV protease overnight at 4°C and gel filtrated on a Superdex 75 16/600 equilibrated in buffer A. Elution fractions were collected, concentrated, frozen in liquid nitrogen and stored at −80°C.

Rotary shadowing electron microscopy

Preparation of rotary-shadowed MRCK1 and ROCK2 was carried out as previously described for ROCK2.[7] Samples were diluted to a final concentration of 50 μg/mL in spraying buffer containing 100 mM ammonium acetate and 30% (v/v) glycerol, pH 7.4. After dilution, the samples were sprayed on freshly cleaved mica chips and immediately transferred into a BAL-TEC MED020 high-vacuum evaporator equipped with electron guns. While rotating, the samples were coated with 0.6 nm platinum at an angle of 4–5°, followed by 10 nm carbon at 90°. The obtained replicas were floated off from the mica chips, picked up on 400 mesh Cu/Pd grids and inspected in an FEI T20 G2 transmission electron microscope operated at 80 kV. Electron micrographs were acquired using an FEI Eagle 4k charge-coupled device camera.

Kinase assay

Kinase assays were done using the ADP-glo kit from Promega according to the manufacturer's instructions. Assays were done in white 96-well plates using substrate concentrations between 2 and 24 μM MLC2. Kinase assays were done for 40 min at RT in a final volume of 25 μL containing 100 nM full length MRCK1, substrate and 1 mM ATP in 50 mM Tris pH 7.5, 100 mM KCl, 1 mM TCEP, and 2 mM $MgCl_2$. 25 μL ADP-glo reagent was added afterward and samples were incubated for another 40 min at RT to deplete any remaining ATP. For luminescence detection 50 μL kinase detection reagent was added to each sample and incubation was done for 1 h at RT. Samples were measured for luminescence in a TECAN Infinite F500 plate reader.

Crystallization and structure determination

$MRCK1^{955-1534}$ was crystallized at 2.6 mg/mL in 100 mM bicine/tris (base) at pH 8.5, 30 mM each of sodium nitrate, disodium hydrogen phosphate and ammonium sulfate, 20% PEG550 MME, 8% PEG20K, 3% glycerol. Crystals grew in space group P1 with unit cell dimensions a = 69.14 Å, b = 97.47 Å, c = 131.41 Å, $\alpha = 81.38^\circ$ $\beta = 77.77^\circ$ $\gamma = 80.39^\circ$. Crystals diffracted to 2.14 Å resolution and contained 5 molecules per asymmetric unit. The structure was solved by molecular replacement with the AlphaFold prediction for residues 955-1534 of *C. elegans* MRCK1 (AF-O01583-F1). The model was rebuilt with Phaser Autobuild,[68] manually checked and regions of ambiguous electron density built in Coot. The final model was refined to $R_{free} = 0.244$ and $R_{work} = 0.195$ (for dataset and model statistics, see Table S1).

Liposome microarray assay (LiMA)

LiMA[45] was performed in the lab of Anne-Claude Gavin (EMBL Heidelberg, Germany) according to.[46] $MRCK^{955-1534}$ C-terminally tagged with EGFP and a positive control, PLCδ1-PH fused to sfGFP, were applied to microarrays printed with different signaling lipids. In brief, lipids of interest were combined with the carrier lipid DOPC, PEGylated PE and PE labeled with Atto 647 dye (PE-Atto 647, 0.1 mol %). Such lipid mixtures contained 2, 5 and 10 mol % of the signaling lipid and were spotted onto a thin agarose layer (TAL). The agarose layers were hydrated using Buffer A: 20 mM Tris-HCl pH 8.5, 200 mM NaCl and vesicles formed spontaneously. Efficiency of liposome formation was verified by fluorescence microscopy. The protein was diluted to 7 μM in buffer A and 40 μL were added to each array. Microarrays were incubated for 20 min at RT and subsequently washed three times with 40 μL of buffer A. Chips were analyzed by automated fluorescence microscopy. Positions of liposomes were determined by tracking the fluorescence of PE-Atto 647 and pictures were taken with exposure times of 3 ms and 5 ms. In parallel the fluorescence of EGFP was determined at eight different exposure times, namely at 1, 5, 10, 30, 75, 100, 200 and 300 ms. Pictures were processed using CellProfiler and CPAnalyst. Only EGFP signals that overlapped with Atto 647 signals were taken into account. Normalized binding intensity (NBI) was calculated as a ratio between EGFP and Atto 647 fluorescence, normalized by exposure time. Three microarrays were examined, carrying liposomes with the following signaling lipids; PIP-chip: DOPA, DOPE, DOPI, DOPS, DODAG, cardiolipin, BMP, DOPI(4,5)P_2, DOPG; GLP-chip: Ceramide C16, ceramide(1)P C16, ceramide(1)P C18, S(1)P, S, SM, DOPI(4,5)P_2, DOPS; SL-chip: DOPI(3)P, brain PI(4)P, DOPI(5)P, DOPI(3,4)P_2, DOPI(3,5)P_2, brain PI(4,5)P_2, DOPI(3,4,5)P_3, DOPS and cholesterol. Each microarray was done in triplicates.

Rhodamine-labeled sucrose-loaded vesicles (SLVs)

Lipids were pipetted into borosilicate test tubes (1 mL of 1 mM solution gives in the end 20 sample runs) and 0.006 mM Rhodamine-DHPE was included. Lipids were dried to a thin film using a dry nitrogen stream. 1 mL of 20 mM HEPES pH 7.5, 0.3 M sucrose was added and samples were vortexed vigorously. Samples were split into 4 x 250 μL aliquots and 4 freeze-thaw cycles in liquid nitrogen followed by thawing in sonicating water bath were performed. To 250 μL SLVs, 300 μL of 20 mM HEPES pH 7.5, 100 mM KCl were added and samples were spun at 278,337 x g for 30 min at RT in a TLA 100 rotor. The supernatant was removed and pellets were resuspended in 250 μL of 20 mM HEPES pH 7.5 and 100 mM KCl.

Liposome pelleting assay

For liposome pelleting assays 1.5 μM full length MRCK1 or $MRCK^{955-1534}$ were incubated with or without liposomes at RT for 30 min. Final concentration of liposomes was 0.5 mg/mL. Samples were centrifuged at 19,179 x g using a TLA 100 rotor for 30 min at RT. Supernatant and pellet fractions were evaluated by densitometry of Coomassie-stained SDS-PAGE gels.

Cdc42 nucleotide exchange

$Cdc42^{2-178}$ (co-purified with a mixture of GDP and GTP) was incubated with Dbs exchange factor (5:1) in a 100-fold molar excess of GMPPNP, 30 min at RT. $Cdc42^{2-178}$ was separated from Dbs and free nucleotide by size exclusion chromatography. The extent of GMPPNP loading was determined by native mass spectrometry (see below).

Mass spectrometry

The protein mass was determined on a Synapt G2-Si Q-ToF mass spectrometer (Waters) coupled to an Ultimate 3000 HPLC system (Dionex, Thermo Fisher Scientific) via a ZSpray ESI source (Waters). Proteins were separated on an Aeris Widepore C4 column (3.6 μm particle size, dimensions 2.1 × 150 mm, Phenomenex) with a working temperature of 55°C, applying a 10 min gradient from 8% to 63% acetonitrile in 0.1% formic acid at a flow rate of 300 μL/min. On the mass spectrometer the sampling cone voltage was 40 V, the desolvation gas temperature 450°C and the source temperature 120°C.

For MS experiments under native conditions, the buffer of the protein solutions was exchanged to 50 mM ammonium acetate, pH 6.8. Measurements were performed on the Synapt G2-Si equipped with the NanoLockSpray electrospray source (Waters) using pre-opened PicoTip emitters (New Objective). Electrospray voltage was set at 1.8 kV, the source temperature at 80°C and sampling cone voltage at 80 V. All data were analyzed in MassLynx V 4.1 using the MaxEnt 1 process to reconstruct the uncharged average protein mass.

Mass photometry

Mass photometry experiments were carried out on a Refeyn OneMP instrument. Data were acquired using AcquireMP (Refeyn) and processed using DiscoverMP (Refeyn). Microscope coverslips (24 × 50 mm) were cleaned with both 100% isopropanol and Milli-Q water in a sonicating water bath for 5 min and dried with a nitrogen stream. Chambers were made by sticking silicone gaskets (3 × 1 mm) on top of the slides. Mass calibration was performed using NativeMark Unstained Protein Standard (Invitrogen) by fitting a contrast-to-mass calibration curve to 146, 242, and 480 kDa standards. Purified full length MRCK1 was diluted to 100 nM in buffer (50 mM Tris pH 7.5, 200 mM KCl, 1 mM TCEP), filtered through 0.22 μm PES filters, and loaded into the coverslip chambers. Data was collected for 60 s at a 1 kHz frame rate.

Fluorescence anisotropy

The binding affinity of the *C. elegans* MRCK1 CRIB motif (residues 1543-1572) was determined by titration of purified $Cdc42^{2-178}$ loaded either with GDP or GMPPNP into a buffer containing 100 nM fluorescein-labeled peptide. Fluorescence anisotropy was measured on a Perkin-Elmer LS50 fluorimeter with λ_{ex} = 500 nm and λ_{em} = 518 nm, at 20°C in 20 mM Tris pH 8.0, 100 mM NaCl, and 1 mM TCEP. Each concentration of $Cdc42^{2-178}$ was measured 50 times with an integration time of 1 s and the mean plotted. The error bars represent the SD of the measurements. Three independent titrations were performed. The obtained binding curves were fit with a one-site binding model to estimate the binding affinity.

QUANTIFICATION AND STATISTICAL ANALYSIS

Particles of MRCK1 and ROCK2 were measured in ImageJ by determining the contour length of their coiled-coil domains using the Measure tool. Kinase activity data were fitted with Michaelis-Menten kinetics in GraphPad Prism. Liposome binding in the LiMA assay[45,46] was quantified as the normalized binding intensity (NBI), which is the ratio of EGFP fluorescence to Atto647, normalized by exposure time. Binding to sucrose-loaded vesicles was quantified by Coomassie densitometry in ImageJ.

Structure, Volume *31*

Supplemental Information

Structure and regulation of the myotonic dystrophy kinase-related Cdc42-binding kinase

Linda Truebestein, Sumire Antonioli, Elisabeth Waltenberger, Charlotte Gehin, Anne-Claude Gavin, and Thomas A. Leonard

Structure and regulation of the myotonic dystrophy kinase-related Cdc42-binding kinase

Linda Truebestein[1,2], Sumire Antonioli[1,2,3], Elisabeth Waltenberger[1,2], Charlotte Gehin[4,5], Anne-Claude Gavin[4,6] and Thomas A. Leonard[1,2,7,*]

[1]Department of Structural and Computational Biology, Max Perutz Labs, Campus Vienna Biocenter 5, 1030 Vienna, Austria
[2]Department of Medical Biochemistry, Medical University of Vienna, 1090 Vienna, Austria
[3]Vienna BioCenter PhD Program, Doctoral School of the University of Vienna and Medical University of Vienna, 1030, Vienna, Austria
[4]European Molecular Biology Laboratory, EMBL, Meyerhofstrasse 1, D-69117 Heidelberg, Germany
[5]École Polytechnique Fédérale de Lausanne (EPFL), AI 1108, Station 19, CH-1015 Lausanne, Switzerland
[6]University of Geneva, Department of Cell Physiology and Metabolism, CMU Rue Michel-Servet 1 1211 Genève 4, Switzerland
[7]Lead contact

[*]Correspondence: thomas.leonard@meduniwien.ac.at

Supplementary Figures 1-4

Supplementary Table 1

Supplementary Figure Legends

Figure S1. Full-length MRCK adopts a ROCK-like extended, dimeric conformation, related to Figure 1.

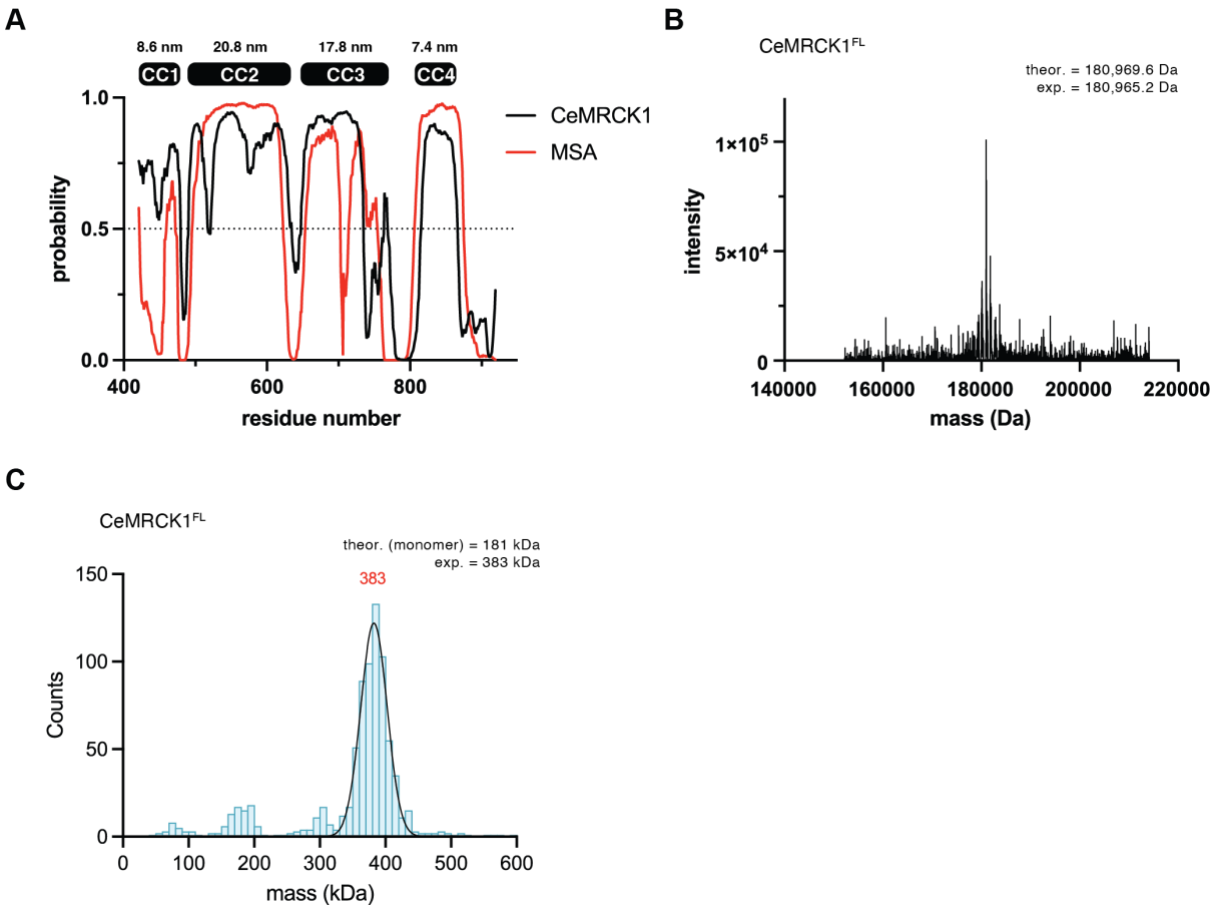

A. DeepCoil2 prediction of the coiled-coil domain of MRCK. Black line: *C. elegans* MRCK1; red line: prediction from multiple sequence alignment (MSA). Estimated lengths of contiguous predicted coiled-coil segments are indicated above the chart.

B. Intact, denaturing mass spectrometry of purified, full length CeMRCK1.

C. Mass photometry of purified, full length CeMRCK1 at 100nM.

Figure S2. Structure and properties of the C1-PH-CNH module of MRCK1, related to Figure 2.

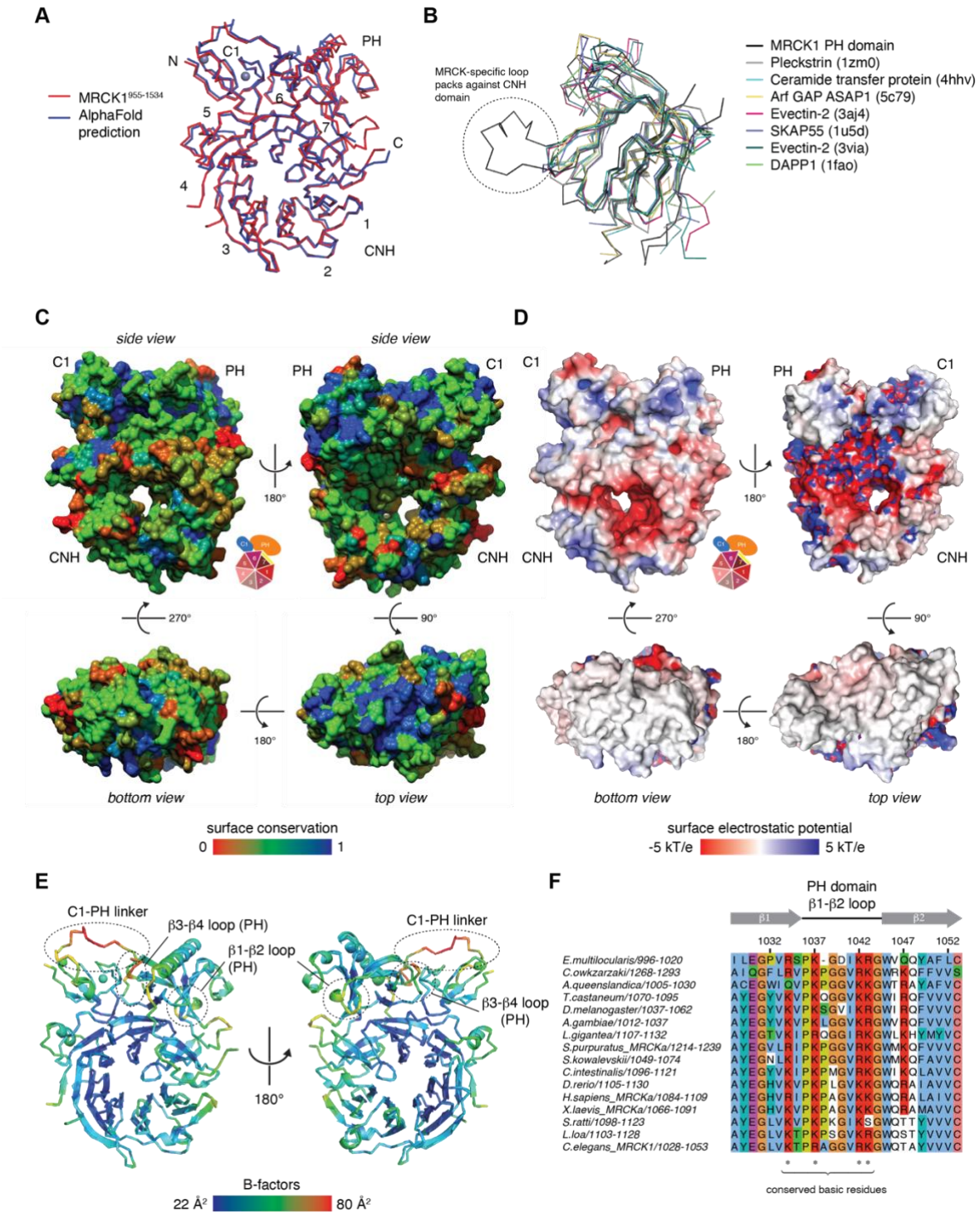

A. Superposition of AlphaFold prediction of MRCK1$^{955\text{-}1534}$ with experimentally determined structure. R.m.s.d. over all atoms = 0.906 Å.

B. Superposition of MRCK1 PH domain with closest structural homologs. Circled:

MRCK-specific loop that packs against the CNH domain.

C. Surface conservation maps of the MRCK1 C1-PH-CNH module. Color gradient: red (least conserved) – green – blue (most conserved).
D. Surface electrostatic potential analysis of MRCK1$^{955\text{-}1534}$.
E. B-factors of final refined model. Regions of higher B-factors include the C1-PH interdomain linker, and the β1-β2 and β3-β4 loops of the PH domain.
F. Sequence alignment of the β1-β2 loop of the PH domain of MRCK. Conserved basic residues in the canonical lipid binding pocket are indicated.

Figure S3. C1-PH-CNH module binds to activated Cdc42, related to Figure 4.

A

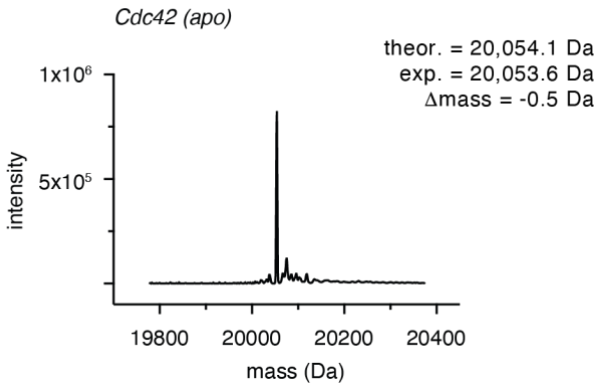

A. Intact, denaturing mass spectrometry of purified, C-terminally truncated Cdc42 (residues 2-178).

Figure S4. Model of DMPK kinases as molecular rulers, related to Figure 5.

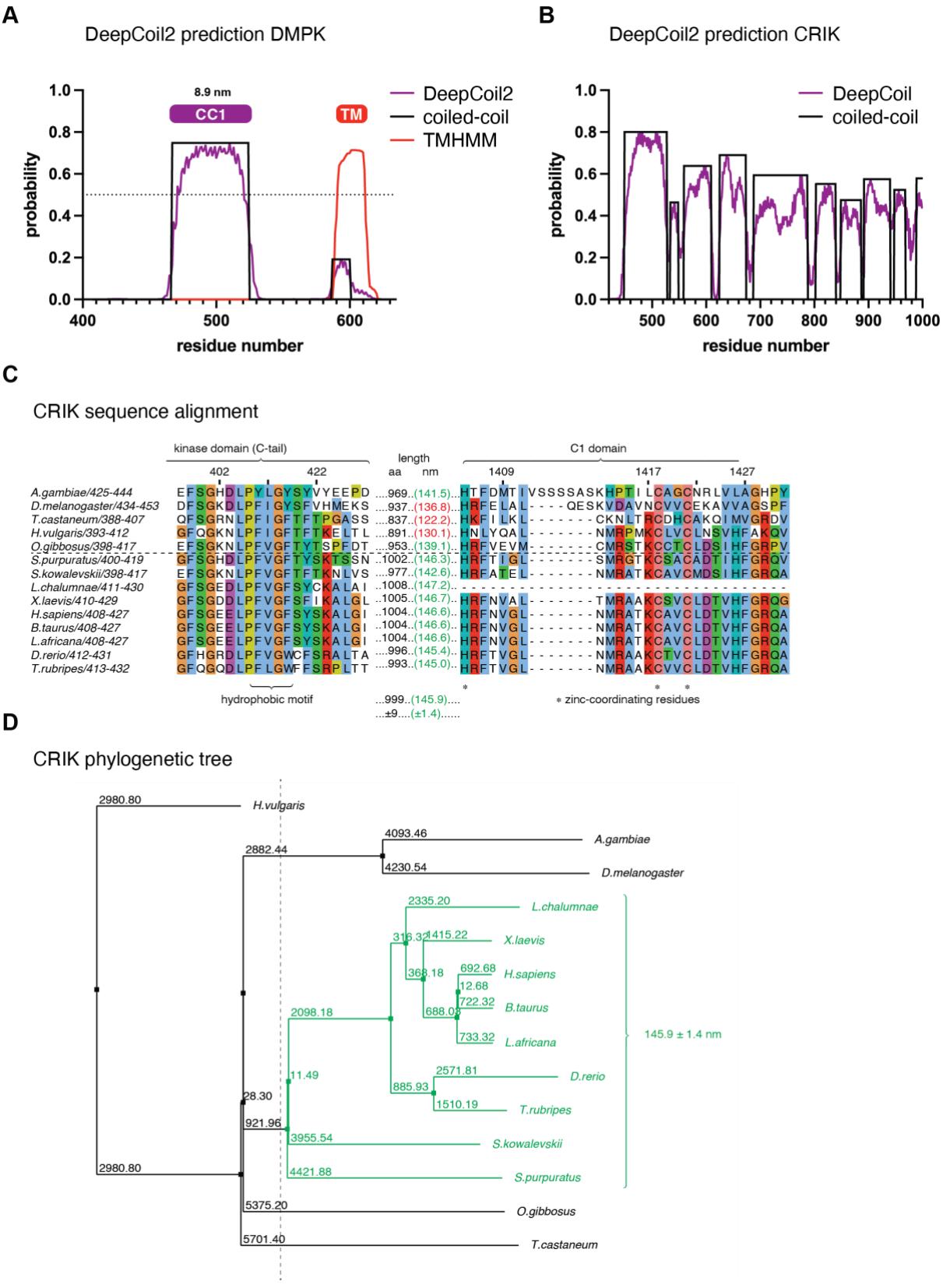

A. DeepCoil2 prediction of the coiled-coil domain (black) and TMHMM prediction of the transmembrane helix (red) of DMPK1.
B. DeepCoil2 prediction of the coiled-coil domain (black) of CRIK.
C. Partial sequence alignment of CRIK orthologs. The length of the intervening sequence between the end of the kinase domain and the beginning of the C1 domain is indicated as number of amino acids (black) and predicted length of a canonical parallel coiled-coil (green). Sequences below the dotted line all belong to the deuterostome branch of the phylogenetic tree which evolved ~550 Myr ago (dashed line).
D. Phylogenetic tree of CRIK orthologs. Deuterostomes are indicated with green branches. The mean predicted length and standard deviation of the coiled-coil domain for deuterostome CRIK orthologs is indicated.

Table S1. Data collection and refinement statistics for MRCK1$^{955-1534}$, related to Figure 2.

	MRCK1$^{955-1534}$ (PDB ID: 7Z6E)
Wavelength	0.97
Resolution range	49.07 - 2.14 (2.216 - 2.14)
Space Group	P1
Unit Cell	69.14 97.47 131.41 81.38 77.77 80.39
Total reflections	569580 (55034)
Unique reflections	171080 (16283)
Multiplicity	3.3 (3.3)
Completeness (%)	93.96 (89.59)
Mean I/sigma(I)	6.92 (1.05)
Wilson B-factor	35.63
R-merge	0.12 (1.17)
R-meas	0.15 (1.40)
R-pim	0.08 (0.76)
CC1/2	0.99 (0.43)
CC*	1.00 (0.77)
Reflections used in refinement	170148 (16275)
Reflections used for R-free	8480 (803)
R-work	0.19 (0.31)
R-free	0.24 (0.33)
CC(work)	0.96 (0.72)
CC(free)	0.93 (0.69)
Number of non-hydrogen atoms	21847
Macromolecules	20742
Ligands	10
Solvent	1095
Protein residues	
Chain A	957-1010, 1019-1064, 1071-1121, 1127-1351, 1366-1508
Chain B	957-1038, 1040-1063, 1071-1351, 1367-1509
Chain C	957-1065, 1068-1099, 1102-1121, 1127-1351, 1362-1509
Chain D	957-1011, 1016-1062, 1071-1351, 1367-1508
Chain E	957-1011, 1018-1064, 1070-1286, 1290-1347, 1368-1507
RMS(bonds)	0.01
RMS(angles)	0.99
Ramachandran favored (%)	96.21
Ramachandran allowed (%)	3.75
Ramachandran outliers (%)	0.04
Rotamer outliers (%)	3.57
Clashscore	6.52
Average B-factor	51.46
Macromolecules	51.80
Ligands	47.21
Solvent	45.09
Number of TLS groups	18

3.4 PHLPP2 is a pseudophosphatase that lost activity in the metazoan ancestor

3.4.1 Preamble

The growth-promoting protein kinase AKT is frequently reported to be hyperactive in many cancers. AKT activity is dependent on phosphorylation of its two regulatory motifs: its activation loop and its hydrophobic motif. Therefore, the phosphatases responsible for dephosphorylating these motifs play a crucial role in the negative regulation of cell growth and proliferation. One such phosphatase, PHLPP2, has been reported to dephosphorylate the hydrophobic motif of AKT, however the mechanism of its specificity is not known.

Upon further investigation, we found that PHLPP2 is actually a pseudophosphatase with no intrinsic catalytic activity. Key residues within the active site of PHLPP2 are not conserved and coordinate a single zinc ion as opposed to the typical two or three manganese ions. We demonstrate that an ancestral phosphatase belonging to the same genetic lineage as PHLPP2 from the amoebazoan *S. stenapodia* possesses catalytic activity, which was lost in the metazoan ancestor of PHLPP1 and PHLPP2.

This work has been published by PNAS in 2025.

3.4.2 Contribution statement

My main contribution to this publication was the supervision of the first author T. Husremović, who was my master's student for one year. In some cases, I worked with T. Husremović to purify recombinant proteins and perform experiments.

3.4.3 Publication

Husremović T., Meier V., Piëch L., Siess K.M., Antonioli S., Grishkovskaya I., Kircheva N., Angelova S.E., Wenzl K., Brandstätter A., Veis J., Miočić-Stošić F., Anrather D., Hartl M., Truebestein L., Cerron-Alvan L.M., Leeb M., Žagrović B., Hann S., Bock C., Ogris E., Dudev T., Irwin N.A.T., Haselbach D., Leonard T.A. (2025) PHLPP2 is a pseudophosphatase that lost activity in the metazoan ancestor. *Proc Natl Acad Sci U S A* 122 (14): e2417218122

PNAS RESEARCH ARTICLE | BIOCHEMISTRY OPEN ACCESS

PHLPP2 is a pseudophosphatase that lost activity in the metazoan ancestor

Tarik Husremović[a,1], Vanessa Meier[a,1], Lucas Pïech[a,b], Katharina M. Siess[a], Sumire Antonioli[a,b], Irina Grishkovskaya[c], Nikoleta Kircheva[d], Silvia E. Angelova[d,e], Karoline Wenzl[a], Andreas Brandstätter[f], Jiri Veis[a], Fran Miočić-Stošić[a,b,g], Dorothea Anrather[h,i], Markus Hartl[h,i], Linda Truebestein[a], Luis M. Cerron-Alvan[a,b,j], Martin Leeb[a,j], Bojan Žagrović[a,g], Stephan Hann[f], Christoph Bock[k,l], Egon Ogris[a], Todor Dudev[m], Nicholas A. T. Irwin[n], David Haselbach[c], and Thomas A. Leonard[a,2]

Affiliations are included on p. 11.

Edited by Wolfgang Peti, UConn Health, Farmington, CT; received August 23, 2024; accepted February 28, 2025 by Editorial Board Member Natalie G. Ahn

The phosphoinositide 3-kinase (PI3K) pathway is a major regulator of cell and organismal growth. Consequently, hyperactivation of PI3K and its downstream effector kinase, Akt, is observed in many human cancers. Pleckstrin homology domain leucine-rich repeat-containing protein phosphatases (PHLPP), two paralogous members of the metal-dependent protein phosphatase family, have been reported as negative regulators of Akt signaling and, therefore, tumor suppressors. However, the stoichiometry and identity of the bound metal ion(s), mechanism of action, and enzymatic specificity of these proteins are not known. Seeking to fill these gaps in our understanding of PHLPP biology, we unexpectedly found that PHLPP2 has no catalytic activity in vitro. Instead, we found that PHLPP2 is a pseudophosphatase with a single zinc ion bound in its catalytic center. Furthermore, we found that cancer genomics data do not support the proposed role of PHLPP1 or PHLPP2 as tumor suppressors. Phylogenetic analyses revealed an ancestral phosphatase that arose more than 1,000 Mya, but that lost activity at the base of the metazoan lineage. Surface conservation indicates that while PHLPP2 has lost catalytic activity, it may have retained substrate binding. Finally, using phylogenomics, we identify coevolving genes consistent with a scaffolding role for PHLPP2 on membranes. In summary, our results provide a molecular explanation for the inconclusive results that have hampered research on PHLPP and argue for a focus on the noncatalytic roles of PHLPP1 and PHLPP2.

phosphatase | Akt | PHLPP | signaling | cancer

Significance

PHLPP1 and PHLPP2 have previously been reported as protein phosphatases that specifically inactivate Akt, a pro-growth and survival kinase hyperactivated in many human cancers. Unexpectedly, we found that purified PHLPP2 has no detectable enzymatic activity in vitro. This observation can be rationalized by its unusual active site, which has diverged significantly from that of canonical metal-dependent phosphatases. Furthermore, we show that cancer genomics does not support a role for either PHLPP1 or PHLPP2 in cancer. Our findings argue for the exploration of alternative hypotheses regarding the role of PHLPP in Akt signaling and cancer, with a focus on its non-catalytic functions.

Cell and organismal growth depend on growth factors that activate receptor tyrosine kinases (RTKs) expressed on the surface of cells. RTK activation leads to the recruitment and activation of the small guanosine triphosphatase (GTPase) Ras and the lipid kinase phosphoinositide 3-kinase (PI3K), which synergistically drive the conversion of phosphatidylinositol-4,5-bisphosphate (PIP_2) in the plasma membrane into the lipid second messenger phosphatidylinositol-3,4,5-trisphosphate (PIP_3). PIP_3, in turn, recruits and activates a number of effector proteins, including the serine/threonine protein kinase Akt and its upstream activator phosphoinositide-dependent kinase 1 (PDK1) (1). PDK1 and Akt control essential aspects of cell growth, proliferation, differentiation, and metabolism, including glucose homeostasis (2). The lipid phosphatase and tumor suppressor, phosphatase and tensin homolog (PTEN), attenuates PI3K signaling by converting PIP_3 back into PIP_2. Mutations in Ras and PI3K, as well as loss of PTEN, are frequently observed in human cancers (3). Akt itself is also found mutated in cancer (4) and the rare overgrowth disorder, *Proteus* syndrome (5).

Akt is an AGC kinase, consisting of a PIP_3-binding pleckstrin homology (PH) domain and a kinase domain which bears two regulatory phosphorylation motifs. PDK1 phosphorylates Akt1 at T308 in its activation loop (6), while mTORC2 is widely believed to phosphorylate S473 in its hydrophobic motif (7). A third phosphorylation site in the C-terminal tail, the turn motif, is constitutively phosphorylated and controls Akt stability (8). Phosphorylation of T308 and S473 promotes disorder-to-order transitions of their respective motifs, leading to Akt activation (9).

PIP_3 turnover by PTEN leads to the dissociation and inactivation of Akt. An important, but poorly understood aspect of Akt inactivation is the dephosphorylation of T308 and S473 by protein phosphatases. T308 is dephosphorylated by protein phosphatase 2A (PP2A) (10, 11), whereas S473 has been reported to be the target of the PH domain leucine-rich repeat-containing protein phosphatases PHLPP1 and PHLPP2 (12, 13). The original identification of PHLPP as an Akt phosphatase was guided by the hypothesis that since S473

Author contributions: T.H., V.M., L.P., K.M.S., S.A., N.K., S.E.A., D.A., M.H., B.Ž., T.D., N.A.T.I., and T.A.L. designed research; T.H., V.M., L.P., K.M.S., S.A., N.K., S.E.A., K.W., A.B., F.M.-S., D.A., T.D., N.A.T.I., and T.A.L. performed research; J.V., L.T., S.H., and E.O. contributed new reagents/analytic tools; T.H., K.M.S., I.G., N.K., S.E.A., K.W., A.B., F.M.-S., D.A., M.H., L.M.C.-A., M.L., C.B., T.D., N.A.T.I., D.H., and T.A.L. analyzed data; C.B. advised on cancer genomics data analysis; and T.A.L. wrote the paper.

The authors declare no competing interest.

This article is a PNAS Direct Submission. W.P. is a guest editor invited by the Editorial Board.

[1]T.H. and V.M. contributed equally to this work.

[2]To whom correspondence may be addressed. Email: thomas.leonard@meduniwien.ac.at.

This article contains supporting information online at https://www.pnas.org/lookup/suppl/doi:10.1073/pnas.2417218122/-/DCSupplemental.

Published April 1, 2025.

phosphorylation is growth factor or serum-sensitive, such a phosphatase might contain a PH domain. The PH domain would presumably target it to the same membranes where Akt is activated (12). While PHLPP1 and PHLPP2 double knockout mice exhibit only a mild colitis resistance phenotype (14), their proposed repressive effects on Akt signaling have led to their designation as tumor suppressor genes (12, 15, 16). However, the mechanisms by which these phosphatases target Akt for dephosphorylation and the structural basis for their specificity are currently unknown.

Here, we show that—in contrast to previous reports—PHLPP2 is actually a pseudophosphatase. We show that PHLPP2 has a divergent catalytic site, exhibits no activity in vitro, and that cancer genomics does not support a role for either PHLPP1 or PHLPP2 in cancer. We corroborate the absence of phosphatase activity by showing that PHLPP evolved from an ancestral phosphatase that lost activity in the metazoan ancestor. Our findings refute the notion that PHLPP is an Akt phosphatase and question efforts to pharmacologically target PHLPP activity (15, 17). Finally, we establish a molecular and evolutionary basis for reassessing the biological roles of PHLPP1 and PHLPP2 as membrane-associated scaffold proteins.

Results

PHLPP2 Exhibits No Detectable Activity against Akt. We expressed GST-tagged, full-length human PHLPP2 in baculovirus-infected Sf9 insect cells and purified it to homogeneity by sequential affinity, ion exchange, and size-exclusion chromatography (*SI Appendix*, Fig. S1*A*). PHLPP2 was confirmed to be predominantly monomeric by mass photometry (*SI Appendix*, Fig. S1*B*) and the masses of all recombinant PHLPP2 constructs were verified by denaturing mass spectrometry (*SI Appendix*, Fig. S1 *C–E*). PHLPP2 and all mutants were confirmed to be properly folded by analytical size-exclusion chromatography (*SI Appendix*, Fig. S1*F*) and thermal stability assays (*SI Appendix*, Fig. S1*G*). Addition of EDTA to PHLPP2 did not affect its global thermal stability (*SI Appendix*, Fig. S1*G*).

Akt has been reported as a substrate of both PHLPP1 and PHLPP2 in mammalian cells (12, 13, 18). Fig. 1*A* shows the structure of the kinase domain of Akt alongside the sequence motifs of its activation loop and hydrophobic motif. According to reports, PHLPP is specific for the hydrophobic motif (pS473). To test the activity of recombinant PHLPP2 against synthetic Akt phosphopeptides, we monitored phosphate production in a malachite green assay (MGA). As a control, we assayed a mutant of PHLPP2 (D1024N) (*SI Appendix*, Fig. S1*E*), designed to abrogate catalytic activity (18). Unexpectedly, PHLPP2^{D1024N} exhibited comparable activity to wild-type PHLPP2 against the Akt1 activation loop peptide (Fig. 1*B*). When assayed against both the activation loop and hydrophobic motif peptides, we detected very low, but variable activity from multiple independent preparations of wild-type PHLPP2. This activity, however, was entirely lost upon treatment of each preparation with 12.5 nM okadaic acid (Fig. 1 *C* and *D*), a highly specific PP2A/PP4/PP6 inhibitor and toxin produced by several species of dinoflagellate (19, 20). Since previous reports have implicated PP2A in Akt1 dephosphorylation (10, 11, 21), we suspected contamination of purified PHLPP2 with PP2A. As a control, we assayed the activity of recombinant PP2A against both peptides, which exhibited a specific activity 50-fold greater than any of our PHLPP2 preparations (Fig. 1 *E* and *F*). Inhibition of all phosphatase activity in our PHLPP2 assays occurred despite PHLPP2 being present in molar excess over okadaic acid in all but one concentration. Finally, PHLPP2 exhibited no activity against either pT308 or pS473 of stoichiometrically phosphorylated full-length Akt1 (prepared according to ref. 22) under the assay conditions of the study that reported phosphatase activity of PHLPP for the first time (12) (*SI Appendix*, Fig. S2 *A–C*).

Suspecting that recombinant PHLPP2 preparations may be contaminated with one or more phosphatases of the PP2A family, we subjected purified PHLPP2 to peptide fingerprinting mass spectrometry. While PHLPP2 was estimated to be more than 99.9% pure, peptides of all three subunits of *Spodoptera frugiperda* PP2A were detected (Fig. 1*G*). A total of 13 unique peptides corresponding to the PP2A catalytic (C) subunit (2), A-subunit (9), and B55 (B) regulatory subunit (2) were measured. With a mass of 157 kDa, the PP2A heterotrimer is very close in mass to PHLPP2 (147 kDa), such that they cannot be separated by size-exclusion chromatography. The identification of PP2A holoenzymes in recombinant PHLPP2 preparations explains the okadaic acid sensitivity of the observed phosphatase activity (Fig. 1 *C* and *D*).

To assess whether contaminating phosphatase activity may have been the source of literature reports of PHLPP activity, we immunoprecipitated ectopically expressed V5-tagged PHLPP2 from HEK293 cells using V5 nanobody-conjugated magnetic beads and subjected the beads to a series of successive wash steps, while measuring phosphatase activity at each step in the absence and presence of okadaic acid (Fig. 1*H*). We observed that all of the measurable phosphatase could be successively washed away while keeping PHLPP2 constant, and that any residual activity could be inhibited by okadaic acid (Fig. 1*I* and *SI Appendix*, Fig. S2*D*).

The absence of phosphatase activity in PHLPP2 immunoprecipitated from mammalian cells suggested that PHLPP2 may not, in fact, attenuate Akt signaling. To address this directly, we generated PHLPP2 knockout HEK293 cells by CRISPR/Cas9 (*SI Appendix*, Fig. S3 *A* and *B*) and subjected them to transcriptomics analysis by RNAseq. Akt directly phosphorylates transcription factors of the FoxO family, leading to their sequestration in the nucleus by 14-3-3 proteins and consequent changes in the transcription of FoxO-activated genes (23). Deletion of PHLPP2 in HEK293 cells resulted in a significant deregulation of 641 genes (adj, $P \leq 0.05$; *SI Appendix*, Fig. S3*C* and Table S2). These genes were significantly enriched in RNA regulation and transcription, but no functional enrichment directly related to Akt activity was detected. Further supporting a role independent of the regulation of Akt, we could not detect a significant preferential deregulation of reported FOXO1 target genes in PHLPP2 KO cells (*SI Appendix*, Fig. S3 *D–G*) (24, 25).

PHLPP2 Is a Pseudophosphatase. To confirm that the activity detectable in our purified PHLPP2 came from contaminating PP2A, we modified our purification protocol to include the reverse affinity-based removal of PP2A. Produced by the cyanobacterium, *Microcystis aeruginosa,* microcystin-LR is a high-affinity irreversible inhibitor of PP1, PP2A, PP3, PP4, and PP6 phosphatases that forms a covalent bond to PP2A C269 (Fig. 2*A*) and binds to PP2A in the same binding site as okadaic acid (Fig. 2*B*) (20). Microcystin-LR can be covalently coupled to sepharose beads to create phosphatase inhibitor beads (PIBs, Fig. 2*C*) (26). We confirmed that our PIBs were highly effective in enriching PP2A from PHLPP2-expressing Sf9 cell lysates by label-free quantitative mass spectrometry (Fig. 2*D*). As a control, we treated an equivalent lysate with 500 nM okadaic acid to inhibit all okadaic acid-sensitive phosphatases. Since okadaic acid and microcystin-LR bind to the same pocket, PIBs should not enrich these phosphatases in the okadaic acid-treated control. Mass spectrometry analysis confirmed a 1,200-, 540-, and 65-fold enrichment of the PP2A C, A, and B subunits respectively. The three most enriched proteins

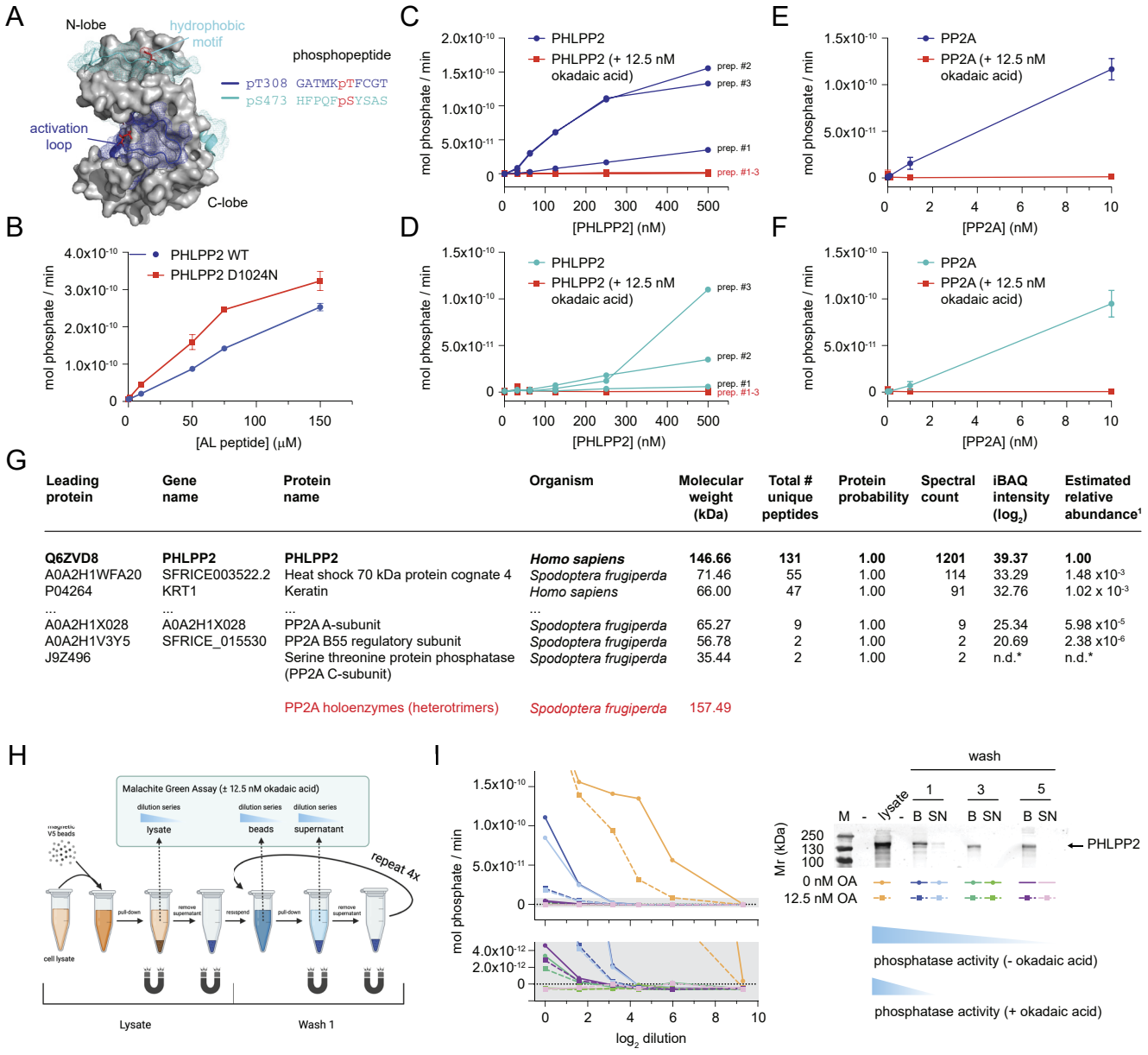

G

Leading protein	Gene name	Protein name	Organism	Molecular weight (kDa)	Total # unique peptides	Protein probability	Spectral count	iBAQ intensity (log_2)	Estimated relative abundance[1]
Q6ZVD8	**PHLPP2**	**PHLPP2**	***Homo sapiens***	**146.66**	**131**	**1.00**	**1201**	**39.37**	**1.00**
A0A2H1WFA20	SFRICE003522.2	Heat shock 70 kDa protein cognate 4	*Spodoptera frugiperda*	71.46	55	1.00	114	33.29	1.48 x 10^{-3}
P04264	KRT1	Keratin	*Homo sapiens*	66.00	47	1.00	91	32.76	1.02 x 10^{-3}
...	...	...	...						
A0A2H1X028	A0A2H1X028	PP2A A-subunit	*Spodoptera frugiperda*	65.27	9	1.00	9	25.34	5.98 x 10^{-5}
A0A2H1V3Y5	SFRICE_015530	PP2A B55 regulatory subunit	*Spodoptera frugiperda*	56.78	2	1.00	2	20.69	2.38 x 10^{-6}
J9Z496		Serine threonine protein phosphatase (PP2A C-subunit)	*Spodoptera frugiperda*	35.44	2	1.00	2	n.d.*	n.d.*
		PP2A holoenzymes (heterotrimers)	*Spodoptera frugiperda*	157.49					

Fig. 1. PHLPP2 exhibits no detectable activity against Akt. (*A*) Structure of the Akt1 kinase domain depicting activation loop (T308, blue) and hydrophobic motif (S473, cyan) phosphopeptides used in phosphatase assays. (*B*) Protein phosphatase activity of purified $PHLPP2^{D1024N}$ (red) compared to $PHLPP2^{WT}$ (blue) against the activation loop peptide of Akt. (*C*) Dephosphorylation of the activation loop peptide by three independent preparations of recombinant PHLPP2 purified from Sf9 insect cells (blue) ±12.5 nM okadaic acid (red). (*D*) Dephosphorylation of the hydrophobic motif peptide by three independent preparations of recombinant PHLPP2 purified from Sf9 insect cells (cyan) ±12.5 nM okadaic acid (red). (*E*) Dephosphorylation of the activation loop peptide by purified PP2A (blue) ±12.5 nM okadaic acid (red). (*F*) Dephosphorylation of the hydrophobic motif peptide by purified PP2A (cyan) ±12.5 nM okadaic acid (red). (*G*) Peptide fingerprinting mass spectrometry to identify proteins in recombinant PHLPP2 purified from insect cells. Red: molecular weight of Sf9 PP2A heterotrimers. (*H*) Schematic for immunoprecipitation of PHLPP2 from HEK293 cells and subsequent phosphatase assay. (*I*) Phosphatase activity of immunoprecipitated PHLPP2 determined after successive wash steps ±12.5 nM okadaic acid. B = beads, SN = supernatant.

correspond to the same three contaminating PP2A proteins observed in PHLPP2 preparations (Fig. 2*D* and *SI Appendix*, Fig. S4). Importantly, recombinant PHLPP2 was not observed to be enriched over the control lysate (Fig. 2*D*).

To remove contaminating PP2A from PHLPP2, we incubated the purified protein with PIBs following anion exchange chromatography and prior to size-exclusion chromatography (Fig. 2*E*). PIB-treated PHLPP2 lost all detectable activity against both Akt phosphopeptides (Fig. 2*F*), even at concentrations 500-fold above its known physiological concentration (27). Finally, we evaluated the capacity of PHLPP2 to dephosphorylate *para*-nitrophenyl phosphate (pNPP). PHLPP2 that had been purified via the scheme shown in Fig. 2*E* exhibited no activity against pNPP even in the absence of okadaic acid (Fig. 2*G*). As a positive control, pNPP was robustly dephosphorylated by lambda phosphatase under the same conditions (Fig. 2*G*). Importantly, since lambda phosphatase depends on manganese ions for its activity (28), which is also the case for PP2C family phosphatases (29, 30), this experiment explicitly rules out that PHLPP2 exhibits activity in the presence of millimolar concentrations of manganese. In summary, we were unable to detect any phosphatase activity associated with purified, PP2A-free PHLPP2.

The lack of PHLPP2 activity immediately begs the question of which phosphatase dephosphorylates and, thereby, inactivates Akt in cells. To assess the capacity of PP2A holoenzymes to dephosphorylate Akt1, we generated knockouts of the PP2A regulatory

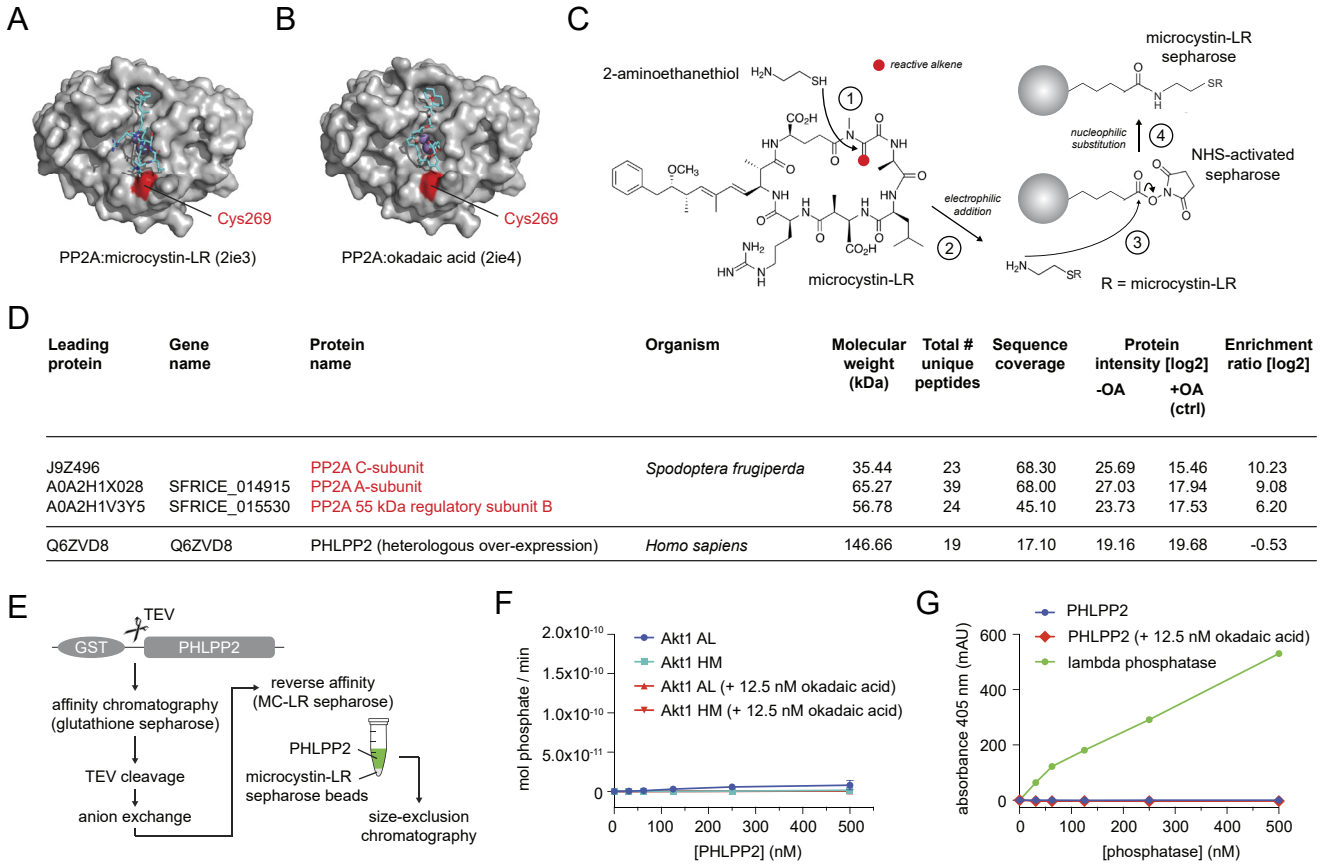

Leading protein	Gene name	Protein name	Organism	Molecular weight (kDa)	Total # unique peptides	Sequence coverage	Protein intensity [log2] -OA	Protein intensity [log2] +OA (ctrl)	Enrichment ratio [log2]
J9Z496		PP2A C-subunit	*Spodoptera frugiperda*	35.44	23	68.30	25.69	15.46	10.23
A0A2H1X028	SFRICE_014915	PP2A A-subunit		65.27	39	68.00	27.03	17.94	9.08
A0A2H1V3Y5	SFRICE_015530	PP2A 55 kDa regulatory subunit B		56.78	24	45.10	23.73	17.53	6.20
Q6ZVD8	Q6ZVD8	PHLPP2 (heterologous over-expression)	*Homo sapiens*	146.66	19	17.10	19.16	19.68	-0.53

Fig. 2. PHLPP2 is a pseudophosphatase. (*A*) Structure of the PP2A catalytic subunit bound to the covalent inhibitor microcystin-LR. (*B*) Structure of the PP2A catalytic subunit bound to okadaic acid. (*C*) Schematic for covalently coupling microcystin-LR to NHS-activated sepharose beads (26). (*D*) Tandem mass spectrometry analysis of proteins bound to microcystin-LR-conjugated beads after incubation with cell lysates of Sf9 cells heterologously overexpressing PHLPP2. (*E*) Purification scheme for affinity-based removal of PP2A family phosphatases from purified PHLPP2. (*F*) Dephosphorylation of activation loop (blue) and hydrophobic motif (cyan) peptides by PHLPP2 purified according to the scheme in *E* ± 12.5 nM okadaic acid (red). (*G*) Dephosphorylation of the generic phosphatase substrate para-nitrophenyl phosphate (pNPP, blue) by PHLPP2 purified according to the scheme in *E* ± 12.5 nM okadaic acid (red) or lambda phosphatase (green). Assay buffer includes 2 mM $MnCl_2$.

subunits B56α, B56β, B56ε, and a double knockout of B56α/ε in HAP1 cells. We compared the phosphorylation state of Akt1 T308 and S473 to wild-type HAP1 cells, including okadaic acid as a control. Knocking out the B56β subunit of PP2A led to a significant increase in Akt1 phosphorylation on both T308 and S473, while inhibition of all PP2A, PP4, and PP6 enzymes with okadaic acid led to a dramatic increase in Akt1 phosphorylation (*SI Appendix*, Fig. S5 *A–D*). These observations indicate that the PP2A B56β phosphatase is primarily responsible for Akt dephosphorylation in cells.

PHLPP2 Is a Zinc-Binding Protein with Altered Metal Ion Stoichiometry. Members of the metal-dependent family of protein phosphatases (PPM), exemplified by protein phosphatase Mg^{2+}/Mn^{2+}-dependent (PPM1A), depend on two or three divalent metal ions in their active site for catalysis (29–31) (Fig. 3*A*). PHLPP1 and PHLPP2, however, exhibit poor conservation of a number of key residues required for metal ion coordination (Fig. 3*B*).

To investigate whether the metal ion-binding properties of PHLPP2 could explain the lack of catalytic activity, we determined the identity and stoichiometry of any metal ions copurifying with PHLPP2 by size-exclusion chromatography coupled to inductively coupled plasma mass spectrometry (SEC-ICP-MS). This analysis revealed a single zinc ion in three independent preparations of the protein (Fig. 3 *C* and *D* and *SI Appendix*, Fig. S6 *A* and *B*). No signal for iron, copper, manganese, or calcium was detected (Fig. 3*C*).

Using the AlphaFold2-predicted structure of the phosphatase domain, which superimposes on the experimentally determined structure of PPM1A with a rmsd of 1.09 Å, the most likely constellation of zinc-coordinating residues was identified as C799, D820, D822, and D1024, which correspond to the M2 metal ion binding site (*SI Appendix*, Fig. S6*C*). The crystal structure of the related pseudophosphatase, [Transforming growth factor β-activated kinase 1]-binding protein 1 (TAB1), also revealed a single manganese ion in the M2 site (33) (*SI Appendix*, Fig. S6*D*). The M1 and M3 binding sites can be excluded on the basis of a lack of conservation of suitable residues at these positions. All four putative Zn^{2+}-coordinating residues (C799, D820, D822, and D1024) are invariant in chordate PHLPP1 and PHLPP2 genes (Fig. 3*B*). No other candidate cysteine, histidine, aspartate, or glutamate residues exist in the vicinity of the M2 site.

To determine experimentally whether C799 was a coordinating ligand of the zinc ion, we alkylated purified PHLPP2 under native conditions with iodoacetamide (IAA), followed by methyl methanethiosulfonate (MMTS) under denaturing conditions (Fig. 3*E*) and analyzed the peptides by tandem mass spectrometry (Fig. 3*F* and *SI Appendix*, Fig. S6*E*). C467 and C690 exhibited very high ratios of MMTS- to IAA-modified peptides, consistent with them being buried in the hydrophobic core of the LRR domain. Conversely, residues in the intrinsically disordered C-terminal tail all exhibited very low ratios, consistent with high solvent accessibility. C799, though predicted to be solvent exposed, exhibited a high MMTS to IAA ratio, indicating that it is protected from

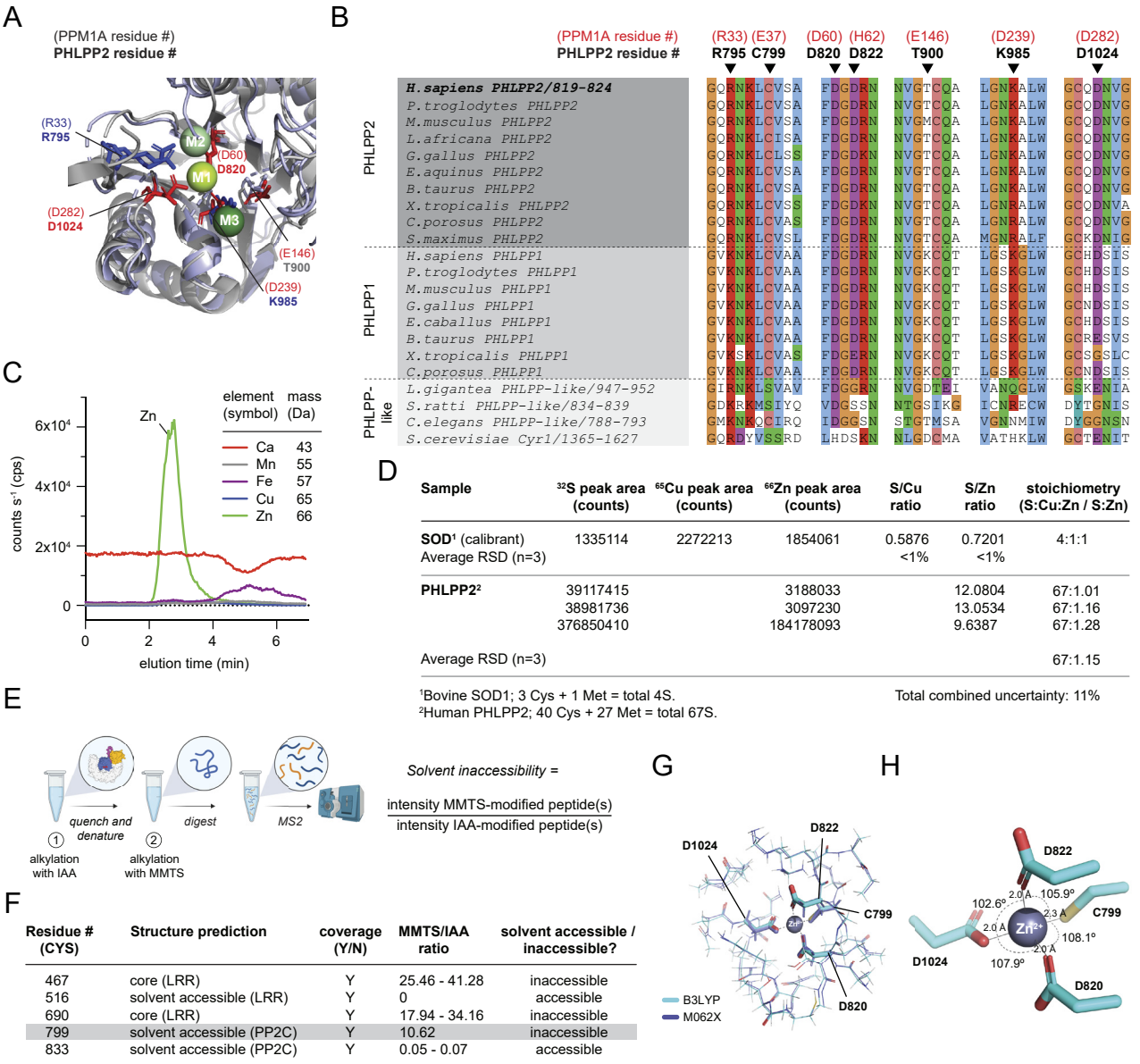

Sample	^{32}S peak area (counts)	^{65}Cu peak area (counts)	^{66}Zn peak area (counts)	S/Cu ratio	S/Zn ratio	stoichiometry (S:Cu:Zn / S:Zn)
SOD[1] (calibrant)	1335114	2272213	1854061	0.5876	0.7201	4:1:1
Average RSD (n=3)				<1%	<1%	
PHLPP2[2]	39117415		3188033		12.0804	67:1.01
	38981736		3097230		13.0534	67:1.16
	376850410		184178093		9.6387	67:1.28
Average RSD (n=3)						67:1.15

[1]Bovine SOD1; 3 Cys + 1 Met = total 4S.
[2]Human PHLPP2; 40 Cys + 27 Met = total 67S.
Total combined uncertainty: 11%

F

Residue # (CYS)	Structure prediction	coverage (Y/N)	MMTS/IAA ratio	solvent accessible / inaccessible?
467	core (LRR)	Y	25.46 - 41.28	inaccessible
516	solvent accessible (LRR)	Y	0	accessible
690	core (LRR)	Y	17.94 - 34.16	inaccessible
799	solvent accessible (PP2C)	Y	10.62	inaccessible
833	solvent accessible (PP2C)	Y	0.05 - 0.07	accessible

Fig. 3. PHLPP2 is a zinc-binding protein. (*A*) Catalytic site of PPM1A phosphatase (gray) superimposed on the AF2 model of the PHLPP2 PP2C domain (lilac). M1, M2, and M3 metal ions shown in spheres; metal coordinating amino acids shown in stick representation. PPM1A residue numbers shown in parentheses. (*B*) Multiple sequence alignment of the metal ion-coordinating motifs of PHLPP1, PHLPP2, and PHLPP-like proteins across a wide evolutionary time. PPM1A residue numbers shown above the alignment in parentheses. (*C*) ICP-MS chromatograms for recombinant human PHLPP2. (*D*) Calibration of PHLPP2:Zn^{2+} stoichiometry for three biological replicates. (*E*) Differential alkylation of PHLPP2 under native and denaturing conditions, coupled to mass spectrometry. (*F*) Differential alkylation of five different peptides of PHLPP2 (two representing buried cysteines, 2 representing surface exposed cysteines, and one encompassing C799). (*G*) Quantum mechanical simulation of zinc ion coordination sphere using the ONIOM method (32). Results of two quantum mechanical frameworks (B3LYP and M062X) are shown. (*H*) Geometry of the zinc-binding site from the simulations showing bond angles and lengths.

alkylation under native conditions. We therefore concluded that C799, in the M2 binding site, coordinates the single zinc ion that copurifies with PHLPP2.

To obtain a reasonable starting structure for the bound zinc ion, we performed explicit-solvent molecular dynamics (MD) simulations starting from the predicted PHLPP2 structure and using distance restraints between the ion and the coordinating atoms obtained from the structure of the C1D3 zinc finger of α-klotho (32). During the simulations, the global atom-positional rmsd with respect to the initially equilibrated structure reached a stable level of 0.2 to 0.25 nm after 10 ns, indicating that placement of the zinc ion in the M2 site is compatible with the folded conformation of the PP2C domain (*SI Appendix*, Fig. S6*F*). Since MD is not capable of modeling the electronic environment with sufficient accuracy, we modeled the binding site using the ONIOM approach (34). Here, atoms three bonds away from the zinc ion were treated quantum-mechanically, while atoms further away were treated semiempirically. To validate the ONIOM method, we simulated the zinc-binding site of α-klotho (32). The best scoring models of the zinc-binding site obtained from two quantum mechanical frameworks exhibited near tetrahedral geometry and bond lengths consistent with experimentally determined zinc clusters (Fig. 3 *G* and *H* and *SI Appendix*, Fig. S6 *G* and *H*). The free energy change associated with substitution of zinc for either manganese (Mn^{2+}) or iron (Fe^{2+}) was 7 to 12 kcal/mol (*SI Appendix*, Fig. S6*I*), indicating that the binding site is energetically optimized for zinc.

Since all known PPM family phosphatases require a minimum of two metal ions (M1 and M2) for catalytic activity, the absence of PHLPP2 activity can be explained.

Cancer Genomics Does Not Support a Role for PHLPP1 or PHLPP2 as Tumor Suppressors. Since we could not measure any detectable phosphatase activity of PHLPP2, we investigated the evidence for the role of PHLPP1 or PHLPP2 as tumor suppressors. Akt1, Akt2, and Akt3 are all established oncogenes with gain-of-function (GOF) mutational hotspots (4, 35) (Fig. 4*A*). To assess somatic mutations in either PHLPP1 or PHLPP2 associated with cancer, we plotted synonymous (silent) and nonsynonymous (missense) mutations reported in the Catalog of Somatic Mutations In Cancer (COSMIC) database (36) and compared them to two Cancer Gene Census (CGC) (35) tumor suppressor genes, two CGC oncogenes, and two randomly chosen olfactory receptor genes as negative controls (genes that are very unlikely to be functionally involved in cancer development). Fig. 4*B* shows that the rate of both synonymous and nonsynonymous mutations in *PHLPP1* and *PHLPP2* is comparable to those of the olfactory receptor genes *OR2A4* and *OR51E2*, while the rates of nonsynonymous mutations in both *PTEN* and *TP53*, as well as *KRAS* and *BRAF*, are significantly higher in human cancers. As expected, nonsynonymous loss-of-function (LOF) mutations are significantly enriched at hotspots (red) known to disrupt the function of *PTEN* and *TP53* tumor suppressor genes, while GOF mutations are enriched in *KRAS* and *BRAF* oncogenes (Fig. 4*C*). In contrast, *PHLPP1* and *PHLPP2* show comparable rates of nonsynonymous mutations to *OR2A4* and *OR51E2* throughout their coding regions. To determine whether copy number variants (CNVs) are significantly enriched in human cancers, we plotted copy number losses (CNL) and gains (CNG) for each of the genes in Fig. 4*B*. *PTEN* and *TP53* exhibit a high frequency of CNL (red) consistent with their tumor suppressive function, while *KRAS* and *BRAF* exhibit a high frequency of CNG (green) consistent with their oncogenic potential (Fig. 4*D*). In contrast, *PHLPP1* and *PHLPP2* show comparable rates of CNVs to *OR2A4* and *OR51E2*.

To assess whether PHLPP1 or PHLPP2 is an essential gene in cancer cells, we plotted the gene effect score for 1,100 cancer cell lines reported in the Dependency Map (DepMap) Public 23Q4+Score (Chronos) CRISPR knockout screens (37–40), 710 cancer cell lines reported in the Achilles+DRIVE+Marcotte (DEMETER2) RNA interference (RNAi) knockdown screens (41–44), and 317 cancer cell lines reported in copy number effect-corrected (39) CRISPR knockout screens (*SI Appendix*, Fig. S7 *A* and *B*). Neither PHLPP1 nor PHLPP2 were found to be essential in any of these screens. These observations are consistent with the viability of single knockout mice for both PHLPP1 (45, 46) and PHLPP2 (14), as well as a *PHLPP1*$^{-/-}$ *PHLPP2*$^{-/-}$ double knockout mouse (14), none of which have been reported to exhibit a significantly higher propensity to develop tumors.

Finally, we mapped the results of genome-wide association studies (GWAS) for the genetic loci of *PHLPP1* and *PHLPP2*. An intron variant in the neighboring *BCL2* gene has been associated with prostate carcinoma in two GWASs with *P*-values < 5.0×10^{-8} (47, 48), but no cancer associations have been reported for either *PHLPP1* or *PHLPP2* (*SI Appendix*, Fig. S7 *C* and *D*). Analysis of synthetic lethal screens of cancer cells also found no evidence for synthetic lethal interactions involving either PHLPP1 or PHLPP2 (49). In summary, there is scant evidence from disease genotypes, clinically reported variants, or GWASs to support that dysregulation of either PHLPP1 or PHLPP2 is associated with cancer.

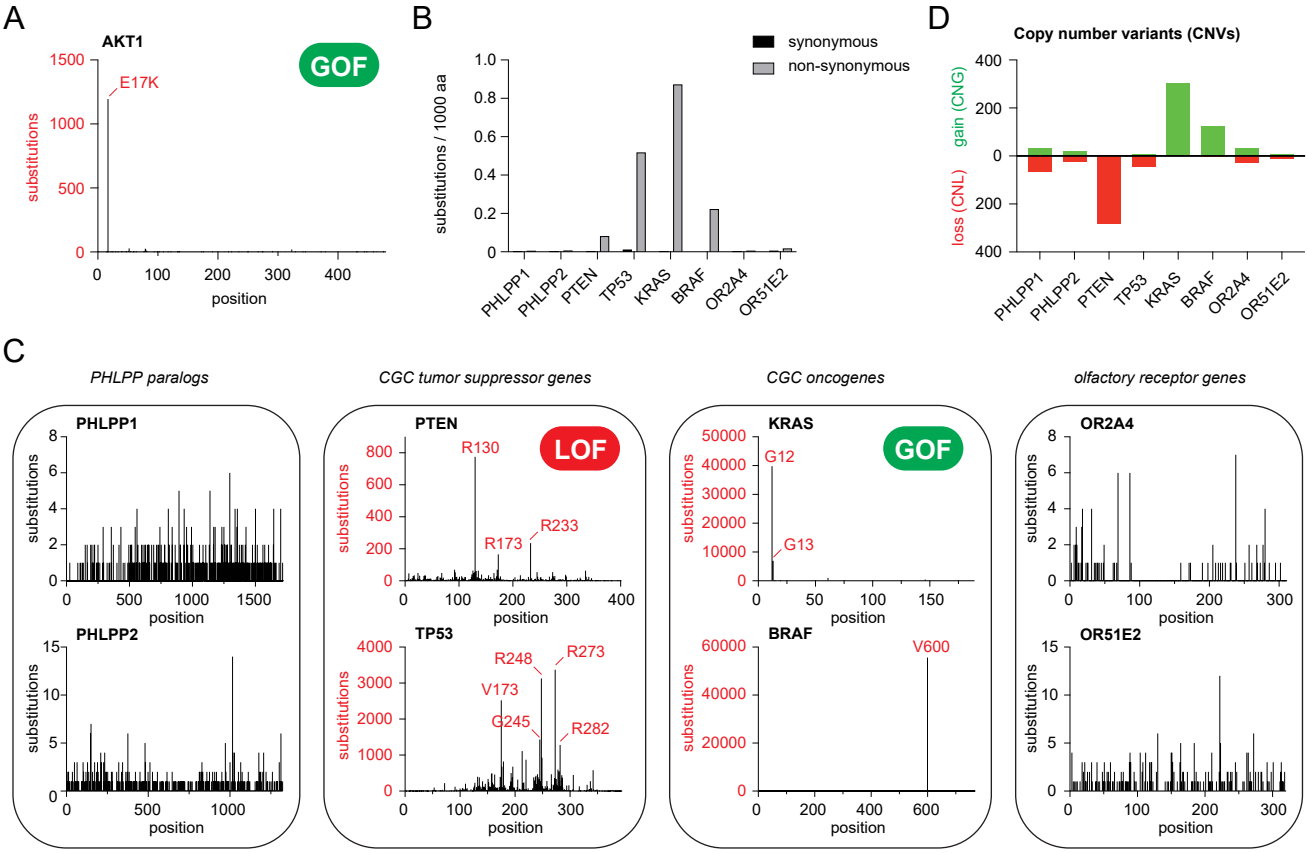

Fig. 4. Cancer genomics does not support a role of PHLPP1 or PHLPP2 as tumor suppressors. (*A*) Distribution of nonsynonymous mutations within the coding sequence of Akt1 (Tier 1 Cancer Gene Census cancer gene). Red: known hotspot mutations. (*B*) Number of synonymous and nonsynonymous substitutions per 1,000 amino acids reported in COSMIC for: PHLPP1 and PHLPP2; the tumor suppressor genes PTEN and TP53; the oncogenes KRAS and BRAF; the olfactory receptor genes OR2A4 and OR51E2. (*C*) Distribution of nonsynonymous mutations within the coding sequence of the genes represented in (*A*). Red: known hotspot mutations in CGC genes. (*D*) CNV for the genes represented in (*B*). Green: CNG; red: CNL.

PHLPP2 Exhibits a Conserved Arrangement of Its Regulatory Domains. Both PHLPP1 and PHLPP2 comprise an N-terminal Ras-associated (RA) domain followed by a PH domain, an LRR domain, and a C-terminal protein phosphatase 2C (PP2C) domain (Fig. 5*A*). Rotary shadowing electron microscopy revealed particles with a regular horseshoe-shaped conformation (Fig. 5 *B*, *Inset*) consistent with the AlphaFold2-predicted structure of PHLPP2 (Fig. 5 *C* and *D*). We next determined the structure of PHLPP2 by single-particle cryoelectron microscopy (cryoEM). We obtained two distinct reconstructions from the sample (see *SI Appendix*, Fig. S8 for sample micrographs, 2D class averages, and Fourier Shell Correlation curves). We interpret these as endpoints of a conformational continuum, which explains why the resolution of both maps is limited to 6 Å. The two conformations differ in the location of the PH domain, which appears to be very flexible and is the least resolved part of the structure. Furthermore, the LRR exhibits bending while the PP2C and RA domains show compaction, potentially changing the accessibility of the phosphatase domain. Nevertheless, the AlphaFold2 prediction of PHLPP2 fits well into the particle volumes for both conformations (Fig. 5 *E* and *F*).

Evolution and Diversification of PHLPP Genes. To provide clues to PHLPP function, we used phylogenetics to reconstruct the evolutionary history of the PHLPP protein family. The presence of PHLPP homologs in distantly related eukaryotes such as amoebozoans and parabasalids, suggests that the PHLPP family emerged early in eukaryotic evolution, presumably following the fusion of an LRR protein with a PP2C family phosphatase (Fig. 6 *A* and *B*). The ancestral gene encoded all residues known to be required for catalytic activity, including coordination of the M1 and M2 metal ions (Fig. 6 *C* and *D*). To confirm that the evolutionary ancestor of PHLPP was a bona fide phosphatase, we expressed and purified recombinant PHLPP-related LRR-PP2C phosphatase from the amoebazoan *Stenamoeba stenapodia* (SsLRR-PP2C). The correct mass of the recombinant protein was confirmed by mass spectrometry and mass photometry (*SI Appendix*, Fig. S9 *A* and *B*). As predicted, SsLRR-PP2C exhibited concentration-dependent phosphatase activity which was insensitive to okadaic acid and completely abrogated by divalent metal ion chelation (Fig. 6*E*).

In the last common ancestor of opisthokonts (e.g., animals and fungi), around 1,000 Mya, the ancestral LRR-PP2C gene gained an RA domain and was subsequently duplicated. Shortly thereafter, one copy of the gene gained a PH and a kinase domain, giving rise to the PHLPP family, whereas the other paralog gained a class III adenylate cyclase (AC), resulting in the emergence of the Cyr1 family (Fig. 6*B*). Retention of PHLPP and Cyr1 in unicellular holozoans [$P = 4.56 \times 10^{-5}$, Δ log-likelihood = 114.7, approximately unbiased (AU) test for monophyly], the closest unicellular relatives of animals, indicates that this duplication was followed by reciprocal loss of Cyr1 in metazoa and PHLPP in fungi. The ancestral Cyr1 was likely a pseudophosphatase given the lack of catalytic residues, but it later acquired a dimerization domain in fungi (Fig. 6 *A*–*C*). This contrasts with PHLPP, which only lost its active site in metazoans. Indeed, PHLPP homologs in unicellular holozoans not only encode active site residues, but in some cases include a C-terminal kinase domain (Fig. 6 *A*–*C*). Nonetheless, PHLPP was conserved throughout animal evolution before giving rise to PHLPP1 and PHLPP2 following a duplication event in the common ancestor of vertebrates or gnathostomes. To better understand the impact of these evolutionary changes on PHLPP structure, we

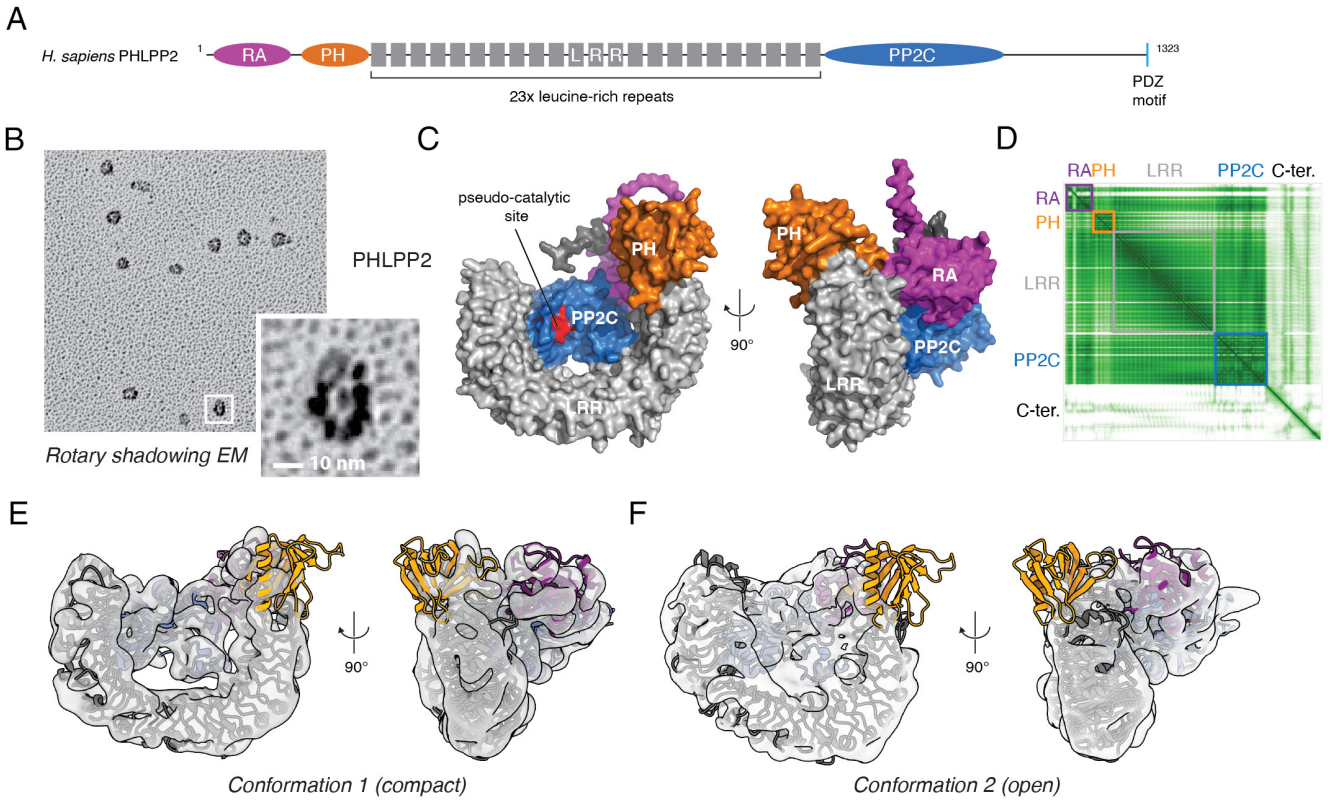

Fig. 5. PHLPP exhibits a conserved arrangement of its regulatory domains. (*A*) Domain architecture of human PHLPP2 [RA domain, magenta; PH domain, orange; LRR (gray); PP2C, blue; pseudo-catalytic site of PP2C domain, red]. (*B*) Rotary shadowing electron microscopy of recombinant PHLPP2. (*C*) Top-ranked AlphaFold2 model of human PHLPP2 [putative active site of PP2C domain, red]. (*D*) Predicted alignment error (PAE) plot for AF2 prediction in (*C*). PHLPP2 domain boundaries are indicated by colored boxes. (*E*) CryoEM maps of human PHLPP2 (conformation 1) at 6 Å resolution with the AlphaFold2-predicted structure of PHLPP2 fit to the map. (*F*) CryoEM maps of human PHLPP2 (conformation 2) at 6 Å resolution with the AlphaFold2-predicted structure of PHLPP2 fit to the map.

employed AlphaFold2 to predict the three-dimensional structures of representative proteins from across the LRR-PP2C phylogeny. The LRR-PP2C phosphatase of *Entamoeba* is structurally consistent with each of the evolutionarily descended derivatives, including vertebrate PHLPP1 and PHLPP2 and fungal Cyr1 (Fig. 6*F*). Together, these data suggest that PHLPP emerged through a complex history of neo- and subfunctionalization, based on a conserved LRR-PP2C chassis which repeatedly lost phosphatase activity, including at the origin of animals.

The structure and function of Cyr1 provide a useful comparison when considering the functional diversification of PHLPP. The acquisition of an RA domain, which preceded gene duplication at the base of the opisthokont clade, apparently gave rise to a Ras-dependent functionality in fungal Cyr1. *Saccharomyces cerevisiae* Cyr1 AC activity is stimulated by GTP-bound RAS1 or RAS2 (51), homologs of human KRAS. AlphaFold2 prediction of the RAS1/2:Cyr1 interaction converges on five identical models of very high confidence (*SI Appendix*, Fig. S9*C*) that are superimposable with experimentally determined structures of KRAS in complex with RA domains from AF6 (52) and RGL1 (53) (*SI Appendix*, Fig. S9*D*).

Reconstitution of yeast Cyr1 AC activity in the heterologous host *Escherichia coli* implies that Cyr1 and RAS are necessary and sufficient for cAMP production (51). Since RAS binding to the RA domain of Cyr1 is not predicted to induce any conformational change in the RA domain, an allosteric mechanism can, most likely, be ruled out. Class III ACs, of which Cyr1 is a member, depend on the homo-, hetero-, or pseudodimerization of two cyclase domains for cAMP production (54). Farnesylation of RAS is essential for Cyr1 activation (55), suggesting that RAS.GTP-dependent recruitment of Cyr1 to the plasma membrane may drive dimerization of the Cyr1 AC domain. AlphaFold2 prediction of a putative dimer of full-length Cyr1 converges on near-identical models (*SI Appendix*, Fig. S9*E*) in which the C-terminal ~400 amino acids exhibit a dimeric arrangement (*SI Appendix*, Fig. S9*F*) superimposable with the AC domains of Cya (*SI Appendix*, Fig. S9*G*), a bacterial AC, the structure of which has been experimentally determined by cryoelectron microscopy (56).

The C-terminal domain (CTD) predicted to dimerize Cyr1 has been reported to bind cyclase-associated protein (CAP), a multidomain protein which links Cyr1 to the actin cytoskeleton (57). Biochemical studies have narrowed down the region of CAP essential for Cyr1 binding to the N-terminal 36 amino acids (58). AlphaFold2 prediction of the complex between the CTD of Cyr1 and CAP converges on 5 identical and high-confidence models in which the dimeric CTD binds the N-terminal helix of CAP in a heterotetrameric arrangement (*SI Appendix*, Fig. S9*H*). This model therefore reconciles the mode and stoichiometry of binding of CAP to Cyr1. By combining the predicted models of interaction of Cyr1, RAS, and CAP, a high-confidence prediction of a Cyr1-RAS-CAP heterohexamer (2:2:2) can be obtained (*SI Appendix*, Fig. S9*I*).

Similar to Cyr1, acquisition of a PH domain in the PHLPP family appears to have coincided with C-terminal neofunctionalization through the emergence of a kinase domain. Curiously, phylogenetics suggests that this domain belongs to the AGC kinase family, which includes AKT and protein kinase C, another previously proposed target of PHLPP (*SI Appendix*, Fig. S9*J*) (59). Like the AC of Cyr1, this kinase domain was appended to the PHLPP C-terminus and may be positionally flexible, as indicated by AlphaFold2 predicted alignment error (PAE) plots (Fig. 6*F*). The kinase domain was subsequently lost in the metazoan ancestor, concurrently with the phosphatase active site. The functional implications of this domain remain unclear, but could imply an ancestral connection between PHLPP and AGC kinases.

PHLPP May Have an Alternative Scaffolding Role on Membranes. Despite the apparent pseudogenization of PHLPP, surface conservation maps of vertebrate PHLPP indicate two regions of high conservation: one on the surface of the PH domain and one corresponding to an ~50 amino acid insertion in the PP2C domain (Fig. 7*A*). Importantly, while the RA domain has been retained in vertebrate PHLPP, its binding to RAS has not. In fact, the surface of the RA domain used by Cyr1 to bind RAS exhibits the highest sequence divergence of any region in PHLPP1 and PHLPP2 (Fig. 7*A*). The acquisition of a PH domain may have substituted for RAS binding, although in the unicellular holozoan, *Corallichytrium limacisporum*, the PH domain appears to have been lost (Fig. 6*A*), suggesting a period of functional redundancy. Electrostatic surface potential analysis of PHLPP2 indicates a basic surface overlapping with the binding sites of phosphoinositides in structural homologs of the PH domain (60, 61) (Fig. 7*B*), suggesting a role for PHLPP at cellular membranes. Consistent with this hypothesis, PHLPP2 exhibited strong binding to phosphoinositides (PIs) in a protein–lipid overlay assay, with a preference for monophosphorylated PIs, particularly PI(4)P (Fig. 7*C*). Surface conservation within the LRR-PP2C cradle is coincident with an insertion between strands β7 and β8 of the PP2C domain called the FLAP subdomain (62) that is known to be important for substrate binding in PP2C phosphatases from bacteria (63) to higher eukaryotes (64). PP2C phosphatases found in *Desulfobacteria* exhibit homologous FLAP domains to PHLPP2 (Fig. 7*D*), suggesting that the evolutionary ancestor of the PHLPP2 PP2C domain may have originated in bacteria. These observations imply that vertebrate PHLPP lost phosphatase activity, but may have retained substrate binding.

To identify proteins associated with PHLPP2, we examined the distribution of PHLPP paralogs across the gnathostome phylogeny. Despite its presumed role in AKT and PKC regulation, PHLPP2 has been lost in at least four animal lineages, including twice independently in turtles, the squamata (snakes and lizards), and caecilians (Fig. 7*E*). Notably, these losses occurred despite the retention of AKT and PKC orthologs. To identify alternative coevolving genes, we used phylogenomic profiling, which revealed six genes with correlated distributions (Fig. 7*E*). While these genes lack clear functional connections to PHLPP2, many are membrane associated or secreted, suggesting the possibility of alternative, AKT-independent functional interactions at the membrane.

Discussion

PHLPP2 Is a Pseudophosphatase. We show that purified full-length PHLPP2 exhibits no detectable activity in vitro against either T308 or S473 of Akt, as well as the generic substrate pNPP, even at concentrations 500-fold higher than that found in the cell and at substrate concentrations >1,500-fold higher. This contrasts with the evolutionary ancestor of PHLPP, which exhibits robust metal-dependent, but okadaic acid-insensitive, activity. Our identification of contaminating PP2A in preparations of recombinant PHLPP2 highlights the need for more stringent purification conditions than have previously been employed in order to make confident assessments of the biochemical activity of PHLPP proteins.

Phosphatases of the PPM family catalyze hydrolysis of phosphorylated serine or threonine residues by virtue of a binuclear catalytic site in which two manganese ions are coordinated by a combination of aspartate side chains and ordered water molecules (30). A bridging water molecule coordinated by both Mn^{2+} ions is poised for nucleophilic attack on the substrate phosphate (29, 30) and the M2 metal ion determines the rate-limiting step in substrate hydrolysis (66). Mutations that disrupt metal binding

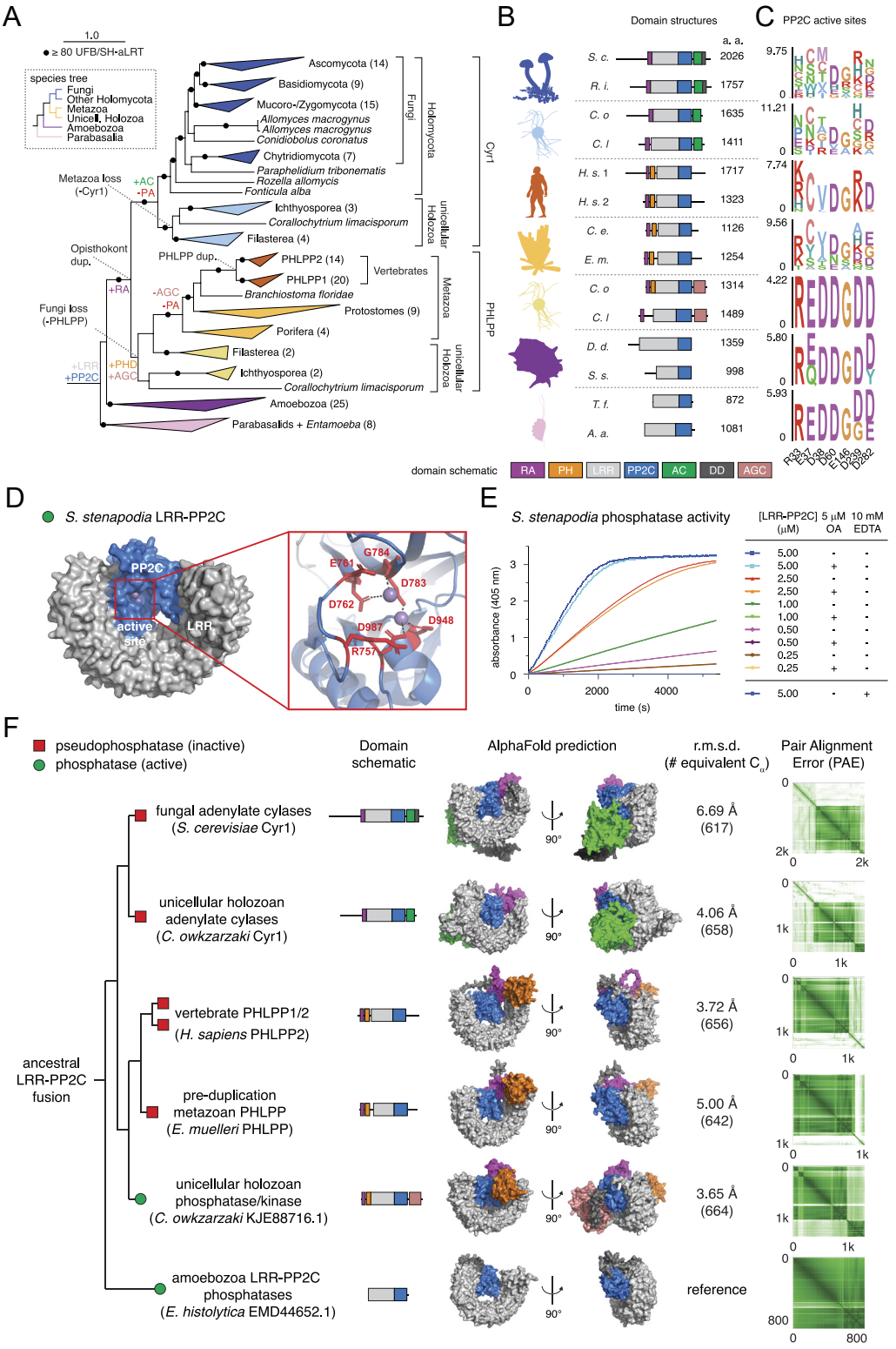

Fig. 6. Evolution and diversification of PHLPP genes. (*A*) Maximum-likelihood phylogeny of the LRR-PP2C protein family. Species and clade names have been added and the number of sequences within collapsed nodes are noted in parentheses. The gain and loss of genes, domains, and the PP2C active site (PA) have been mapped across the phylogeny based on Dollo parsimony. A species tree based on the taxa present in the phylogeny and current eukaryotic taxonomy (50) is shown for reference. The full phylogeny, domain annotations, and active site residues can be viewed at https://itol.embl.de/shared/9pitR7NesER8. (*B*) Representative domain architectures of proteins from across the LRR-PP2C phylogeny. Taxonomic groups are noted with cartoons obtained from Phylopic.org and protein lengths are shown in amino acids (a. a.). *S. c.*, *Saccharomyces cerevisiae*; *R. i.*, *Rhizophagus irregularis*; *C. o.*, *Capsaspora owczarzaki*; *C. l.*, *Corallochytrium limacosporum*; *H. s. 1*, *Homo sapiens* PHLPP1; *H. s.* 2, *Homo sapiens* PHLPP2; *C. e.*, *Caenorhabditis elegans*; *E. m.*, *Ephydatia muelleri*; *D. d.*, *Dictyostelium discoideum*; *S. s.*, *Stenamoeba stenapodia*; *T. f.*, *Tritrichomonas foetus*; *A. a.*, *Anaeramoeba ignava*. RA, Ras binding domain; AC, adenylate cyclase; PH, PH-domain; DD, dimerization domain; LRR, leucine-rich repeat; AGC, AGC kinase domain; PP2C, PP2C domain. (*C*) Sequence logos showing PP2C active site conservation. PPM1A residues are noted for reference. (*D*) AlphaFold3 prediction of *S. stenapodia* LRR-PP2C. *Inset*: predicted coordination of M1 and M2 metal ions in the catalytic site. (*E*) Phosphatase activity of *S. stenapodia* LRR-PP2C against pNPP. (*F*) Domain architectures, AlphaFold2-predicted structures, and their associated confidence metrics (PAE plots). The rmsd of the LRR-PP2C domains (over C_α atoms) of each structure from the ancestral LRR-PP2C phosphatase of *Entamoeba histolytica* is shown for comparison. Red squares: pseudophosphatase (inactive); green circles: phosphatase (active).

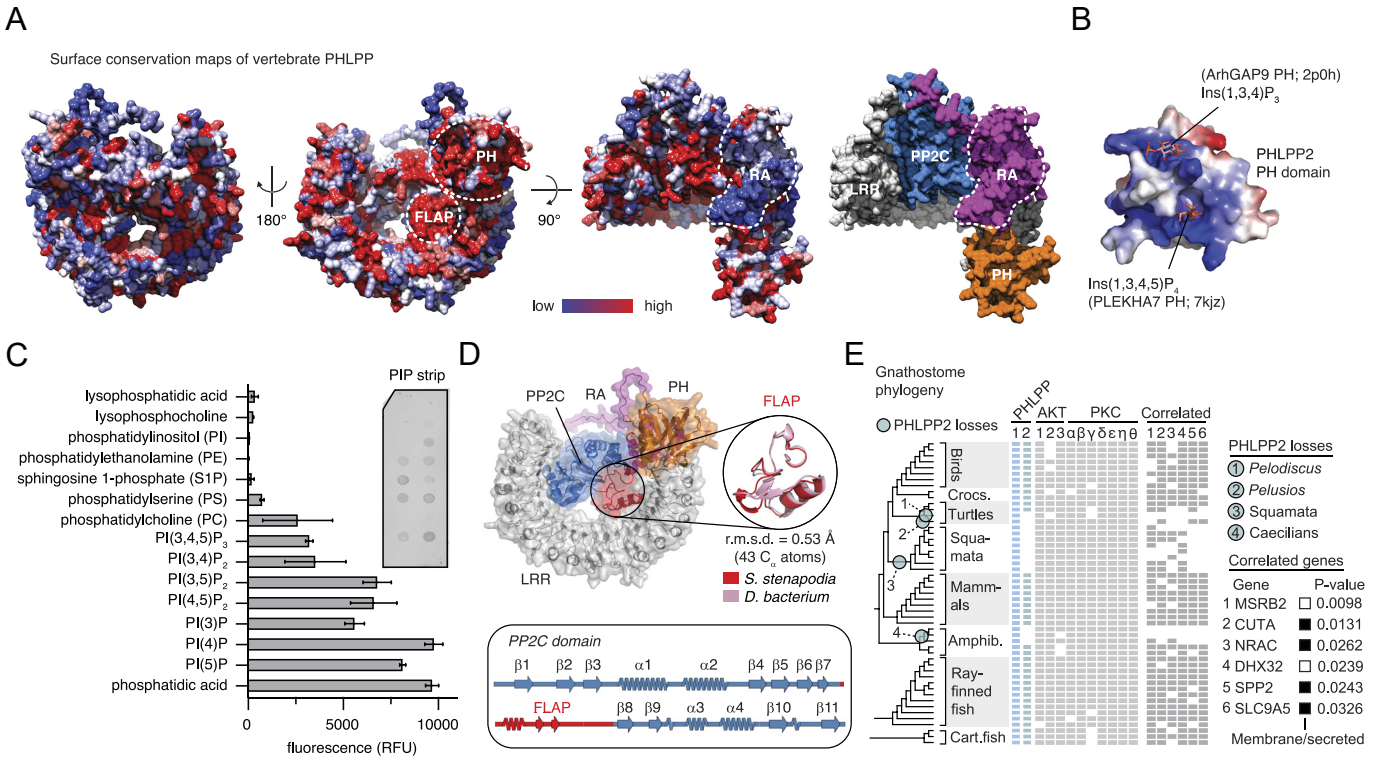

Fig. 7. PHLPP may have an alternative scaffolding role on membranes. (*A*) Surface conservation maps of vertebrate PHLPP. Low conservation (blue) to high conservation (red). Dashed white line: surface of the RA domain used to bind RAS in Cyr1. (*B*) Electrostatic surface potential map of the PH domain of H. sapiens PHLPP2. Phosphoinositide headgroup ligands superimposed from experimentally determined structures of homologous ArhGAP9 and PLEKHA7 PH domains identified by FoldSeek (65). (*C*) Lipid-protein overlay assay of PHLPP2 with phospholipids. Quantified signal is the mean of two independent replicates. (*D*) Conservation of the FLAP subdomain of the PHLPP PP2C domain. Secondary structure topology of the PP2C domain, indicating the FLAP subdomain in red. Circle *Inset*: superposition of AlphaFold-derived structures of FLAP-subdomain of *S. stenapodia* LRR-PP2C and a homologous PP2C phosphatase from the bacterium *Desulfobacterota bacterium*. (*E*) Phylogenomic profiling of gnathostomes to identify correlated gene presence and absence patterns for PHLPP2. Six of the most highly correlated genes are shown, alongside the presence/absence patterns of previously reported PHLPP2 substrates, Akt and PKC.

or divalent cations other than Mn^{2+} or Fe^{2+} (including Zn^{2+}) either abolish or strongly inhibit PPM1A activity (29, 67, 68). The observation of a single zinc ion in PHLPP2 with a complete coordination sphere suggests that PHLPP2 is incapable of canonical, binuclear-catalyzed phosphoester hydrolysis. Curiously, the carboxyl group of D822 in PHLPP2 occupies the same position as the phosphate group of a phosphorylated substrate peptide crystallized in complex with PPM1A (29), suggesting that loss of phosphatase activity may have coincided with a mutation that created a high-affinity zinc-binding site. Reports of pharmacologically active small molecule inhibitors of PHLPP should therefore be treated cautiously (15, 17). Since all known metal-dependent phosphatases of the PPM family, including ancient PPM homologs in cyanobacteria, depend on two or three divalent cations in their active sites for catalysis (69), the lack of phosphatase activity of PHLPP2 and the related PPM family pseudophosphatase TAB1 (33) is expected. On this basis, in fact, both PHLPP1 and PHLPP2 have previously been classified as pseudophosphatases (70). Although not explicitly tested in this study, the predicted loss of activity in the last common ancestor of metazoans implies that PHLPP1 is also a pseudophosphatase. This raises the obvious question of what function PHLPP fulfills in the cell.

Evidence Does Not Support a Role of PHLPP1 and PHLPP2 in Cancer. Conceptually, a tumor suppressive function of PHLPP follows logically from its identification as an Akt phosphatase. However, the lack of detectable phosphatase activity in vitro does not support this role. Reports characterizing PHLPP as a tumor suppressor have relied heavily on correlations between PHLPP expression levels and Akt phosphorylation in cancer cell lines (12, 13). Causation was originally inferred from observations that reintroduction of PHLPP into a glioblastoma cell line resulted in suppression of tumor growth (12). Knockdown of PHLPP2 in cells also resulted in a significant increase in Akt S473 phosphorylation, which was interpreted to be a direct consequence of the loss of phosphatase activity (13). In the context of our findings, however, some of the previously reported effects on Akt phosphorylation may have been a pleiotropic effect of the ectopic overexpression of PHLPP. In particular, dominant negative effects on membrane signaling cannot be ruled out given the binding of PHLPP to phosphoinositides. However, a recent study revealed that adipose tissue-specific ablation of PHLPP2 in mice as well as siRNA-mediated knockdown of PHLPP2 in 3T3-L1 adipocytes did not lead to any significant differences in Akt S473 phosphorylation (71), suggesting that PHLPP2 may not be involved in Akt signaling, even indirectly.

Oncogenes and tumor suppressor genes have been carefully curated in the Cancer Gene Census, regularly updated by the COSMIC curation team (35). This list, which now numbers more than 700 human genes, requires indisputable mutation patterns in specific cancers reported in at least two independent studies from different groups. Consistent with the lack of somatic mutations in cancer, background mutation rates comparable to olfactory receptor genes, and no patterns of copy number loss in cancer, neither PHLPP1 nor PHLPP2 qualifies as a tumor suppressor. This contrasts starkly with Akt, which is a comprehensively validated oncogene. Taken together with the observation that PHLPP2 is a pseudophosphatase, the proposed role of PHLPP in cancer deserves further scrutiny, with an emphasis on its noncatalytic functions.

PHLPP Evolved from an Ancestral Phosphatase. The evolution of PHLPP from an ancestral phosphatase into two structurally homologous, but possibly functionally unrelated proteins is an example of neo- and subfunctionalization of a protein scaffold. The acquisition of an RA domain early in evolution implies that ancestral homologs of PHLPP were once able to bind RAS, but later lost this ability, supported by the absence of PHLPP in the proximal interactome of human RAS proteins (72). It seems highly probable that the RA domain was retained, despite loss of RAS binding, due to the intimate contacts it makes between the PP2C and LRR domains. The loss of RAS binding coincides with the acquisition of a PH domain that binds phosphoinositides, presumably substituting RAS interaction with direct membrane binding as a means of membrane localization. In principle, this should narrow the search for components of whatever biological pathway PHLPP is involved in. That pathway, however, is unlikely to involve AC, since this was an adaptation in the paralogous gene family to PHLPP. Although CAP is highly conserved in vertebrates, including its N terminus, there is no evidence of any structural homolog of the CTD of Cyr1 in animals (65). Whatever PHLPP interacts with, it is most likely mediated by the highly conserved FLAP subdomain of its phosphatase domain, an insert in PP2C family phosphatases with a well-characterized role in substrate binding. It is curious that genes that have been lost coincidentally with PHLPP2 are predominantly plasma membrane or secreted proteins. Coupled with the preferential binding of PHLPP2 to PI(4)P, a marker of the secretory pathway, a scaffolding role on a membrane-bound subcompartment seems plausible. However, this will undoubtedly require further investigation in a cellular context.

Finally, it should be noted that PHLPP1 was originally identified and annotated as suprachiasmatic nucleus (SCN) circadian oscillatory protein (SCOP), on account of the circadian pattern of its gene expression in the SCN (73). SCOP was later proposed to play a role in the regulation of mitogen-activated protein kinase (MAPK) signaling and memory formation in the hippocampus (74). These data, in combination with the possible ancestral connection between PHLPP and AGC kinases, implied by the presence of a kinase domain in early PHLPP homologs, could suggest that PHLPP regulates kinases through noncatalytic mechanisms or may participate in vestigial nonfunctional kinase interactions.

In summary, PHLPP is a pseudophosphatase. Public cancer repositories and genome-wide datasets provide no evidence for a role of either PHLPP1 or PHLPP2 in cancer. Phylogenetic and biochemical analyses indicate that the ancestral gene that gave rise to PHLPP was a bona fide phosphatase, but that this activity was lost early in evolution. Although genetic ablation of either or both genes in mice is not lethal and results in no reported predisposition to cancer, an evolutionary pressure of some sort has retained both PHLPP1 and PHLPP2 in vertebrates. Efforts to determine the biological pathways that PHLPP participates in will undoubtedly require a focus on its tissue expression patterns, subcellular localization, and interactome. Many clues almost certainly lie in its evolution.

Materials and Methods

Protein Expression and Purification. Recombinant human PHLPP2 and *S. stenapodia* LRR-PP2C were expressed as N-terminal GST fusion proteins in baculovirus-infected *Spodoptera frugiperda* (Sf9) cells and purified to homogeneity using affinity, ion-exchange, and size-exclusion chromatography. Details of the buffers can be found in *SI Appendix*.

Electron Microscopy. Purified, recombinant PHLPP2 samples were diluted to a final concentration of 50 μg/mL in spraying buffer containing 100 mM ammonium acetate and 30% (v/v) glycerol, pH 7.4. After dilution, the samples were sprayed onto freshly cleaved mica chips and immediately transferred into a BAL-TEC MED020 high-vacuum evaporator equipped with electron guns. While rotating, the samples were coated with 0.7 nm platinum at an angle of 4 to 5°, followed by 10 nm carbon at 90°. The obtained replicas were floated off the mica chips and picked up on 400 mesh Cu/Pd grids. Grids were inspected in an FEI Morgagni 286D transmission electron microscope operated at 80 kV. Electron micrographs were acquired using an 11-megapixel Morada CCD camera from Olympus-SIS. Detailed methods for the preparation of samples for cryoelectron microscopy and image analysis can be found in *SI Appendix*.

MGA. MGAs were carried out according to the protocol of the Serine/Threonine Phosphatase Assay System (Promega). Serial dilutions of purified PHLPP2 or PP2A were incubated with 400 nM phospho-AL peptide (GATMKpTFCGT) or phospho-HM peptide (HFPQFpSYSAS) (GenScript) in the presence or absence of 12.5 nM okadaic acid for 1 h at 25 °C. For PHLPP2 immunoprecipitated from HEK293 cells, serial dilutions (five times 1:3 and one 1:10) were prepared in a 96-well plate. The samples were split into two groups, with one group supplemented with okadaic acid to a final concentration of 12.5 nM. All samples were combined with phosphorylated Akt1 activation loop peptide to a final concentration of 0.4 mM. Phosphate production was measured at 620 nm in a TECAN Spark® spectrofluorometer and converted into reaction rates (mol product/min) using a calibration curve derived from phosphate standards.

pNPP Phosphatase Assay. Serial dilutions of purified PHLPP2 or lambda phosphatase (purified in-house) were incubated with 10 mM pNPP in 20 mM Tris, pH 7.5, 150 mM KCl, 1 mM TCEP, and 2 mM $MnCl_2$ in the presence or absence of 12.5 nM okadaic acid for 1 h at 25 °C. For *S. stenapodia* LRR-PP2C, serial dilutions were incubated with 10 mM pNPP in 50 mM Tris, pH 7.5, 150 mM NaCl, 1 mM TCEP, and 0.1 mM MnCl2 in the presence or absence of 5 μM okadaic acid or 10 mM EDTA at 25 °C. Absorbance at 405 nm was measured every 30 s for 90 min in a TECAN Spark spectrofluorometer.

Data, Materials, and Software Availability. Mass spectrometry data have been deposited in PRIDE; EMDB (PXD045891; PXD045978; PXD052551; EMDB-51182; EMDB-51183) (75–79).

ACKNOWLEDGMENTS. We thank M. Brandstetter and the Electron Microscopy Facility of the Vienna Biocenter Core Facilities (VBCF) for help collecting rotary-shadowed EM images of PHLPP2. We acknowledge Diamond for access and support of the cryo-EM facilities at the UK national electron Bio-Imaging Centre, proposal BI25222-3, as well as local contact Alistair Siebert for support. Proteomics analyses were performed by the Mass Spectrometry Facility at Max Perutz Labs using the VBCF instrument pool. This work was supported by Austrian Science Fund grants P33066, P36212, and W1261 as well as a Scientific and Technological Cooperation Grant (Austria-Bulgaria) of the Austrian Agency for Education and Internationalisation (BG 05/2023) to T.A.L. and a Bulgarian National Science Fund grant to T.D. (KP-06-Austria/1). K.M.S. was supported by an Austrian Academy of Sciences DOC PhD Fellowship. F.M.-S. was supported by the Austrian Science Fund doc.fund program (B-112). D.H. and the Haselbach lab are supported by Boehringer Ingelheim.

Author affiliations: [a]Max Perutz Labs, University of Vienna and Medical University of Vienna, Vienna 1030, Austria; [b]Vienna BioCenter PhD Program, a Doctoral School of the University of Vienna and the Medical University of Vienna, Vienna A-1030, Austria; [c]Research Institute of Molecular Pathology, Vienna BioCenter, Vienna 1030, Austria; [d]Institute of Optical Materials and Technologies "Acad. J. Malinowski", Bulgarian Academy of Sciences, Sofia 1113, Bulgaria; [e]University of Chemical Technology and Metallurgy, Sofia 1756, Bulgaria; [f]Department of Chemistry, Institute of Analytical Chemistry, University of Natural Resources and Life Sciences, Vienna 1190, Austria; [g]Department of Structural and Computational Biology, Center for Molecular Biology, University of Vienna, Vienna 1030, Austria; [h]Max Perutz Labs, Mass Spectrometry Facility, Vienna Biocenter Campus, Vienna 1030, Austria; [i]Department of Biochemistry and Cell Biology, Center for Molecular Biology, University of Vienna, Vienna 1030, Austria; [j]Department of Microbiology, Immunobiology and Genetics, Center for Molecular Biology, University of Vienna, Vienna 1030, Austria; [k]Research Center for Molecular Medicine, Austrian Academy of Sciences, Vienna 1090, Austria; [l]Center for Medical Data Science, Institute of Artificial Intelligence, Medical University of Vienna, Vienna 1090, Austria; [m]Faculty of Chemistry and Pharmacy, Sofia University "St. Kliment Ohridski", Sofia 1164, Bulgaria; and [n]Gregor Mendel Institute, Austrian Academy of Sciences, Vienna BioCenter, Vienna 1030, Austria

1. K. M. Siess, T. A. Leonard, Lipid-dependent Akt-ivity: Where, when, and how. *Biochem. Soc. Trans.* **47**, 897–908 (2019).
2. B. D. Manning, A. Toker, AKT/PKB signaling: Navigating the network. *Cell* **169**, 381–405 (2017).
3. D. A. Fruman *et al.*, The PI3K pathway in human disease. *Cell* **170**, 605–635 (2017).
4. J. D. Carpten *et al.*, A transforming mutation in the pleckstrin homology domain of AKT1 in cancer. *Nature* **448**, 439–444 (2007).
5. M. J. Lindhurst *et al.*, A mosaic activating mutation in AKT1 associated with the Proteus syndrome. *N. Engl. J. Med.* **365**, 611–619 (2011).
6. D. Stokoe *et al.*, Dual role of phosphatidylinositol-3,4,5-trisphosphate in the activation of protein kinase B. *Science* **277**, 567–570 (1997).
7. D. D. Sarbassov, D. A. Guertin, S. M. Ali, D. M. Sabatini, Phosphorylation and regulation of Akt/PKB by the rictor-mTOR complex. *Science* **307**, 1098–1101 (2005).
8. W. J. Oh *et al.*, mTORC2 can associate with ribosomes to promote cotranslational phosphorylation and stability of nascent Akt polypeptide. *EMBO J.* **29**, 3939–3951 (2010).
9. J. Yang *et al.*, Crystal structure of an activated Akt/Protein Kinase B ternary complex with GSK3-peptide and AMP-PNP. *Nat. Struct. Biol.* **9**, 940–944 (2002).
10. Y.-C. Kuo *et al.*, Regulation of phosphorylation of Thr-308 of Akt, cell proliferation, and survival by the B55alpha regulatory subunit targeting of the protein phosphatase 2A holoenzyme to Akt. *J. Biol. Chem.* **283**, 1882–1892 (2008).
11. S. Padmanabhan *et al.*, A PP2A regulatory subunit regulates C. elegans insulin/IGF-1 signaling by modulating AKT-1 phosphorylation. *Cell* **136**, 939–951 (2009).
12. T. Gao, F. Furnari, A. C. Newton, PHLPP: A phosphatase that directly dephosphorylates Akt, promotes apoptosis, and suppresses tumor growth. *Mol. Cell* **18**, 13–24 (2005).
13. J. Brognard, E. Sierecki, T. Gao, A. C. Newton, PHLPP and a second isoform, PHLPP2, differentially attenuate the amplitude of Akt signaling by regulating distinct Akt isoforms. *Mol. Cell* **25**, 917–931 (2007).
14. Y.-A. Wen *et al.*, Loss of PHLPP protects against colitis by inhibiting intestinal epithelial cell apoptosis. *Biochim. Biophys. Acta* **1852**, 2013–2023 (2015).
15. D. G. Nowak *et al.*, The PHLPP2 phosphatase is a druggable driver of prostate cancer progression. *J. Cell Biol.* **218**, 1943–1957 (2019).
16. M. Chen *et al.*, Identification of PHLPP1 as a tumor suppressor reveals the role of feedback activation in PTEN-mutant prostate cancer progression. *Cancer Cell* **20**, 173–186 (2011).
17. E. Sierecki, W. Sinko, J. A. McCammon, A. C. Newton, Discovery of small molecule inhibitors of the PH domain leucine-rich repeat protein phosphatase (PHLPP) by chemical and virtual screening. *J. Med. Chem.* **53**, 6899–6911 (2010).
18. E. Sierecki, A. C. Newton, Biochemical characterization of the phosphatase domain of the tumor suppressor PH domain leucine-rich repeat protein phosphatase. *Biochemistry* **53**, 3971–3981 (2014).
19. K. Tachibana *et al.*, Okadaic acid, a cytotoxic polyether from two marine sponges of the genus Halichondria. *J. Am. Chem. Soc.* **103**, 2469–2471 (1981).
20. Y. Xing *et al.*, Structure of protein phosphatase 2A core enzyme bound to tumor-inducing toxins. *Cell* **127**, 341–353 (2006).
21. M. Andjelković *et al.*, Activation and phosphorylation of a pleckstrin homology domain containing protein kinase (RAC-PK/PKB) promoted by serum and protein phosphatase inhibitors. *Proc. Natl. Acad. Sci. U.S.A.* **93**, 5699–5704 (1996).
22. L. Truebestein *et al.*, Structure of autoinhibited Akt1 reveals mechanism of PIP3-mediated activation. *Proc. Natl. Acad. Sci. U.S.A.* **118**, e2101496118 (2021).
23. A. Brunet *et al.*, Akt promotes cell survival by phosphorylating and inhibiting a Forkhead transcription factor. *Cell* **96**, 857–868 (1999).
24. L. Santini *et al.*, FoxO transcription factors actuate the formative pluripotency specific gene expression programme. *Nat. Commun.* **15**, 7879 (2024).
25. D.-J. Shin *et al.*, Genome-wide analysis of FoxO1 binding in hepatic chromatin: Potential involvement of FoxO1 in linking retinoid signaling to hepatic gluconeogenesis. *Nucleic Acids Res.* **40**, 11499–11509 (2012).
26. B. L. Brauer *et al.*, Affinity-based profiling of endogenous phosphoprotein phosphatases by mass spectrometry. *Nat. Protoc.* **16**, 4919–4943 (2021).
27. M. Y. Hein *et al.*, A human interactome in three quantitative dimensions organized by stoichiometries and abundances. *Cell* **163**, 712–723 (2015).
28. W. C. Voegtli, D. J. White, N. J. Reiter, F. Rusnak, A. C. Rosenzweig, Structure of the bacteriophage lambda Ser/Thr protein phosphatase with sulfate ion bound in two coordination modes. *Biochemistry* **39**, 15365–15374 (2000).
29. S. Debnath *et al.*, A trapped human PPM1A-phosphopeptide complex reveals structural features critical for regulation of PPM protein phosphatase activity. *J. Biol. Chem.* **293**, 7993–8008 (2018).
30. A. K. Das, N. R. Helps, P. T. Cohen, D. Barford, Crystal structure of the protein serine/threonine phosphatase 2C at 2.0 A resolution. *EMBO J.* **15**, 6798–6809 (1996).
31. K. Tanoue *et al.*, Binding of a third metal ion by the human phosphatases PP2Cα and Wip1 is required for phosphatase activity. *Biochemistry* **52**, 5830–5843 (2013).
32. G. Chen *et al.*, α-Klotho is a non-enzymatic molecular scaffold for FGF23 hormone signalling. *Nature* **553**, 461–466 (2018).
33. S. H. Conner *et al.*, TAK1-binding protein 1 is a pseudophosphatase. *Biochem. J* **399**, 427–434 (2006).
34. L. W. Chung *et al.*, The ONIOM method and its applications. *Chem. Rev.* **115**, 5678–5796 (2015).
35. Z. Sondka *et al.*, The COSMIC Cancer Gene Census: Describing genetic dysfunction across all human cancers. *Nat. Rev. Cancer* **18**, 696–705 (2018).
36. Z. Sondka *et al.*, COSMIC: A curated database of somatic variants and clinical data for cancer. *Nucleic Acids Res.* **52**, D1210–D1217 (2024).
37. J. M. Dempster *et al.*, Chronos: A cell population dynamics model of CRISPR experiments that improves inference of gene fitness effects. *Genome Biol.* **22**, 343 (2021).
38. C. Pacini *et al.*, Integrated cross-study datasets of genetic dependencies in cancer. *Nat. Commun.* **12**, 1661 (2021).
39. R. M. Meyers *et al.*, Computational correction of copy number effect improves specificity of CRISPR-Cas9 essentiality screens in cancer cells. *Nat. Genet.* **49**, 1779–1784 (2017).
40. J. M. Dempster *et al.*, Extracting biological insights from the project Achilles genome-scale CRISPR screens in cancer cell lines. bioRxiv [Preprint] (2019). https://doi.org/10.1101/720243. Accessed 2024.
41. A. Tsherniak *et al.*, Defining a cancer dependency map. *Cell* **170**, 564–576.e16 (2017).
42. E. R. McDonald III *et al.*, Project DRIVE: A compendium of cancer dependencies and synthetic lethal relationships uncovered by large-scale, deep RNAi screening. *Cell* **170**, 577–592.e10 (2017).
43. R. Marcotte *et al.*, Functional genomic landscape of human breast cancer drivers, vulnerabilities, and resistance. *Cell* **164**, 293–309 (2016).
44. J. M. McFarland *et al.*, Improved estimation of cancer dependencies from large-scale RNAi screens using model-based normalization and data integration. *Nat. Commun.* **9**, 4610 (2018).
45. S. Miyamoto *et al.*, PHLPP-1 negatively regulates Akt activity and survival in the heart. *Circ. Res.* **107**, 476–484 (2010).
46. B. Chen, J. A. Van Winkle, P. D. Lyden, J. H. Brown, N. H. Purcell, PHLPP1 gene deletion protects the brain from ischemic injury. *J. Cereb. Blood Flow Metab.* **33**, 196–204 (2013).
47. D. V. Conti *et al.*, Trans-ancestry genome-wide association meta-analysis of prostate cancer identifies new susceptibility loci and informs genetic risk prediction. *Nat. Genet.* **53**, 65–75 (2021).
48. F. R. Schumacher *et al.*, Association analyses of more than 140,000 men identify 63 new prostate cancer susceptibility loci. *Nat. Genet.* **50**, 928–936 (2018).
49. S. Srivatsa *et al.*, Discovery of synthetic lethal interactions from large-scale pan-cancer perturbation screens. *Nat. Commun.* **13**, 7748 (2022).
50. F. Burki, A. J. Roger, M. W. Brown, A. G. B. Simpson, The new tree of eukaryotes. *Trends Ecol. Evol.* **35**, 43–55 (2020).
51. I. Uno *et al.*, Reconstitution of the GTP-dependent adenylate cyclase from products of the yeast CYR1 and RAS2 genes in Escherichia coli. *Proc. Natl. Acad. Sci. U.S.A.* **82**, 7855–7859 (1985).
52. M. J. Smith *et al.*, Evolution of AF6-RAS association and its implications in mixed-lineage leukemia. *Nat. Commun.* **8**, 1099 (2017).
53. B. J. Eves *et al.*, Structures of RGL1 RAS-association domain in complex with KRAS and the oncogenic G12V mutant. *J. Mol. Biol.* **434**, 167527 (2022).
54. B. Khannpnavar, V. Mehta, C. Qi, V. Korkhov, Structure and function of adenylyl cyclases, key enzymes in cellular signaling. *Curr. Opin. Struct. Biol.* **63**, 34–41 (2020).
55. Y. Kuroda, N. Suzuki, T. Kataoka, The effect of posttranslational modifications on the interaction of Ras2 with adenylyl cyclase. *Science* **259**, 683–686 (1993).
56. V. Mehta *et al.*, Structure of Mycobacterium tuberculosis Cya, an evolutionary ancestor of the mammalian membrane adenylyl cyclases. *Elife* **11**, e77032 (2022).
57. J. Field *et al.*, Cloning and characterization of CAP, the S. cerevisiae gene encoding the 70 kd adenylyl cyclase-associated protein. *Cell* **61**, 319–327 (1990).
58. Y. Nishida *et al.*, Coiled-coil interaction of N-terminal 36 residues of cyclase-associated protein with adenylyl cyclase is sufficient for its function in Saccharomyces cerevisiae ras pathway. *J. Biol. Chem.* **273**, 28019–28024 (1998).
59. T. Gao, J. Brognard, A. C. Newton, The phosphatase PHLPP controls the cellular levels of protein kinase C. *J. Biol. Chem.* **283**, 6300–6311 (2008).
60. A. E. Aleshin *et al.*, Structural basis for the association of PLEKHA7 with membrane-embedded phosphatidylinositol lipids. *Structure* **29**, 1029–1039.e3 (2021).
61. D. F. J. Ceccarelli *et al.*, Non-canonical interaction of phosphoinositides with pleckstrin homology domains of Tiam1 and ArhGAP9. *J. Biol. Chem.* **282**, 13864–13874 (2007).
62. K. E. Pullen *et al.*, An alternate conformation and a third metal in PstP/Ppp, the M. tuberculosis PP2C-Family Ser/Thr protein phosphatase. *Structure* **12**, 1947–1954 (2004).
63. S. Caban-Penix, K. Ho, Z. Yang, R. Baral, N. Bradshaw, Docking interactions determine substrate specificity of members of a widespread family of protein phosphatases. *J. Biol. Chem.* **300**, 107700 (2024).
64. D. Waschbüsch *et al.*, Structural basis for the specificity of PPM1H phosphatase for Rab GTPases. *EMBO Rep.* **22**, e52675 (2021).
65. M. van Kempen *et al.*, Fast and accurate protein structure search with Foldseek. *Nat. Biotechnol.* **42**, 243–246 (2024).
66. C. Pan *et al.*, The catalytic role of the M2 metal ion in PP2Cα. *Sci. Rep.* **5**, 8560 (2015).
67. C. C. Fjeld, J. M. Denu, Kinetic analysis of human serine/threonine protein phosphatase 2Calpha. *J. Biol. Chem.* **274**, 20336–20343 (1999).
68. C. Pan *et al.*, Cadmium is a potent inhibitor of PPM phosphatases and targets the M1 binding site. *Sci. Rep.* **3**, 2333 (2013).
69. Y. Shi, Serine/threonine phosphatases: Mechanism through structure. *Cell* **139**, 468–484 (2009).
70. M. J. Chen, J. E. Dixon, G. Manning, Genomics and evolution of protein phosphatases. *Sci. Signal.* **10**, eaag1796 (2017).
71. K. Kim *et al.*, Adipocyte PHLPP2 inhibition prevents obesity-induced fatty liver. *Nat. Commun.* **12**, 1822 (2021).
72. J. R. Kovalski *et al.*, The functional proximal proteome of oncogenic Ras includes mTORC2. *Mol. Cell* **73**, 830–844.e12 (2019).
73. K. Shimizu, M. Okada, A. Takano, K. Nagai, SCOP, a novel gene product expressed in a circadian manner in rat suprachiasmatic nucleus. *FEBS Lett.* **458**, 363–369 (1999).
74. K. Shimizu, T. Phan, I. M. Mansuy, D. R. Storm, Proteolytic degradation of SCOP in the hippocampus contributes to activation of MAP kinase and memory. *Cell* **128**, 1219–1229 (2007).
75. W. Chen, T. A. Leonard, PHLPP2 is a pseudophosphatase that lost activity in the metazoan ancestor. Proteomics Identifications Database (PRIDE). https://www.ebi.ac.uk/pride/archive/projects/PXD045891. Accessed 4 October 2023.
76. W. Chen, T. A. Leonard, PHLPP2 is a pseudophosphatase that lost activity in the metazoan ancestor. Proteomics Identifications Database (PRIDE). https://www.ebi.ac.uk/pride/archive/projects/PXD045978. Accessed 4 October 2023.
77. D. Anrather, T. A. Leonard, PHLPP2 is a pseudophosphatase that lost activity in the metazoan ancestor. Proteomics Identifications Database (PRIDE). https://www.ebi.ac.uk/pride/archive/projects/PXD052551. Accessed 24 May 2024.
78. D. Haselbach, T. A. Leonard, PHLPP2 is a pseudophosphatase that lost activity in the metazoan ancestor. Electron Microscopy Data Bank. https://www.ebi.ac.uk/emdb/EMD-51182. Accessed 28 July 2024.
79. D. Haselbach, T. A. Leonard, PHLPP2 is a pseudophosphatase that lost activity in the metazoan ancestor. Electron Microscopy Data Bank. https://www.ebi.ac.uk/emdb/EMD-51183. Accessed 28 July 2024.

Supporting Information

PHLPP2 is a pseudophosphatase that lost activity in the metazoan ancestor

Tarik Husremović[a,1], Vanessa Meier[a,1], Lucas Piëch[a,b], Katharina M. Siess[a], Sumire Antonioli[a,b], Irina Grishkovskaya[c], Nikoleta Kircheva[d], Silvia E. Angelova[d,e], Karoline Wenzl[a], Andreas Brandstätter[f], Jiri Veis[a], Fran Miočić-Stošić[a,b,g], Dorothea Anrather[h,i], Markus Hartl[h,i], Linda Truebestein[a], Luis M. Cerron-Alvan[a,b,j], Martin Leeb[a,j], Bojan Žagrović[a,g], Stephan Hann[f], Christoph Bock[k,l], Egon Ogris[a], Todor Dudev[m], Nicholas A.T. Irwin[n], David Haselbach[c] and Thomas A. Leonard[a,2]

[a]Max Perutz Labs, University of Vienna and Medical University of Vienna, Vienna 1030, Austria

[b]Vienna BioCenter PhD Program, a Doctoral School of the University of Vienna and the Medical University of Vienna, Vienna 1030, Austria

[c]Research Institute of Molecular Pathology, Vienna BioCenter, Vienna 1030, Austria

[d]Institute of Optical Materials and Technologies "Acad. J. Malinowski", Bulgarian Academy of Sciences, Sofia 1113, Bulgaria

[e]University of Chemical Technology and Metallurgy, Sofia 1756, Bulgaria

[f]Department of Chemistry, Institute of Analytical Chemistry, University of Natural Resources and Life Sciences, Vienna 1190, Austria

[g]Department of Structural and Computational Biology, Center for Molecular Biology, University of Vienna, Vienna 1030, Austria

[h]Max Perutz Labs, Mass Spectrometry Facility, Vienna Biocenter Campus, Vienna 1030, Austria

[i]Department of Biochemistry and Cell Biology, Center for Molecular Biology, University of Vienna, Vienna 1030, Austria

[j]Department of Microbiology, Immunobiology and Genetics, Center for Molecular Biology, University of Vienna, Vienna 1030, Austria

[k]Research Center for Molecular Medicine, Austrian Academy of Sciences, Vienna 1090, Austria

[l]Center for Medical Data Science, Institute of Artificial Intelligence, Medical University of Vienna, Vienna 1090, Austria

[m]Faculty of Chemistry and Pharmacy, Sofia University "St. Kliment Ohridski", Sofia 1164, Bulgaria

[n]Gregor Mendel Institute, Austrian Academy of Sciences, Vienna BioCenter, Vienna 1030, Austria

[1]T.H. and V.M. contributed equally to this work

[2]Correspondence: thomas.leonard@meduniwien.ac.at

Contains: Supplementary Methods
Supplementary Figures 1-9
Supplementary Table 1
Supplementary References

Supplementary Methods

Protein expression and purification

Recombinant human PHLPP2 and mutants thereof were expressed as N-terminal GST fusion proteins in baculovirus-infected *Spodoptera frugiperda* (Sf9) cells using a pFastBac Dual vector. Cells were harvested and lysed in buffer containing 50 mM Tris, pH 7.5, 150 mM KCl, 1 mM TCEP, 2 mM $MgCl_2$, 125 U DENARASE (c-LEcta), and protease inhibitor cocktail (Sigma, P8849). After 1 h incubation at 4°C, the lysate was clarified by centrifugation at 39,000 g, 30 min, 4°C. The supernatant was incubated with glutathione Sepharose 4B resin for 2 h, 4°C. After washing with lysis buffer, PHLPP2 was cleaved off the beads with TEV protease overnight. The eluate from the beads was then applied to a 1 ml HiTrap Q column (Cytiva) and PHLPP2 was eluted with a linear salt gradient. Fractions containing PHLPP2 were pooled, concentrated to 0.5 ml and applied to a Superdex 200 30/300 column equilibrated in 20 mM Tris, pH 7.5, 150 mM KCl, 1 mM TCEP. The peak fractions containing PHLPP2 were pooled, concentrated, flash frozen in liquid nitrogen, and stored at -80°C. $Akt1^{3P}$ was prepared according to Truebestein et al, 2021 (1).

The gene sequence of *S. stenapodia* LRR-PP2C (TRINITY_DN5630_c0_g1_i3.p1) was synthesized *de novo* (Twist Bioscience) and cloned into a pFastBac Dual vector for expression in Sf9 cells. Purification followed the same procedure as human PHLPP2 with the omission of the final gel filtration step due to low protein yields. Further minor modifications include the supplementation of all buffers with 0.1 mM $MnCl_2$ and the replacement of KCl with NaCl.

Mass photometry

The mass distribution of purified PHLPP2 particles was measured on a Refeyn TwoMP mass photometer at a concentration of 25 nM. The mass of the respective peaks was estimated by fitting a Gaussian distribution to the histogram of particle masses.

RNA extraction and RNA-seq

RNA samples were extracted using the RNA isolation kit (RNAisomag) provided by the VBC Molecular Tools Shop and processed with the KingFisher Flex robot (Thermo Fisher

Scientific). For RNA sequencing, libraries were prepared using the Lexogen 3' mRNA-Seq Library Prep Kit. Sequencing was performed on a NovaSeq X 10B instrument with an XP flowcell in paired-end mode (150 bp reads) on a single lane by the NGS Facility (VBCF, Austria). FASTQ files were processed using the Nextflow 24.10.1/5930/nf-core/rnaseq v3.17.0 pipeline. Quality control was conducted with fastQC (v0.12.1). Transcript mapping to the hg38 human reference genome was performed using Salmon (v1.10.3) for pseudoalignment and STAR (v2.7.11b) as the aligner. DESeq2 (v1.42.1) was used to generate normalized count tables and perform differential expression analysis (FDR-adjusted p-value ≤ 0.05). Data visualization was performed in R using pheatmap (v1.0.12). Functional enrichment analysis was performed using enrichr (2). The RNA-seq data was uploaded to the Gene Expression Omnibus (GEO) database (accession number GSE287792).

PP2A purification

2L of yeast cells (YJV1181; gal. prom. TAP-Pph21 endogenous, BY 4741) were grown to a density of OD_{600nm}=1 in 1% raffinose and TAP-Pph21 was expressed for 4 hours by addition of 1% galactose, yielding a final cell density of OD_{600nm}=2-3. Cells were harvested by filtration and frozen in liquid nitrogen. Cells were broken up using a Freezer Mill™ cryogenic grinder (SPEX) and resuspended in 20 ml ice-cold lysis buffer (50 mM MES pH 6.5, 150 mM NaCl, 1 mM EDTA, 1% Triton X-100, Complete protease inhibitor cocktail Roche). The lysate was pre-cleared by centrifugation (15' at 16 000 g) and incubated with 300 µl IgG Sephrose™ 6 Fast Flow beads (Cytiva 17096901) for 2h at 4°C. Beads were packed into a chromatographic column and washed 1x with 20 ml lysis buffer and 3x with 20ml cleavage buffer (50 mM MES pH6.5, 150 mM NaCl, 0.1% NP40). Beads were taken up in 800 µl cleavage buffer and Pph21 was cleaved by incubating the beads for 2h at 16°C with 500 U TEV protease (NEB P8112S). Eluted Pph21 was mixed with glycerol to a final conc of 50% and stored at -20°C.

CRISPR/Cas9-mediated knockouts

HAP1 wild-type, B56β deletion (ΔB56β), and B56ε deletion (ΔB56ε) cells were obtained from Haplogene/Horizon Discovery (wild-type: #C631, ΔB56β: #HZGHC003153c009, ΔB56ε: #HZGHC003156c001). B56α was deleted in HAP1 wild-type and ΔB56ε cells

respectively by targeting exon 3 of *PPP2R5A* with CRISPR/Cas9. The guide RNA (sgRNA: 5'-AACCCACGCTTGAGGCCTCT-3') was cloned into pSpCas9(BB)-2A-Puro (PX459) V2.0 (Addgene #62988) via BbsI (B56α guide s: caccgAACCCACGCTTGAGGCCTCT, B56α guide as: aaacAGAGGCCTCAAGCGTGGGTTc) and transfected into cells using TurboFectin 8.0 (OriGene Technologies #TF81001). Co-transfection with dsRed allowed the selection of successfully transfected cells by single-cell sorting. The deletions were confirmed by western blot analysis and Sanger Sequencing. All HAP1 cell lines were cultured in GlutaMAX containing Iscove's Modified Dulbecco's Medium (IMDM) (Thermo Fisher Scientific #31980048, lot 2858891) supplemented with 10% Fetal Calf Serum (FCS) (Sigma-Aldrich #F7524, lot 0001671876) and 1% penicillin-streptomycin (Sigma-Aldrich #P4333) at 37°C and 5% CO_2.

HEK293 cell lines were cultured in DMEM high glucose (Sigma Aldrich) supplemented with 10 % FBS (Sigma Aldrich) and 1 % Penicillin/Streptomycin (Sigma Aldrich) at 37 °C and 5 % CO_2. PHLPP2 knockout HEK293 cells were generated by nucleofection of gRNA-Cas9 complexes. 150 pmol of each gRNA (AGAGAAAUAUGAAACGCAAU, AAGGACGAGAUGUAAGUCAG, Genscript) was added to 2.4 µL of RNP buffer (580 mM KCl, 40 mM Tris-HCl pH 7.5, 20 % v/v glycerol, 2 mM TCEP-HCl pH 7.5, 2 mM $MgCl_2$) and incubated for 5 min at 70 °C. 50 pmol of Cas9 (in-house purified) was added and the complex incubated for 10 min at 37°C. H_2O was added to a final volume of 10 µL. Nucleofection was performed according to the manufacturer's protocol using program CM130 (Lonza, Cell Line Nucleofector kit S). The cells were recovered for 7 days, detached and washed twice with PBS. The cells were resuspended in FACS Buffer (PBS, 10 % FBS, 1 mM EDTA) and single-cell sorted (Aurora CS) into two 96-well plates. Cells were grown to confluency and moved up to 12-well plates from which 5 x 10^5 cells were pelleted down and genomic DNA extracted using gDNA purification kit (Thermo Scientific) according to the producer´s manual. The genomic DNA samples were genotyped by PCR using the following primer combinations: AGGAGGGGATACTTGAGCAGA (upstream of KO-region) and CAGTGGTAGTGTCTGCTCCA (located inside the KO-region), or GCCCAGTGAGTCCGTAATCA (outside the cut-out region), and compared to wild-type HEK293 genomic DNA. The amplicons were gel purified in 2 % agarose gels and the deletion confirmed by Sanger sequencing.

Immunoblotting

After incubation with PHLPP2 under different conditions, the phosphorylation state of Akt1^{3P} was monitored by western blotting, using antibodies against Akt1 pT308 (Cell Signaling Technology #C31E5E) and pS473 (Cell Signaling Technology #193H12). Briefly, samples were separated by SDS-PAGE on a 12% tris-glycine gel and blotted onto nitrocellulose (0.4 μm pore size). The membrane was blocked for 1 h at room temperature with 5% BSA in 20 mM Tris, pH 7.5, 150 mM NaCl, 0.1% Tween 20. Membranes were incubated with primary antibodies at a ratio of 1:1000, overnight at 4°C, followed by washing and incubation with IRDye 800CW Goat anti-Rabbit IgG Secondary Antibody (LICOR, 926-32211) at a ratio of 1:15000, 1 h at room temperature. After washing, the membranes were imaged using a LICOR Odyssey CLx fluorescence imager.

For Akt immunoblotting in HAP1 cells, cells were grown to approx. 80% confluency, harvested and lysed in IP-Lysis buffer with protease and phosphatase inhibitors (5 mM sodium fluoride (Merck #6449), 2 mM sodium pyrophosphate (Merck #1.06591) 1 mM sodium-orthovanadate (Sigma-Aldrich #S6508), 10 mM β-glycerophosphate (Sigma-Aldrich #G6251), EDTA-free cOmplete (Roche #11836170001), Aprotinin (Sigma-Aldrich #A6279)). Lysates were cleared at 13000 g and extracted proteins were quantified with the Bio-Rad protein assay (Bio-Rad Laboratories #5000002), adjusted to equal amounts and boiled in protein sample buffer at 95°C for 5 min. Proteins were separated on 10% SDS polyacrylamide gels and transferred onto nitrocellulose membranes (GE Healthcare, 0.2μm). Membranes were stained with PonceauS and blocked using 3% skim milk (Millipore #999999-99-4, lot VM1001463145) in phosphate-buffered saline 0.05% Tween20 (PBS-T). For western blot analysis, primary phospho-specific antibodies were diluted in 5% bovine serum albumin (BSA) in Tris-buffered saline (TBS), 0.5% Tween20. All other antibodies were diluted in 0.5% skimmed milk powder in PBS-T. Antibodies [pan Akt (C67E7, Cell Signaling Technology #4691), phospho-Akt Thr308 (244F9, Cell Signaling Technology #4056), phospho-Akt Ser473 (D9E, Cell Signaling Technology #4060), B56α C-term (3A6-D3-D10-G1, Ogris Lab, directed against amino acids 463-486), B56β (6H4-3C2, Ogris Lab, directed against an N-terminal fragment encompassing amino acids 1-135), and B56ε C-term (3D1-H7-3E5-3H9, Ogris Lab, directed against amino acids 448-467)] were applied overnight at 4°C followed by incubation with horseradish peroxide-

coupled secondary antibodies directed against mouse and rabbit heavy chain IgG (Jackson Immuno Research #115-035-008, and Jackson Immuno Research #111-035-008) for 2h at room temperature. Signals were detected by incubation of the blots with Clarity Western ECL Substrate (Bio-Rad Laboratories #1705061) and subsequent imaging with the ChemiDoc Imaging System (Bio-Rad Laboratories #12003153).

Densitometric quantification was performed using the Image Lab Software. For lysate quantifications, a dilution series of the lysates was fit to a linear, exponential or logarithmic trend line by Excel. The equation of the scan with the best R^2 value was used to calculate the values of the western blot signals. Datasets were normalised to the arithmetic sum of each individual experiment (3) and means and standard deviations for each cell line were calculated. Statistical significance of immunoblotting data was assessed using one-way analysis of variance (ANOVA) and Tukey's honestly significantly different (HSD) post hoc test for multiple comparisons. In all cases, P values of <0.05 were considered to be statistically significant and are indicated with $*P < 0.05$, $**P < 0.01$, $***P < 0.005$, $****P < 0.001$. Statistical analysis was performed in GraphPad Prism.

Size-exclusion chromatography coupled to inductively-coupled plasma mass spectrometry

Water was purified employing an Ultra Clear basic reverse osmosis system (SGWasseraufbereitung und RegenierstationGmbH, Barsbuettel, Germany) and subsequently subboiled (MLS, Leutkirch). Formic acid Suprapure® (purity 98-100%, item no. 111670), nitric acid (purity for analysis EMSURE® Reag. Ph Eur, ISO, item no. 100456), acetic acid Suprapure® (purity 100%. Item no. 100066) and ammonia solution (purity for analysis EMSURE® Reag. Ph Eur, ISO, item no. 1005432) were purchased from Merck (KGaA, Darmstadt,Germany). Nitric acid was double subboiled and stored in perfluoralkoxy-polymer bottles. Lyophilized bovine erythrocytes Cu/Zn-superoxide dismutase (Cu/Zn-SOD, item no. S7571) was purchased from Sigma-Aldrich Chemie GmbH (Vienna, Austria).

Samples were stored at -80 °C prior to measurement. All vials and materials which came into contact with the sample, blank and standard solutions were pre-cleaned via soaking for 24 h in 10% and 24 h in 1% nitric acid followed by flushing with distilled water and drying under a class 100 laminar flow clean bench. Measurements were performed under clean room conditions (class 10000). Between the sample runs

1% formic acid solution was injected to eliminate carry over, followed by one buffer blank for assessment of possible contamination.

A NexSAR Speciation Analysis Ready HPLC system from Perkin Elmer (Massachusetts, USA) controlled by Clarity 8.8 software was used for the size exclusion separation. The mobile phase consisted of 50 mmol/L ammonium acetate at pH 7 and the flow rate was set to 0.4 mL min^{-1}. The injection volume for injection of samples, blank solutions and standards onto the ACQUITY UPLC Protein BEH 450Å SEC column (Waters™) was 15 µL. For elemental detection, the system was combined with an NexION 2000 quadrupole ICP-MS from Perkin Elmer (Massachusetts, USA). The reaction cell was filled with oxygen to induce the formation of $^{32}S^{16}O^{+}$ and circumvent the $^{16}O_2^{+}$ interference on the most abundant sulfur isotope ^{32}S. Zinc was detected as ^{66}Zn. Bovine Cu/Zn-SOD was employed to determine the intensity ratio between the ^{66}Zn and the $^{32}S^{16}O$ signals. The stoichiometric zinc ratio was calculated from the number of sulfur atoms per protein. ICP-MS parameters and data evaluation were optimized according to (4). pH measurements were conducted with an Education Line EL20 pH-meter with a micro electrode (inLab Micro, Mettler, Toledo, USA).

Phosphatase inhibitor beads (PIBs)

PIBs were prepared according to (5).

Molecular dynamics

The geometry of the predicted Zn^{2+} binding site in PHLPP2 was determined using a two-step procedure involving explicit-solvent molecular dynamics (MD) simulation followed by quantum-mechanical optimization. For MD simulations of the full-length PHLPP2, the GROMACS simulation package v. 2023 (6), the all-atom Amber99SB-ILDN force field (7) and the TIP4P-D water model (8) were used. The initial configuration of the full-length PHLPP2 protein was obtained from an AlphaFold (9) prediction for PHLPP2, including manual placement of the zinc ion in the proposed active site. To prepare the system, an energy minimization, a 10-ns constant volume equilibration (NVT) and 10-ns constant pressure equilibration (NPT) were first performed without distance restraints using the parameters given below and reaching the final all-atom RMSD with respect to the AlphaFold structure of 0.13 nm. The system was simulated in a cubic water box (8 nm x

8 nm x 8 nm) with 0.15 M NaCl to mimic experimental conditions. We also studied the influence of Zn^{2+} binding on the stability of the whole PHLPP2 structure. Due to inherent limitations, MD simulations cannot capture the quantum behavior of the metal-ion binding sites. Thus, distance restraints (k= 5000 kJ/mol/nm^2) between coordinating atoms and the zinc ion as well as between coordinating atoms themselves were included to stabilize the tetrahedral arrangement using the target distances from the X-ray structure of α-klotho (10). The restrained simulations were run for a total length of 100 ns. A leap-frog algorithm was used for integration under periodic boundary conditions. In both energy minimization and production runs, neighbor-lists were updated every 20 steps, following a Verlet-scheme based grid-search approach. The bonds involving H atoms were constrained using LINCS (11). Temperature control was achieved using a V-rescale thermostat (12), with a relaxation time of 0.1 ps, while pressure was controlled using a Parrinello-Rahman barostat (13). Compressibility for the barostat was set to 4.5 x 10^{-5} and the relaxation time was 2 ps. Coupling was done separately for water and protein in all cases. A twin-range spherical cut-off (1.0 nm/1.2 nm) was used for van der Waals interactions, while electrostatics were treated using the Particle-Mesh Ewald (PME) approach with a real space cut-off of 1.2 nm, a 0.16-nm grid and cubic interpolation. During the restrained simulation, the all-atom RMSD with respect to the to the final structure of NPT equilibration reached a stable level of 0.2-0.25 nm after 10 ns (Supplementary Figure 2F), suggesting that the placement of the zinc ion in the M2 site does not affect the structural integrity of the rest of the PHLPP2 structure. Similarly, the RMSD of coordinating atoms relative to their positions in the initial structure for the restrained simulations remains under 0.05 nm throughout the simulation (Supplementary Figure 2H). Further quantum-mechanical optimization was performed starting with a structure from the pool with the lowest 5% in binding site RMSD with respect to the equilibrated unrestrained geometry.

Quantum mechanical modeling (ONIOM)

Calculations were performed with the Gaussian 16 (Revision C.01) quantum chemistry software package (14). To reduce the computational time given the size of the system, we employed the ONIOM method (15) as implemented in the Gaussian 16 program. A two-layer QM/QM method that combines different QM methods is applied: a high-level

of accuracy for the atoms three bonds away from the zinc ion and a low level for the rest of the systems – cut from the corresponding initial structures (crystal structure of a 1:1:1 FGF23-FGFR1c-α-Klotho Ternary Complex, PDB 5W21, and MD generated model) at approximately 12 Å in radius around the metal cation where the amino acid chains logically end with methyl groups. In all calculations for the α-Klotho model system, a DFT function (M062X, B3LYP, or ωB97XD) was adopted for the inner layer, while a semi-empirical method (PM3) was used for the treatment of the real system. Different basis sets (6-31G(d,p), 6-31+G(d,p) and 6-31+G(3d,p)) in conjunction with the selected DFT functions were assessed for an accurate prediction of structural parameters (Zn-S and Zn-O bond lengths). The sulfur atom of the cysteine was modeled in its deprotonated state, in accordance with the known interaction of sulfur with zinc, which has been theoretically predicted (16) and experimentally visualized in atomic resolution crystal structures. All the methods tested predicted Zn-S bond lengths in the range 2.32-2.40 Å, and the average lengths of the three Zn-O bonds were 1.96-2.02 Å. It was concluded that both oniom(ωB97XD/6-31G(d,p):PM3) and oniom(B3LYP/6-31+G(3d,p):PM3) methods are suitable for proper description of the geometry of the α-Klotho Zn center.

Sample preparation for tandem mass spectrometry

Pellet of 1L Sf9 culture was lysed in 20 mL lysis buffer (2 mM benzamidine, 200 µL Protease inhibitor stock, 2mM MgCl2, 1 mM TCEP, 0.4 µL benzonase, 0.25% Chaps) for approximately 1 h at 4˚C in the cold room and then spun down (30 min, 18k rpm, 4˚C). The clarified supernatant was assessed for protein concentration using the Bradford assay, and two equal aliquots (1 mg/mL) were prepared. As a control, 0.5 µM okadaic acid was added to one of the samples. The two lysate samples (1 mL each) were then incubated with 20 µL of phosphatase inhibitor beads (PIBs) at 4°C for 1 hour. After incubation, the supernatant was carefully removed, and the PIBs were washed three times with 0.5 mL of Lysis buffer. Subsequently, the washed beads were incubated with 120 µL of 2% SDS for 1 hour at 65˚C and the eluates collected using Pierce Micro-Spin columns.

The samples were mixed with 5µL 100mM Tris HCl pH 8.5 and heated at 95°C for 5min. Then disulfide bonds were reduced with 4 µL of 250 mM dithiothreitol (DTT) for 30 min at room temperature before adding 4 µL of 500 mM iodoacetamide and incubating for 30 min at room temperature in the dark. The remaining iodoacetamide was quenched

with 2 µL of 250 mM DTT for 10 min. Sera-MagSpeed Beads mix (GE Life Sciences, cat. nos. 45152105050350 and 65152105050350) was added to the sample at beads:protein ratio of 10:1 and mixed with ethanol to reach 50% final ethanol concentration. The tubes were kept in a thermomixer for 10min at 1000rpm for 24min to let protein bind to the beads. Then the supernatant was removed using a magnetic rack and the beads were washed with 180 µL 80% ethanol in water off the rack. And the wash procedure was repeated 3 more times. Afterwards, 30µL 50mM ammonium bicarbonate with 120 ng trypsin (Trypsin Gold, Promega) was added to the beads and incubated at 37°C 1000rpm overnight. The beads were settled on a magnetic rack and the supernatant was transferred to a new tube. The beads were rinsed with 30µL ammonium bicarbonate and sonicated for 30s and the supernatant was pooled to the supernatant from the previous step. Then the samples were centrifuged at 20000g for 1min and the supernatant was transferred to a new tube to remove any remaining beads. Trifluoroacetic acid was added to reach a final concentration of 0.5%.

For the analysis of recombinant PHLPP2, ~5 µg protein (5 µL) was mixed with 15 µL 8M urea 50mM ammonium bicarbonate. Disulfide bonds were reduced with 0.8 µL of 250 mM dithiothreitol (DTT) for 30 min at room temperature before adding 0.8 µL of 500 mM iodoacetamide and incubating for 30 min at room temperature in the dark. The remaining iodoacetamide was quenched with 0.4 µL of 250 mM DTT for 10 min. 50mM ammonium bicarbonate was added to dilute the urea to 1M. The protein was digested with 160 ng trypsin (Trypsin Gold, Promega) at 37°C overnight. The digest was stopped by adding trifluoroacetic acid to reach a final concentration of 0.5% and the peptides were desalted using C18 Stagetips (17).

For the differential alkylation experiment purified PHLPP2 was incubated in 5 mM iodoacetamide for 30 minutes in the dark alkylating accessible thiol groups. Unreacted iodoacetamide was removed by buffer exchange to 50 mM ammonium bicarbonate using Bio-Rad Micro Bio-Spin™ columns. Solid urea was added to the eluate to reach a concentration > 6 M urea. Subsequently disulfide bridges were reduced adding tris (2-carboxyethyl) phosphine (TCEP) to a final concentration of 1 mM and incubated for 30 minutes. Free thiols were then modified with methyl methanethiosulfonate (MMTS) at a concentration of 5 mM. After diluting to 1 M urea with 50 mM ammonium bicarbonate the sample was digested with trypsin at a protease:protein ratio of 1:30 at 37°C

overnight. The digest was stopped by adding trifluoroacetic acid to reach a final concentration of 0.5 % and the peptides were desalted using C18 Stagetips.
As reference samples, the protein was denatured in 6.4M urea, reduced in 1mM TCEP and free thiols alkylated either with 5 mM iodoacetamide or 5 mM MMTS for 30 minutes in the dark prior digest and clean-up as described above.

Liquid chromatography- tandem mass spectrometry

Peptides were separated on an Ultimate 3000 RSLC nano-flow chromatography system (Thermo-Fisher), using a pre-column for sample loading (Acclaim PepMap C18, 2 cm × 0.1 mm, 5 µm, Thermo-Fisher), and a C18 analytical column (Acclaim PepMap C18, 50 cm × 0.075 mm, 2 µm, Thermo-Fisher), applying a segmented linear gradient from 2% to 35% and finally 80% solvent B (80% acetonitrile, 0.1% formic acid; solvent A 0.1% formic acid) at a flow rate of 230 nL/min over 60min . Eluting peptides were analyzed on an Exploris 480 Orbitrap mass spectrometer (Thermo Fisher), which was coupled to the column with a FAIMS pro ion-source (Thermo Fisher) using coated emitter tips (PepSep, MSWil).

For analysis of peptides obtained from PIB eluates, the mass spectrometer was operated in DIA mode with the FAIMS CV set to -45, the survey scans were obtained in a mass range of 350-1200 m/z, at a resolution of 60k at 200 m/z and a normalized AGC target at 300%. 31 MSMS spectra with variable isolation width between 13 and 24 m/z covering 349.5-1200.5 m/z range including 1 m/z windows overlap, were acquired in the HCD cell at 30% collision energy at a normalized AGC target of 1000% and a resolution of 30k. The max. injection time was set to auto.

For analysis of peptides obtained from purified, recombinant PHLPP2, the mass spectrometer was operated in DDA mode with two FAIMS compensation voltages (CV) set to -45 or -60 and 1 s cycle time per CV. The survey scans were obtained in a mass range of 350-1500 m/z, at a resolution of 60k at 200 m/z, and a normalized AGC target at 100%. The most intense ions were selected with an isolation width of 1.2 m/z, fragmented in the HCD cell at 28% collision energy, and the spectra recorded for max. 100 ms at a normalized AGC target of 100% and a resolution of 15k. Peptides with a charge of +2 to +6 were included for fragmentation, the peptide match feature was set to

preferred, the exclude isotope feature was enabled, and selected precursors were dynamically excluded from repeated sampling for 20 seconds.

For the differential alkylation experiments, the Exploris 480 Orbitrap mass spectrometer was run without FAIMS. The survey scans were obtained in a mass range of 350-1500 m/z, at a resolution of 60k at 200 m/z, and a normalized AGC target at 300%. The 10 most intense ions were selected with an isolation width of 1.2 m/z, fragmented in the HCD cell at 30% collision energy, and the spectra recorded for max. 100 ms at a normalized AGC target of 200% and a resolution of 15k.

MS data analysis

Raw data were processed using Spectronaut software (version 18.3, https://biognosys.com/software/spectronaut/) with the DirectDIA+ workflow or FragPipe (version 19.1) (18). The Uniprot Spodoptera_frugiperda proteome (version 2023.03), PHLP2_HUMAN protein sequence, as well as a database of most common contaminants were used. The searches were performed with full trypsin specificity and a maximum of 2 missed cleavages at a protein and peptide spectrum match false discovery rate of 1%. Carbamidomethylation of cysteine residues were set as fixed, oxidation of methionine and N-terminal acetylation as variable modifications. The cross-run normalization was turned off and all other settings were left as default. For the differential alkylation analysis, modification of cysteines with iodoacetamide or MMTS were defined as variable modifications.

Computational analysis was performed using Python and the in-house developed Python library MsReport (version 0.0.19) (19). Protein intensity less than 1000 was set to missing to remove the low-quality quantification values. LFQ protein intensities reported by SpectroNaut were log2-transformed and normalized across samples using the ModeNormalizer from MsReport. The missing normalized LFQ intensity values were imputed by drawing random values from a normal distribution after filtering out contaminants, proteins with less than 2 peptides and less than 1 quantified values in at least one group. Using MsReport, iBAQ intensities were calculated from the raw intensities reported by FragPipe.

The proteomics data have been deposited to the ProteomeXchange Consortium via the PRIDE partner repository (20) with the dataset identifiers PXD045891, PXD045978 and PXD052551.

Immunoprecipitation of PHLPP2

HEK293 cells ($5x10^6$) were transiently transfected with a plasmid encoding N-terminally V5-tagged PHLPP2 using Lipofectamine 3000 according to the manufacturer's protocol. Cells were harvested after two days, lysed with 3 repeated freeze/thaw cycles in liquid nitrogen, and then resuspended in 500 µL lysis buffer: 50 mM Tris pH 7.5, 150 mM KCl, 1 mM TCEP, 0.25% CHAPS, 2 mM $MgCl_2$, 2 mM benzamidine, supplemented with 0.01 µL DENARASE® and 5 µL protease inhibitor cocktail, (Sigma P8849).

The lysate was combined with 25 µL of V5-trap magnetic beads (Chomotek v5tma) pre-equilibrated in wash buffer (50 mM Tris pH 7.5, 150 mM KCl, 1 mM TCEP) and incubated for 3 h at 4°C on a rotary plate. A magnetic rack was used to pull down the beads and the supernatant (lysate) was removed. The beads were resuspended in wash buffer (beads). The wash step was repeated 5 times. Samples of the lysate, beads, and supernatant were taken after each wash step. All samples were subjected to a malachite green assay (Sigma-Aldrich MAK307) as described in the Methods section of the manuscript.

For western blotting, the samples were resolved by SDS-PAGE on a 12% Tris-Glycine gel. Transfer onto a 0.2 µm nitrocellulose membrane was performed at 120 V and 4°C for 2.5 h. The membrane was incubated with 5 % BSA in TBST for 1 h while gently shaking. V5-Tag rabbit monoclonal antibody (Cell Signaling, #13202) and β-actin mouse monoclonal antibody (Cell Signaling, #3700) were diluted 1:1000 in 3% BSA in TBST to a final volume of 5 mL and incubated with the membrane overnight at 4°C. The membrane was washed 3 times with TBST for 5 min each. Goat anti-rabbit secondary antibody (LI-COR, 926-32211) and goat anti-mouse secondary antibody (LI-COR, 926-68070) were diluted 1:15000 in 3% BSA in TBST to a final volume of 5 mL and incubated with the membrane in the dark for 1 h at room temperature while gently shaking. The membrane was washed 3 times with TBST for 5 min each and imaged using a LI-COR Odyssey CLx fluorescence imager.

AlphaFold2 structure prediction

The structures of PHLPP2 and Cyr1 homologs, as well as the Cyr1 dimer and complexes of Cyr1 with RAS1/RAS2 and CAP were predicted with AlphaFold2 multimer_v3 (9) installed on a local cluster. The top five models output in each case were compared to each other for convergence by calculating the r.m.s.d. over equivalent Ca atoms and evaluated according to their respective pair alignment error plots (PAE).

Cryo-electron microscopy

Grid preparation. Open-hole cupper 200 mesh grids overlayed with R 2/2 carbon film (Quantifoil) were used for plunge freezing. Grids were glow-discharged with a BalTec SCD 005 sputter coater for 60 s at 25 mA using residual air. 4 µl of the sample at concentration of 0.1 mg/ml was applied onto the carbon side and front-side blotted using the Leica GP2 plunge freezer. The sample was blotted for 2 seconds including the integrated blot sensor.

Data collection. Initial grid screening was performed on a 200kV Glacios microscope (ThermoFisher) using a Falcon III detector (ThermoFisher). For high-resolution structure determination, data collection was performed at Diamond Light Source Krios I using a K3 detector (Gatan). Images were collected at super-resolution pixel size of 0.53 Å/pix with a cumulative fluence of 35 $e^-/Å^2$ in a defocus range from 1.7 to 2.5 µm in 0.2µm increments using EPU (ThermoFisher).

Image processing. Images were preprocessed using the cryosparc (21) live pipeline. In short, micrograph movies were aligned, fourier binned by a factor of two and the CTF parameters were determined. Particles were picked initially via blob picking. Clustering these results in 2D led to new templates that have been subsequently been used for particle selection. Particles underwent 2 rounds of 2D clustering and an ab-initio model was generated and refined. These preprocessed particles were transferred to relion 5 (22). 3D Clustering generated two classes with distinct features but only one was refining to subnanometer resolution. Refinement was performed using Blush regularisation (23).

Modelling. Into the map an alphafold (9) model was placed using UCSF ChimeraX (24). Models were adjusted and refined using MDFF in Namdinator (25).

Phylogenetic and sequence analysis

To examine the evolutionary history of PHLPP, we generated a database of genome-predicted eukaryotic reference proteomes from UniProt (*n* = 181, downloaded 25 January 2024) (26). This database was taxonomically balanced by selecting the best two proteomes per genus based on BUSCO (Benchmarking Universal Single Copy Orthologues) completeness (27). For metazoans, fungi, and embryophytes, more strict taxonomic criteria were set by selecting the best proteome per phyla for metazoans (*n* = 17), the best proteome per class for fungi (max two per phylum, *n* = 12), and the best proteome per order for embryophytes (max three per class, *n* = 11). To identify PHLPP homologs, the database was searched using Diamond BLASTp v2.0.9 with human PHLPP1 (UniProt accession: O60346) as a query (query coverage ≥ 25%, E < 10^{-5}, sensitive mode) (28). The resulting hits were aligned using MAFFT v7.520 trimmed using trimAl v1.4.rev15 with a gap threshold of 50%, and a maximum-likelihood phylogeny was inferred with IQ-Tree v2.2.6 using the LG4M substitution model with topology support assessed using Shimodaira-Hasegawa approximate likelihood ratio tests (SH-aLRT, *n* = 1,000) and ultra-fast bootstraps (*n* = 1,000) (29–33). The phylogenies were inspected manually in FigTree v1.4 (http://tree.bio.ed.ac.uk/software/figtree/) and paralogs were excluded. The resulting homologs were then used for two additional iterative BLAST searches with stricter E-values of 10^{-25}, and the hits were analyzed phylogenetically and curated as described. To improve taxonomic sampling, we conducted an additional search using the EukProt V3 database and incorporated the resulting hits to produce a complete set of LRR-PP2C homologues from diverse eukaryotes (34).

Phylogenetic analyses were used to reconstruct the evolutionary history of PHLPP. To this end, the identified PHLPP homologues were aligned with MAFFT using the high accuracy L-Ins-i algorithm and the alignment was trimmed as before. A maximum likelihood phylogeny was inferred using the LG4M+F+R7 substitution model which was selected based on Bayesian information criteria using ModelFinder (35). Statistical support was inferred as before using SH-aLRT and the phylogeny was rooted

based on recent eukaryotic species phylogenies (36). The monophyly of the unicellular holozoans was assessed using an approximately unbiased (AU) test implemented in IQ-Tree using a constrained phylogeny inferred under the same model as the unconstrained tree (37). The phylogenies were visualized and annotated using iTOL v6 (38).

Protein domain annotations were accomplished by mapping profile hidden Markov models (HMM) obtained from the Pfam-A database to protein sequences using HMMER v3.4 ($E < 10^{-3}$) (39, 40). However, to improve HMM sensitivity, the mapped domains were extracted, aligned using MAFFT, and used to produce new HMMs. This process was repeated iteratively three times until consistent domain annotations were obtained. Active site residue conservation was investigated using sequence logos generated with Skylign using weighted counts (41).

Lastly, to identify the origin of the unicellular holozoan kinase domains, the reference database was searched using Diamond BLASTp ($E < 10^{-5}$, query coverage ≥ 50%, sensitive mode, max 250 targets per query sequence) and the holozoan kinases as a query. The kinase domains of the resulting proteins were excised and subsequently aligned with the PHLPP kinases using MAFFT L-Ins-i. The alignment was then trimmed using trimAl with a gap threshold of 50% and a phylogeny was generated using IQ-Tree as described above, using the LG4M+I+R10 substitution model selected with ModelFinder. Proteins were annotated based on BLAST searches against SWISS-PROT (42).

Phylogenomic profiling

To examine the distribution of PHLPP paralogs across the gnathostome phylogeny an additional database of representative craniate species was assembled using predicted reference proteomes from UniProt (downloaded 12 November 2024). PHLPP1 and PHLPP2 along with AKT and PKC orthologues were identified across craniate species as described above. When orthologues were missing, previously identified orthologues were used as queries for tBLASTn ($E < 10^{-5}$) searches against animal genomes and protein predictions were inferred using Exonerate v2.2(see https://github.com/nickatirwin/Phylogenomic-analysis; (43) and phylogenetically curated. To identify proteins with correlated distributions, craniate

proteomes were clustered in hierarchical orthogroups (N0) using OrthoFinder v2.5.5 (using ultra-sensitive Diamond and FastTree for tree inference). Co-evolutionary patterns were detected based on previously established methods (44). In brief, for each gene, orthologue presence was recoded in binary and, to account for taxonomic sampling, median values were inferred for each clade containing or lacking PHLPP2. Orthologoues found in less than 30 species were excluded and the associations between PHLPP2 and each orthologue were inferred using point biserial correlations, given the binary nature of PHLPP2 presence. Statistical significance was inferred using permutation tests by recreating orthogroups by randomly sampling sequences across all proteomes without replacement and re-calculating correlations (n = 10,000, $p < 0.05$). Positively correlated clusters were further refined through additional homology searches and manual phylogenetic curation.

Lipid-protein overlay assay

PIP strips (P-6001) were purchased from Echelon Biosciences and a lipid-protein overlay assay was performed according to the manufacturer's protocol in duplicates. In brief, the membrane was blocked with 3% lipid-free BSA in PBS-T. GST-tagged recombinant PHLPP2 was added to a final concentration of 1.8 μg/mL in PBS-T and incubated for 1 h at 25 °C. The membrane was washed three times with PBS-T and subsequently incubated with primary mouse anti-GST antibody (Invitrogen, MA4-004) at 25 °C for 1h. The membrane was washed three times with PBS-T followed by an incubation with secondary goat anti-mouse antibody (Licor, IRDye 680RD Goat anti-Mouse IgG Secondary Antibody). The membrane was washed three times with PBS-T and imaged using a LI-COR Odyssey CLx fluorescence imager.

Supplementary Figure Legends

Supplementary Figure 1. Biochemical and biophysical analysis of purified PHLPP2.

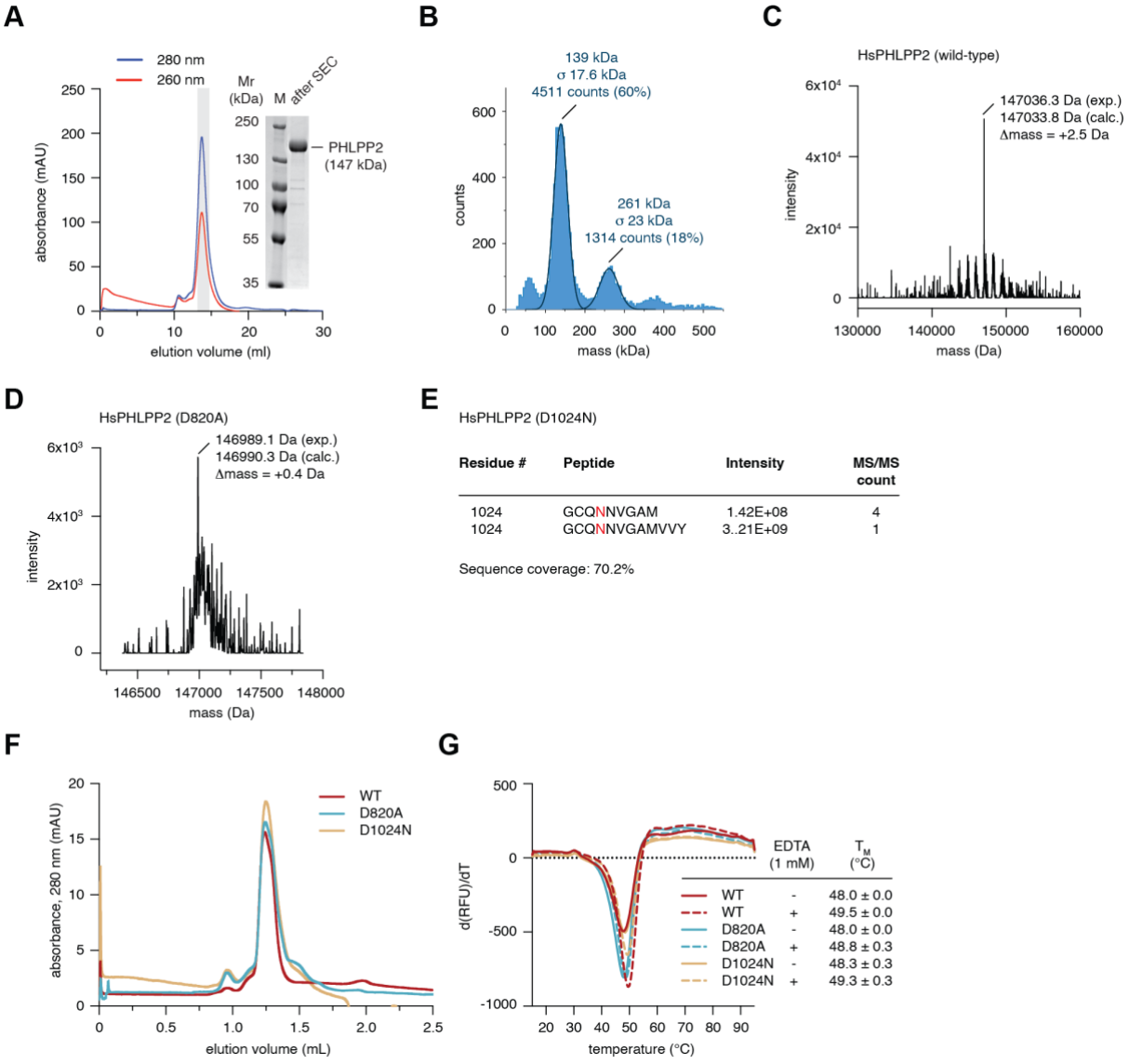

A. Size-exclusion chromatography of purified, recombinant human PHLPP2.

B. Mass photometry of recombinant PHLPP2.

C. Mass spectrum of recombinant human PHLPP2^{WT}.

D. Mass spectrum of recombinant human PHLPP2^{D820A}.

E. Peptide fingerprinting of recombinant human PHLPP2^{D1024N}. The -1 Da mass difference of the mutant was detected by tandem mass spectrometry analysis of chymotryptic peptides.

F. Analytical size exclusion chromatography of wild-type PHLPP2, PHLPP2^{D820A} and PHLPP2^{D1024N}.

G. Thermal stability measurements of wild-type PHLPP2, PHLPP2^{D820A} and PHLPP2^{D1024N} in the presence and absence of 1 mM EDTA.

Supplementary Figure 2. PHLPP2 exhibits no detectable activity against Akt.

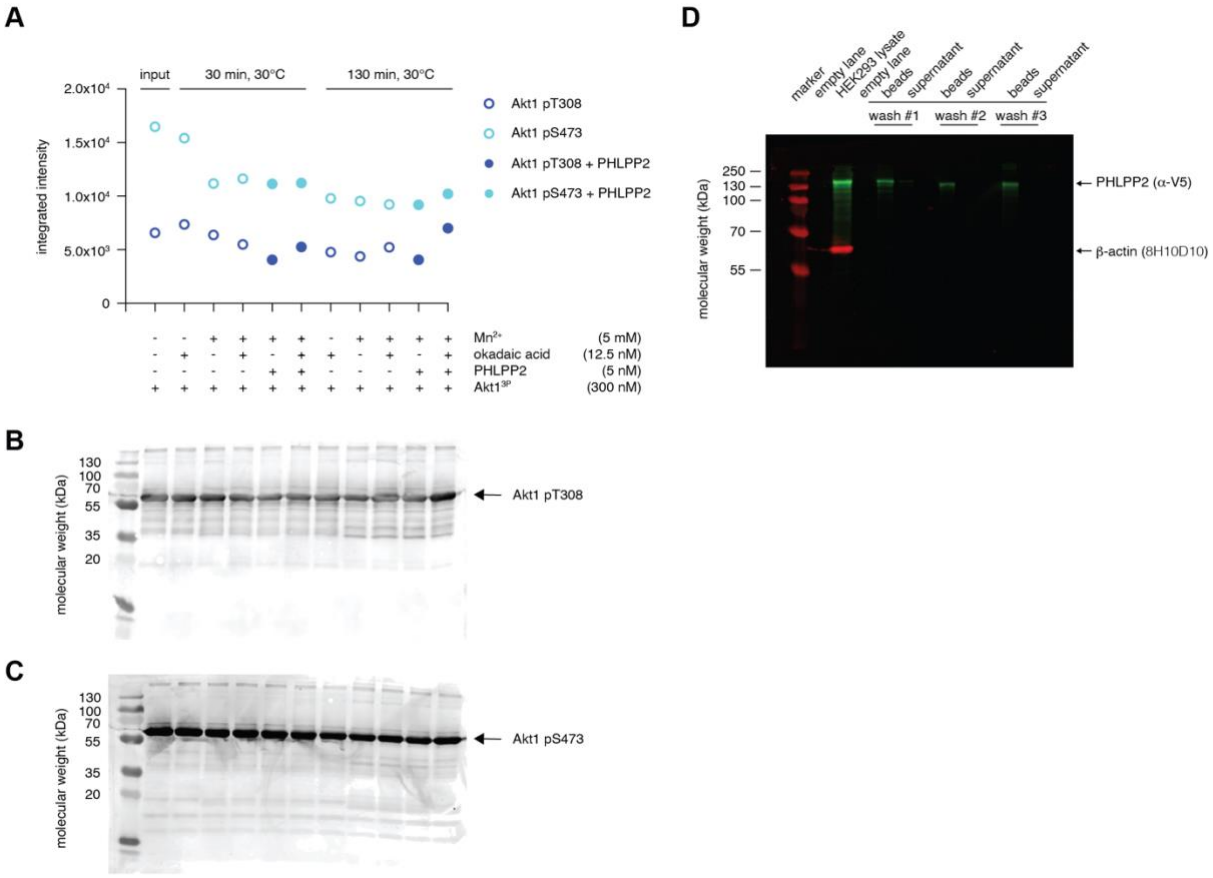

A. Akt1^{3P} dephosphorylation by purified PHLPP2, according to the assay conditions of Gao et al (45). Quantification of western blots shown in panels B and C.

B. Western blot of Akt1 pT308.

C. Western blot of Akt1 pS473.

D. Western blot of samples analyzed for phosphatase activity in Figure 4H. Immunoblotting was carried out with mouse anti-β-actin antibody and a rabbit anti-V5 antibody followed by detection with AlexaFluor-647 anti-mouse IgG and AlexaFluor-488 conjugated anti-rabbit IgG secondary antibodies respectively.

Supplementary Figure 3. Akt-FOXO1 signaling is unaffected by PHLPP2 knockout.

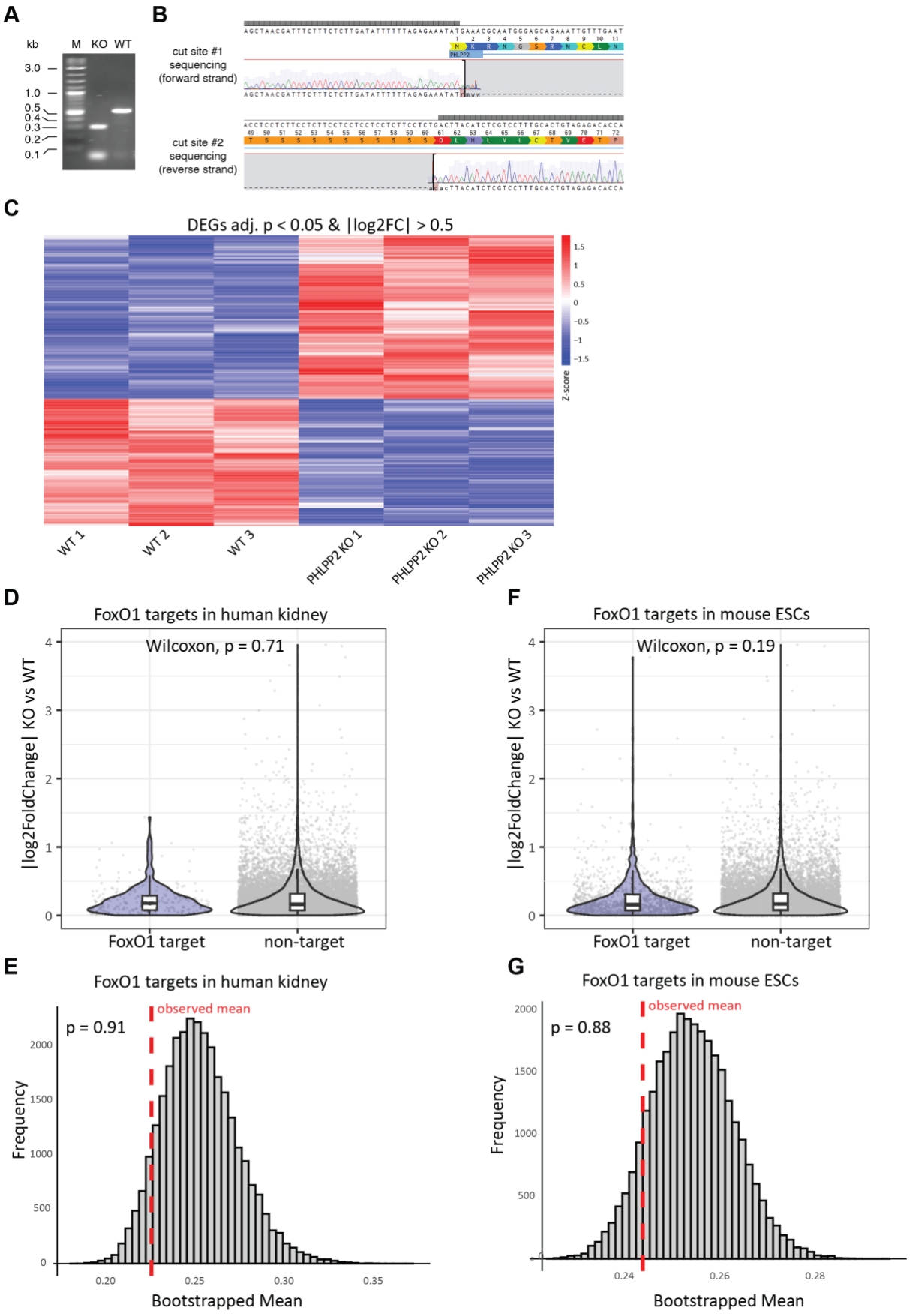

A. PCR genotyping of PHLPP2 KO compared to WT HEK293 cells.

B. Sanger sequencing of deletion in PHLPP2 KO cells.

C. Heatmap showing Z-transformed normalized counts of genes identified as significantly differentially expressed between PHLPP2 KO and WT in all replicates.

D. Plot showing the absolute log2FCs (PHLPP2 KO vs WT) of FOXO1 targets in kidney compared to non-targets in the PHLPP2 KO RNA-seq dataset. The *p*-value indicates significance.

E. Bootstrapping analysis. 50,000 random draws of 367 genes (=number of FOXO1 targets in kidney) from the PHLPP2 KO RNA-seq dataset. The distribution of average log2FC (PHLPP2 KO vs WT) is plotted, with *p*-value indicating the probability of the predicted exceeding the measured effect-size.

F. Similar to D with plot showing the absolute log2FCs (PHLPP2 KO vs WT) of FOXO1 targets in mouse embryonic stem cells and in early differentiation compared to non-targets in the PHLPP2 KO RNA-seq dataset. p-values indicate significance.

G. Similar to C with draws of 2513 gens (=number of FOXO1 targets in mouse embryonic stem cells and in early differentiation).

Supplementary Figure 4. Phosphatase inhibitor beads selectively enrich PP2A, PP4 and PP6.

A

Leading protein	Gene name	Protein name	Organism	Molecular weight (kDa)	Total # unique peptides	Sequence coverage	Imputed LFQ intensity [log2]		Enrichment ratio [log2]
							-OA	+OA (ctrl)	
A0A2H1WUX1	SFRICE_008486	60S ribosomal protein L24	*Spodoptera frugiperda*	17.39	2	13.50	25.37	15.00	10.37
J9Z496		PP2A C-subunit		35.44	23	68.30	25.69	15.46	10.23
A0A2H1W5F9	SFRICE_005114	Abl tyrosine kinase		63.75	2	4.80	20.68	10.74	9.94
A0A2H1X028	SFRICE_014915	PP2A A-subunit		65.27	39	68.00	27.03	17.94	9.08
A0A2H1WQP4	SFRICE_007634	PP2A 56 kDa γ-like subunit*		9.37	2	31.80	17.65	9.20	8.45
A0A2H1VFZ6	SFRICE_004402	Protein Phosphatase 4 C-subunit		35.53	10	27.70	23.37	15.53	7.84
A0A2H1WYQ1	SFRICE_025240	PP2A 56 kDa ε regulatory subunit		41.67	15	37.50	20.99	13.68	7.31
A0A2H1W1C4	SFRICE_000120	uncharacterized protein		20.10	3	17.70	16.82	9.94	6.88
A0A2H1V7H1	SFRICE_001858	Striatin-interacting protein (STRIPAK)		141.61	22	19.10	20.80	14.26	6.53
A0A2H1VCR1	SFRICE_002609	Striatin-3 (PP2A B-subunit)		75.12	30	54.30	22.48	16.20	6.28
A0A2H1V3Y5	SFRICE_015530	PP2A 55 kDa regulatory subunit B		56.78	24	45.10	23.73	17.53	6.20
A0A2H1WL05	SFRICE_022984	MOB kinase activator-like 4		25.51	9	36.70	22.69	16.74	5.95
A0A2H1VWP9	SFRICE_003851	Protein phosphatase 6 regulatory subunit 3-A		91.52	17	20.10	23.07	17.66	5.42
A0A2H1WE70	SFRICE_008170	Protein phosphatase 4 regulatory subunit 3		90.35	23	31.30	18.20	13.49	4.71
A0A2H1V4G9	SFRICE_023010	Myelin P2 protein		21.00	2	10.60	18.11	13.77	4.34
A0A2H1X0P5	SFRICE_029750	Protein phosphatase 6 C-subunit		34.86	13	37.60	22.00	17.74	4.26
A0A2H1W001	SFRICE_003894	Protein phosphatase 4 regulatory subunit 2		54.77	20	46.30	19.80	15.59	4.21
A0A2H1X3N4	SFRICE_031227	Microtubule-associated protein RP/EB 1		41.94	2	4.80	15.15	10.99	4.16
Q6ZVD8	Q6ZVD8	PHLPP2 (heterologous over-expression)	*Homo sapiens*	146.66	19	17.10	19.16	19.68	-0.53

A. Tandem mass spectrometry analysis of proteins bound to microcystin-LR-conjugated beads after incubation with cell lysates of Sf9 cells heterologously over-expressing PHLPP2. Red: protein phosphatases and protein-phosphatase-associated regulatory proteins.

Supplementary Figure 5. PP2A B56β dephosphorylates Akt in HAP1 cells.

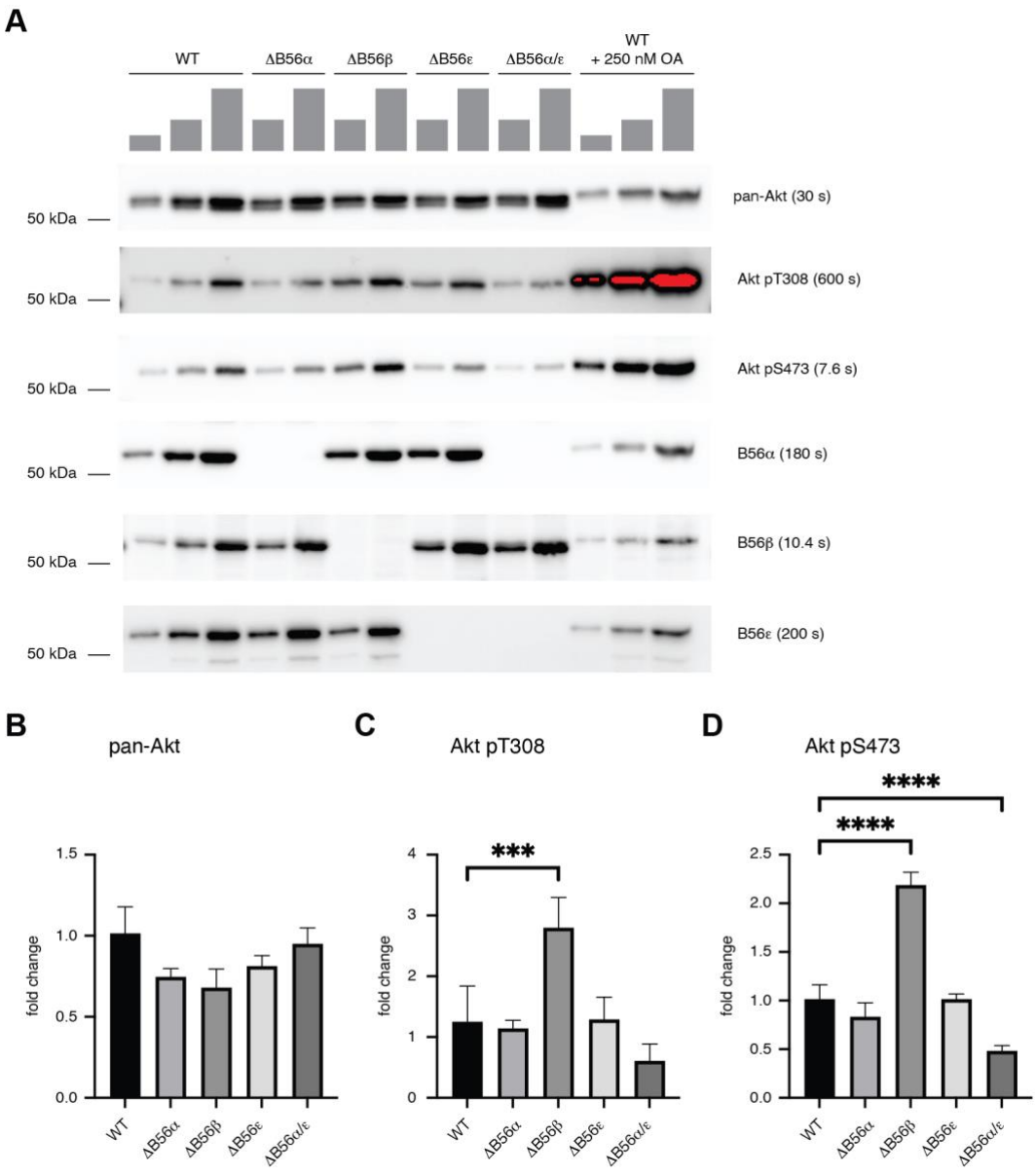

A. Immunoblotting of HAP1 wild-type, ΔB56α, ΔB56β, ΔB56ε, ΔB56α/ε, and okadaic acid treated (250nM for 3h) wild-type cell lysates using indicated antibodies. The blots are representative of n=4 experiments. Signals obtained from pan-Akt, Akt pT308, Akt pS473 were quantified, and Akt pT308 and Akt pS473 were normalised to pan-Akt. The data is shown as mean values ± s.d. relative to the wild-type, set to 1. Statistical significance was assessed by performing an ordinary one-way ANOVA. *P < 0.05 ***P < 0.005, ****P < 0.001.

B. Quantification of pan-Akt signal (n=4).

C. Quantification of Akt pT308 signal (n=4).

D. Quantification of Akt pS473 signal (n=4).

Supplementary Figure 6. PHLPP2 is a zinc-binding protein.

A

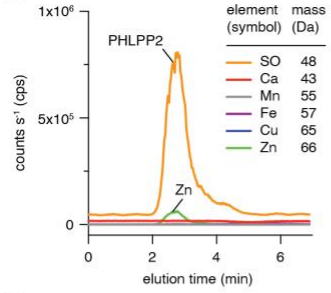

B

Sample	^{32}S peak area (counts)	^{65}Cu peak area (counts)	^{66}Zn peak area (counts)	S/Cu ratio	S/Zn ratio	stoichiometry (S:Cu:Zn)
SOD[1] (calibrant)	1324513	2253245	1854913	0.5878	0.7141	4:1:1
	1321345	2249440	1826849	0.5874	0.7233	
	1359483	2313953	1880422	0.5875	0.7230	
Average				0.5876	0.7201	
RSD (n=3)				<1%	<1%	
PHLPP2[2]	50032296	448795	3674225	111.4815	13.6171	67 : 0.09 : 0.88
(replicate #1)	48727540	415543	4204563	117.2623	11.5920	67 : 0.08 : 1.04
	18592408	111698	1685312	166.4532	11.0320	67 : 0.06 : 1.09
Average						67 : 0.08 : 1.01
RSD (n=3)			Total combined uncertainty of the measured stoichiometry: 11%			
PHLPP2[2]	38036679	-	2752163	-	13.8207	67 : - : 1.09
(replicate #2)	23377197	-	1600115	-	14.6097	67 : - : 1.03
	55531332	-	4939412	-	11.2425	67 : - : 1.35
Average						67 : - : 1.16
RSD (n=3)			Total combined uncertainty of the measured stoichiometry: 14%			
PHLPP2[2]	350283355	-	35552871	-	9.8525	67 : - : 1.25
(replicate #3)	403417464	-	42803314	-	9.4249	67 : - : 1.31
Average						67 : - : 1.28
RSD (n=2)			Total combined uncertainty of the measured stoichiometry: 10%			

[1]Bovine SOD1; 3 Cys + 1 Met = total 4S.
[2]Human PHLPP2; 40 Cys + 27 Met = total 67S.

C

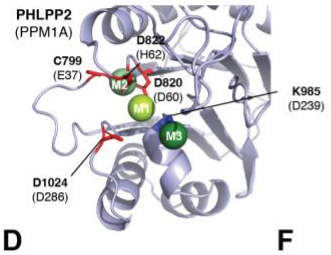

D

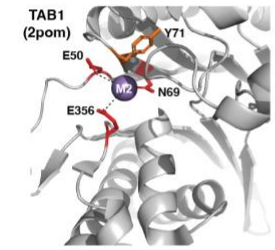

F

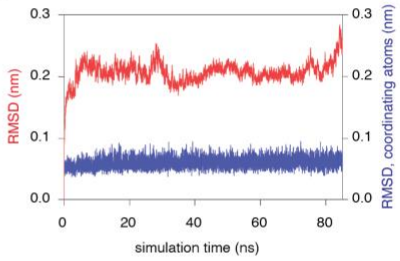

G

ONIOM validation (α-klotho)	Bond S - Zn^{2+} (Å)	Bond O - Zn^{2+} (Å)
experimental structure (5W21)	2.30	1.99
B3LYP/6-31G(d,p):PM3	2.34	1.97
B3LYP/6-31+G(d,p):PM3	2.36	2.02
B3LYP/6-31+G(3d,p):PM3	2.34	2.01
MO62X/6-31G(d,p):PM3	2.39	1.99
MO62X/6-31+G(d,p):PM3	2.39	2.00
MO62X/6-31+G(3d,p):PM3	2.40	2.01
ωB97XD/6-31G(d,p):PM3	2.33	2.96
ωB97XD/6-31+G(d,p):PM3	2.32	2.01

E

Residue # (CYS)	Structure prediction	coverage (Y/N)	MMTS/IAA ratio	solvent accessible / inaccessible?
133	solvent accessible (RA)	Y	0.23	accessible
143	solvent accessible loop (RA)	Y	0.01 - 0.02	accessible
177	PH-LRR interface	Y	n.d.	n.d.
180	PH-LRR interface	Y	n.d.	n.d.
189	solvent accessible (PH)	Y	0	accessible
258	solvent accessible (RA-LRR)	Y	0.27	accessible
402	solvent accessible (LRR)	Y	0.06	accessible
460	solvent accessible (LRR)	Y	n.d.	n.d.
467	core (LRR)	Y	25.46 - 41.28	inaccessible
516	solvent accessible (LRR)	Y	0	accessible
522	core (LRR)	Y	3.67	partially accessible
690	core (LRR)	Y	17.94 - 34.16	inaccessible
799	solvent accessible (PP2C)	Y	10.62	inaccessible
833	solvent accessible (PP2C)	Y	0.05 - 0.07	accessible
878	core (PP2C)	Y	n.d.	n.d.
901	core (PP2C)	Y	n.d.	n.d.
906	core (PP2C)	Y	n.d.	n.d.
948	solvent accessible (PP2C)	Y	6.5	
949	solvent accessible (PP2C)	Y	9.21	
955	solvent accessible (PP2C)	Y	0.47 - 3.38	partially accessible
1118	solvent accessible (C-ter.)	Y	2.83 - 2.87	partially accessible
1173	solvent accessible (C-ter.)	Y	0.13 - 0.22	accessible
1174	solvent accessible (C-ter.)	Y	0.13 - 0.22	accessible
1193	solvent accessible (C-ter.)	Y	0.14 - 1.45	accessible
1202	solvent accessible (C-ter.)	Y	0.04 - 0.10	accessible
1234	solvent accessible (C-ter.)	Y	0.00 - 0.01	accessible
9	solvent accessible (N-ter.)	N	-	-
32	core (RA)	N	-	-
67	core (RA)	N	-	-
77	core (RA)	N	-	-
319	core (LRR)	N	-	-
331	solvent accessible (LRR)	N	-	-
351	solvent accessible (LRR)	N	-	-
613	solvent accessible (LRR)	N	-	-
636	core (LRR)	N	-	-
722	LRR-PP2C interface	N	-	-
1014	core (PP2C)	N	-	-
1022	core (PP2C)	N	-	-
1040	solvent accessible (C-ter.)	N	-	-
1042	solvent accessible (C-ter.)	N	-	-

n.d. = not determined

H

Residue	Bond	Molecular Dynamics (Å)	Quantum Mechanics B3LYP/ 6-31+G(3,d,p):PM3 (Å)	Quantum Mechanics ωB97XD/ 6-31G(d,p):PM3 (Å)
C799	S - Zn^{2+}	3.0	2.34	2.33
D820	O - Zn^{2+}	1.8	2.04	1.96
D822	O - Zn^{2+}	1.9	2.03	1.97
D1024	O - Zn^{2+}	1.8	1.99	1.94

I

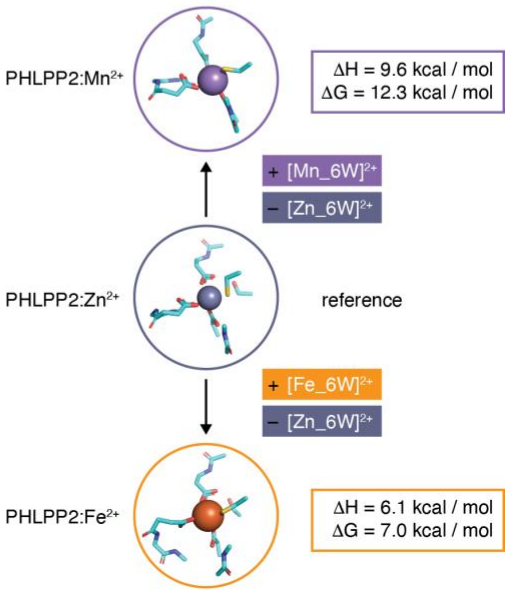

A. ICP-MS chromatograms for recombinant human PHLPP2, including the sulfur signal from the protein.

B. Calibration of PHLPP2:Zn^{2+} stoichiometry for three biological replicates, each with duplicate or triplicate technical replicates.

C. Metal ion positions of PPM1A (PDB ID: 6b67) superimposed on AF2 model of PHLPP2 PP2C domain.

D. Experimentally determined structure of TAB1 pseudophosphatase, with one metal ion bound in the M2 position.

E. Tandem mass spectrometry analysis of differentially alkylated tryptic peptides from $PHLPP2^{WT}$ under native and denaturing conditions.

F. Cartesian root-mean-square deviation (RMSD) from the initial equilibrated structure over either all PHLPP2 atoms (red) or distance restrained groups (blue) as a function of time in MD simulations.

G. Validation of the ONIOM method for the experimentally determined C1D3 zinc finger of α-klotho (10) (PDB ID 5W21). Comparison of bond lengths optimized by three quantum mechanical methods, each with different basis sets, to the experimentally determined bond lengths.

H. Comparison of interatomic distances between Zn^{2+} and coordinating atoms in the MS2 binding site (carboxy atoms in aspartic acid or sulfur in cysteine) in the final MD structure and the final QM-optimized structure.

I. B3LYP/6-31+G(3d,p) fully optimized structures of metal binding sites of PHLPP2 comprising ligands from the first and second coordination layer, and enthalpies and Gibbs energies for $[M(H_2O)_6]^{2+}$ + [PHLPP2-Zn]$^{2-}$→ [PHLPP2-M]$^{2-}$ + $[Zn(H_2O)_6]^{2+}$ (M = Mn or Fe). Solvent accessible metal binding sites characterized with dielectric constant of 29 are considered. Calculation methodology according to (46).

Supplementary Figure 7. Cancer genomics does not support a role for PHLPP1 or PHLPP2 as tumor suppressors.

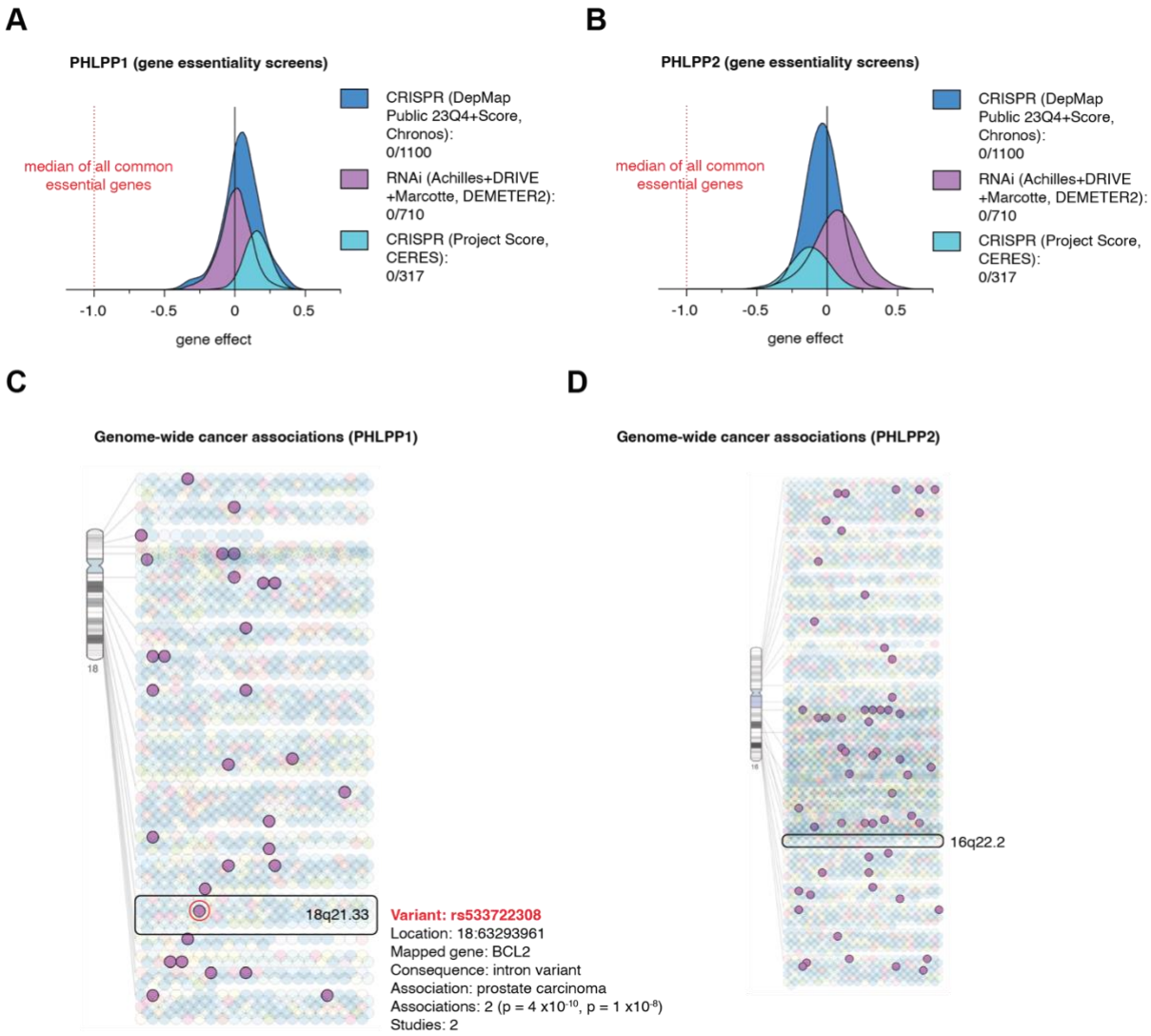

A. PHLPP1 essentiality determined from CRISPR knockout (blue) and RNAi (purple) screens for 1100 and 710 lines respectively. Copy number-corrected CRISPR knockout (CERES) gene effect scores for 317 cancer cell lines (cyan).

B. PHLPP2 essentiality determined from CRISPR knockout (blue) and RNAi (purple) screens for 1100 and 710 lines respectively. Copy number-corrected CRISPR knockout (CERES) gene effect scores for 317 cancer cell lines (cyan).

C. Genome-wide cancer associations in the chromosomal locus 18q21.33 containing the PHLPP1 gene. Red: single cancer-associated variant with a p-value < 5.0×10^{-8}, which maps to an intron of the BCL2 gene.

D. Genome-wide cancer associations in the chromosomal locus 16q22.2 containing the PHLPP2 gene.

Supplementary Figure 8. Cryo-electron microscopy structure of PHLPP2.

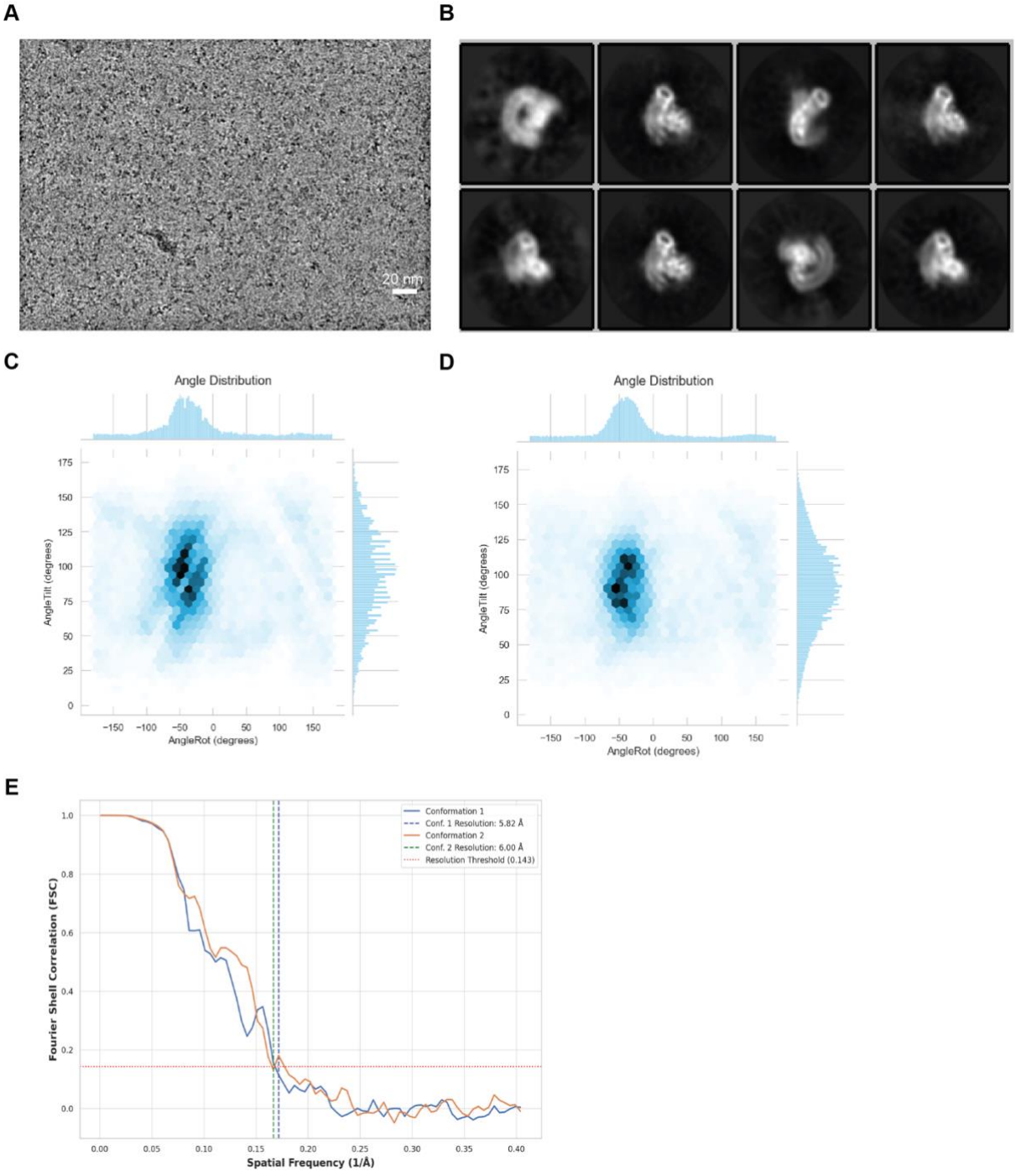

A. Representative micrograph.

B. Selected class averages representing the different viewing directions in the dataset.

C. Angle distribution plot of conformation 1.

D. Angle distribution plot of conformation 2.

E. Fourier shell correlation curves for each conformation.

Supplementary Figure 9. Evolution and diversification of PHLPP genes.

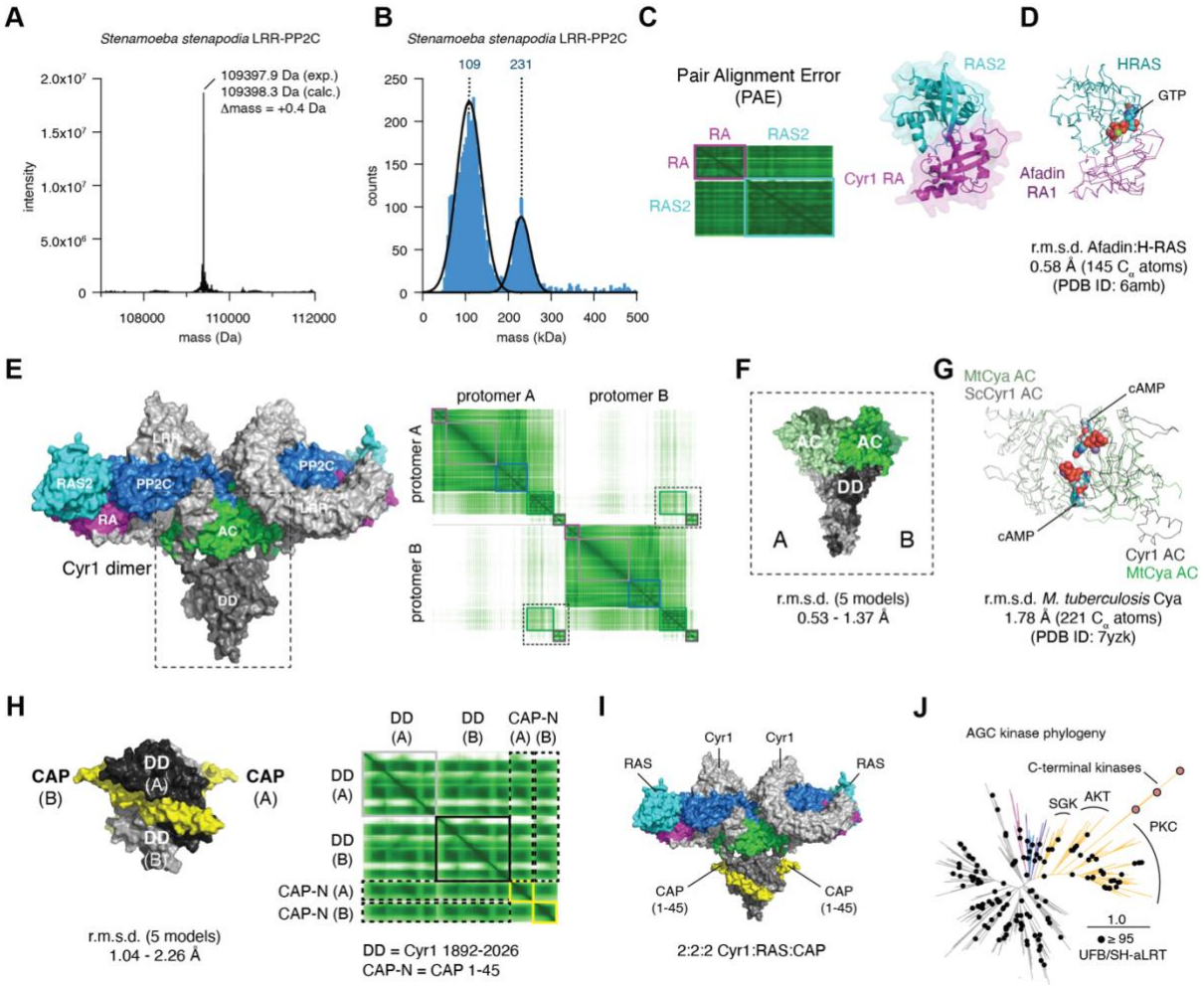

A. Mass spectrum of recombinant *Stenamoeba stenapodia* LRR-PP2C.

B. Mass photometry of recombinant *Stenamoeba stenapodia* LRR-PP2C.

C. Structure prediction and associated PAE plot for the complex between the RA domain of *S. cerevisiae* Cyr1 (magenta) and RAS2 (cyan).

D. Superposition of the predicted Cyr1 RA:RAS2 structure (magenta/cyan) with the experimentally determined structure of the Afadin RA domain with GTP-bound H-RAS (purple/teal) (6amb). R.m.s.d. determined over 145 equivalent C_α atoms.

E. Structure prediction and associated PAE plot for dimeric *S. cerevisiae* Cyr1. Dashed rectangle: dimerization of the AC and CTD domains of Cyr1.

F. Structure prediction and associated PAE plot for dimeric AC-CTD domain of *S. cerevisiae* Cyr1. Agreement of 5 independent models shown by the r.m.s.d. over all C_α atoms.

G. Superposition of the predicted Cyr1 AC-CTD dimer (black/grey) with the experimentally determined structure of the AC domain of *M. tuberculosis* Cya (dark green/light green) (7yzk). R.m.s.d. determined over 221 equivalent C_α atoms.

H. Structure prediction and associated PAE plot for the dimeric CTD domain of *S. cerevisiae* Cyr1 (black/grey) in complex with two molecules of CAP (amino acids 1-45; yellow). Agreement of 5 independent models shown by the r.m.s.d. over all C_α atoms.

I. Structure prediction of the Cyr1:RAS2:CAP heterohexamer (2:2:2).

J. Maximum-likelihood phylogeny of kinase domains. The C-terminal kinase domains of unicellular holozoan Cyr1 cluster with AGC kinases of the Akt and PKC families. The kinase domain phylogeny can be viewed at https://itol.embl.de/shared/9pitR7NesER8.

Supplementary Table 1. Cryo-EM data collection, refinement statistics

	PHLPP conf1 (EMDB-51182)	PHLPP conf2 (EMDB-51183)
Data collection and processing		
Magnification	130 k	
Voltage (kV)	300	
Electron exposure (e–/Å^2)	35	
Defocus range (μm)	1.7-2.5	
Pixel size (Å)	0.55 (super resolution)	
Symmetry imposed	C1	
Initial particle images (no.)	958089	
Final particle images (no.)	118375	355036
Map resolution (Å) FSC threshold 0.143	6.0	5.8

Supplementary References

1. L. Truebestein, *et al.*, Structure of autoinhibited Akt1 reveals mechanism of PIP3-mediated activation. *Proc. Natl. Acad. Sci. U. S. A.* **118** (2021).

2. E. Y. Chen, *et al.*, Enrichr: interactive and collaborative HTML5 gene list enrichment analysis tool. *BMC Bioinformatics* **14**, 128 (2013).

3. A. Degasperi, *et al.*, Evaluating strategies to normalise biological replicates of Western blot data. *PLoS One* **9**, e87293 (2014).

4. S. Hann, G. Koellensperger, C. Obinger, P. G. Furtmüller, G. Stingeder, SEC-ICP-DRCMS and SEC-ICP-SFMS for determination of metal–sulfur ratios in metalloproteins. *J. Anal. At. Spectrom.* **19**, 74–79 (2004).

5. B. L. Brauer, *et al.*, Affinity-based profiling of endogenous phosphoprotein phosphatases by mass spectrometry. *Nat. Protoc.* **16**, 4919–4943 (2021).

6. M. J. Abraham, *et al.*, GROMACS: High performance molecular simulations through multi-level parallelism from laptops to supercomputers. *SoftwareX* **1–2**, 19–25 (2015).

7. K. Lindorff-Larsen, *et al.*, Improved side-chain torsion potentials for the Amber ff99SB protein force field. *Proteins* **78**, 1950–1958 (2010).

8. S. Piana, A. G. Donchev, P. Robustelli, D. E. Shaw, Water dispersion interactions strongly influence simulated structural properties of disordered protein states. *J. Phys. Chem. B* **119**, 5113–5123 (2015).

9. J. Jumper, *et al.*, Highly accurate protein structure prediction with AlphaFold. *Nature* 1–7 (2021).

10. G. Chen, *et al.*, α-Klotho is a non-enzymatic molecular scaffold for FGF23 hormone signalling. *Nature* **553**, 461–466 (2018).

11. B. Hess, H. Bekker, H. J. C. Berendsen, J. G. E. M. Fraaije, LINCS: A linear constraint solver for molecular simulations. *J. Comput. Chem.* **18**, 1463–1472 (1997).

12. G. Bussi, D. Donadio, M. Parrinello, Canonical sampling through velocity rescaling. *J. Chem. Phys.* **126**, 014101 (2007).

13. M. Parrinello, A. Rahman, Polymorphic transitions in single crystals: A new molecular dynamics method. *J. Appl. Phys.* **52**, 7182–7190 (1981).

14. M. J. Frisch, *et al.*, *Gaussian 16 Rev. C.01* (2016).

15. S. Dapprich, I. Komáromi, K. S. Byun, K. Morokuma, M. J. Frisch, A new ONIOM implementation in Gaussian98. Part I. The calculation of energies, gradients, vibrational frequencies and electric field derivatives1Dedicated to Professor Keiji Morokuma in celebration of his 65th birthday.1. *Journal of Molecular Structure: THEOCHEM* **461–462**, 1–21 (1999).

16. T. Dudev, C. Lim, Factors governing the protonation state of cysteines in proteins: an Ab initio/CDM study. *J. Am. Chem. Soc.* **124**, 6759–6766 (2002).

17. J. Rappsilber, M. Mann, Y. Ishihama, Protocol for micro-purification, enrichment, pre-fractionation and storage of peptides for proteomics using StageTips. *Nat. Protoc.* **2**, 1896–1906 (2007).

18. A. T. Kong, F. V. Leprevost, D. M. Avtonomov, D. Mellacheruvu, A. I. Nesvizhskii, MSFragger: ultrafast and comprehensive peptide identification in mass spectrometry-based proteomics. *Nat. Methods* **14**, 513–520 (2017).

19. D. M. Hollenstein, *et al.*, Chemical Acetylation of Ligands and Two-Step Digestion Protocol for Reducing Codigestion in Affinity Purification-Mass Spectrometry. *J. Proteome Res.* **22**, 3383–3391 (2023).

20. Y. Perez-Riverol, *et al.*, The PRIDE database and related tools and resources in 2019: improving support for quantification data. *Nucleic Acids Res.* **47**, D442–D450 (2019).

21. A. Punjani, J. L. Rubinstein, D. J. Fleet, M. A. Brubaker, cryoSPARC: algorithms for rapid unsupervised cryo-EM structure determination. *Nat. Methods* **14**, 290–296 (2017).

22. D. Kimanius, L. Dong, G. Sharov, T. Nakane, S. H. W. Scheres, New tools for automated cryo-EM single-particle analysis in RELION-4.0. *Biochem. J* **478**, 4169–4185 (2021).

23. D. Kimanius, *et al.*, Data-driven regularisation lowers the size barrier of cryo-EM structure determination. *bioRxiv* 2023.10.23.563586 (2023).

24. T. D. Goddard, *et al.*, UCSF ChimeraX: Meeting modern challenges in visualization and analysis. *Protein Sci.* **27**, 14–25 (2018).

25. R. T. Kidmose, *et al.*, Namdinator - automatic molecular dynamics flexible fitting of structural models into cryo-EM and crystallography experimental maps. *IUCrJ* **6**, 526–531 (2019).

26. UniProt Consortium, UniProt: a worldwide hub of protein knowledge. *Nucleic Acids Res.* **47**, D506–D515 (2019).

27. F. A. Simão, R. M. Waterhouse, P. Ioannidis, E. V. Kriventseva, E. M. Zdobnov, BUSCO: assessing genome assembly and annotation completeness with single-copy orthologs. *Bioinformatics* **31**, 3210–3212 (2015).

28. B. Buchfink, K. Reuter, H.-G. Drost, Sensitive protein alignments at tree-of-life scale using DIAMOND. *Nat. Methods* **18**, 366–368 (2021).

29. S. Capella-Gutiérrez, J. M. Silla-Martínez, T. Gabaldón, trimAl: a tool for automated alignment trimming in large-scale phylogenetic analyses. *Bioinformatics* **25**, 1972–1973 (2009).

30. S. Guindon, *et al.*, New algorithms and methods to estimate maximum-likelihood phylogenies: assessing the performance of PhyML 3.0. *Syst. Biol.* **59**, 307–321 (2010).

31. K. Katoh, D. M. Standley, MAFFT Multiple Sequence Alignment Software Version 7: Improvements in Performance and Usability. *Mol. Biol. Evol.* **30**, 772–780 (2013).

32. L. T. Nguyen, H. A. Schmidt, A. Von Haeseler, B. Q. Minh, IQ-TREE: A fast and effective stochastic algorithm for estimating maximum-likelihood phylogenies. *Mol. Biol. Evol.* **32**, 268–274 (2015).

33. D. T. Hoang, O. Chernomor, A. von Haeseler, B. Q. Minh, L. S. Vinh, UFBoot2: Improving the Ultrafast Bootstrap Approximation. *Mol. Biol. Evol.* **35**, 518–522 (2018).

34. D. J. Richter, *et al.*, EukProt: A database of genome-scale predicted proteins across the diversity of eukaryotes. *Peer Community Journal* **2** (2022).

35. S. Kalyaanamoorthy, B. Q. Minh, T. K. F. Wong, A. Von Haeseler, L. S. Jermiin, ModelFinder: Fast model selection for accurate phylogenetic estimates. *Nat. Methods* **14**, 587–589 (2017).

36. F. Burki, A. J. Roger, M. W. Brown, A. G. B. Simpson, The New Tree of Eukaryotes. *Trends Ecol. Evol.* **35**, 43–55 (2020).

37. H. Shimodaira, An approximately unbiased test of phylogenetic tree selection. *Syst. Biol.* **51**, 492–508 (2002).

38. I. Letunic, P. Bork, Interactive Tree of Life (iTOL) v6: recent updates to the phylogenetic tree display and annotation tool. *Nucleic Acids Res.* (2024). https://doi.org/10.1093/nar/gkae268.

39. J. Mistry, R. D. Finn, S. R. Eddy, A. Bateman, M. Punta, Challenges in homology search: HMMER3 and convergent evolution of coiled-coil regions. *Nucleic Acids Res.* **41**, e121 (2013).

40. J. Mistry, *et al.*, Pfam: The protein families database in 2021. *Nucleic Acids Res.* **49**, D412–D419 (2021).

41. T. J. Wheeler, J. Clements, R. D. Finn, Skylign: a tool for creating informative, interactive logos representing sequence alignments and profile hidden Markov models. *BMC Bioinformatics* **15**, 7 (2014).

42. B. Boeckmann, *et al.*, The SWISS-PROT protein knowledgebase and its supplement TrEMBL in 2003. *Nucleic Acids Res.* **31**, 365–370 (2003).

43. G. S. C. Slater, E. Birney, Automated generation of heuristics for biological sequence comparison. *BMC Bioinformatics* **6**, 31 (2005).

44. N. A. T. Irwin, *et al.*, The function and evolution of motile DNA replication systems in ciliates. *Curr. Biol.* **31**, 66-76.e6 (2021).

45. T. Gao, F. Furnari, A. C. Newton, PHLPP: a phosphatase that directly dephosphorylates Akt, promotes apoptosis, and suppresses tumor growth. *Mol. Cell* **18**, 13–24 (2005).

46. T. Dudev, K. Mazmanian, C. Lim, Competition between Li+ and Na+ in sodium transporters and receptors: Which Na+-Binding sites are “therapeutic” Li+ targets? *Chem. Sci.* **9**, 4093–4103 (2018).

4 Discussion

Recent studies that correlate MAST kinase mutations with NDDs has initiated a growing interest in the MAST kinase field. However, the field is still emerging, and little is understood about the biological role the MAST kinases play. This work is one of the first to probe the molecular mechanisms of MAST kinase activity and shed light on the pathways it might be involved in.

4.1 Three new players in MAST1 signalling

We have identified three interactors of MAST1: an upstream kinase PAK, a regulatory binder 14-3-3η, and a substrate Tau [158]. PAK4 was found to phosphorylate S90 in the DUF of MAST1 *in vitro*, although published single-cell datasets suggest that PAK6 may be the physiologically relevant paralog. 14-3-3η binds to both p-S90 and p-S161 of MAST1, but the mechanistic role of binding is not yet understood. Using mouse models of human disease combined with *in vivo* phosphoproteomics and *in vitro* biochemistry, S214 of the microtubule-associated protein Tau was identified as a MAST1 substrate. Together, these findings start to build a picture of the MAST1 pathway.

4.1.1 14-3-3 proteins

14-3-3 proteins are highly abundant cytosolic proteins, existing in the cell as constitutive dimers. There are seven human 14-3-3 paralogs: β, γ, ε, η, τ, ζ, and σ. 14-3-3 proteins adopt a cup-shaped conformation within which an amphipathic binding groove recognises and binds phosphorylated serines. A sequence motif of either RSX(pS)XP or RXXX(pS)XP typically surrounds the phosphorylated serine, however this consensus is flexible, with slight variations reported for many 14-3-3-binding proteins [118,119].

14-3-3 proteins are frequently involved in the regulation of protein kinases, with the ability to serve multiple purposes. The binding of 14-3-3 to a regulatory phosphorylation site on a kinase can protect that site from dephosphorylation, while its sequestration can prevent the site from docking to regulatory regions on the kinase. Additionally, due to the dimeric nature of 14-3-3 proteins, two proteins can be forced into close proximity when bound to either protomer of 14-3-3, promoting their interaction. For example, p-S294 of phosphatidylinositol 4-kinase β (PI4KB) binds to 14-3-3, which not only protects it from dephosphorylation, but also acts as an adaptor protein,

recruiting brefeldin A ADP-ribosylated substrate (BARS) to its opposing protomer [159]. The resultant 2:1:1 complex induces the interaction between PI4KB and BARS.

A well-studied example of 14-3-3-mediated regulation of kinase activity is BRAF, previously mentioned in the introduction. BRAF possesses two 14-3-3 binding sites, one between its cysteine-rich domain and kinase domain (S365) and another immediately following its kinase domain (S729). In the inactive state, both sites are phosphorylated and simultaneously recognised by each protomer of a 14-3-3 dimer, forming a heterotrimer in which the membrane binding C1 domain is buried in autoinhibitory intramolecular contacts (Figure 14A). Upon mitogen stimulation, the RAS-binding domain of BRAF binds to RAS-GTP at the membrane, causing a conformational change in BRAF that both releases the C1 domain and p-S365 from 14-3-3. The newly freed 14-3-3 cradle is then available to bind another molecule of BRAF via p-S729, forming a heterotetramer (Figure 14B-D). This promotes the back-to-back dimerisation of BRAF, which allosterically triggers the formation of the active conformation [120–123]. In this complex, BRAF can phosphorylate its downstream substrate MEK1.

Like BRAF, the presence of two 14-3-3-binding motifs within one protein is commonly observed, as it allows tighter regulation by 14-3-3. In fact, a 30-fold increase in binding affinity was reported between 14-3-3 and a phosphopeptide with tandem binding motifs, compared to a single binding motif [119]. Often, one binding site termed the 'gatekeeper' initiates the interaction with 14-3-3, and is followed by binding of a lower-affinity secondary site, only made possible by the increase in local concentration [160]. Alternatively, the gatekeeper site could serve to pre-assemble 14-3-3 binding, such that the secondary site can dock instantly into the free 14-3-3 protomer upon its phosphorylation. Both PKCε and leucine-rich repeat kinase 2 (LRRK2) possess tandem 14-3-3-binding sites, and only form high affinity, stable complexes when both sites are engaged [161–163].

In this study, we found that MAST1 also has two 14-3-3-binding sites in tandem: S90 and S161. The sequences of these sites, GRRW(S)LAS and PRSR(S)LSP respectively, show loose fits to the known sequence motifs, with S161 exhibiting a closer fit and correspondingly higher binding affinity. The presence of both sites appear to have a synergistic effect on 14-3-3 binding (Chapter 3.1.3, Figure 1F-H) [158], however it is not yet

understood whether one site acts as a gatekeeper, and if both sites bind simultaneously or sequentially. This will be discussed in more detail in Chapter 4.2.

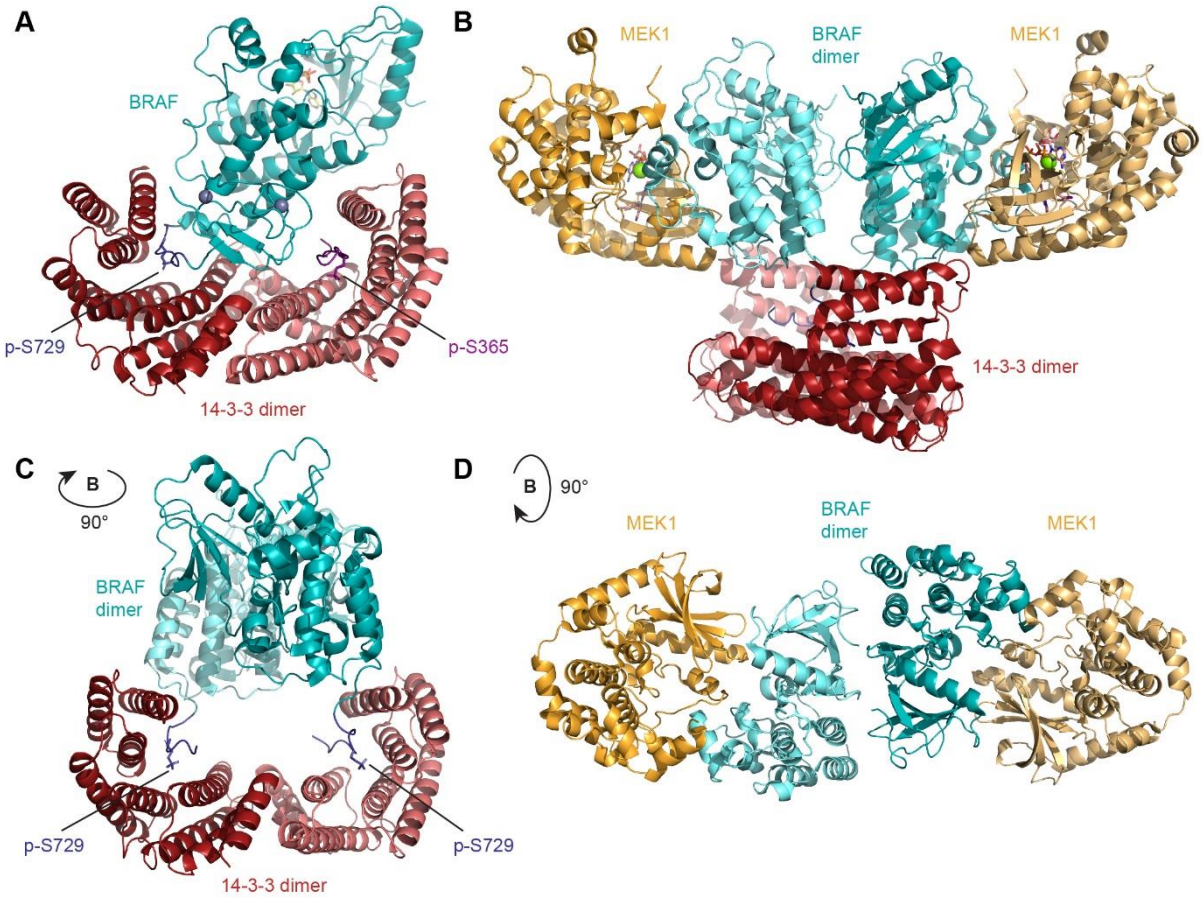

Figure 14. Mechanism of BRAF regulation by 14-3-3.

A. Structure of inactive trimer of BRAF (teal) and 14-3-3 dimer (dark and light red) determined by electron microscopy (PDB: 6NYB) [120]. Both p-S365 (purple) and p-S729 (dark blue) are simultaneously bound to either protomer of the 14-3-3 dimer. **B.** Structure of active tetramer of BRAF dimer (dark and light teal) and 14-3-3 dimer (dark and light red), with MEK1 bound to either BRAF protomer (dark and light orange) determined by X-ray crystallography (PDB: 6Q0J) [120]. **C.** Structure from (B) turned 90° about its z axis. p-S729 from both BRAF protomers (dark blue) are simultaneously bound to either protomer of the 14-3-3 dimer. MEK1 hidden for clarity. **D.** Structure from (B) turned 90° about its x axis. BRAF forms a back-to-back dimer, with its active site facing outwards towards its substrate MEK1. 14-3-3 hidden for clarity.

Figure 1F-H of Chapter 3.1.3 also revealed that 14-3-3η was consistently the highest enriched paralog with MAST1 [158], despite having the lowest abundance in the HEK293 cells used in the experiment [164]. 14-3-3η is also highly abundant in brain tissue compared to other tissues [165,166]. This suggests that 14-3-3η may be the physiologically relevant paralog for MAST1 signalling; however, given the high abundance of many other 14-3-3 paralogs in the brain [165,166], their involvement cannot be excluded.

4.1.2 The upstream kinase PAK

The PAKs comprise PAK1-6, and are divided into two groups: group I (PAK1-3) and group II (PAK4-6), differing in their modes of regulation [167,168] and substrate specificity [169]. With a combination of AP-MS (Chapter 3.1.3, Figure 1F-H) *in vitro* kinase assays (Chapter 3.1.3, Figure 2C), and tandem MS experiments (Chapter 3.1.3, Figure 2E), and supported by the ScoreSite prediction tool (Chapter 3.1.3, Figure 2B) [170], we have shown that a group II PAK is responsible for phosphorylating MAST1 on S90 [158].

Consistent with their association with MAST1 signalling, group II PAKs are involved in many neurodevelopmental pathways. PAK4 is reported to play an important role in neurogenesis, including neural progenitor cell growth [171], and neuronal differentiation and migration, [172] while PAK6 has been implicated in neurite outgrowth [173]. Additionally, a double knockout of PAK5 and PAK6 in mice resulted in several neurodevelopmental issues such as motor and learning defects [174]. The PAKs are known to achieve these roles through their regulation of the actin cytoskeleton, by phosphorylating LIM kinase 1 (LIMK1), which subsequently phosphorylates and disables the actin polymeriser cofilin [175]. It is not surprising that a kinase involved in the regulation of the actin cytoskeleton is also involved in the regulation of MAST1, a microtubule-associated kinase. As the actin and microtubule networks are coupled, they must be regulated in a coordinated manner, particularly in processes such as neurite outgrowth (as discussed in Chapter 1.1.3). Hence, certain signalling mechanisms must be in place to facilitate communicate between actin and microtubules, in which PAK and MAST1 might play a role.

Group II PAKS are activated by the Rho-family GTPase Cdc42, upon recruitment via their N-terminal Cdc42/Rac interactive binding (CRIB) domain to active Cdc42 at the membrane [167,176,177]. Cdc42 regulates myriad biological processes including cell polarisation, differentiation, and migration, by controlling the actin cytoskeleton and microtubule dynamics [178]. All group II PAKs (PAK4-6) have been observed to localise to cell-cell junctions in a Cdc42-dependent manner, while PAK1, a group I PAK, does not [179,180]. Additionally, depletion of either Cdc42 or PAK4 resulted in cell polarity defects in a number of cell types [179]. If phosphorylation of MAST1 S90 by PAK is required for its activation, this would place MAST1 signalling downstream of active Cdc42. Taken together, our findings suggest that Cdc42-activated PAK branches into two pathways; one

to regulate the reorganisation of actin via LIMK1, and another to modulate microtubule dynamics via MAST1. Here, a single signal for changes in cell morphology could be transduced through Cdc42 and PAK to control both actin and microtubules in a coupled manner.

While PAK4 was employed for the radiometric kinase assay in this study (Chapter 3.1.3, Figure 2C), it is possible that PAK6 is the physiologically relevant paralog for MAST1 phosphorylation, due to the similar expression patterns between PAK6 and MAST1 in the developing brain [73]. Since PAK6 is not expressed in HEK293 cells [164], it was not detected alongside PAK4 in the AP-MS (Chapter 3.1.3, Figure 1F-H). Given the group II PAKs recognise almost identical sequences, any could accomplish *in vitro* phosphorylation of MAST1, and specificity is likely based on cellular context.

4.1.3 The downstream substrate Tau

The identification of Tau as a potential substrate of MAST1 is supported by multiple observations. Two different MAST1-mutant mouse models used for phosphoproteomics independently revealed S214 of Tau to be significantly hypophosphorylated in the mutants (Chapter 3.1.3, Figure 6A-E) [158]. This was validated with an *in vitro* kinase assay where purified MAST1 was capable of phosphorylating S214 of purified Tau (Chapter 3.1.3, Figure 6F-H) [158]. Furthermore, the sequence surrounding S214 of Tau perfectly conforms to an AGC kinase recognition motif, and displays high similarity to a potential autophosphorylation site in MAST1 (S161). Not only do both Tau and MAST1 localise to microtubules, but they are also expressed in the same cell types during cortical development [73].

Tau plays a major role in microtubule reorganisation, by promoting stability and rigidity of microtubules when bound, and vice versa. The binding of Tau to microtubules is largely regulated by its phosphorylation state. Tau possesses several phosphorylation sites within its proline-rich domain and repeat domains, and in most cases, phosphorylation of these sites drives dissociation of Tau from microtubules. This has been observed with our phosphosite of interest, S214, where phosphorylation reduced the binding affinity of Tau to microtubules, subsequently resulting in higher flexibility and destabilisation of microtubules [181–183]. Interestingly, 14-3-3 was also shown in our

work and others to bind to p-S214 of Tau (Chapter 3.1.3, Figure 6I) [158,184,185], which functions to sequester Tau from microtubules and protect S214 from dephosphorylation.

MAST1 was observed to additionally phosphorylate S262, S324, and S356 of Tau *in vitro* (Chapter 3.1.3, Figure 6H). As these sites deviate slightly from canonical AGC motif sequences, it is not clear whether they arose from unspecific phosphorylation *in vitro* (Figure 15). However, all three sites are reported to regulate Tau's affinity to microtubules, similarly to S214 [186–188]. If physiologically relevant, this suggests a role for MAST1 in the hyperphosphorylation of Tau, to further its dissociation from microtubules.

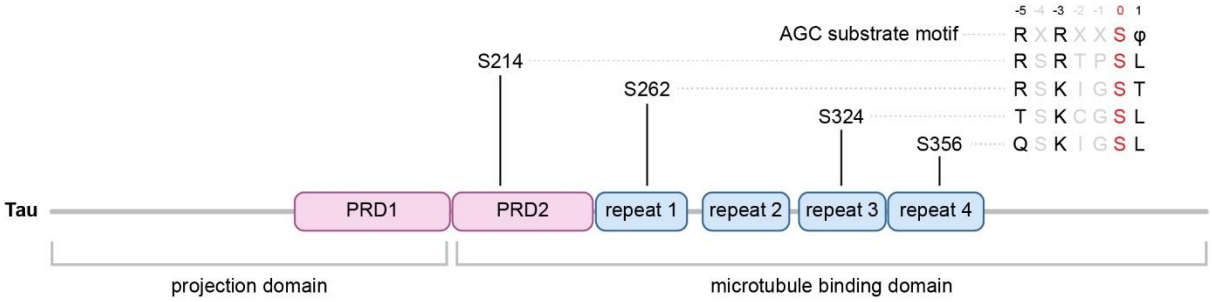

Figure 15. Tau domains and phosphosites.

Tau is divided into two regions: a projection domain, including the proline rich domain 1 (PRD1, pink), and a microtubule binding domain, including the proline rich domain 2 (PRD2, pink) and four repeat domains (blue). S214, S262, S324 and S356 were all phosphorylated by purified MAST1 *in vitro*. The four phosphosites share some similarities, with S214 displaying a perfect match to the AGC substrate motif. Numbering of residues is based on human Tau isoform F.

These findings raise an important question: what is the implication of Tau phosphorylation by MAST1 in cortical development? Knowing that S214 phosphorylation causes Tau to dissociate from microtubules, MAST1 activity would promote a higher proportion of destabilised and flexible microtubules. Since MAST1 mutations are strongly associated with MCC, and given its microtubule association, it is possible that MAST1-mediated microtubule remodelling contributes to the growth and navigation of callosal axons during the development of the corpus callosum. However, this hypothesis has not been specifically addressed in this study and further investigation is required to bridge the gap between MAST1 phosphorylation of Tau and the MCC phenotype observed in patients with MAST1 mutations. This will be discussed further in Chapter 4.2.3.

4.2 A preliminary model of MAST1 signalling

Based on the observations of this study, we have proposed a preliminary model of MAST1 activation and signalling [158]. First, a group II PAK is activated at the plasma membrane by active Cdc42, upon which it phosphorylates MAST1 on S90. p-S90 acts as the gatekeeper phosphosite, binding first to 14-3-3η and forming a heterotrimeric complex. This serves to pre-assemble the MAST1:14-3-3η complex. Then, upon a certain stimulus, an unknown activator binds to MAST1 and induces the formation of the active conformation. Once activated, MAST1 autophosphorylates its own S161 residue, which until this point was sitting in and blocking the substrate binding cleft of MAST1. p-S161 is expelled from the active site and is immediately caught by the free protomer of the 14-3-3 dimer, forming the open MAST1 complex. MAST1 is then able to phosphorylate its downstream substrate Tau on S214, which subsequently dissociates from microtubules, resulting in microtubule destabilisation.

The specific mechanism of 14-3-3 binding to MAST1, including the order in which S90 and S161 associate with 14-3-3 and the stoichiometry of the complex, was inferred by combining the observations from the AP-MS experiment (Chapter 3.1.3, Figure 1F-I), fluorescence anisotropy, (Chapter 3.1.3, Figure 1J), AlphaFold predictions (Chapter 3.1.3, Figure 1D-E), and *in vitro* reconstitution of the complex (Chapter 3.1.3, Figure 4) [158]. Our data shows that the interaction between 14-3-3η and S161 of MAST1 only occurs when S90 of MAST1 is also present. This suggests that S90 must bind to 14-3-3η prior to S161. However, there is currently no data that indicates whether S90 and S161 simultaneously occupy the 14-3-3η dimer, or whether S161 outcompetes and replaces S90 in one 14-3-3η protomer. Since we only observed a MAST1:14-3-3η trimer, and never a tetramer, it is plausible that both sites are bound simultaneously, although we cannot exclude the possibility that tetramer formation requires conditions not yet tested. Clearly, the molecular details of MAST1:14-3-3η complex formation need to be probed further, and here, structural studies would be highly informative.

4.3 Open questions and future perspectives

There are still many aspects of the model outlined above that are poorly understood. In order to obtain a clear and complete picture of MAST1 signalling, the following open questions should be addressed in future works.

4.3.1 How does PAK find MAST1?

In order for PAK to phosphorylate MAST1 in a timely manner, the two must come into proximity efficiently within the crowded environment of the cell. One mechanism to achieve this is co-localisation. As activated PAK localises to Cdc42 in the plasma membrane [167,176,177], it is possible that MAST1 increases its chances of meeting PAK by also localising to the membrane. While MAST1 does not have any typical membrane binding domains, it may use its PDZ domain to interact with other membrane-associated proteins.

Several studies have reported interactors of MAST1's PDZ domain. The first study to characterise MAST1 suggested that it binds to β2-syntrophin at post-synaptic densities, via its PDZ domain [70]. β2-syntrophin is associated with the dystrophin/utrophin network at the plasma membrane, providing a potential pathway for MAST1 recruitment to the membrane. However, most experiments in this study were performed in adult mouse samples, where MAST1 expression is diminished, hence these findings may not fully reflect the developmental context. As discussed in Chapter 1.2.2, MAST1's PDZ domain was also shown to interact with PTEN [75], a phosphatase acting on PIP_3 at the plasma membrane [189]. Nevertheless, this would temporally restrict MAST1's membrane localisation to periods of active PTEN signalling.

Further investigation is required to determine if and how MAST1 and PAK encounter one another at the plasma membrane. Their localisation could be visualised with immunofluorescence, together with a plasma membrane marker. Due to a lack of reliable commercial MAST1 antibodies, it may be necessary to generate a new antibody and validate its specificity by comparing WT and MAST1 KO samples. To identify binders of the PDZ domain of MAST1, an AP-MS experiment could be performed, comparing interactors of full length MAST1 with MAST1 lacking its PDZ domain, to distinguish PDZ-specific enrichment. Given the abundance of proteins harbouring PDZ-binding motifs, this experiment would require tagging and editing of endogenous MAST1, as

overexpression would largely capture irrelevant PDZ-binders. In both immunofluorescence and AP-MS experiments, the use of a relevant cell line is crucial, to capture the localisation and interaction partners in the context of early brain development.

4.3.2 What activates MAST1 catalytic activity?

The most pressing open question resulting from this study is: what is required to activate the kinase activity of MAST1? Although MAST1 displays some intrinsic catalytic activity against its substrate Tau as well as itself, this activity is substantially below the level typically achieved by fully active kinases. It is highly likely that another, currently unknown MAST1 interaction partner is required to induce the active conformation of MAST1's kinase domain.

Indeed, there are precedents for this type of activation. The NDR kinases, which are closely related to the MAST kinases, utilise a protein cofactor called MOB1 for activation. MOB1 binds to a helical N-terminal regulatory domain of NDR, shortly ahead of its kinase domain, which assists to position NDR's activation loop and HM into the active conformation [129]. The DMPKs use one of their own domains to regulate activity. They forms homodimers through their CHB domain, forcing the CHB to sandwich the regulatory C-tail of the kinase domain against the N-lobe of the kinase. In doing this, the HM of the C-tail is pressed into the hydrophobic pocket, stabilising the active conformation of the kinase [131]. In both examples, the HM of the kinase's C-tail is a key regulatory component affected by the binding of the activating cofactor/domain. The HM of MAST1 has the sequence IRQFS, with an isoleucine in place of the canonical starting phenylalanine. Curiously, MAST1 has a glutamate residue (E442 in human) instead of the glutamine in the β4 strand that typically hydrogen bonds with the phosphorylated serine or threonine of the HM (Figure 10B). The amide group of glutamine involved in this interaction would be replaced by the carboxyl group of glutamate, which is incapable of hydrogen-bonding to a negatively-charged phosphate. Therefore, MAST1 would not rely on HM phosphorylation, and likely requires an additional factor to hold its HM in place, similarly to NDR and ROCK.

Clearly, further investigation is required to search for a potential MAST1 activator. Following the hypothesis that the activator secures MAST1's C-tail, screening for C-tail-

specific binders would be a suitable starting point. Like the AP-MS experiment proposed to identify PDZ domain interactors in the previous chapter, interactors of full length MAST1 could be compared with MAST1 lacking its C-tail (Figure 16A). Again, the use of a relevant cell line is essential as a MAST1 activator is likely only expressed in certain cell types and developmental periods.

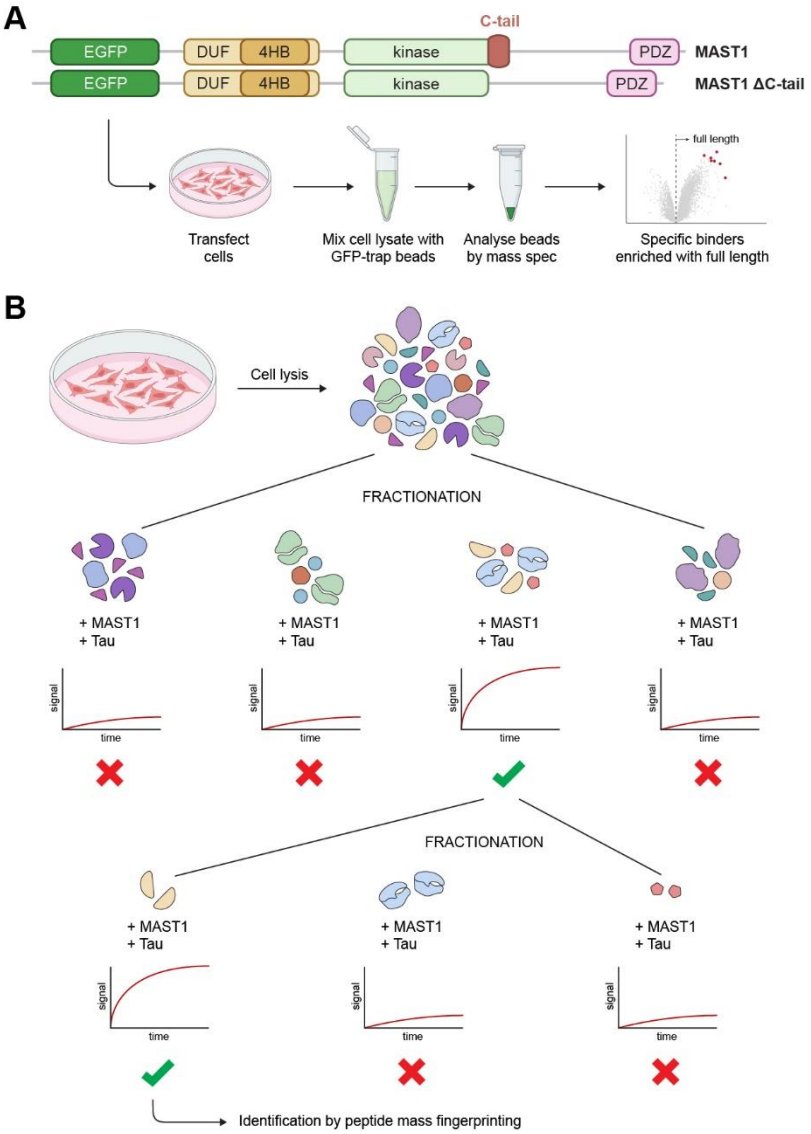

Figure 16. Two approaches to identify a MAST1 activator.

A. A MAST1 activator likely interacts with the C-tail of the kinase domain. To find proteins that bind specifically to the C-tail, an AP-MS experiment could be performed, comparing EGFP-tagged full length MAST1 with a C-tail truncation (MAST1 ΔC-tail). These constructs would be transfected into a suitable cell line, pulled out with GFP-trap beads, and the bound proteins analysed by mass spectrometry. Proteins highly enriched in the full-length construct compared to the truncation represent specific binders of the C-tail. **B.** Functional screening for a MAST1 activator could be performed with fractionation. The proteome of the lysate of a suitable cell line would be fractionated, and each fraction subjected to a kinase assay with purified MAST1 and Tau. Fractions that induce an increase in MAST1 kinase activity would be further fractionated and tested, repeating this process until the complexity of the fraction is reduced enough for analysis by mass spectrometry.

In addition to searching for MAST1 interactors, a functional screen for the missing cofactor would provide an immediate readout of kinase activation. A fractionation experiment could help to narrow down a potential activator (Figure 16B), where a cell lysate from a relevant cell line can be arbitrarily fractionated (for example by size exclusion chromatography), and each fraction tested in a radiometric MAST1 kinase assay. Fractions that significantly increase MAST1 activity can then be further fractionated, and the process repeated until the activating pool is simplified enough for analysis by peptide mass fingerprinting. The pool of candidates can be further narrowed down by generating AlphaFold predictions of each identified protein with MAST1. Experimental validation of the proteins with high-scoring interaction predictions would then be required to pinpoint the MAST1 activator.

4.3.3 What is the origin of the dominant-negative effect?

As mentioned in Chapter 1.2.3, the MCC-associated MAST1 mutations must act in a dominant-negative fashion, as a MAST1 KO mouse model displays no phenotype. Further investigation by Tripathy *et al* as well as this study revealed that MAST2-3 protein abundances increase to compensate for a loss of MAST1, while MAST1-3 protein levels all decrease in response to MAST1 MCC mutations [58,158]. This indicates that the mutations do not only affect MAST1 itself, but many members of the MAST kinase family.

In this work, we demonstrate that the 4HB mutations E194del, K276del and L278del result in misfolding of the domain (Chapter 3.1.3, Figure 7B). In the context of the cell, this misfolding could promote the degradation of MAST1, explaining the observed reduction in Chapter 3.1.3, Figure 5H and Tripathy *et al* [58,158]. MAST2 and MAST3 may also be targeted for degradation if they interact with MAST1 or form part of a complex with it. Here, the dimeric nature of the MAST1:14-3-3η complex provides a potential explanation. If a 14-3-3η dimer were to bind both MAST1 and MAST2 simultaneously, a misfolding mutation in MAST1 could subject the entire complex to degradation, although this would require the formation of as-yet unobserved heterotetramers.

On the other hand, the G519S kinase domain mutation (G517S in human) has very different consequences. While it permits normal folding of the protein, it significantly reduces MAST1 catalytic activity against Tau (Chapter 3.1.3, Figure 7D-E) [158]. This raises

the question of how the G519S mutation produces the same phenotype as the 4HB mutations, rather than behaving like a MAST1 KO. Notably, the presence of a non-functional MAST1 is distinct from the complete loss of the MAST1 protein itself. It is possible that mutant MAST1 titrates out interaction partners or localisation docking sites, reducing their availability for compensatory MAST2 and MAST3.

By uncovering the origins of the dominant negative effect and its effects on MAST1's function, we can begin to question how that results in the enlargement of the corpus callosum observed in patients. Currently, not enough is understood about the downstream effects of MAST1 signalling to bridge the gap from mechanism to phenotype, however one could hypothesise that it is related to microtubule-mediated axon navigation during corpus callosum development. Future studies utilising the MCC-mutant mouse models are essential here, to probe for differences in microtubule dynamics in callosal axons of mouse embryos. A recently developed *in vitro* model of the corpus callosum tract also provides a useful tool for examining corpus callosum development in a readily manipulable system [190,191]. With this, changes in callosal projection across the tract can be measured when comparing WT cells with MAST1 mutant cells. To further probe the role of MAST1-mediated Tau phosphorylation in this process, a Tau S214A mutant could be utilised.

4.4 Closing remarks

Research into the mechanisms, functions, and interactors of the MAST kinases is beginning to expand. Given the recent influx of reported NDD-associated MAST mutations, there is a high demand to understand exactly how these kinases function. In turn, a better understanding of MAST kinase biology will deepen our knowledge of brain development and is essential for the development of potential therapeutics.

In this work, three players in the MAST1 pathway have been revealed: 14-3-3η, PAK, and Tau. We have begun piecing together the mode of regulation of MAST1, and have identified the key open question for further research: what activates MAST1 catalytic activity? In summary, this study has laid the groundwork for future studies to further dissect the molecular mechanisms governing MAST activity, elucidate its role in neurodevelopment, and rationalise pathogenic mutations in human disease.

References

1. Watanabe, H., Fujisawa, T. & Holstein, T. W. Cnidarians and the evolutionary origin of the nervous system. *Dev. Growth Differ.* **51**, 167–183 (2009).

2. Sarnat, H. B. & Netsky, M. G. When does a ganglion become a brain? Evolutionary origin of the central nervous system. *Semin. Pediatr. Neurol.* **9**, 240–253 (2002).

3. Silbereis, J. C., Pochareddy, S., Zhu, Y., Li, M. & Sestan, N. The Cellular and Molecular Landscapes of the Developing Human Central Nervous System. *Neuron* **89**, 248 (2016).

4. Rakic, P. Specification of cerebral cortical areas. *Science (80-.).* **241**, 170–176 (1988).

5. Huttner, W. B. & Brand, M. Asymmetric division and polarity of neuroepithelial cells. *Curr. Opin. Neurobiol.* **7**, 29–39 (1997).

6. Jiang, X. & Nardelli, J. Cellular and molecular introduction to brain development. *Neurobiol. Dis.* **92**, 3–17 (2016).

7. Sauer, M. E. & Walker, B. E. Radioautographic Study of Interkinetic Nuclear Migration in the Neural Tube. *Proc. Soc. Exp. Biol. Med.* **101**, 557–560 (1959).

8. Rakic, P. Specification of cerebral cortical areas. *Science (80-.).* **241**, 170–176 (1988).

9. Huttner, W. B. & Brand, M. Asymmetric division and polarity of neuroepithelial cells. *Curr. Opin. Neurobiol.* **7**, 29–39 (1997).

10. Florio, M. & Huttner, W. B. Neural progenitors, neurogenesis and the evolution of the neocortex. *Dev.* **141**, 2182–2194 (2014).

11. Florio, M. & Huttner, W. B. Neural progenitors, neurogenesis and the evolution of the neocortex. *Dev.* **141**, 2182–2194 (2014).

12. Haubensak, W., Attardo, A., Denk, W. & Huttner, W. B. Neurons arise in the basal neuroepithelium of the early mammalian telencephalon: A major site of neurogenesis. *Proc. Natl. Acad. Sci. U. S. A.* **101**, 3196–3201 (2004).

13. Miyata, T. *et al.* Asymmetric production of surface-dividing and non-surface-dividing cortical progenitor cells. *Development* **131**, 3133–3145 (2004).

14. Noctor, S. C., Martinez-Cerdeño, V., Ivic, L. & Kriegstein, A. R. Cortical neurons arise in symmetric and asymmetric division zones and migrate through specific phases. *Nat. Neurosci.* **7**, 136–144 (2004).

15. Angevine, J. B. & Sidman, R. L. Autoradiographic study of cell migration during histogenesis of cerebral cortex in the mouse. *Nature* **192**, 766–768 (1961).

16. Molyneaux, B. J., Arlotta, P., Menezes, J. R. L. & Macklis, J. D. Neuronal subtype specification in the cerebral cortex. *Nat. Rev. Neurosci.* **8**, 427–437 (2007).

17. Bystron, I., Blakemore, C. & Rakic, P. Development of the human cerebral cortex: Boulder Committee revisited. *Nat. Rev. Neurosci.* **9**, 110–122 (2008).

18. Pollen, A. A. *et al.* Molecular Identity of Human Outer Radial Glia during Cortical Development. *Cell* **163**, 55–67 (2015).

19. Mizutani, K. I., Yoon, K., Dang, L., Tokunaga, A. & Gaiano, N. Differential Notch signalling distinguishes neural stem cells from intermediate progenitors. *Nature* **449**, 351–355 (2007).

20. Spassky, N. *et al.* Adult ependymal cells are postmitotic and are derived from radial glial cells during embryogenesis. *J. Neurosci.* **25**, 10–18 (2005).

21. Johnson, J. I., Kirsch, J. A. W. & Switzer, R. C. Phylogeny through brain traits: Fifteen characters which adumbrate mammalian genealogy. *Brain. Behav. Evol.* **20**, 72–83 (1982).

22. Lau, Y. C. *et al.* Autism traits in individuals with agenesis of the corpus callosum. *J. Autism Dev. Disord.* **43**, 1106 (2013).

23. Parrini, E., Conti, V., Dobyns, W. B. & Guerrini, R. Genetic basis of brain malformations. *Mol. Syndromol.* **7**, 220–233 (2016).

24. Siffredi, V., Anderson, V., Leventer, R. J. & Spencer-Smith, M. M. Neuropsychological profile of agenesis of the corpus callosum: A systematic review. *Dev. Neuropsychol.* **38**, 36–57 (2013).

25. Fame, R. M., MacDonald, J. L. & Macklis, J. D. Development, specification, and diversity of callosal projection neurons. *Trends Neurosci.* **34**, 41–50 (2011).

26. Shoukimas, G. M. & Hinds, J. W. The development of the cerebral cortex in the embryonic mouse: An electron microscopic serial section analysis. *J. Comp. Neurol.* **179**, 795–830 (1978).

27. Barnes, A. P. & Polleux, F. Establishment of axon-dendrite polarity in developing neurons. *Annu. Rev. Neurosci.* **32**, 347–381 (2009).

28. Norris, C. R. & Kalil, K. Guidance of callosal axons by radial glia in the developing cerebral cortex. *J. Neurosci.* **11**, 3481–3492 (1991).

29. Piper, M. *et al.* Neuropilin 1-Sema Signaling Regulates Crossing of Cingulate Pioneering Axons during Development of the Corpus Callosum. *Cereb. Cortex (New York, NY)* **19**, i11 (2009).

30. Shu, T., Sundaresan, V., McCarthy, M. M. & Richards, L. J. Slit2 guides both precrossing and postcrossing callosal axons at the midline in vivo. *J. Neurosci.* **23**, 8176–8184 (2003).

31. López-Bendito, G. *et al.* Robo1 and Robo2 cooperate to control the guidance of major axonal tracts in the mammalian forebrain. *J. Neurosci.* **27**, 3395–3407 (2007).

32. Mire, E. *et al.* Developmental Upregulation of Ephrin-B1 Silences Sema3C/Neuropilin-1 Signaling during Post-crossing Navigation of Corpus Callosum Axons. *Curr. Biol.* **28**, 1768-1782.e4 (2018).

33. Keeble, T. R. *et al.* The Wnt receptor Ryk is required for Wnt5a-mediated axon guidance on the contralateral side of the corpus callosum. *J. Neurosci.* **26**, 5840–5848 (2006).

34. Gavrish, M. *et al.* Molecular mechanisms of corpus callosum development: a four-step journey. *Front. Neuroanat.* **17**, (2023).

35. Mitchison, T. & Kirschner, M. Dynamic instability of microtubule growth. *Nature* **312**, 237–242 (1984).

36. Atkins, M., Nicol, X. & Fassier, C. Microtubule remodelling as a driving force of axon guidance and pruning. *Semin. Cell Dev. Biol.* **140**, 35–53 (2023).

37. Gomez, T. M. & Letourneau, P. C. Actin Dynamics in Growth Cone Motility and Navigation. *J. Neurochem.* **129**, 221 (2013).

38. Forscher, P. & Smith, S. J. Actions of cytochalasins on the organization of actin filaments

and microtubules in a neuronal growth cone. *J. Cell Biol.* **107**, 1505–1516 (1988).

39. Burnette, D. T. *et al.* Myosin II Activity Facilitates Microtubule Bundling in the Neuronal Growth Cone Neck. *Dev. Cell* **15**, 163 (2008).

40. Zhou, F. Q., Waterman-Storer, C. M. & Cohan, C. S. Focal loss of actin bundles causes microtubule redistribution and growth cone turning. *J. Cell Biol.* **157**, 839–849 (2002).

41. Schaefer, A. W., Kabir, N. & Forscher, P. Filopodia and actin arcs guide the assembly and transport of two populations of microtubules with unique dynamic parameters in neuronal growth cones. *J. Cell Biol.* **158**, 139–152 (2002).

42. Del Río, J. A. *et al.* MAP1B is required for netrin 1 signaling in neuronal migration and axonal guidance. *Curr. Biol.* **14**, 840–850 (2004).

43. Walters, G. B. *et al.* MAP1B mutations cause intellectual disability and extensive white matter deficit. *Nat. Commun.* **9**, (2018).

44. Elie, A. *et al.* Tau co-organizes dynamic microtubule and actin networks. *Sci. Rep.* **5**, (2015).

45. Ramkumar, A., Jong, B. Y. & Ori-McKenney, K. M. ReMAPping the Microtubule Landscape: How Phosphorylation Dictates the Activities of Microtubule-Associated Proteins. *Dev. Dyn.* **247**, 138 (2017).

46. Sabariego-Navarro, M., Fernández-Blanco, Á., Sierra, C. & Dierssen, M. Neurodevelopmental disorders: 2022 update. *Free Neuropathol.* **3**, (2022).

47. Ogundele, M. O. & Morton, M. Classification, prevalence and integrated care for neurodevelopmental and child mental health disorders: A brief overview for paediatricians. *World J. Clin. Pediatr.* **11**, 120 (2022).

48. Yang, Y. *et al.* Prevalence of neurodevelopmental disorders among US children and adolescents in 2019 and 2020. *Front. Psychol.* **13**, (2022).

49. American Psychiatric Association. Diagnostic and Statistical Manual of Mental Disorders. *Diagnostic Stat. Man. Ment. Disord.* (2013) doi:10.1176/APPI.BOOKS.9780890425596.

50. McRae, J. F. *et al.* Prevalence and architecture of de novo mutations in developmental disorders. *Nature* **542**, 433–438 (2017).

51. Rabbani, B., Tekin, M. & Mahdieh, N. The promise of whole-exome sequencing in medical genetics. *J. Hum. Genet. 2014 591* **59**, 5–15 (2013).

52. Bednarz, H. M. & Kana, R. K. Advances, challenges, and promises in pediatric neuroimaging of neurodevelopmental disorders. *Neurosci. Biobehav. Rev.* **90**, 50–69 (2018).

53. Parrini, E., Conti, V., Dobyns, W. B. & Guerrini, R. Genetic basis of brain malformations. *Mol. Syndromol.* **7**, 220–233 (2016).

54. Rivière, J. B. *et al.* De novo germline and postzygotic mutations in AKT3, PIK3R2 and PIK3CA cause a spectrum of related megalencephaly syndromes. *Nat. Genet.* **44**, 934–940 (2012).

55. Mirzaa, G. M. *et al.* De novo CCND2 mutations leading to stabilization of cyclin D2 cause megalencephaly-polymicrogyria-polydactyly-hydrocephalus syndrome. *Nat. Genet.* **46**, 510–515 (2014).

56. Poirier, K. *et al.* Mutations in TUBG1, DYNC1H1, KIF5C and KIF2A cause malformations of

cortical development and microcephaly. *Nat. Genet.* **45**, 639–647 (2013).

57. Esen, T. E., Ardiçli, D., Keçelİ, A. M. & Çavdarli, B. Thick Corpus Callosum: An Unusual Finding of TUBGCP2-Related Tubulinopathy. *Am. J. Med. Genet. Part A* (2025) doi:10.1002/AJMG.A.64134,.

58. Tripathy, R. *et al.* Mutations in MAST1 Cause Mega-Corpus-Callosum Syndrome with Cerebellar Hypoplasia and Cortical Malformations. *Neuron* **100**, 1354-1368.e5 (2018).

59. ME, R.-G. *et al.* MAST1 variant causes mega-corpus-callosum syndrome with cortical malformations but without cerebellar hypoplasia. *Am. J. Med. Genet. A* **182**, 1483–1490 (2020).

60. L, H. *et al.* The Clinical Picture of a Bilateral Perisylvian Syndrome as the Initial Symptom of Mega-Corpus-Callosum Syndrome due to a MAST1-Gene Mutation. *Neuropediatrics* **51**, 435–439 (2020).

61. Yi, S. *et al.* A genetic variant in the MAST1 gene is associated with mega-corpus-callosum syndrome with hypoplastic cerebellar vermis, in a fetus. *Mol. Genet. Genomic Med.* **12**, (2024).

62. Xu, X. *et al. Solution NMR Structure of Microtubule-associated serine/threonine-protein kinase 1 from Homo sapiens, Northeast Structural Genomics Consortium (NESG) Target HR9151A*. https://www.rcsb.org/structure/2M9X.

63. Ugochukwu, E. *et al.* PDZ domain from Human microtubule-associated serine/threonine-protein kinase 1. *Worldw. Protein Data Bank* (2010) doi:10.2210/PDB3PS4/PDB.

64. Terrien, E. *et al.* Solution structure of MAST2-PDZ complexed with the C-terminus of PTEN. *Worldw. Protein Data Bank* (2011) doi:10.2210/PDB2KYL/PDB.

65. Roos, A. *et al.* The crystal structure of the PDZ domain of human Microtubule Associated Serine/Threonine Kinase 3 (MAST3). (2009) doi:10.2210/PDB3KHF/PDB.

66. Jumper, J. *et al.* Highly accurate protein structure prediction with AlphaFold. *Nature* **596**, 583–589 (2021).

67. Ishida, T. & Kinoshita, K. PrDOS: prediction of disordered protein regions from amino acid sequence. *Nucleic Acids Res.* **35**, (2007).

68. Kannan, N., Haste, N., Taylor, S. S. & Neuwald, A. F. The hallmark of AGC kinase functional divergence is its C-terminal tail, a cis-acting regulatory module. *PNAS* vol. 104 1272–1277 (2007).

69. Pearce, L. R., Komander, D. & Alessi, D. R. The nuts and bolts of AGC protein kinases. *Nature Reviews Molecular Cell Biology* vol. 11 9–22 (2010).

70. Lumeng, C. *et al.* Interactions between beta 2-syntrophin and a family of microtubule-associated serine/threonine kinases. *Nat. Neurosci.* **2**, 611–617 (1999).

71. Garland, P., Quraishe, S., French, P. & O'Connor, V. Expression of the MAST family of serine/threonine kinases. *Brain Res.* **1195**, 12–19 (2008).

72. Developmental Transcriptome :: BrainSpan: Atlas of the Developing Human Brain. https://www.brainspan.org/rnaseq/searches?search_type=user_selections.

73. La Manno, G. *et al.* Molecular architecture of the developing mouse brain. *Nature* **596**, 92–96 (2021).

74. Walden, P. D. & Cowan, N. J. A novel 205-kilodalton testis-specific serine/threonine

protein kinase associated with microtubules of the spermatid manchette. *Mol. Cell. Biol.* **13**, 7625–7635 (1993).

75. Valiente, M. *et al.* Binding of PTEN to Specific PDZ Domains Contributes to PTEN Protein Stability and Phosphorylation by Microtubule-associated Serine/Threonine Kinases. *J. Biol. Chem.* **280**, 28936–28943 (2005).

76. Jin, L. *et al.* MAST1 Drives Cisplatin Resistance in Human Cancers by Rewiring cRaf-Independent MEK Activation. *Cancer Cell* **34**, 315-330.e7 (2018).

77. Andrade, E. C. *et al.* ARPP-16 Is a Striatal-Enriched Inhibitor of Protein Phosphatase 2A Regulated by Microtubule-Associated Serine/Threonine Kinase 3 (Mast 3 Kinase). *J. Neurosci.* **37**, 2709–2722 (2017).

78. Musante, V. *et al.* Reciprocal regulation of ARPP-16 by PKA and MAST3 kinases provides a cAMP-regulated switch in protein phosphatase 2A inhibition. *Elife* **6**, (2017).

79. McMichael, G. *et al.* Whole-exome sequencing points to considerable genetic heterogeneity of cerebral palsy. *Mol. Psychiatry* **20**, 176–182 (2015).

80. Ben-Mahmoud, A., Al-Shamsi, A. M., Ali, B. R. & Al-Gazali, L. Evaluating the Role of MAST1 as an Intellectual Disability Disease Gene: Identification of a Novel De Novo Variant in a Patient with Developmental Disabilities. *J. Mol. Neurosci.* **70**, 320–327 (2019).

81. Shu, L. *et al.* The Role of Microtubule Associated Serine/Threonine Kinase 3 Variants in Neurodevelopmental Diseases: Genotype-Phenotype Association. *Front. Mol. Neurosci.* **14**, (2022).

82. Sloboda, N. *et al.* MAST1-related mega-corpus-callosum syndrome with central hypogonadism. *Eur. J. Med. Genet.* **66**, (2023).

83. Spinelli, E. *et al.* Pathogenic MAST3 Variants in the STK Domain Are Associated with Epilepsy. *Ann. Neurol.* **90**, 274–284 (2021).

84. Landoulsi, Z. *et al.* Clinical and genetic study of Tunisian families with genetic generalized epilepsy: contribution of CACNA1H and MAST4 genes. *Neurogenetics* **19**, 165–178 (2018).

85. Zhang, X. *et al.* De novo variants in MAST4 related to neurodevelopmental disorders with developmental delay and infantile spasms: Genotype-phenotype association. *Front. Mol. Neurosci.* **16**, 62 (2023).

86. Pan, C. *et al.* Hsp90B enhances MAST1-mediated cisplatin resistance by protecting MAST1 from proteosomal degradation. *J. Clin. Invest.* **129**, 4110–4123 (2019).

87. Tyagi, A. *et al.* CRISPR/Cas9-based genome-wide screening for deubiquitinase subfamily identifies USP1 regulating MAST1-driven cisplatin-resistance in cancer cells. *Theranostics* **12**, 5949–5970 (2022).

88. Karapurkar, J. K. *et al.* USP28 promotes tumorigenesis and cisplatin resistance by deubiquitinating MAST1 protein in cancer cells. *Cell. Mol. Life Sci.* **81**, (2024).

89. DR, R. *et al.* Functionally recurrent rearrangements of the MAST kinase and Notch gene families in breast cancer. *Nat. Med.* **17**, 1646–1651 (2011).

90. Clay, M. R., Varma, S. & West, R. B. MAST2 and NOTCH1 translocations in breast carcinoma and associated pre-invasive lesions. *Hum. Pathol.* **44**, 2837–2844 (2013).

91. Beretov, J. *et al.* Proteomic analysis of urine to identify breast cancer biomarker candidates using a label-free LC-MS/MS approach. *PLoS One* **10**, (2015).

92. Deng, N., Kang, W., Du, J., Rong, X. & Han, Q. Microtubule associated serine/threonine kinase-3 inhibits the malignant phenotype of breast cancer by promoting phosphorylation-mediated ubiquitination degradation of yes-associated protein. *Breast Cancer Res.* **27**, (2025).

93. Tomoshige, K. *et al.* Germline mutations causing familial lung cancer. *J. Hum. Genet.* **60**, 597–603 (2015).

94. Jiao, Y., Li, Y., Jiang, P., Fu, Z. & Liu, Y. High MAST2 mRNA expression and its role in diagnosis and prognosis of liver cancer. *Sci. Rep.* **9**, (2019).

95. Chen, L. W. *et al.* Clinical Outcomes and Genomic Alterations in Gleason Score 10 Prostate Cancer. *Cancers (Basel).* **17**, (2025).

96. Walden, P. D. & Millette, C. F. Increased Activity Associated with the MAST205 Protein Kinase Complex during Mammalian Spermiogenesis'. *Biol. Reprod.* **55**, 1039–1044 (1996).

97. Huang, N. *et al.* A Screen for Genomic Disorders of Infertility Identifies MAST2 Duplications Associated with Nonobstructive Azoospermia in Humans. *Biol. Reprod.* **93**, 61 (2015).

98. Lee, S. J. *et al.* Mast4 knockout shows the regulation of spermatogonial stem cell self-renewal via the FGF2/ERM pathway. *Cell Death Differ.* **28**, 1441–1454 (2021).

99. Lee, S. J. *et al.* MAST4 controls cell cycle in spermatogonial stem cells. *Cell Prolif.* **56**, (2023).

100. Jing, T. *et al.* MAST1 modulates neuronal differentiation and cell cycle exit via P27 in neuroblastoma cells. *FEBS Open Bio* **10**, 1104–1114 (2020).

101. Loh, S. H. Y., Francescut, L., Lingor, P., Bähr, M. & Nicotera, P. Identification of new kinase clusters required for neurite outgrowth and retraction by a loss-of-function RNA interference screen. *Cell Death Differ.* **15**, 283–298 (2008).

102. Khan, Z. *et al.* Structure-based optimization of a PDZ-binding motif within a viral peptide stimulates neurite outgrowth. *J. Biol. Chem.* **294**, 13755–13768 (2019).

103. Wyatt, L. A., Filbin, M. T. & Keirstead, H. S. PTEN inhibition enhances neurite outgrowth in human embryonic stem cell-derived neuronal progenitor cells. *J. Comp. Neurol.* **522**, 2741–2755 (2014).

104. Kwon, C. H. *et al.* Pten Regulates Neuronal Arborization and Social Interaction in Mice. *Neuron* **50**, 377–388 (2006).

105. Endicott, J. A., Noble, M. E. M. & Johnson, L. N. The structural basis for control of eukaryotic protein kinases. *Annu. Rev. Biochem.* **81**, 587–613 (2012).

106. Nolen, B., Taylor, S. & Ghosh, G. Regulation of protein kinases: Controlling activity through activation segment conformation. *Mol. Cell* **15**, 661–675 (2004).

107. Yang, J. *et al.* Crystal structure of an activated Akt/Protein Kinase B ternary complex with GSK3-peptide and AMP-PNP. *Nat. Struct. Biol.* **9**, 940–944 (2002).

108. Knighton, D. R. *et al.* Crystal structure of the catalytic subunit of cyclic adenosine monophosphate-dependent protein kinase. *Science (80-.).* **253**, 407–414 (1991).

109. De Bondt, H. L. *et al.* Crystal structure of cyclin-dependent kinase 2. *Nature* **363**, 595–602 (1993).

110. Levinson, N. M. *et al.* A Src-Like Inactive Conformation in the Abl Tyrosine Kinase Domain. *PLoS Biol.* **4**, e144 (2006).

111. Skamnaki, V. T. *et al.* Catalytic mechanism of phosphorylase kinase probed by mutational studies. *Biochemistry* **38**, 14718–14730 (1999).

112. Zheng, C. F. & Guan, K. L. Activation of MEK family kinases requires phosphorylation of two conserved Ser/Thr residues. *EMBO J.* **13**, 1123–1131 (1994).

113. Alessi, D. R. *et al.* Identification of the sites in MAP kinase kinase-1 phosphorylated by p74raf-1. *EMBO J.* **13**, 1610–1619 (1994).

114. Seger, R. *et al.* Purification and characterization of mitogen-activated protein kinase activator(s) from epidermal growth factor-stimulated A431 cells. *J. Biol. Chem.* **267**, 14373–14381 (1992).

115. Levina, A., Fleming, K. D., Burke, J. E. & Leonard, T. A. Activation of the essential kinase PDK1 by phosphoinositide-driven trans-autophosphorylation. *Nat. Commun. 2022 131* **13**, 1–16 (2022).

116. Mora, A., Komander, D., Van Aalten, D. M. F. & Alessi, D. R. PDK1, the master regulator of AGC kinase signal transduction. *Semin. Cell Dev. Biol.* **15**, 161–170 (2004).

117. Reinhardt, R. *et al.* PKD autoinhibition in trans regulates activation loop autophosphorylation in cis. *Proc. Natl. Acad. Sci. U. S. A.* **120**, e2212909120 (2023).

118. Muslin, A. J., Tanner, J. W., Allen, P. M. & Shaw, A. S. Interaction of 14-3-3 with signaling proteins is mediated by the recognition of phosphoserine. *Cell* **84**, 889–897 (1996).

119. Yaffe, M. B. *et al.* The structural basis for 14-3-3:phosphopeptide binding specificity. *Cell* **91**, 961–971 (1997).

120. Park, E. *et al.* Architecture of autoinhibited and active BRAF/MEK1/14-3-3 complexes. *Nature* **575**, 545 (2019).

121. Kondo, Y. *et al.* Cryo-EM structure of a dimeric B-Raf:14-3-3 complex reveals asymmetry in the active sites of B-Raf kinases. *Science (80-.).* **366**, 109–115 (2019).

122. Rajakulendran, T., Sahmi, M., Lefrançois, M., Sicheri, F. & Therrien, M. A dimerization-dependent mechanism drives RAF catalytic activation. *Nature* **461**, 542–545 (2009).

123. Wan, P. T. C. *et al.* Mechanism of activation of the RAF-ERK signaling pathway by oncogenic mutations of B-RAF. *Cell* **116**, 855–867 (2004).

124. Hubbard, S. R. Crystal structure of the activated insulin receptor tyrosine kinase in complex with peptide substrate and ATP analog. *EMBO J.* **16**, 5572–5581 (1997).

125. Reinhardt, R. *et al.* PKD autoinhibition in trans regulates activation loop autophosphorylation in cis. *Proc. Natl. Acad. Sci. U. S. A.* **120**, e2212909120 (2023).

126. Jeffrey, P. D. *et al.* Mechanism of CDK activation revealed by the structure of a cyclinA-CDK2 complex. *Nature* **376**, 313–320 (1995).

127. Bichsel, S. J., Tamaskovic, R., Stegert, M. R. & Hemmings, B. A. Mechanism of activation of NDR (nuclear Dbf2-related) protein kinase by the hMOB1 protein. *J. Biol. Chem.* **279**, 35228–35235 (2004).

128. Devroe, E., Erdjument-Bromage, H., Tempst, P. & Silver, P. A. Human Mob proteins regulate the NDR1 and NDR2 serine-threonine kinases. *J. Biol. Chem.* **279**, 24444–24451 (2004).

129. Gógl, G. *et al.* The Structure of an NDR/LATS Kinase–Mob Complex Reveals a Novel Kinase–Coactivator System and Substrate Docking Mechanism. *PLOS Biol.* **13**, e1002146 (2015).

130. Taylor, S. S., Buechler, J. A. & Yonemoto, W. cAMP-dependent protein kinase: framework for a diverse family of regulatory enzymes. *Annu. Rev. Biochem.* **59**, 971–1005 (1990).

131. Yamaguchi, H., Kasa, M., Amano, M., Kaibuchi, K. & Hakoshima, T. Molecular mechanism for the regulation of rho-kinase by dimerization and its inhibition by fasudil. *Structure* **14**, 589–600 (2006).

132. Elkins, J. M. *et al.* Crystal structure of CDC42 binding protein kinase alpha (MRCK alpha). *Worldw. Protein Data Bank* (2012) doi:10.2210/PDB4AW2/PDB.

133. Elkins, J. M. *et al.* Structure of dystrophia myotonica protein kinase. *Protein Sci.* **18**, 782–791 (2009).

134. Jacobs, M. *et al.* The structure of dimeric ROCK I reveals the mechanism for ligand selectivity. *J. Biol. Chem.* **281**, 260–268 (2006).

135. Heikkila, T. *et al.* Co-Crystal Structures of Inhibitors with MRCKβ, a Key Regulator of Tumor Cell Invasion. *PLoS One* **6**, e24825 (2011).

136. Truebestein, L., Elsner, D. J., Fuchs, E. & Leonard, T. A. A molecular ruler regulates cytoskeletal remodelling by the Rho kinases. *Nat. Commun.* **6**, (2015).

137. Structure and regulation of the myotonic dystrophy kinase-related Cdc42-binding kinase. *Structure* (2023) doi:10.1016/J.STR.2023.02.002.

138. Yang, J. *et al.* Molecular Mechanism for the Regulation of Protein Kinase B/Akt by Hydrophobic Motif Phosphorylation. *Mol. Cell* **9**, 1227–1240 (2002).

139. Hauge, C. *et al.* Mechanism for activation of the growth factor-activated AGC kinases by turn motif phosphorylation. *EMBO J.* **26**, 2251–2261 (2007).

140. Hao, Y., Chun, A., Cheung, K., Rashidi, B. & Yang, X. Tumor suppressor LATS1 is a negative regulator of oncogene YAP. *J. Biol. Chem.* **283**, 5496–5509 (2008).

141. Heikkila, T. *et al.* Co-Crystal Structures of Inhibitors with MRCKβ, a Key Regulator of Tumor Cell Invasion. *PLoS One* **6**, e24825 (2011).

142. Carpten, J. D. *et al.* A transforming mutation in the pleckstrin homology domain of AKT1 in cancer. *Nature* **448**, 439–444 (2007).

143. Lindhurst, M. J. *et al.* A Mosaic Activating Mutation in AKT1 Associated with the Proteus Syndrome . *N. Engl. J. Med.* **365**, 611–619 (2011).

144. Kuo, Y. C. *et al.* Regulation of phosphorylation of Thr-308 of Akt, cell proliferation, and survival by the B55α regulatory subunit targeting of the protein phosphatase 2A holoenzyme to Akt. *J. Biol. Chem.* **283**, 1882–1892 (2008).

145. Padmanabhan, S. *et al.* A PP2A Regulatory Subunit Regulates C. elegans Insulin/IGF-1 Signaling by Modulating AKT-1 Phosphorylation. *Cell* **136**, 939–951 (2009).

146. Gao, T., Furnari, F. & Newton, A. C. PHLPP: A phosphatase that directly dephosphorylates Akt, promotes apoptosis, and suppresses tumor growth. *Mol. Cell* **18**, 13–24 (2005).

147. Brognard, J., Sierecki, E., Gao, T. & Newton, A. C. PHLPP and a Second Isoform, PHLPP2, Differentially Attenuate the Amplitude of Akt Signaling by Regulating Distinct Akt Isoforms. *Mol. Cell* **25**, 917–931 (2007).

148. Husremović, T. *et al.* PHLPP2 is a pseudophosphatase that lost activity in the metazoan ancestor. *Proc. Natl. Acad. Sci. U. S. A.* **122**, (2025).

149. Reynhout, S. *et al.* De Novo Mutations Affecting the Catalytic Cα Subunit of PP2A, PPP2CA, Cause Syndromic Intellectual Disability Resembling Other PP2A-Related Neurodevelopmental Disorders. *Am. J. Hum. Genet.* **104**, 139–156 (2019).

150. Houge, G. *et al.* B56δ-related protein phosphatase 2A dysfunction identified in patients with intellectual disability. *J. Clin. Invest.* **125**, 3051–3062 (2015).

151. Butler, M. G. *et al.* Subset of individuals with autism spectrum disorders and extreme macrocephaly associated with germline PTEN tumour suppressor gene mutations. *J. Med. Genet.* **42**, 318–321 (2005).

152. Herman, G. E. *et al.* Increasing knowledge of PTEN germline mutations: Two additional patients with autism and macrocephaly. *Am. J. Med. Genet. A* **143A**, 589–593 (2007).

153. McBride, K. L. *et al.* Confirmation study of PTEN mutations among individuals with autism or developmental delays/mental retardation and macrocephaly. *Autism Res.* **3**, 137–141 (2010).

154. Orrico, A. *et al.* Novel PTEN mutations in neurodevelopmental disorders and macrocephaly. *Clin. Genet.* **75**, 195–198 (2009).

155. Lancaster, M. A. *et al.* Cerebral organoids model human brain development and microcephaly. *Nature* **501**, 373–379 (2013).

156. Birtele, M., Lancaster, M. & Quadrato, G. Modelling human brain development and disease with organoids. *Nat. Rev. Mol. Cell Biol.* **26**, 389–412 (2025).

157. Naas, J. *et al.* Quantitative profiling of human brain organoid cell diversity across four protocols and multiple cell lines. *Cell Rep.* **44**, (2025).

158. Antonioli, S. *et al.* A complex of MAST1 and 14-3-3η regulates Tau phosphorylation in the developing cortex. *bioRxiv* 2025.07.09.663707 (2025) doi:10.1101/2025.07.09.663707.

159. Valente, C. *et al.* A 14-3-3γ 3 dimer-based scaffold bridges CtBP1-S/BARS to PI(4)KIIIβ 2 to regulate post-Golgi carrier formation. *Nat. Cell Biol.* **14**, 343–354 (2012).

160. Yaffe, M. B. How do 14-3-3 proteins work? – Gatekeeper phosphorylation and the molecular anvil hypothesis. *FEBS Lett.* **513**, 53–57 (2002).

161. Saurin, A. T. *et al.* The regulated assembly of a PKCe complex controls the completion of cytokinesis. *Nat. Cell Biol.* **10**, 891–901 (2008).

162. Kostelecky, B., Saurin, A. T., Purkiss, A., Parker, P. J. & McDonald, N. Q. Recognition of an intra-chain tandem 14-3-3 binding site within PKCe. *EMBO Rep.* **10**, 983–989 (2009).

163. Stevers, L. M. *et al.* Structural interface between LRRK2 and 14-3-3 protein. *Biochem. J.* **474**, 1273–1287 (2017).

164. Cho, N. H. *et al.* OpenCell: Endogenous tagging for the cartography of human cellular organization. *Science (80-.).* **375**, (2022).

165. Takahashi, H., Lassmann, T., Murata, M. & Carninci, P. 5′ end-centered expression profiling using cap-analysis gene expression and next-generation sequencing. *Nat. Protoc.* **7**, 542–561 (2012).

166. Uhlén, M. *et al.* Tissue-based map of the human proteome. *Science (80-.).* **347**, (2015).

167. Baskaran, Y., Ng, Y. W., Selamat, W., Ling, F. T. P. & Manser, E. Group I and II mammalian

PAKs have different modes of activation by Cdc42. *EMBO Rep.* **13**, 653–659 (2012).

168. Ha, B. H. *et al.* Type II p21-activated kinases (PAKs) are regulated by an autoinhibitory pseudosubstrate. *Proc. Natl. Acad. Sci. U. S. A.* **109**, 16107–16112 (2012).

169. Rennefahrt, U. E. E. *et al.* Specificity profiling of Pak kinases allows identification of novel phosphorylation sites. *J. Biol. Chem.* **282**, 15667–15678 (2007).

170. Johnson, J. L. *et al.* An atlas of substrate specificities for the human serine/threonine kinome. *Nature* **613**, 759–766 (2023).

171. Tian, Y., Lei, L. & Minden, A. A key role for Pak4 in proliferation and differentiation of neural progenitor cells. *Dev. Biol.* **353**, 206–216 (2011).

172. Qu, J. *et al.* PAK4 kinase is essential for embryonic viability and for proper neuronal development. *Mol. Cell. Biol.* **23**, 7122–7133 (2003).

173. Civiero, L. *et al.* Leucine-rich repeat kinase 2 interacts with p21-activated kinase 6 to control neurite complexity in mammalian brain. *J. Neurochem.* **135**, 1242–1256 (2015).

174. Nekrasova, T., Jobes, M. L., Ting, J. H., Wagner, G. C. & Minden, A. Targeted disruption of the Pak5 and Pak6 genes in mice leads to deficits in learning and locomotion. *Dev. Biol.* **322**, 95–108 (2008).

175. Dan, C., Kelly, A., Bernard, O. & Minden, A. Cytoskeletal changes regulated by the PAK4 serine/threonine kinase are mediated by LIM kinase 1 and cofilin. *J. Biol. Chem.* **276**, 32115–32121 (2001).

176. Abo, A. *et al.* PAK4, a novel effector for Cdc42Hs, is implicated in the reorganization of the actin cytoskeleton and in the formation of filopodia. *EMBO J.* **17**, 6527–6540 (1998).

177. Ha, B. H. & Boggon, T. J. CDC42 binds PAK4 via an extended GTPase-effector interface. *Proc. Natl. Acad. Sci. U. S. A.* **115**, 531–536 (2018).

178. Etienne-Manneville, S. Cdc42 - The centre of polarity. *J. Cell Sci.* **117**, 1291–1300 (2004).

179. Selamat, W., Tay, P. L. F., Baskaran, Y. & Manser, E. The Cdc42 effector kinase PAK4 localizes to cell-cell junctions and contributes to establishing cell polarity. *PLoS One* **10**, (2015).

180. Morse, E. M. *et al.* PAK6 targets to cell–cell adhesions through its N-terminus in a Cdc42-dependent manner to drive epithelial colony escape. *J. Cell Sci.* **129**, 380 (2016).

181. Yoshida, H. & Goedert, M. Sequential phosphorylation of tau protein by cAMP-dependent protein kinase and SAPK4/p38δ or JNK2 in the presence of heparin generates the AT100 epitope. *J. Neurochem.* **99**, 154–164 (2006).

182. Illenberger, S. *et al.* The endogenous and cell cycle-dependent phosphorylation of tau protein in living cells: implications for Alzheimer's disease. *Mol. Biol. Cell* **9**, 1495–1512 (1998).

183. Hong, Y. *et al.* SRPK2 phosphorylates tau and mediates the cognitive defects in Alzheimer's disease. *J. Neurosci.* **32**, 17262–17272 (2012).

184. Sadik, G. *et al.* Phosphorylation of tau at Ser214 mediates its interaction with 14-3-3 protein: implications for the mechanism of tau aggregation. *J. Neurochem.* **108**, 33–43 (2009).

185. Neves, J. F. *et al.* Phosphorylated full-length Tau interacts with 14-3-3 proteins via two short phosphorylated sequences, each occupying a binding groove of 14-3-3 dimer. *FEBS*

J. **288**, 1918–1934 (2021).

186. Biernat, J., Gustke, N., Drewes, G., Mandelkow, E. & Mandelkow, E. Phosphorylation of Ser262 strongly reduces binding of tau to microtubules: distinction between PHF-like immunoreactivity and microtubule binding. *Neuron* **11**, 153–163 (1993).

187. Schneider, A., Biernat, J., Von Bergen, M., Mandelkow, E. & Mandelkow, E. M. Phosphorylation that detaches tau protein from microtubules (Ser262, Ser214) also protects it against aggregation into Alzheimer paired helical filaments. *Biochemistry* **38**, 3549–3558 (1999).

188. Carlomagno, Y. *et al.* An acetylation-phosphorylation switch that regulates tau aggregation propensity and function. *J. Biol. Chem.* **292**, 15277–15286 (2017).

189. Nguyen, H. N. *et al.* Opening the conformation is a master switch for the dual localization and phosphatase activity of PTEN. *Sci. Rep.* **5**, (2015).

190. Kirihara, T. *et al.* A Human Induced Pluripotent Stem Cell-Derived Tissue Model of a Cerebral Tract Connecting Two Cortical Regions. *iScience* **14**, 301–311 (2019).

191. Martins-Costa, C. *et al.* ARID1B controls transcriptional programs of axon projection in an organoid model of the human corpus callosum. *Cell Stem Cell* **31**, 866-885.e14 (2024).

Abbreviations

Abbreviation	Full name
4HB	four-helix bundle
ADP	adenosine diphosphate
AGC	protein kinase A, protein kinase G, protein kinase C
AKT	protein kinase B
ANP-PNP	adenylyl imidodiphosphate
AP-MS	affinity-purification mass spectrometry
ARPP-16	cAMP-regulated phosphoprotein of 16 kDa
ASD	autism spectrum disorder
AST	active-site tether
ATP	adenosine triphosphate
BRAF	B-Raf proto-oncogene serine/threonine kinase
cAMP	cyclic adenosine monophosphate
Cdc42	cell division control protein 42
CDK2	cyclin-dependent kinase 2
CHB	capped-helix bundle
C-lobe	C-terminal lobe
CLT	C-lobe tether
CRIK	Citron Rho-interacting kinase
C-tail	C-terminal tail
DFG	aspartate-phenylalanine-glycine
DMPK	dystonia myotonica protein kinase
DUF	domain of unknown function
ERK	extracellular signal-regulated kinase
GFP	green fluorescent protein
GTP	guanosine triphosphate
HM	hydrophobic motif
HRD	histidine-arginine-aspartate
INM	interkinetic nuclear migration
IVT	*in vitro* transcription
KO	knock-out
LATS	large tumour suppressor kinase
LIMK1	LIM kinase 1
MAP	microtubule-associated protein
MAPT/Tau	microtubule-associated protein Tau
MAST	microtubule-associated serine/threonine kinase
MCC	mega-corpus callosum syndrome
MCC-CH-CM	mega-corpus callosum syndrome with cerebellar hypoplasia and cortical malformations
MEK1	mitogen-activated protein kinase kinase 1
MOB1	Mps one binder homolog 1
MRCK	myotonic dystrophy kinase-related Cdc42-binding kinase
MS	mass spectrometry

MYPT1	myosin phosphatase target subunit 1
NDD	neurodevelopmental disorder
NDR	nuclear Dbf2-related kinase
N-lobe	N-terminal lobe
NLT	N-lobe tether
PAK	p21-activated protein kinase
PDK1	phosphoinositide-dependent kinase 1
PDZ	PSD-95, Dlg, ZO-1
PHLPP	PH domain leucine-rich repeat protein phosphatase
PIP3	phosphatidylinositol (3,4,5)-triphosphate
PKA	protein kinase A
PKC	protein kinase C
PKD1	protein kinase D1
PKG	protein kinase G
PP2A	protein phosphatase 2A
PTEN	phosphatase and tensin homolog
PTM	post-translational modification
RAS	rat sarcoma
RGC	radial glial cell
ROCK	Rho-associated coiled-coil kinase
TM	turn motif
UTR	untranslated region
WES	whole-exome sequencing
WT	wild-type

Zusammenfassung

Die Entwicklung des Kortex ist ein essentieller Prozess in der Entwicklung, dessen molekulare Programme zeitlich und räumlich streng reguliert sind. Fehler in der Regulierung können zu einer Vielzahl neurologischer Entwicklungsstörungen (NES) führen, welche etwa ein Zehntel der Bevölkerung betreffen. Ein seltenes Mitglied der NES, das Mega-Corpus Callosum Syndrom (MCC), zeichnet sich durch eine Vergrößerung des Corpus Callosum und eine allgemeine Verzögerung in der Entwicklung aus. Die einzig bekannte Ursache dieses Syndroms sind genetische Mutationen in der Mikrotubulin-assoziierten Serin/Threonin Kinase 1 (MAST1). Sowohl MAST1 als auch andere Mitglieder der MAST Kinase Familie werden immer häufiger in Verbindung mit einer Vielzahl an NES und neurologischen Störungen wie Autismus, geistiger Behinderung, Epilepsie und Zerebralparese gebracht. Trotz dessen sind die biologische Funktion und die Wirkmechanismen der MAST Kinase Familie noch weitgehend unbekannt.

Das Ziel dieser Arbeit ist es diese Lücke, durch die Erforschung der MAST Kinase Familie, ihrer Substrate, Interaktionspartner und Mechanismen durch die ihre Aktivierung reguliert wird zu schließen. Wir zeigen, dass 14-3-3η ein Interaktionspartner von MAST1 ist und abhängig von Phosphorylierung an die Aminosäuren S90 und S161 von MAST1 bindet. Weiters zeigen wir, dass die p21-aktivierte Proteinkinase (PAK) in der Signalweiterleitung vor MAST1 steht und diese auf ihrer Aminosäure S90 phosphoryliert, sowie die Fähigkeit von MAST1 zur Autophosphorylierung auf der Aminosäure S161. Durch *in vivo* Phosphoproteomik in Mausmodellen mit mutiertem MAST1 identifizieren wir das Mikrotubulin-assoziierte Protein Tau (MAPT, Tau) als bislang unbekanntes Substrat von MAST1. Zu guter Letzt zeigen wir, dass Mutationen in MAST1 die im Zusammenhang mit Krankheiten stehen entweder die korrekte Faltung oder die Kinaseaktivität von MAST1 stören. Gestützt auf diese Erkenntnisse schlagen wir ein Modell vor, bei dem MAST1 die Verbindung zwischen PAK, einem Regulator des Aktin-Zytoskelettes, und der Umgestaltung der Mikrotubuli durch Tau bildet. Unsere Ergebnisse tragen zu einem besseren Verständnis der MAST Kinasen bei und bilden ein Fundament für zukünftige Studien um die Funktionen und Regulierungsmechanismen dieser Kinasen weiter zu erforschen.